The Dissertation Committee for Ross Edward Falcon
certifies that this is the approved version of the following dissertation:

Creating and Measuring White Dwarf Photospheres in a Terrestrial Laboratory

Committee:

Don E. Winget, Supervisor

Michael H. Montgomery

Gregory A. Rochau

James E. Bailey

Edward L. Robinson

Chris Sneden

Creating and Measuring White Dwarf Photospheres in a Terrestrial Laboratory

by

Ross Edward Falcon, B.S.Ast.; M.A.

DISSERTATION

Presented to the Faculty of the Graduate School of

The University of Texas at Austin

in Partial Fulfillment

of the Requirements

for the Degree of

DOCTOR OF PHILOSOPHY

THE UNIVERSITY OF TEXAS AT AUSTIN

August 2014

Dedicated to Oliver, Alessa, and Emma.

Acknowledgments

Thank you, Don Winget, for your patience and guidance. If I had anyone else besides you as my advisor during my intermediate years as a graduate student – personally the most difficult time of my life – I don't know how I would have stayed in school. Thank you, Mike Montgomery, for providing balanced counterpoint to Don's tutelage. Thank you, Greg Rochau and Jim Bailey, for teaching me, an astronomer with no laboratory experience, how to properly perform experiments and how to conduct myself at a major facility. Thank you, Jeremy Murphy and JJ Hermes, for your graduate brotherhood. Thank you, Seth Redfield, for showing me my first research ropes as an undergraduate and allowing me to witness your passion for science. Thank you, Alan Carlson, for teaching me how to operate in a laboratory. Thank you, Taisuke Nagayama, for being a bottomless resource for knowledge of the scientific method. Thank you, Guillaume Loisel, for always taking time to answer my questions. Thank you, Kurtis Williams, for providing valuable perspective complementing Don and Mike's guidance particularly when I was a young graduate student. Thank you, Matt Gomez, for showing me how to assimilate as a student into the national laboratory environment. Thank you, Jennifer Ellis, Sean Moorhead, and Zach Swindle for being receptive, as undergraduates, to my still-maturing mentorship. Thank you, Thomas Gomez, for joining the project and bringing your enthusiasm. Thank you, Nate Joseph, for being my first friend at Sandia and in Albuquerque and for allowing me into your home. Thank you,

Tom Lockard, for your remote graduate brotherhood. Thank you, Marcelino Vigil, Tom Strizic, and Daniel Sandoval, for providing your expertise and tolerating my requests regarding the gas cell designs. Thank you, Dave Bliss, for happily assisting me in tedious calibration measurements. Thank you, Pier-Emmanuel Tremblay for providing your calculated line profiles. Thank you, Kepler Oliveira and Jay Farihi, for sharing your humble scientific perspective. Thank you, Roger Bengtson, Stephanie Hansen, Roberto Mancini, and Yitzhak Maron, for insightful discussions. Thank you, Keegan Shelton and Jose Villalva, for your careful installation of the gas cell in the *Z* vacuum chamber and for handling the gas fill. Thank you, Linda Nielsen-Weber, for developing so much film. Thank you, Judi James at the Brazosport Planetarium in Clute, TX, for being my first astronomy teacher. Thank you, University of Texas Department of Astronomy and Sandia National Laboratories *Z* Facility team, for your support throughout the years. Thank you, Alan Wootton, for championing our quest for pursuing fundamental science at a national laboratory.

Thank you, Dad and Carrie, for providing me your unique loving support.

Thank you, Mom, for watching over me the entire time.

Preface

I will not attempt to naïvely convince you that my graduate career has been any more of an odyssey than that of anyone else. I will not attempt to convince you that this dissertation deserves to be set apart from those that have come before it or that I am justified in stepping away from the norm, as if an unorthodox path of graduate study grants permission.

To me, though, it has been epic. It has been *an* epic. My graduate study follows a story, as everyone's does, and this story is not merely intimately connected with the learning that has taken place. It *is* the learning. It *is* the people involved. It *is* the progress being made. For this reason, I include a narrative component throughout this dissertation. I beg your patience as I struggle to find the appropriate balance with traditional scientific writing. To create something abominable in the eyes of my mentors while genuinely trying to document Truth would be a grave, personal tragedy.

Don't worry. There's plenty of science to discuss.

Creating and Measuring White Dwarf Photospheres in a Terrestrial Laboratory

Publication No. _____

Ross Edward Falcon, Ph.D.
The University of Texas at Austin, 2014

Supervisor: Don E. Winget

As the ultimate fate of nearly all stars, including our Sun, white dwarfs (WDs) hold rich and informative histories in their observable light. To determine a fundamental parameter of WDs, mass, we perform the first measurement of the average gravitational redshift of an ensemble of WDs. We find a larger mean mass than that determined from the primary and expansive technique known as the *spectroscopic method*. The potential inaccuracy of this method has broad astrophysical implications, including for our understanding of Type 1a supernova progenitors and for constraining the age of the Universe.

This motivates us to investigate the WD atmosphere models used with the spectroscopic method, particularly the input theoretical line profiles, by developing a new experimental platform to create plasmas at WD photospheric conditions ($T_{\rm e} \sim 1\,{\rm eV}, n_{\rm e} \sim 10^{17}\,{\rm cm}^{-3}$). Instead of observing WD spectra to infer the plasma conditions at the surface of the star, we set the conditions and measure the emergent spectra in the laboratory. X-rays from a z-pinch dynamic hohlraum generated

at the *Z* Pulsed Power Facility at Sandia National Laboratories irradiate a gas cell to initiate formation of a large (120x20x10 mm or 24 cm^3) plasma. We observe multiple Balmer lines from our plasma in emission and in absorption simultaneously along relatively long ($\sim$ 120 mm) lines of sight perpendicular to the heating radiation. Using a large, radiation-driven plasma aides us to achieve homogeneity along our observed lines of sight. With time-resolved spectroscopy we measure lines at a range of electron densities that spans an order of magnitude, and we do this within one pulsed power shot experiment. Observing our plasma in absorption not only provides the signal-to-noise to measure relative line shapes, it allows us to measure relative line strengths because the lines share the same lower level population. This constrains the theoretical reduction factors used to describe ionization potential depression or the occupation probabilities associated with these Balmer lines. We compare our measured line shapes with the theoretical ones used in WD atmosphere models as part of the first fruits of this rich experimental platform.

Table of Contents

List of Tables

List of Figures

Chapter 1

Introduction

What is she going to share today? I don't care. It'll be great. It'll be *cool*. She's my big sis, so everything she does or says is cool. By definition. I'm just getting my feet wet with this whole school thing. Don't even do a full day yet. It's a half-day for us. Next year in first grade it'll go longer. So I hear.

Carrie busts in through the door, noticeably tired from marching band practice. Doesn't stop me from ambushing her.

"Tell me about the stars!"

She drops her backpack to the floor, and the thick, sharp thud of a dense book scythes across the den. Mathematics? She lets out a sigh, then a smile. Her second wind. Leaps into the couch, legs crossing in mid flight, proceeds to recount today's lesson in her Astronomy class, a high school course taught at the local junior college's planetarium.

I don't understand any of the details. I'm only five! But I close my eyes and her stories morph into life. The blackness of the inside of my eyelids becomes littered with twinkling lights. I'm suddenly up, up, way up! And I see our planet Earth

below me. It's a ball, and it's spinning! And in the distance, more balls. Planets. All circling the Sun (don't stare). I *feel* the space between things. **Outer space.** There's so much room. Everything's so big, everything's so far, but I see it all! It's so wonderful.

Tell me more!

1.1 Retired Stars

I like to think of white dwarfs (WDs) as retired stars. These objects, having performed the alchemy of turning hydrogen into helium in their cores via thermonuclear fusion (for billions of years), are content to hang up their cleats and relax by simply cooling off with time (Mestel 1952). We participate in extending this analogy by observing these stars to learn from their light, like an eager audience gathered to witness elders disseminate wisdom. We listen (observe) because they have lived it. They have done it before. They tell us what is going to be.

The most massive stars ($\gtrsim 8\,M_\odot$, where $M_\odot$ is the symbol for the mass of the Sun) end their *main sequence* (hydrogen-fusing) lives as supernovae (e.g., Woosley & Weaver 1986; Smartt 2009). However, stars this massive are scarce (e.g., Miller & Scalo 1979). The overwhelming majority of all stars – more than $97\,\%$ – transition out of the main sequence to become WDs (e.g., Fontaine et al. 2001). This includes our Sun. Therefore, WDs are representative.

Our host star, when it comes to mass, is a fairly ordinary main sequence star.

Let us briefly review the prognosis of a main sequence star like our Sun (see, e.g., Chandrasekhar 1939; Salpeter 1955; Iben 1991; Hansen et al. 2004).

1.1.1 Stellar Evolution: Prequel to a White Dwarf

A stars shines because of what happens in its interior (or, as we encounter in Section 1.1.2, because of what *happened* in its interior). Here in its center the star is hot enough and dense enough for nuclear fusion to occur. Hydrogen nuclei combine into helium nuclei, producing photons (light) in the process. During this main sequence phase of its life, which lasts several billion years, helium ash accumulates in the center of the star with hydrogen fusion continuing in a surrounding shell. We refer to it as ash because it cannot yet fuse (burn) into even heavier elements at its temperature and density. With decreased thermal support supplied by fusion in the center of the star, the helium core begins to contract under its own gravity, heating up in the process. This heating causes the rate of hydrogen shell-burning to increase, which puffs up the star, increasing its volume and decreasing its overall density to transition it into the *red giant* phase.

The core is now hotter and denser. It ceases to contract when electron degeneracy pressure prevents it from going any further. Eventually the star becomes sufficiently hot for helium to fuse into carbon and oxygen. In a degenerate environment, though, ignition leads to a thermal runaway, so this event is known as the *helium flash*. For more massive stars ($\gtrsim 5\,M_\odot$), the core is not degenerate. Helium burning is therefore stable and does not flash. The shell-burning process continues with subsequently heavier elements accumulating in the core and sweeping into

concentric burning shells as the stellar interior gets hotter. For stars with masses similar to that of our Sun, the process fails to go beyond helium fusion.

After tens or a few hundreds of millions of years (depending on mass), the red giant phase ends with the envelope of the star becoming no longer gravitationally bound. The star lazily sheds a significant fraction, if not most, of its mass, leaving its glowing hot (effective temperatures can approach $200,000\,\mathrm{K}$; Werner et al. 1991) carbon/oxygen ember of a core nearly naked – a pre-white dwarf star (e.g., Schoenberner 1983; Blöcker 1995).

1.1.2 Stellar Evolution: Life of a Retiree

With nuclear fusion sputtering out, the star has no (significant) mechanism to generate energy. It is now a *white dwarf*, and, like a thermometer removed from a pot of boiling water, exponentially cools, asymptotically approaching the ambient temperature of its environment (outer space). Most of the stellar mass and radius is commandeered by its electron degenerate core, which makes for a fantastic conductor and can be considered isothermal. A thin, non-degenerate envelope blankets the core, and since energy transport is not as efficient here, it regulates the rate of cooling.

The cooling evolution of a WD is relatively slow because, even though the object starts off quite hot, its surface area from which to expel heat is small – comparable in size to that of our Earth. Evolutionary models for single WDs describe in detail how the star cools, taking into account a number of factors, including properties of the progenitor, stellar mass, surface composition and convection, and phase

Table 1.1. Spectral Types of White Dwarfs

Spectral Type	Photosphere
DA	HI
DB	HeI
DC	Continuum
Hot DQ	CI, CII, OI, OII
Cool DQ	C_2
DO	HeII, HeI, H
DZ	Metals

separation and crystallization in the core (e.g., Wood 1995; Althaus & Benvenuto 1998; Montgomery et al. 1999; Salaris et al. 2010; Renedo et al. 2010; Chen & Hansen 2011).

We classify WDs by their surface composition or spectral type as observed in the optical part of the electromagnetic spectrum (see, e.g., Sion et al. 1983). Though the classification scheme undergoes refinements (Liebert & Sion 1994) and discoveries perpetually surprise the community (e.g., Dufour et al. 2007), thus precluding an official, static scheme, we boldly present a compilation of WD spectral types in Table 1.1. The table connects the kinds of WDs with their dominant spectroscopic feature(s) (or, for the DC, lack thereof). In this context, a metal is any element heavier than helium (except for carbon, which has its own designation). Spectral type DA (hydrogen-dominated atmosphere) tops the list since most WDs reside in this category[1]. The next most abundant type is DB (helium-dominated atmosphere). All other types make up trace amounts. Several suffixes can be ap-

pended as well. A DAV, for instance, is a DA white dwarf that is variable, which means that its brightness periodically oscillates in time. Magnetic WDs with and without detectable polarization are denoted with "P" and "H" suffixes, respectively. Sometimes it can be appropriate to hybridize a spectral type when abundances are comparable (i.e., DAZ, DAB, or DBA); the dominant constituent is always first.

Since the photosphere is the part of the WD we can actually see (with our own eyes), it follows that its features supply us with the fundamental stellar atmospheric parameters, namely, effective temperature, $T_{\rm eff}$, and surface gravity, $\log g$, upon which studies in WD astronomy and the rest of astrophysics critically depend. For this reason, the WD photosphere is the focus of this dissertation. Let us peruse a few of the research threads founded upon WD photospheres or atmospheres.

1.2 WD Photospheres/Atmospheres as a Foundation for Astrophysics

Cosmochronology

Since these objects cool with time, the coolest WDs are therefore the oldest. Identifying the coolest WDs puts strict observational constraints, independent of cosmological models, on the ages of stellar populations within our Galaxy and, since it can be no younger than its constituents, the Universe (Winget et al. 1987; Peebles 1993; Hansen et al. 2007). The accuracy with which one determines an

[1]The relative fraction of DAs to non-DAs changes with $T_{\rm eff}$ and is difficult to precisely determine. See, e.g., Greenstein (1986); D'Antona (1987); Fontaine & Wesemael (1987); Tremblay & Bergeron (2008) for discussions.

individual WD age first rests in the accuracy of the $T_{\rm eff}$ measurement. This specifies its temporal location along its cooling evolution, and this evolution significantly depends on the WD mass.

Asteroseismology

Strike a chime, pluck a guitar string, or puff into a trumpet. The pitch and timbre you hear uniquely describe the instrument releasing the music. As such, astronomers apply the same physical principles to diagnose the interiors of stars when instabilities in their envelopes cause their brightnesses (sounds) to vary at regular periods (pitches). For stars that pulsate at multiple periods, the ensemble of frequencies (timbre) paints a picture of their internal composition. We use this to probe the properties of dark matter axions (Bischoff-Kim et al. 2008b; Córsico et al. 2012), constrain the details of crystallization in dense plasmas (Montgomery & Winget 1999; Winget et al. 2009), and measure WD cooling evolution in real time (e.g., Kepler et al. 1991; Mukadam et al. 2013). Asteroseismological studies remain unconstrained and never pass the starting line, however, until they establish surface boundary conditions from accurate atmospheric parameters. See, e.g., Winget & Kepler (2008), and references therein, for a review on WD asteroseismology, including on the various kinds of variable WDs; and Hermes et al. (2012, 2013b,a) for a description of the newly-discovered variable WDs of extremely low mass.

Supernova Progenitors

The initial stellar configuration for a Type Ia supernova is a close binary

system consisting of a massive WD near the Chandrasekhar limit (Chandrasekhar 1931) and a mass-transferring companion. The donation of mass prompts the envelope of the WD to contract and heat, igniting thermonuclear fusion, which adds carbon and oxygen to the core, exceeding the mass limit and thus detonating into a supernova (e.g., Wheeler & Hansen 1971; Whelan & Iben 1973). Since the progenitor conditions of this event – especially the unique mass – are so consistent, the resulting light curves are also consistent, motivating their use as *standard candles* to measure extragalactic distances (e.g., Colgate 1979; Hamuy et al. 1995), which allows for the observation of our accelerating Universe (Riess et al. 1998). The detailed understanding of these supernovae starts with understanding their progenitors (e.g., Wheeler 2012), which depends upon the observed atmospheric conditions of the WD.

1.3 Straddling Two Fields

In the pages to follow I detail the work that has brought me, an astronomer, into the field of experimental physics to perform experiments at a major facility, the *Z* Pulsed Power Accelerator at Sandia National Laboratories. My rise as a laboratory astrophysicist coincides with the development of the *Z* Astrophysical Plasma Properties (ZAPP) Collaboration (Rochau et al. 2014), uniting academia with national laboratories to fruitfully exchange their respective expertise, to uniquely address outstanding puzzles in astrophysics, and to spawn a new generation of scientists possessing skill sets that span multiple fields of physics.

Chapter 2 describes our determination of the mean mass of DA WDs using a

gravitational redshift technique. We find a discrepancy with the mean mass as determined from the spectroscopic method. This result, along with recent modifications to the theoretical line profiles used in WD atmosphere models (e.g., Tremblay & Bergeron 2009), motivate us to perform experiments to test theoretical line profiles of hydrogen at WD photospheric conditions ($T_{\rm e} \sim 1\,{\rm eV}, n_{\rm e} \sim 10^{17}\,{\rm cm}^{-3}$). In Chapter 3 we develop an experimental platform to measure these relative line shapes of hydrogen Balmer lines. The experiments use a z-pinch dynamic hohlraum as an x-ray source to initiate plasma formation inside a gas cell. We continue to evolve the experimental platform, focusing on the gas cell design in Chapter 4. Chapter 5 describes the data acquisition using streaked visible spectroscopy as our primary diagnostic instrument. We elaborate on our data processing and calibration methods. Chapter 6 discusses how we extract line profiles and plasma conditions from our time-resolved spectroscopic data. We present the results of the comparisons of our measured line profiles with theoretical profiles in Chapter 7, summarize our conclusions, and provide an outlook to future work.

Though I don't hang around the observatory nearly as often as I did at the start of my graduate career, I still gaze at the spectral features emanating from white dwarf stellar photospheres, fascinated by the stories – the mysteries – they yearn to share with me. It's just not from atmospheres that reside lifetimes away. It's from ones right here on Earth. Ones that I make.

Chapter 2

Gravitational Redshift in DA White Dwarfs

A young graduate student. I don't know what I'm doing. I've been spinning my wheels. It's January 2009. I'm supposed to do my second-year defense in May. But I don't really have a project, so I certainly don't have any results to report.

Lately I've been fixated on two concepts: gravitational redshift and the SPY survey (I'll discuss this survey in this chapter). I can't remember how I got interested in gravitational redshift, but I find it fascinating – as a way to determine the mass of a white dwarf. I have no clear idea of how to do it, but I just have this *feeling* that something can be said about an ensemble characteristic of gravitational redshifts of white dwarfs. You see, unless you have an independent measure of the space motion of the white dwarf (like if it's in a binary system), it's impossible to disentangle the stellar radial velocity from the gravitational redshift. So you can't derive a mass.

At the same time, I've discovered the SPY survey. And it's such a rich data set. High-resolution. Tons of white dwarfs. There's no other survey like it!

Don and Mike have heard me ranting about these two concepts for our past few meetings. I haven't really had anything productive to say about either of them except that I think they're extremely intriguing. But today our conversation goes further.

It's not even noon and I'm already letting out a heavy sigh of embarrassment as I point out to Don that, once again, we are sporting the same tee-shirt. Thanks, Department of Astronomy, for always re-supplying us with McDonald Observatory apparel at beginnings of semesters, Christmas parties, and other convivial occasions.

I apologize. I take back the sarcasm. The shirts are great, really. It's on me. I'm the one who needs more shirts. More options in the morning.

"Great minds think alike!" Don finds it funny. Sips his coffee.

Mike pays no mind to the trivial exchange.

(I'm paraphrasing the next bit of dialogue.)

"Okay, Ross. But how are you supposed to get a mass from gravitational redshift if the white dwarf is not in a binary?" Mike says this more to himself than to me as an idea starts to coalesce in his brain. But maybe he's tired. He gives up on developing the idea and throws up his arms. "If only we could just average a bunch of stars together."

Don grabs the proto-idea like a baton. His eyes light up. "Wait, Mike. We can!"

Within minutes I'm running back to my office to begin work on an idea, the results of which I'll present at my second-year defense four months from now.

Dictating the life and evolution of a star, mass is one of the most fundamental stellar properties. There are several methods for mass determination of white dwarfs (WDs), though each has its limitations.

The most-widely used WD mass determination method involves comparing predictions from atmosphere models with observations to obtain effective temperatures ($T_{\rm eff}$) and/or surface gravities ($\log g$). One can then compare these quantities with predictions from evolutionary models (e.g., Althaus & Benvenuto 1998; Montgomery et al. 1999). Shipman (1979), Koester et al. (1979), and McMahan (1989) use radii determined from trigonometric parallax measurements along with $T_{\rm eff}$ from photometry to determine masses. Of course this technique is limited to target stars with measured parallaxes, so users of photometry have more often used observed color indices, or magnitudes through broadband (hundreds or thousands of Å in visible or infrared wavelengths, respectively) filters, to determine both $T_{\rm eff}$ and $\log g$ (e.g., Koester et al. 1979; Wegner 1979; Shipman & Sass 1980; Weidemann & Koester 1984; Fontaine et al. 1985). With the exception of the parallax variant (Kilic et al. 2008), the photometric method is seldom used in recent WD research.

Another variant of this method uses mainly spectroscopic rather than photometric observations (e.g., Bergeron et al. 1992; Finley et al. 1997; Liebert et al.

2005). With more recent large-scale surveys, such as the European Southern Observatory (ESO) SN Ia progenitor survey (SPY; Napiwotzki et al. 2001) and the Sloan Digital Sky Survey (SDSS; York et al. 2000), the comparison of observed WD spectra with spectral energy distributions of theoretical atmosphere models has become the primary WD mass determination method, yielding masses for thousands of WDs (e.g., Koester et al. 2001; Kleinman et al. 2004; Eisenstein et al. 2006; Kepler et al. 2007; Limoges & Bergeron 2010; Kleinman et al. 2013).

This spectroscopic method, however, is still developing. Kowalski & Saumon (2006) improve the interpretation of cool DA (hydrogen-dominated; see Table 1.1) atmospheres by accounting for the opacity due to the far red wing of the hydrogen Lyα absorption line. Independent from this effect, cool WDs have been particularly difficult to analyze (Bergeron et al. 2007; Koester et al. 2009a; Tremblay et al. 2010; Saumon et al. 2014). For a number of years an unphysical increase in the derived mean surface gravity (and mass) of DAs with decreasing effective temperature appeared in spectroscopic studies (e.g., Liebert et al. 2005; Kepler et al. 2007; DeGennaro et al. 2008). Recent work in 3D modeling of convection in DA atmospheres stymies this artifact (Tremblay et al. 2011b, 2013a,b). Yet another important component of atmosphere models – line profiles – continues to be the subject of investigation (Tremblay & Bergeron 2009; Santos & Kepler 2012).

With the spectroscopic method in constant flux and new work resulting in significant systematic changes to our determination of WD properties (e.g., Tremblay & Bergeron 2009), we look to other mass determination methods that are independent of atmosphere models to constrain or benchmark the accuracy of this

primary method. One is the astrometric technique (e.g., Gatewood & Gatewood 1978). Another is pulsational mode analysis (e.g., Winget et al. 1991). Unfortunately, neither of these methods are widely applicable to WDs. The former requires stellar systems with multiple stars, and the latter is limited to WDs and pre-WDs which lie in a narrow $T_{\rm eff}$ and $\log g$ parameter space of pulsational instability.

Another method that is mostly independent of atmosphere models uses the gravitational redshift of absorption lines. The difficulty in disentangling the stellar radial velocity shift from the gravitational redshift has caused this method to only be used for WDs in common proper motion binaries or open clusters (Greenstein & Trimble 1967; Koester 1987; Wegner & Reid 1991; Reid 1996; Silvestri et al. 2001). The simplicity of this method, however, prompts us to extend the investigation beyond those cases.

This chapter details the work of Falcon et al. (2010b). By using a large, high-resolution spectroscopic data set, we circumvent the radial velocity–gravitational redshift degeneracy to measure a *mean* gravitational redshift of WDs in our sample and use that to arrive at a mean mass. We uncover an intriguing agreement with the mean DA WD mass of Tremblay & Bergeron (2009), whose newly calculated line profiles systematically increase masses determined using the spectroscopic method compared to the masses resulting from previously used line profiles. This becomes a main motivator for our laboratory work of measuring hydrogen line profiles from photoionized plasmas (Falcon et al. 2010a, 2013a,b).

2.1 Gravitational Redshift

In the weak-field limit, the general relativistic effect of gravitational redshift (z) can be understood, classically, as the energy (E) lost by a photon as it escapes a gravitational potential (Φ) well:

$$z = \frac{-\Delta E}{E} = \frac{-\Phi}{c^2}. \tag{2.1}$$

The fractional change in energy can be written as a fractional change in observed wavelength ($-\Delta E/E = \Delta\lambda/\lambda$). In our case, the gravitational potential is at the surface of a WD of mass M and radius R. In terms of a velocity, the gravitational redshift is

$$v_{\rm g} = \frac{c\Delta\lambda}{\lambda} = \frac{GM}{Rc}, \tag{2.2}$$

where G is the gravitational constant and c is the speed of light.

For WDs, $v_{\rm g}$ is comparable in magnitude to the stellar radial velocity, $v_{\rm r}$, both of which sum to give the apparent velocity we measure from absorption lines: $v_{\rm app} = v_{\rm g} + v_{\rm r}$. These two components cannot be explicitly separated for individual WDs without an independent $v_{\rm r}$ measurement or mass determination.

The method in this chapter is to break this degeneracy not for individual targets but for the sample as a whole. We make the assumption that our WDs are a comoving, local sample. After we correct each $v_{\rm app}$ to the local standard of rest (LSR), only random stellar motions dominate the dynamics of our sample. We assume, for the purposes of this investigation, that these average out. Thus, the mean apparent velocity equals the mean gravitational redshift: $\langle v_{\rm app}\rangle = \langle v_{\rm g}\rangle$. The idea of averaging over a group of WDs to extract a mean gravitational redshift is

not new (Greenstein & Trimble 1967), but the availability of an excellent data set prompts its exploitation. We address the validity of the comoving approximation in Section 2.3.1.

2.2 Observations

We use spectroscopic data from SPY. These observations, taken using the UV-Visual Echelle Spectrograph (UVES; Dekker et al. 2000) at Kueyen, Unit Telescope 2 of the ESO Very Large Telescope (VLT) array, constitute the largest, homogeneous, high-resolution (0.36 Å or $\sim 16\,\mathrm{km\ s^{-1}}$ at Hα) spectroscopic data set for WDs. We obtain reduced data online through the publicly available ESO Science Archive Facility (see Napiwotzki et al. (2001) for details on the data reduction).

2.2.1 Sample

As explained in Napiwotzki et al. (2001), targets for the SPY sample come from the WD catalog of McCook & Sion (1999), the Hamburg ESO Survey (HE; Wisotzki et al. 2000; Christlieb et al. 2001), the Hamburg Quasar Survey (Hagen et al. 1995; Homeier et al. 1998), the Montreal-Cambridge-Tololo survey (MCT; Lamontagne et al. 2000), and the Edinburgh-Cape survey (EC; Kilkenny et al. 1997). The magnitude of the targets is limited to $B < 16.5$, where B follows the Johnson-Morgan photometric system (Johnson & Morgan 1953).

Our main sample consists of 449 analyzed hydrogen-dominated WDs (see Figure 2.1 for the distribution of targets in Galactic coordinates). This is the subset of the SPY sample that meets our sample criteria (explained below) and that shows

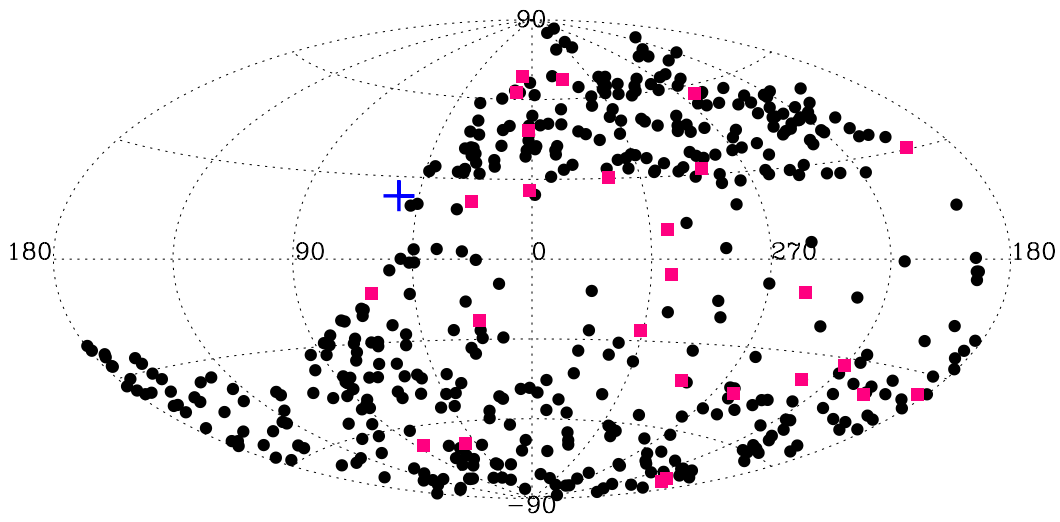

Figure 2.1 Distribution of targets in Galactic longitude, l, and latitude, b. We mark the targets in our main sample as black points and the thick disk WDs as pink squares. We indicate the direction of the movement of the Sun with respect to the LSR (blue cross; Kerr & Lynden-Bell 1986). Since the observations are from the ESO VLT in the Southern Hemisphere, no targets with a declination above $+30^{\circ}$ are in our sample, hence the gap in the left side of the plot.

measurable $v_{\rm app}$ in the Hα (and Hβ) line cores while not showing measurable $v_{\rm app}$ variations in time. A variable velocity across multiple epochs of observation suggests binarity. The method of SPY to search for double degenerate systems is to detect variable radial velocity. For our study, however, we are interested only in non-binary WDs since these presumably have no radial velocity component in addition to random stellar motion after being corrected to the LSR. We exclude known double degenerates and common proper motion binary systems (Finley & Koester

1997; Jordan et al. 1998; Maxted & Marsh 1999; Maxted et al. 2000; Silvestri et al. 2001; Koester et al. 2009b) even if we do not find them to show variable $v_{\rm app}$.

We choose "normal" DAs (criterion 1) from Koester et al. (2009b). Classification as a normal DA does not include WDs that exhibit He absorption in their spectra in addition to H absorption, and it does not include magnetic WDs.

In Falcon et al. (2012) we investigate a sample of 32 non-binary helium-dominated WDs. This includes the first gravitational redshift study of a group of WDs without visible hydrogen lines.

For our main sample, we are also only interested in thin disk WDs (criterion 2), so we exclude halo and thick disk candidates as kinematically classified by Pauli et al. (2006) and Richter et al. (2007). We assume the rest are thin disk objects, the most numerous Galactic component (for descriptions of stellar populations, see, e.g., Binney & Merrifield 1998). Our sample selection is also consistent with the results for the targets in common with Sion et al. (2009). Richter et al. (2007) find only 2% and 6% of their 632 DA WDs from SPY to be from the halo and thick disk, respectively. For WDs within 20 pc, Sion et al. (2009) find no evidence for halo objects and virtually no thick disk objects. We note that unique identification of population membership for WDs is difficult and sometimes not possible because of ambiguous kinematical properties (e.g., Pauli et al. 2003). Based on corrections for these intrinsic contaminations by Napiwotzki (2009), we expect any residual contamination in our sample to be at most $\sim 6\%$. A contamination this size will have a negligible impact on our conclusions. We explain the significance of requiring thin disk WDs in Section 2.3.1, and we explore a mini-sample of thick disk

WDs in Section 2.4.4.

The gravitational redshift method becomes very difficult for hot DAs with $50,000\,\mathrm{K} \gtrsim T_{\mathrm{eff}} \gtrsim 40,000\,\mathrm{K}$ (see the T_{eff} gap in Figure 2.7). As the WD cools through this T_{eff} range, the Balmer line core, which we use to measure v_{app} (Section 2.3), disappears as it transitions from emission to absorption; fortunately only $\sim 5\%$ of the DAs from SPY lie in this range.

2.3 Velocity Measurements

In the wings of absorption lines, and in particular, for the hydrogen Balmer series, the effects of collisional broadening cause asymmetry, making it difficult to measure a velocity centroid (Shipman & Mehan 1976; Grabowski et al. 1987). These effects are much less significant, however, in the sharp, non-LTE line cores formed in the highest levels of the atmosphere (greatest stellar radii) where pressures are lower, and furthermore with decreasing principal quantum number, making both the Hα and Hβ line cores suitable options for measuring an apparent velocity, v_{app}. Higher-order Balmer lines are intrinsically weaker (the Hγ line core, for example, is seldom observable in our data), so finite signal-to-noise (S/N) prevents the number of observable Hβ line cores from matching the number of observable Hα line cores.

We measure v_{app} for each target in our sample by fitting a Gaussian profile to the Hα line core using GAUSSFIT, a nonlinear least-squares fitting routine in IDL (see Figure 2.2 for an example). When available, we combine this measurement with that of the Hβ line core centroid as a mean weighted according to the

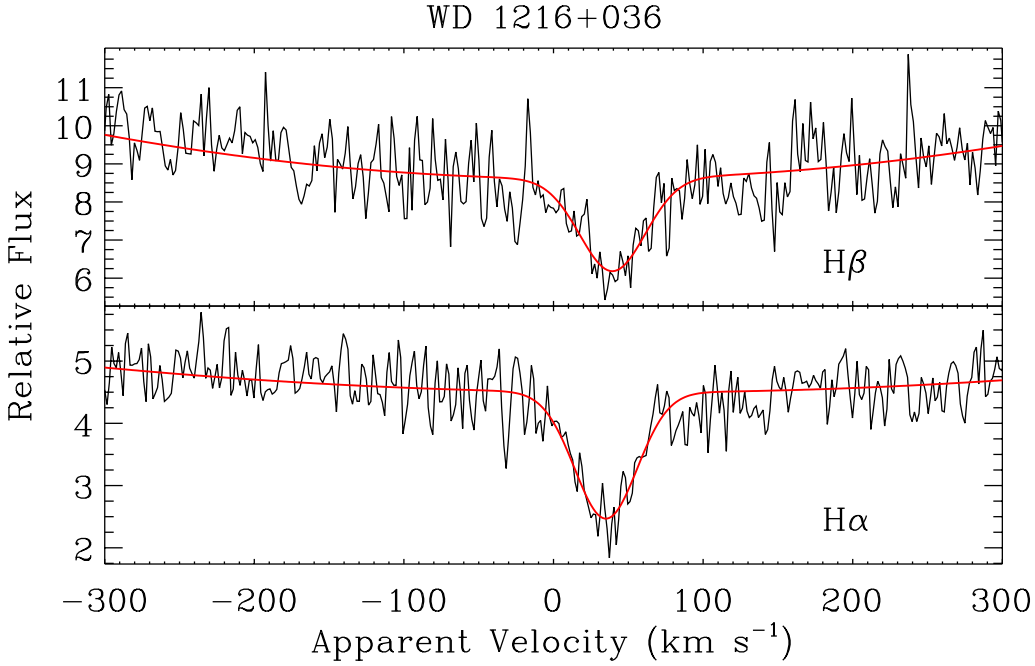

Figure 2.2 Example UVES spectrum for a target in our sample. We measure $v_{\rm app}$ by fitting Gaussian profiles (solid, red lines) to the non-LTE Balmer line cores using a nonlinear least-squares fitting routine. For context we extend the fits beyond the line cores using a 2$^{\rm nd}$-order polynomial. The line cores are well-resolved, allowing for precise centroid determinations.

uncertainties returned by the fitting routine. We include Hβ line core centroid information in 372 of our 449 $v_{\rm app}$ measurements. If multiple epochs of observations exist, we combine these measurements as a weighted mean as well. Apparent velocity measurements of a given observation (i.e., Hα and Hβ line core centroids) are combined before multiple epochs.

Table 2.1 (full version available online; Falcon et al. 2010b) shows our measured $v_{\rm app}$ for Hα and Hβ (when observed) for each observation.

Table 2.1. Apparent Velocity Measurements for Normal DA WDs

Target	Adopted		Date	Time	LSR Correction	Hα		Hβ		Observation	
	$v_{\rm app}$ (km s^{-1})	$\delta v_{\rm app}$ (km s^{-1})	(UT)	(UT)	(km s^{-1})	$v_{\rm app}$ (km s^{-1})	$\delta v_{\rm app}$ (km s^{-1})	$v_{\rm app}$ (km s^{-1})	$\delta v_{\rm app}$ (km s^{-1})	$v_{\rm app}$ (km s^{-1})	$\delta v_{\rm app}$ (km s^{-1})
WD 0000-186	24.530	0.015	2000.09.16	04:53:07	-3.511	24.515	1.267	24.696	4.013	24.531	0.073
			2000.09.17	03:27:31	-3.825	24.190	0.742	29.329	4.231	24.343	1.236
HS 0002+1635	23.518	2.450	2002.12.02	01:07:24	-22.829	23.518	2.450	...	...	23.518	2.450
WD 0005-163	15.006	0.005	2000.09.16	03:31:59	-2.013	15.057	1.892	14.814	3.648	15.006	0.140
			2002.08.04	10:00:19	16.515	15.921	1.860	9.051	4.473	14.907	3.445
WD 0011+000	25.655	0.106	2000.07.14	07:14:10	28.209	23.079	0.949	20.950	2.568	22.823	0.978
			2000.07.17	07:38:21	27.631	25.660	0.657	25.542	4.107	25.657	0.025
WD 0013-241	15.760	0.061	2000.09.16	02:44:05	-3.848	15.754	1.063	15.797	2.591	15.760	0.020
			2000.09.17	01:52:24	-4.237	13.188	1.268	10.630	2.367	12.617	1.505
WD 0016-258	44.969	1.523	2000.09.16	03:01:00	-4.332	45.801	1.451	...	...	45.801	1.451
			2000.09.17	02:09:57	-4.713	44.016	2.194	39.586	6.581	43.573	1.879
WD 0016-220	10.875	1.715	2000.09.16	05:11:37	-2.989	12.101	0.868	16.054	1.894	12.788	2.117
			2000.09.17	03:47:05	-3.294	10.506	0.742	7.857	1.757	10.105	1.343
WD 0017+061	-1.247	3.824	2002.09.26	07:34:49	2.674	-0.139	2.876	-7.848	7.022	-1.247	3.824
WD 0018-339	30.744	0.565	2002.09.15	02:14:27	-6.478	31.118	1.042	29.443	2.256	30.823	0.901
			2002.09.18	02:33:07	-7.790	30.220	1.117	21.817	2.406	28.729	4.539
WD 0024-556	84.029	2.130	2000.08.03	09:18:35	-1.148	84.420	1.490	78.216	5.749	84.029	2.130

Note. — See Falcon et al. (2010b) for this table in its entirety. A portion is shown here for guidance regarding its form and content.

2.3.1 Comoving Approximation

We measure a mean gravitational redshift by assuming that our WDs are a comoving, local sample. With this assumption, only random stellar motions dominate the dynamics of our targets; this falls out when we average over the sample.

For this assumption to be valid, at least as an approximation, our WDs must belong to the same kinematic population; in the case of this work, this is the thin disk. We achieve a comoving group by correcting each measured $v_{\rm app}$ to the kinematical LSR described by Standard Solar Motion (Kerr & Lynden-Bell 1986).

There are reasons to believe that the targets in our sample will *not* significantly lag behind our choice of LSR due to asymmetric drift. Although WDs are considered "old" since they are evolved stars, it is the total age of the star (main sequence lifetime, $\tau_{\rm nuc}$, and cooling time, $\tau_{\rm cool}$) that is of consequence. WDs with $M \sim 0.6\,M_{\odot}$ have main sequence progenitors with $M \sim 2\,M_{\odot}$ (e.g., Williams et al. 2009). This corresponds to $\tau_{\rm nuc} \sim 1.4\,$Gyr (Girardi et al. 2000). $\tau_{\rm cool}$ is on the order of a few hundred million years for most of the WDs in our sample ($T_{\rm eff}$ of a few times $10^4\,$K) and $\sim 2.5\,$Gyr for our coolest WDs ($T_{\rm eff} \sim 7000\,$K); the total age spans a range of roughly 1.5 to 4 Gyr (F/G type stars).

We also make certain that our WDs reside at distances that are small when compared to the size of the Galaxy, thereby making systematics introduced by the Galactic kinematic structure negligible. Figure 2.3 shows the distances (from spectroscopic parallax; Pauli et al. 2006) to the targets in our sample. The mean distance of the targets in the histogram is less than 100 pc, and all are within 600 pc. Over

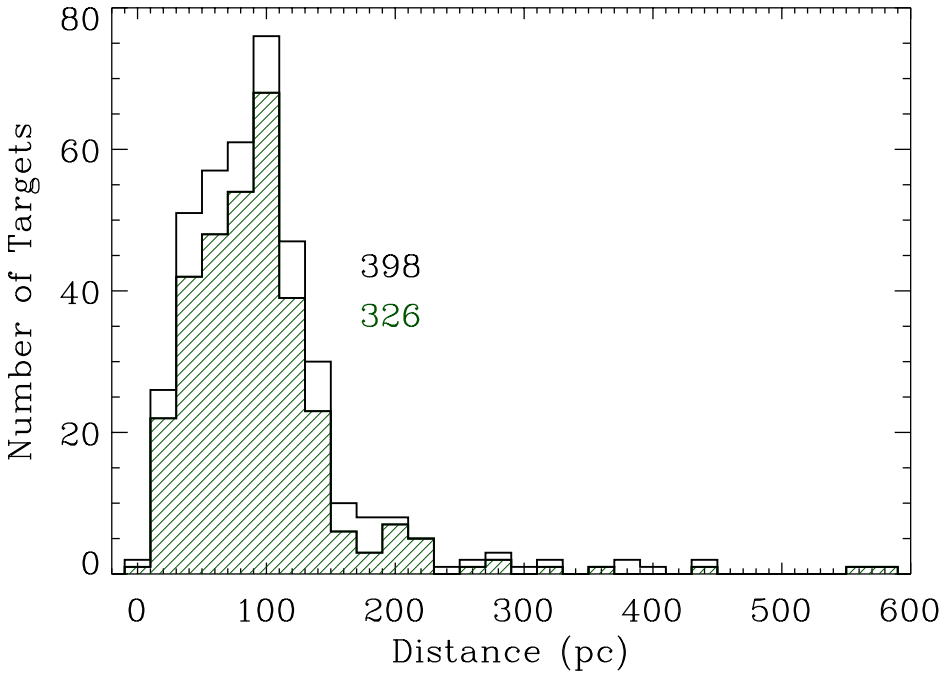

Figure 2.3 Distribution of distances (from spectroscopic parallax) of SPY WDs from Pauli et al. (2006). The shaded, green histogram shows the targets in our sample. The mean is 94.5 pc; the median is 89.2 pc. These distances are short enough to support our comoving approximation. We list the number of targets in each distribution.

these distances, the velocity dispersion with varying height above the disk remains modest (Kuijken & Gilmore 1989), and differential Galactic rotation is negligible (Fich et al. 1989). In Section 2.4.3.2, we perform an empirical check to the assumptions made in this section.

2.4 Results

2.4.1 Mean Apparent Velocities

We present the distribution of our measured apparent velocities in Figure 2.4. Table 2.1 lists individual apparent velocity measurements, and mean apparent velocities are in Table 2.2.

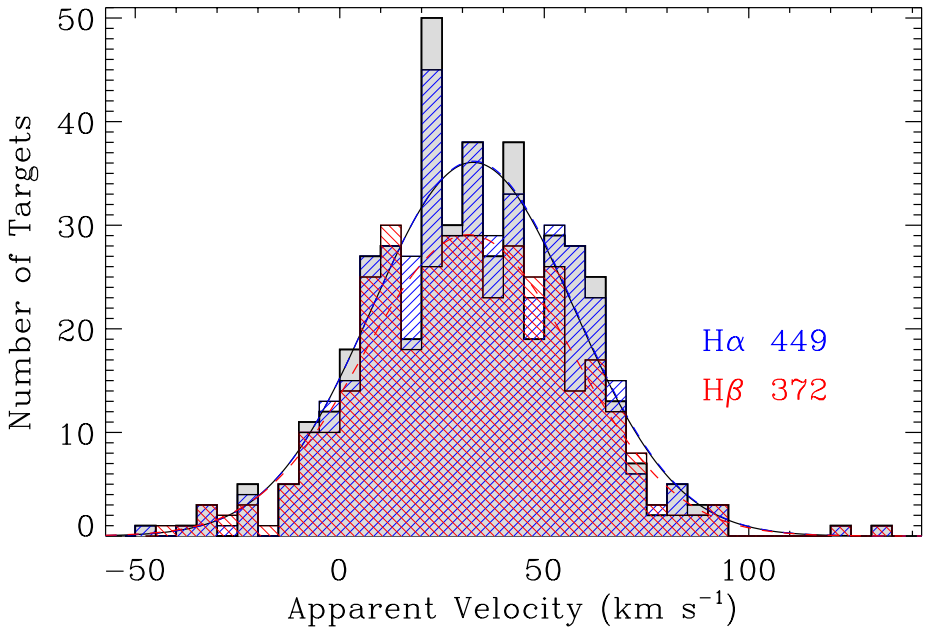

Figure 2.4 Histograms of measured apparent velocities, $v_{\rm app}$, with a bin size of 5 km s^{-1}. The mean $v_{\rm app}$ for all targets in our sample (shaded) is 32.57 ± 1.17 km s^{-1}; the median is 31.94 km s^{-1}; the standard deviation is 24.84 km s^{-1}. Using $v_{\rm app}$ measured from Hα only (red, descending lines): the mean $v_{\rm app}$ is 32.69 ± 1.18 km s^{-1}; the median is 32.05 km s^{-1}; the standard deviation is 24.87 km s^{-1}. Using $v_{\rm app}$ measured from Hβ only (blue, ascending lines): the mean $v_{\rm app}$ is 31.47 ± 1.32 km s^{-1}; the median is 31.55 km s^{-1}; the standard deviation is 25.52 km s^{-1}. The overplotted curves are the Gaussian distribution functions used to determine Monte Carlo uncertainties. We list the number of targets in each distribution.

Table 2.2. Mean Apparent Velocities

Sample	Number of WDs	$\langle v_{\rm app} \rangle$ (km s^{-1})	$\delta\langle v_{\rm app} \rangle$ (km s^{-1})	$\sigma_{v_{\rm app}}$ (km s^{-1})	$\langle \delta v_{\rm app} \rangle$ (km s^{-1})	$\langle M/R \rangle$ ($M_\odot/R_\odot$)	$\delta\langle M/R \rangle$ ($M_\odot/R_\odot$)
Main	449	32.57	1.17	24.84	1.51	51.19	1.84
Hα	449	32.69	1.18	24.87	1.78	51.37	1.85
Hβ	372	31.47	1.32	25.52	3.17	49.45	2.07
Thick	26	32.90	9.59	48.99	1.57	51.70	15.07

Though our main method uses information from both the Hα (Column 7 of Table 2.1) and Hβ (Column 9) line cores to determine $v_{\rm app}$ for a given observation (Column 11), we also perform our analysis using Hα only and Hβ only. We measure Hβ line core centroids for 372 of our 449 targets.

Figure 2.5 shows the distribution of measurement uncertainties associated with each target. Hβ centroid determinations are typically less precise than those for Hα (see Column 6 of Table 2.2), which is expected since the Hα line core is nearly always better defined. We find that the improved precision achieved by combining Hα and Hβ information is not significant when determining the uncertainties to our mean apparent velocities. These uncertainties are dominated by sample size. In fact, we must increase (worsen) our typical measurement uncertainty of $\sim$ 2–10 km s^{-1} to note a $\sim 7\%$ increase in the uncertainty of the mean; a significant increase to measurement uncertainties of ~ 50 km s^{-1} enlarges the uncertainty of the mean by a little more than a factor of two. Thus, using only Hα (or Hβ) centroids is sufficient for the kind of investigation employed in this chapter, and lower-resolution observations are also suitable as long as the Balmer line core is resolved.

The quoted uncertainties of the mean apparent velocities (Column 4 of Ta-

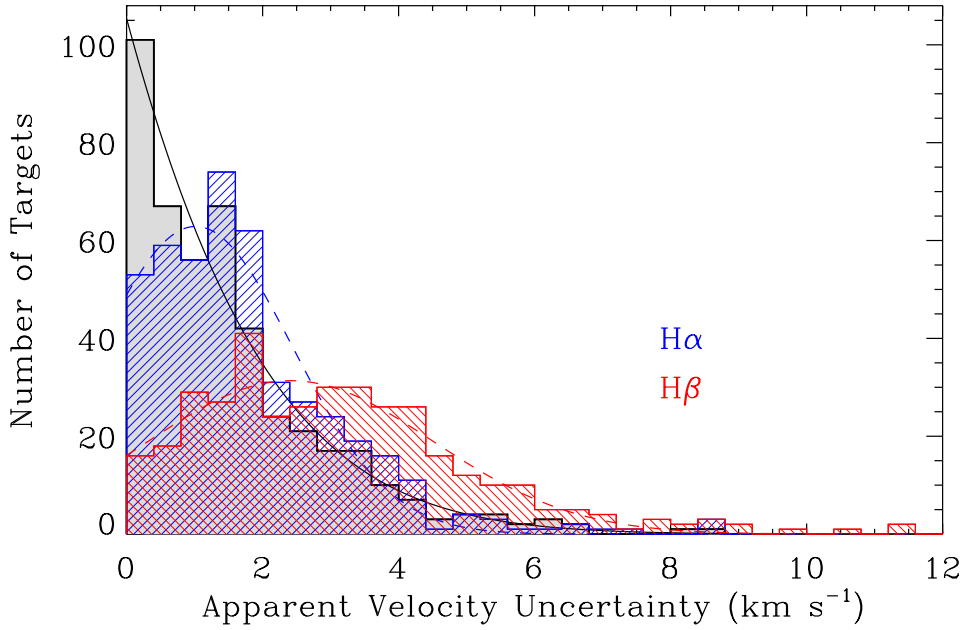

Figure 2.5 Histograms of apparent velocity measurement uncertainties, $\delta v_{\rm app}$, corresponding to the samples in Figure 2.4. The bin size is 0.4 km s^{-1}. The overplotted curves are the empirical distribution functions used to determine Monte Carlo uncertainties. Note that measurements of the Hα line core are more precise than for Hβ. For aesthetics, we leave off two Hβ $\delta v_{\rm app}$ of 13.06 and 17.57 km s^{-1}.

ble 2.2) come from Monte Carlo simulations. For each sample, we recreate a large number of instances (10,000) of the $v_{\rm app}$ distribution by randomly sampling from a convolution of the empirical $v_{\rm app}$ distribution (Gaussian characterized by the parameters in Columns 3 and 5 of Table 2.2) and the empirical measurement uncertainty distribution. We adopt the standard deviation of the resulting simulated mean values as our formal uncertainties. Since the input distributions for our simulations are empirical, our uncertainties are subject to the normal limitations of Frequentist

Table 2.3. Mean Masses

Sample	Number of WDs	$\langle v_{\rm app}\rangle$ (km s^{-1})	$\delta\langle v_{\rm app}\rangle$ (km s^{-1})	$\langle T_{\rm eff}\rangle$ (K)	$\sigma_{T_{\rm eff}}$ (K)	$\langle M\rangle$ ($M_\odot$)	$\delta\langle M\rangle$ ($M_\odot$)
Main	449	32.57	1.17	19400	9950	0.647	$^{+0.013}_{-0.014}$
Thick	26	32.90	9.59	19960	11060	0.652	$^{+0.097}_{-0.119}$
Hot[a]	366	31.61	1.22	21670	9700	0.640	0.014
Cool[a]	75	37.50	3.59	9950	1090	0.686	$^{+0.035}_{-0.039}$

[a]"Hot" refers to WDs with $T_{\rm eff} > 12,000$ K and "cool" to WDs with $12,000\,{\rm K} > T_{\rm eff} > 7000$ K.

statistics. We plot the empirical distribution of our main sample in Figure 2.4 (black curve) along with the distributions for the Hα (dashed, blue curve) and Hβ (dashed, red curve) samples. The corresponding empirical distributions of our measurement uncertainties are in Figure 2.5.

For convenience, Table 2.2 also lists the quantity $\langle M/R\rangle$, which is proportional to $\langle v_{\rm g}\rangle$ (Equation 2.2) and, as we argue in Section 2.3.1, $\langle v_{\rm app}\rangle$.

2.4.2 Mean Masses

The mean apparent velocity, $\langle v_{\rm app}\rangle$, (or $\langle M/R\rangle$) is our fundamental result since it is this quantity that is model independent. To translate this to a mean mass (Table 2.3), we must invoke two dependencies: (1) we need an evolutionary model to give us a mass-radius relation, and (2) since the WD radius does slightly contract during its cooling sequence, we need an estimate of the position along this track for the average WD in our sample (i.e., a mean $T_{\rm eff}$).

Our evolutionary models use $M_{\rm He}/M_\star = 10^{-2}$ and $M_{\rm H}/M_\star = 10^{-4}$ for the surface-layer masses; these are canonical values derived from evolutionary studies (e.g., Lawlor & MacDonald 2006). See Montgomery et al. (1999) for a more complete description of our models. Our dependency on evolutionary models is small. We are interested in the mass-radius relation from these models, and this is relatively straightforward since WDs are mainly supported by electron degeneracy pressure, making the WD radius a weak function of temperature. We estimate that varying the C/O ratio in the core affects the radius by less than 0.5%, whereas changing $M_{\rm H}/M_\star$ from 10^{-4} to 10^{-8} results in about a 4% decrease in radius. See Section 2.4.3.1 for more discussion on the dependency of the hydrogen layer mass.

Figure 2.6 plots M/R versus $T_{\rm eff}$ with cooling tracks from evolutionary models for a range of WD masses. We use $\langle T_{\rm eff}\rangle = 19,400 \pm 300\,{\rm K}$ from the spectroscopically determined values of Koester et al. (2009b) (see Figure 2.7), and, after plotting $\langle M/R\rangle$ from Table 2.2, we interpolate to arrive at a mean mass of $0.647^{+0.013}_{-0.014}\,M_\odot$ for 449 non-binary thin disk normal DA WDs from the SPY sample.

To compare this result with that of the spectroscopic method, we use atmospheric parameters, $T_{\rm eff}$ and $\log g$, from Koester et al. (2009b) along with the mass-radius relation from evolutionary models to derive individual masses for 441 of the targets in our sample (Koester et al. (2009b) did not publish individual WD masses). We derive a sharply peaked mass distribution (Figure 2.8) with width (not uncertainty) $\sigma = 0.13\,M_\odot$ and a mean mass of $0.575 \pm 0.002\,M_\odot$ – significantly lower than the value we obtain from the gravitational redshift method. We com-

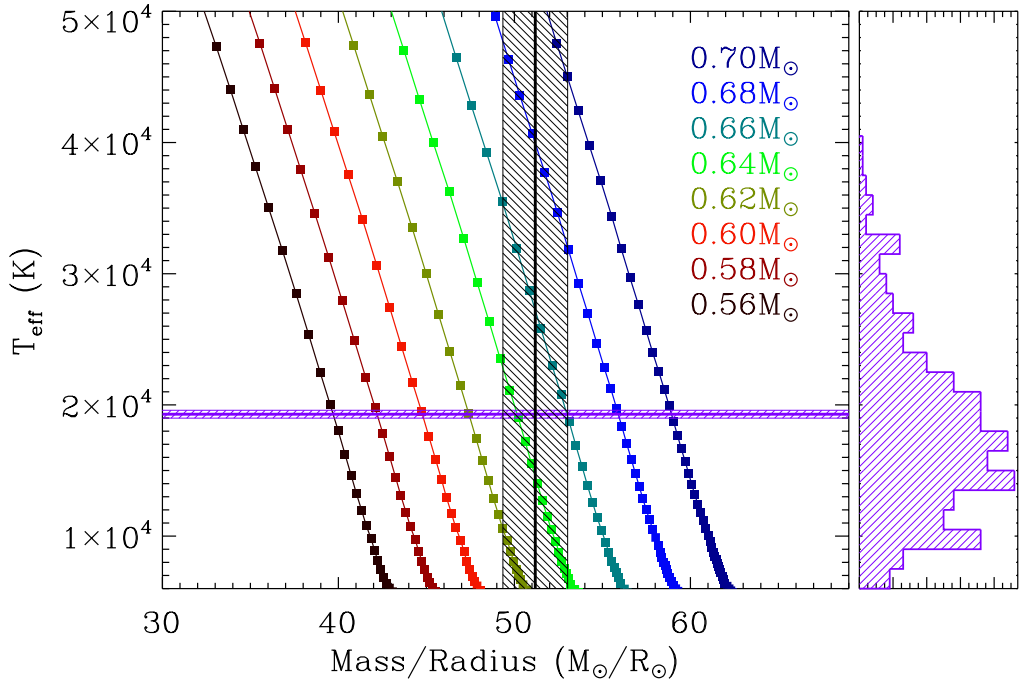

Figure 2.6 Left: plot of M/R versus $T_{\rm eff}$ with cooling tracks from evolutionary models for a range of WD masses. The intersection of the mean measured apparent velocity, $v_{\rm app}$, (vertical, black line) and mean $T_{\rm eff}$ from Figure 2.7 (horizontal, purple line) indicates a mean mass of $0.647^{+0.013}_{+0.014}\,M_{\odot}$. Right: a version of Figure 2.7 with an abbreviated temperature range. We leave off 13 WDs with $T_{\rm eff} > 50,000\,$K from the plot.

pute the uncertainty of the mean using Monte Carlo simulations following the same method described in Section 2.4.1, except instead of using a single Gaussian to represent the mass distribution, we use multiple Gaussians (curve in Figure 2.8).

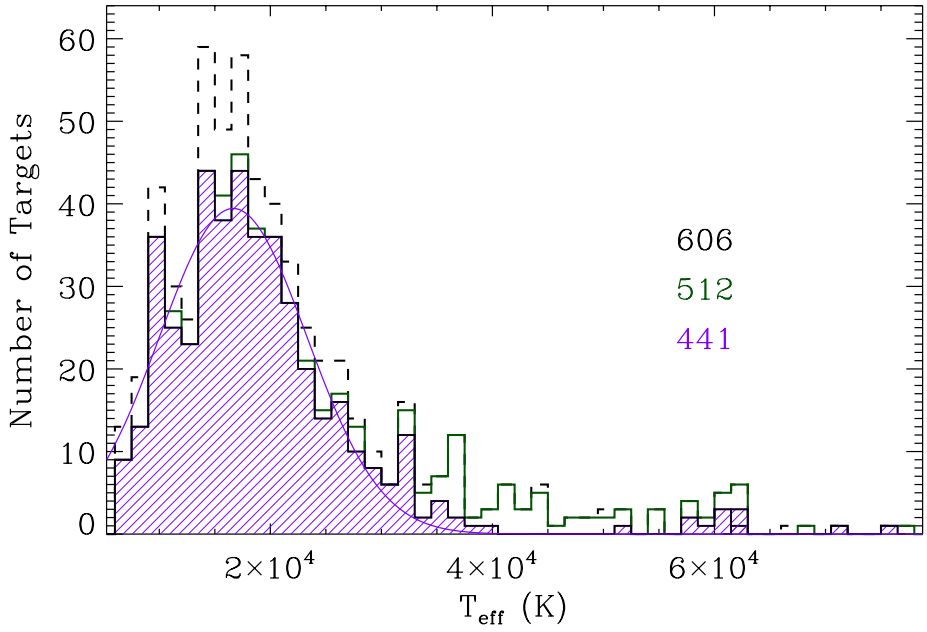

Figure 2.7 Distribution of spectroscopically determined $T_{\rm eff}$ of normal DAs from Koester et al. (2009b, dashed, black histogram). The bin size is 1500 K. The solid, green histogram shows the non-binary thin disk SPY targets, and the shaded, purple histogram shows the targets in our sample. The mean is $19,400 \pm 300$ K; the median is 17,611 K; the standard deviation is 9950 K. The overplotted curve is the empirical distribution function used to determine Monte Carlo uncertainties. We list the number of targets in each distribution.

2.4.3 Systematic Effects

2.4.3.1 From Evolutionary Models

The hydrogen layer masses in DAs are believed to be in the range of $10^{-4} \gtrsim M_{\rm H}/M_{\star} \gtrsim 10^{-8}$, constrained by hydrogen shell burning in the late stages of stellar evolution (Althaus et al. 2002; Lawlor & MacDonald 2006) and convective mixing (Fontaine & Wesemael 1997). In their asteroseismological studies, Bischoff-Kim

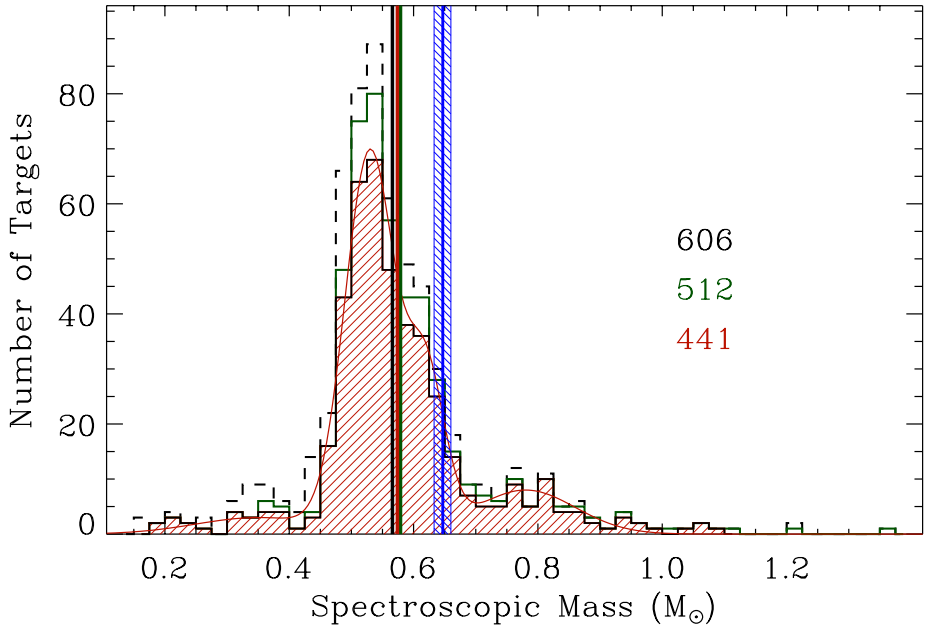

Figure 2.8 Distribution of spectroscopic masses of normal DAs from Koester et al. (2009b) we derive using the published atmospheric parameters, $T_{\rm eff}$ and $\log g$, (dashed, black histogram). The bin size is $0.025\,M_{\odot}$. The solid, green histogram shows the non-binary thin disk SPY targets, and the shaded, orange histogram shows the targets in our sample. The means are $0.567 \pm 0.002\,M_{\odot}$ (vertical, black line), $0.580 \pm 0.002\,M_{\odot}$ (vertical, green line), and $0.575 \pm 0.002\,M_{\odot}$ (vertical, orange line), respectively. Note that the mean spectroscopic masses are similar, indicating that the application of our sample criteria to SPY is not introducing significant additional systematic effects. All the means are also significantly less than the mean mass derived from the gravitational redshift method (vertical, blue line). The overplotted curve is the empirical distribution function used to determine Monte Carlo uncertainties. We list the number of targets in each distribution.

et al. (2008a) also find evidence to support this range of hydrogen layer masses, and this is consistent with the results of Castanheira & Kepler (2009).

Our evolutionary models use the fiducial value of $M_{\rm H}/M_{\star} = 10^{-4}$ for

"thick" hydrogen layers. First, this is suggested by the pre-WD evolutionary models of, e.g., Lawlor & MacDonald (2006), who find that the overwhelming majority of their DA models have thick hydrogen layers. Second, if thin layers were the norm, then convective mixing below 10,000 K would lead to a disappearance of DAs at these temperatures (Fontaine & Wesemael 1997). Both of these reasons lead us to choose thick hydrogen layers for our models.

We find that using a mid-range hydrogen layer mass of $M_{\rm H}/M_\star = 10^{-6}$ decreases the mean mass we derive for our main sample by $0.012\,M_\odot$, while using a thin layer mass of $M_{\rm H}/M_\star = 10^{-8}$ decreases the derived mean mass by an additional $0.003\,M_\odot$ (total mass difference of $0.015\,M_\odot$). Assuming no hydrogen layer ($M_{\rm H}/M_\star = 0$) yields a mean mass that is $\sim 0.018\,M_\odot$ lower than that obtained with the fiducial value of $M_{\rm H}/M_\star = 10^{-4}$.

It is worth noting that the spectroscopic method shares this dependency on evolutionary models and that most of the studies listed in Table 2.5, including Liebert et al. (2005), Kepler et al. (2007) and Tremblay & Bergeron (2009), employ mass-radius relations that use thick hydrogen layers. Column 7 of Table 2.5 notes the assumed hydrogen layer mass in the evolutionary models used in each study. Furthermore, our results are qualitatively less sensitive to the mass-radius relation: for the gravitational redshift method, $v_{\rm g} \propto M/R$, while the surface gravity used by the spectroscopic method scales as $g \propto M/R^2$.

2.4.3.2 Dynamical

We use the kinematical LSR described by Standard Solar Motion (Kerr & Lynden-Bell 1986) as our reference frame for the comoving approximation. To determine if this is a suitable choice, we investigate $\langle v_{\rm app} \rangle$ in the U, V or W directions (by convention, U is positive toward the Galactic center, V is positive in the direction of Galactic rotation, and W is positive toward the North Galactic Pole).

For 237 targets in the direction of the Galactic center ($l \leq 90^\circ$ or $l \geq 270^\circ$) and 212 opposite the Galactic center ($90^\circ < l < 270^\circ$), $\langle v_{\rm app} \rangle = 31.81 \pm 1.71$ and $33.43 \pm 1.64\,{\rm km\ s^{-1}}$, respectively. In the direction of the LSR flow ($l = 90^\circ, b = 0^\circ$; 196 targets) and opposite the flow (253 targets), $\langle v_{\rm app} \rangle = 33.61 \pm 2.09$ and $31.77 \pm 1.34\,{\rm km\ s^{-1}}$. North (185) and south (264) of the Galactic equator, $\langle v_{\rm app} \rangle = 31.59 \pm 1.84$ and $33.26 \pm 1.53\,{\rm km\ s^{-1}}$.

These empirical checks provide independent evidence that the local WDs in our sample move with respect to kinematical LSR with the following values: (U, V, W)=$(-1.62 \pm 3.35, +1.84 \pm 3.43, -1.67 \pm 3.37)\,{\rm km\ s^{-1}}$, which is consistent with *no* movement relative to the LSR. Therefore, we find our choice of reference frame to be suitable for this study.

2.4.3.3 Observational

SPY targets are magnitude-limited to $B < 16.5$, but these targets come from multiple surveys with varying selection criteria, making the combined criteria difficult to precisely determine (Koester et al. 2009b). For this reason, our results pertain mostly to non-binary thin disk normal DA WDs from SPY. Although the

selection bias is likely to have a minimal effect, a detailed comparison of our results with that of the general DA population awaits a closer examination of the selection criteria (see Napiwotzki et al. 2001, 2003).

If we approximate our sample to be free of any target selection bias, our estimates show that we have a net observational bias toward lower mass WDs. There are two competing effects: first, at a given $T_{\rm eff}$, a larger mass (smaller radius) results in a fainter WD, thus biasing the detection of fewer higher mass WDs over a given volume, and second, a larger mass (smaller radius) also results in a slower cooling rate due to a larger heat capacity as well as a diminished surface area. This means more higher-mass WDs as a function of $T_{\rm eff}$. We estimate the observational mass bias correction as follows.

Let $P(M)$ be the distribution of WDs as a function of mass for a magnitude-limited sample of WDs. For simplicity, we take it to have the form of a Gaussian; we take the mean to be $\langle M \rangle \sim 0.65\,M_{\odot}$ and $\sigma \sim 0.1\,M_{\odot}$. As a reference, the spectroscopic mass distribution of DAs shows a sharp Gaussian-like peak with high and low mass wings (e.g., Bergeron et al. 1992; Liebert et al. 2005; Kepler et al. 2007).

Effect (1): ignoring color, the apparent flux of a star scales as $F_{\rm app} \sim L_{\star}/D^2$ and the luminosity as $L_{\star} \sim R^2 T_{\rm eff}^4$, where $L_{\star}$, R, and $T_{\rm eff}$ are the luminosity, radius, and effective temperature of the star; D is its distance. In the non-relativistic limit, the radius, R, of a WD scales as $R \propto M^{-1/3}$ (Chandrasekhar 1939), and for a

(moderately relativistic) $0.6\,M_{\odot}$ WD this relation is approximately $R \propto M^{-1/2}$, so

$$L_{\star} \propto \frac{T_{\rm eff}^4}{M}. \tag{2.3}$$

If $F_{\rm cutoff}$ is the lower limit on flux for the survey, a given WD is visible out to a distance of

$$D \sim \left(\frac{L_{\star}}{F_{\rm cutoff}}\right)^{1/2} \propto \frac{T_{\rm eff}^2}{M^{1/2}}. \tag{2.4}$$

If we make the simplifying assumption that all the WDs are at the observed average temperature, $\langle T_{\rm eff}\rangle$, and that they are distributed uniformly, the volume, V, in which a WD is visible is

$$V \sim D^3 \propto M^{-\frac{3}{2}}. \tag{2.5}$$

Thus, $P(M)$ is biased by this factor.

Effect (2): from simple Mestel theory (Mestel 1952), the WD cooling time, τ, scales as

$$\tau \propto \left(\frac{M}{L_{\star}}\right)^{\frac{5}{7}}, \tag{2.6}$$

which, from Equation 2.3, yields

$$\tau \propto \left(\frac{M^2}{T_{\rm eff}^4}\right)^{\frac{5}{7}} \sim M^{10/7} T_{\rm eff}^{-20/7}. \tag{2.7}$$

Again, assuming that the WDs are all at $\langle T_{\rm eff}\rangle$, the observed distribution will be biased by a factor of $\tau \propto M^{10/7}$.

Thus, the final biased distribution we observe is given by the product of these factors:

$$\begin{aligned} P_{\rm bias}(M) &\propto V\,\tau\,P(M) \\ &\propto M^{-1/14} P(M). \end{aligned} \tag{2.8}$$

This very weak mass bias results in $\langle M \rangle_{\rm bias} = 0.649\,M_{\odot}$, which is a mass bias of $\Delta M = -0.001\,M_{\odot}$. While this is just a crude estimate, it suggests that the bias correction is likely much smaller than the size of our stated random uncertainties.

2.4.3.4 Mass Conversion

In our mean mass determination in Section 2.4.2, we implicitly assume that $\langle M/R \rangle = \langle M \rangle / \langle R \rangle$. These quantities are not entirely equal, and by performing an estimate using a simple analytical form for the WD mass distribution, we find that there is a difference of $\sim 0.5\%$ (i.e., $\langle M/R \rangle \simeq 1.005 \times \langle M \rangle / \langle R \rangle$), which is negligible compared to the mean mass differences we find.

2.4.4 Thick Disk DAs

The kinematics of thick disk stars prohibit us from placing them in the same comoving reference frame as thin disk stars. In Section 2.4.3.2, we show that the kinematical LSR described by Standard Solar Motion is a suitable choice of reference frame for the SPY *thin disk* WDs. As expected, using $v_{\rm app}$ of our thick disk targets corrected to that LSR (the reference frame suitable for the thin disk) give discrepant values for $\langle v_{\rm app} \rangle$ in opposite directions. Since our thick disk sample is small (26 targets), our $\langle v_{\rm app} \rangle$ uncertainties are too large to discern a suitable reference frame. If we correct by the average lag in rotational velocity of the thick disk with respect to the thin disk ($\sim 40\,{\rm km\ s^{-1}}$; Gilmore et al. 1989), then $\langle v_{\rm app} \rangle = 32.90 \pm 9.59\,{\rm km\ s^{-1}}$ for our thick disk sample. Individual $v_{\rm app}$ measurements are listed in Table 2.4. Using $\langle T_{\rm eff} \rangle = 19,960\,{\rm K}$, we find

$\langle M \rangle = 0.652^{+0.097}_{-0.119}\, M_{\odot}$. This is evidence that the mean mass of thick disk DAs is the same as for thin disk DAs within the mass difference of the two samples, $0.005 \pm 0.119\, M_{\odot}$.

Table 2.4. Apparent Velocity Measurements for Thick Disk DAs

Target	Adopted		Date	Time	LSR Correction	Hα		Hβ		Observation	
	$v_{\rm app}$ (km s^{-1})	$\delta v_{\rm app}$ (km s^{-1})	(UT)	(UT)	(km s^{-1})	$v_{\rm app}$ (km s^{-1})	$\delta v_{\rm app}$ (km s^{-1})	$v_{\rm app}$ (km s^{-1})	$\delta v_{\rm app}$ (km s^{-1})	$v_{\rm app}$ (km s^{-1})	$\delta v_{\rm app}$ (km s^{-1})
WD 0158-227	-12.279	2.795	2002.09.20	03:40:17	-5.823	-10.305	1.125	···	···	-10.305	1.125
			2002.09.27	07:46:45	-9.161	-14.259	1.127	···	···	-14.259	1.127
WD 0204-233	82.384	0.304	2000.07.15	07:45:18	8.895	82.192	0.944	80.422	1.662	81.760	1.074
			2000.07.17	08:47:06	8.750	82.364	1.977	83.186	5.477	82.459	0.371
WD 0255-705	47.623	0.527	2000.08.03	09:55:52	-35.536	48.181	1.547	···	···	48.181	1.547
			2000.08.05	08:51:01	-35.778	47.374	1.034	···	···	7.374	1.034
WD 0352+052	-86.636	2.300	2002.03.01	01:09:46	-35.737	-87.408	1.401	···	···	-87.408	1.401
			2002.09.13	09:27:33	19.231	-84.384	1.248	-79.498	2.216	-83.208	2.954
HE 0409-5154	23.915	6.616	2000.09.15	09:10:28	-37.306	22.243	2.047	20.299	1.634	21.056	1.340
			2001.09.13	09:26:42	-37.020	30.762	1.257	34.543	2.406	31.572	2.194
HE 0416-1034	44.087	0.191	2000.12.17	06:13:24	-38.231	43.785	1.509	45.786	3.788	44.059	0.973
			2001.01.15	03:03:25	-48.043	40.481	2.058	47.436	1.631	44.754	4.787
HE 0452-3444	-10.387	0.086	2000.12.13	06:27:39	-44.215	-9.733	1.464	-13.936	3.554	-10.343	2.094
			2001.01.15	02:44:23	-51.955	-9.238	2.210	-13.956	3.712	-10.472	2.932
HE 0508-2343	79.982	2.028	2001.04.07	00:23:02	-59.490	79.124	1.786	80.903	1.307	80.283	1.198
			2001.04.09	00:48:48	-59.118	76.884	1.817	68.789	1.966	73.155	5.706
WD 0732-427	36.295	0.558	2001.04.09	01:16:13	-68.414	36.003	0.756	37.866	1.433	36.409	1.087
			2001.05.03	23:55:10	-69.286	33.730	1.190	40.950	2.679	34.920	3.788
HS 0820+2503	41.390	4.704	2003.02.18	02:42:33	-33.578	41.390	4.704	···	···	41.390	4.704
HE 1124+0144	46.460	0.144	2000.07.01	23:28:45	-55.699	45.879	1.394	48.423	2.799	46.384	1.435
			2000.07.02	23:34:25	-55.550	47.083	1.185	42.748	3.337	46.598	1.932
WD 1152-287	51.828	1.745	2000.07.11	00:57:00	-70.466	50.760	1.594	···	···	50.760	1.594
			2000.07.14	23:01:27	-70.053	53.254	1.841	···	···	53.254	1.841
WD 1323-514	-40.353	0.770	2001.05.15	01:29:38	-42.147	-40.093	0.793	-41.065	2.400	-40.189	0.409
			2001.06.08	02:12:18	-50.778	-42.707	1.018	-40.445	1.821	-42.168	1.362
WD 1334-678	22.946	0.649	2000.07.30	00:47:19	-58.211	22.384	1.473	24.018	3.072	22.689	0.900
			2001.05.15	01:42:37	-40.116	24.128	1.309	20.157	4.143	23.767	1.612
HS 1338+0807	64.191	2.405	2001.08.18	23:52:07	-28.395	64.191	2.405	···	···	64.191	2.405
WD 1410+168	15.184	2.748	2002.04.23	06:08:33	7.586	15.753	0.911	8.557	3.107	15.184	2.748
WD 1426-276	55.800	0.559	2000.07.05	03:56:09	-43.083	55.742	1.182	55.448	3.136	55.705	0.137
			2000.07.06	02:38:26	-43.227	57.693	1.045	56.772	1.755	57.452	0.572
HS 1432+1441	84.966	3.366	2001.08.16	00:01:42	-14.425	82.686	1.642	77.964	3.260	81.730	2.683

Table 2.4 (cont'd)

Target	Adopted		Date	Time	LSR	Hα		Hβ		Observation	
	$v_{\rm app}$ (km s^{-1})	$\delta v_{\rm app}$ (km s^{-1})	(UT)	(UT)	Correction (km s^{-1})	$v_{\rm app}$ (km s^{-1})	$\delta v_{\rm app}$ (km s^{-1})	$v_{\rm app}$ (km s^{-1})	$\delta v_{\rm app}$ (km s^{-1})	$v_{\rm app}$ (km s^{-1})	$\delta v_{\rm app}$ (km s^{-1})
			2001.08.21	00:15:53	-13.555	85.505	1.995	88.323	2.297	86.717	1.973
WD 1507+021	50.907	3.076	2002.06.18	01:25:19	-7.271	52.338	2.198	47.601	3.340	50.907	3.076
WD 1614-128	95.682	0.052	2000.06.06	06:16:38	5.840	94.870	1.239	99.368	2.581	95.713	2.482
			2000.06.08	02:20:56	5.346	94.931	1.088	102.053	3.282	95.637	3.009
WD 1716+020	10.643	1.291	2002.04.23	09:03:16	48.550	11.038	0.846	8.531	1.956	10.643	1.291
WD 1834-781	60.781	0.111	2000.07.06	04:36:43	-35.096	60.857	0.919	60.355	2.395	60.792	0.237
			2000.07.13	05:04:33	-37.059	59.611	1.028	62.217	1.793	60.255	1.589
WD 1952-206	62.701	0.113	2000.07.06	05:09:15	29.248	62.167	0.870	63.309	2.141	62.329	0.563
			2000.07.13	04:43:35	25.831	62.683	0.956	62.931	2.356	62.718	0.122
WD 2029+183	-97.198	1.373	2002.04.24	09:34:58	74.163	-98.949	2.029	-96.770	1.646	-97.635	1.507
			2002.08.05	04:50:45	51.952	-93.455	1.652	-98.577	2.467	-95.041	3.349
WD 2322-181	39.763	1.328	2000.07.13	06:16:26	38.666	42.172	1.462	38.142	2.548	41.173	2.459
			2000.07.16	05:46:18	37.813	39.731	1.648	36.877	3.217	39.138	1.638
WD 2350-083	84.801	0.992	2002.07.11	09:56:33	49.133	84.652	1.390	85.845	2.341	84.963	0.740
			2002.09.13	07:51:37	24.339	80.737	1.489	86.827	3.323	81.756	3.214

One should also note that the dispersion of $v_{\rm app}$ (Column 5 of Table 2.2) is clearly larger than that for the thin disk DAs. Since the $v_{\rm app}$ distribution is a convolution of the true mass distribution and the random stellar velocity distribution, this is consistent with a larger velocity dispersion as expected for the thick disk population (Gilmore et al. 1989).

2.5 Discussion

2.5.1 The log g Upturn

At the time we published the work of Falcon et al. (2010b), a major problem plaguing the field of WDs was the apparent systematic increase in mean $\log g$ for DAs toward low ($\lesssim 12,000\,$K) $T_{\rm eff}$, as determined from spectroscopic fitting of absorption line profiles (Bergeron et al. 2007; Koester et al. 2009a). Recent work on the 3D modeling of convection in DA atmospheres may finally put this issue to rest (Tremblay et al. 2011b, 2013a,b). Here in Sections 2.5.1.1 and 2.5.1.2, we discuss our contribution to constraining this problem.

2.5.1.1 The Problem

This apparent increase is specific to the spectroscopic method. It is absent in photometric $\log g$ determinations (Kepler et al. 2007; Engelbrecht & Koester 2007), which are not strongly dependent on line profiles. A number of effects are known to exist that make theoretical line profile modeling for cool WD atmospheres more difficult than for hotter WDs, such as helium contamination from dredge-up (Bergeron et al. 1990; Tremblay & Bergeron 2008) and the treatment of convective

efficiency (Bergeron et al. 1995a).

The number of studied cool WDs is already relatively low due to the inherent difficulty of observing cool (dim) objects, but the addition of the $\log g$ upturn problem and the subtleties of cool WD atmosphere modeling (e.g., Saumon et al. 2014) has thus far kept that number low by prompting many spectroscopic analyses to be designed to exclude cooler WDs (e.g., Bergeron et al. 1992; Harris et al. 2003; Madej et al. 2004; Liebert et al. 2005; Kepler et al. 2007; DeGennaro et al. 2008). This is tremendously unfortunate. Understanding cool WDs has broad astrophysical relevance, such as in determining the age of the Galactic disk (Winget et al. 1987) and in setting constraints on the physics of crystallization in high-density plasmas (Winget et al. 2009).

Furthermore, decades of focus on hotter WDs (due to the much larger data set and due to the neglect of cooler WDs) have perhaps given researchers in our field a false comfort with these objects. There is a feeling that since hot WD atmospheres are more straightforward to model than cool atmospheres, the spectroscopically determined surface gravities (and masses) must be correct for the hot WDs and not for the cool WDs, given the $\log g$ upturn problem. Recent calculations for Stark broadening of hydrogen lines in WD atmospheres (Tremblay & Bergeron 2009) show that hot WD modeling is still maturing.

2.5.1.2 Avoiding the Upturn

The gravitational redshift method is independent of $\log g$ determinations from atmosphere models and allows us to constrain changes in mean masses across

$T_{\rm eff}$ bins.

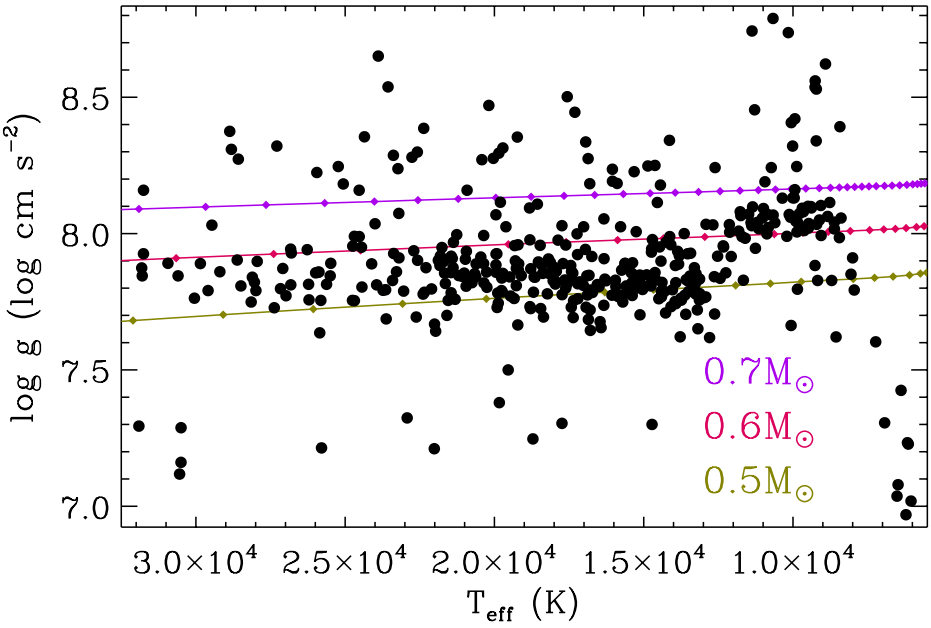

Figure 2.9 Distribution of $T_{\rm eff}$ versus $\log g$ for 419 of our WDs. Spectroscopic parameters for all targets are from Koester et al. (2009b). Note the abrupt increase in the mean $\log g$ around 12,000 K. We also plot cooling tracks from evolutionary models for 0.5, 0.6 and $0.7\,M_\odot$ WDs.

Figure 2.9 plots spectroscopically determined values of $T_{\rm eff}$ and $\log g$ from Koester et al. (2009b) for the targets in our sample, clearly exposing the upturn. This reflects to state of the field before the recent work on 3D WD atmosphere models. We plot evolutionary models for 0.5, 0.6 and $0.7\,M_\odot$ DA WDs to illustrate how a higher surface gravity implies a higher mass and to show the expected weak dependence on $T_{\rm eff}$. Using the mass-radius relation from evolutionary models, we derive mean spectroscopic masses $\langle M \rangle^{\rm hot} = 0.563 \pm 0.002\,M_\odot$

for 358 WDs with $T_{\rm eff} > 12,000\,{\rm K}$ and $\langle M \rangle^{\rm cool} = 0.666 \pm 0.005\,M_{\odot}$ for 75 WDs with $12,000\,{\rm K} > T_{\rm eff} > 7000\,{\rm K}$; $\Delta\langle M \rangle = 0.103 \pm 0.007\,M_{\odot}$. The mass difference is even larger in the SDSS data; Kepler et al. (2007) find $\langle M \rangle^{\rm hot} = 0.593 \pm 0.016\,M_{\odot}$ and $\langle M \rangle^{\rm cool} = 0.789 \pm 0.005\,M_{\odot}$ ($12,000\,{\rm K} \geq T_{\rm eff} \geq 8500\,{\rm K}$); $\Delta\langle M \rangle = 0.196 \pm 0.021\,M_{\odot}$.

In Figure 2.10, we show our distribution of $v_{\rm app}$ (distribution of uncertainties in Figure 2.11) for targets with $T_{\rm eff} > 12,000\,{\rm K}$ (green histogram with ascending lines) and with $12,000\,{\rm K} > T_{\rm eff} > 7000\,{\rm K}$ (pink histogram with descending lines). The corresponding $\langle v_{\rm app} \rangle$ determinations are 31.61 ± 1.22 and $37.50 \pm 3.59\,{\rm km\ s^{-1}}$, respectively, which translate to $\langle M \rangle^{\rm hot} = 0.640 \pm 0.014\,M_{\odot}$ and $\langle M \rangle^{\rm cool} = 0.686^{+0.035}_{-0.039}\,M_{\odot}$ (see Figure 2.12). This is consistent with *no* change in mean mass across a temperature split at $T_{\rm eff} = 12,000\,{\rm K}$, in agreement with the photometric studies by Kepler et al. (2007) and by Engelbrecht & Koester (2007). Prior to 3D DA atmosphere models, no previous large spectroscopic study has seen consistency in mean mass across these temperatures.

2.5.2 Comparison With Other Studies

Table 2.5 lists four studies that employ the gravitational redshift method to determine masses for common proper motion WDs. Because of the small sample sizes (9, 35, 34, and 41 WDs), the uncertainties of the mean masses found by these studies are relatively large – too large to discern a difference in mean mass from that of the spectroscopic method (Silvestri et al. 2001). Other than with the results of Koester (1987), whose sample consists of only 9 DAs, our mean mass agrees

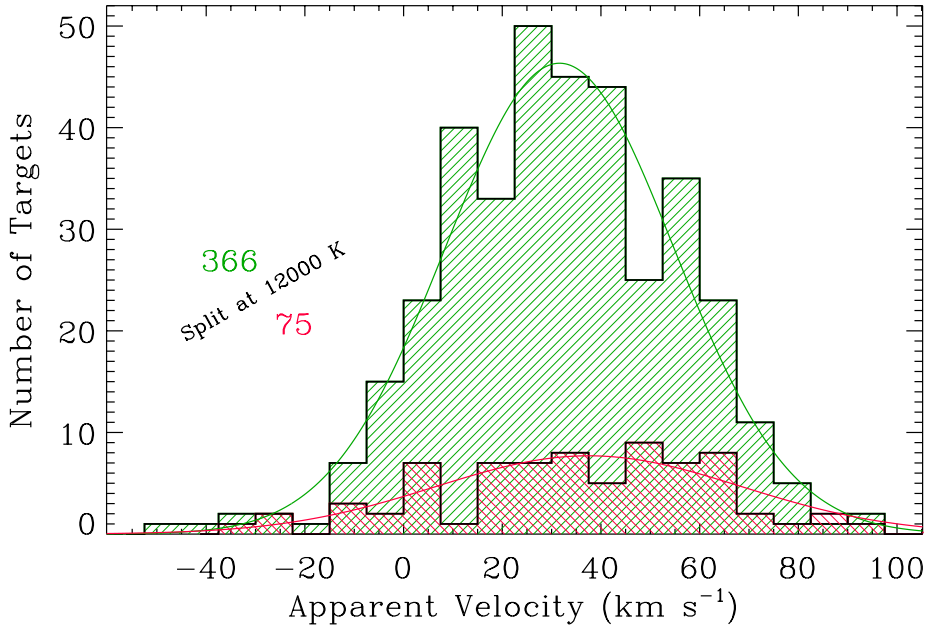

Figure 2.10 Histogram of measured apparent velocities, $v_{\rm app}$, for targets with spectroscopically determined $T_{\rm eff}$ from Koester et al. (2009b). The bin size is 7.5 km s^{-1}. The green histogram with ascending lines corresponds to targets with $T_{\rm eff} > 12,000$ K and the pink histogram with descending lines to $12,000\,{\rm K} > T_{\rm eff} > 7000$ K. The mean $v_{\rm app}$ for the green histogram is 31.61 ± 1.22 km s^{-1}; the median is 31.71 km s^{-1}; the standard deviation is 23.22 km s^{-1}. The mean $v_{\rm app}$ for the pink histogram is 37.50 ± 3.59 km s^{-1}; the median is 36.20 km s^{-1}; the standard deviation is 31.00 km s^{-1}. The overplotted curves are the Gaussian distribution functions used to determine Monte Carlo uncertainties. We list the number of targets in each distribution.

with that of all these studies, and we improve upon the uncertainties (precision) by more than a factor of two.

The mean mass of 512 SPY non-binary thin disk normal DAs from Koester et al. (2009b), as we figure from their spectroscopically determined values of $T_{\rm eff}$

Table 2.5. Mean DA Masses From Selected Studies

Study	Number of WDs	$\langle M \rangle$ ($M_\odot$)	$\delta \langle M \rangle$ ($M_\odot$)	σ_M ($M_\odot$)	Method	Assumed H-Layer[a]	Notes
Koester et al. (1979)	122	0.58	0.10	0.12[b]	Photo	Thin/No	
Koester (1987)	9	0.58	···	0.11	GRS	Thin/No	CPM WDs
McMahan (1989)	50	0.523	0.014	···	Spectro	Thin/No	
Wegner & Reid (1991)	35	0.63	0.03	···	GRS	Thin/No	CPM WDs
Bergeron et al. (1992)	129	0.562	···	0.137	Spectro	Thin/No	$T_{\rm eff} \gtrsim 14,000$ K
Bragaglia et al. (1995)	42	0.609	···	0.157	Spectro	Thin/No	$T_{\rm eff} > 12,000$ K
Bergeron et al. (1995b)	129	0.590	···	0.134	Spectro	Thick	Revised Bergeron et al. (1992) w/ thick H-layers
Reid (1996)	34	0.583	0.078	···	GRS	Thick	CPM WDs
Vennes et al. (1997)	110	0.56*	···	···	Spectro	Thin/No	$75,000\,{\rm K} \gtrsim T_{\rm eff} \gtrsim 25,000\,{\rm K}$
Finley et al. (1997)	174	0.570*	···	0.060*	Spectro	Thick	$T_{\rm eff} \gtrsim 25,000$ K some w/ cool companions
Silvestri et al. (2001)	41	0.68	0.04	···	GRS	Thick	CPM WDs
Madej et al. (2004)	1175	0.562*	···	···	Spectro	Thick	$T_{\rm eff} \geq 12,000$ K
Liebert et al. (2005)	298	0.603	···	0.134	Spectro	Thick	$T_{\rm eff} > 13,000$ K
		0.572*	···	0.188			
Kepler et al. (2007)	1859	0.593	0.016	···	Spectro	Thick	$T_{\rm eff} > 12,000$ K
Tremblay & Bergeron (2009)	~ 250	0.649	···	···	Spectro	Thick	$40,000\,{\rm K} > T_{\rm eff} > 12,000\,{\rm K}$ overlap w/ Liebert et al.
Koester et al. (2009b)[c]	606[d]	0.567[e]	0.002[e]	0.142[e]	Spectro	Thick	SPY
Koester et al. (2009b)[c]	512[d]	0.580[e]	0.002[e]	0.136[e]			SPY non-binary thin disk WDs
Koester et al. (2009b) overlap[c]	441	0.575[e]	0.002[e]	0.128[e]			
Limoges & Bergeron (2010)	136	0.606	···	0.135	Spectro	Thick	$T_{\rm eff} > 13,000$ K
Tremblay et al. (2011a)	1089	0.613	···	0.126	Spectro	Thick	$40,000\,{\rm K} > T_{\rm eff} > 13,000\,{\rm K}$ S/N> 15
Gianninas et al. (2011)	1171	0.661	···	0.160	Spectro	Thick	
Gianninas et al. (2011)	958	0.638	···	0.145			$T_{\rm eff} > 13,000$ K
Kleinman et al. (2013)	3577	0.623	0.002	···	Spectro	Thick	S/N≥ 15
Kleinman et al. (2013)	2217	0.593	0.002	···			S/N≥ 15 $T_{\rm eff} > 13,000$ K
This Work	449	0.647	$^{+0.013}_{-0.014}$	···	GRS	Thick	SPY non-binary thin disk WDs

Note. — Masses marked with an asterisk are peaks/widths of mass distributions from Gaussian fitting.

[a]Hydrogen layer mass used in mass-radius relation from evolutionary models. "Thick" corresponds to $M_{\rm H}/M_\star \approx 10^{-4}$ and "Thin/No" to $M_{\rm H}/M_\star \lesssim 10^{-8}$ or no hydrogen layer.

[b]Two-thirds of the stars are within $0.12\ M_\odot$.

[c]Masses do not appear in this reference. We compute masses from the published values of $\log g$ and $T_{\rm eff}$ using the mass-radius relation from evolutionary models.

[d]Excludes double degenerates.

[e]We compute these means, uncertainties, and standard deviations (see Section 2.4.2).

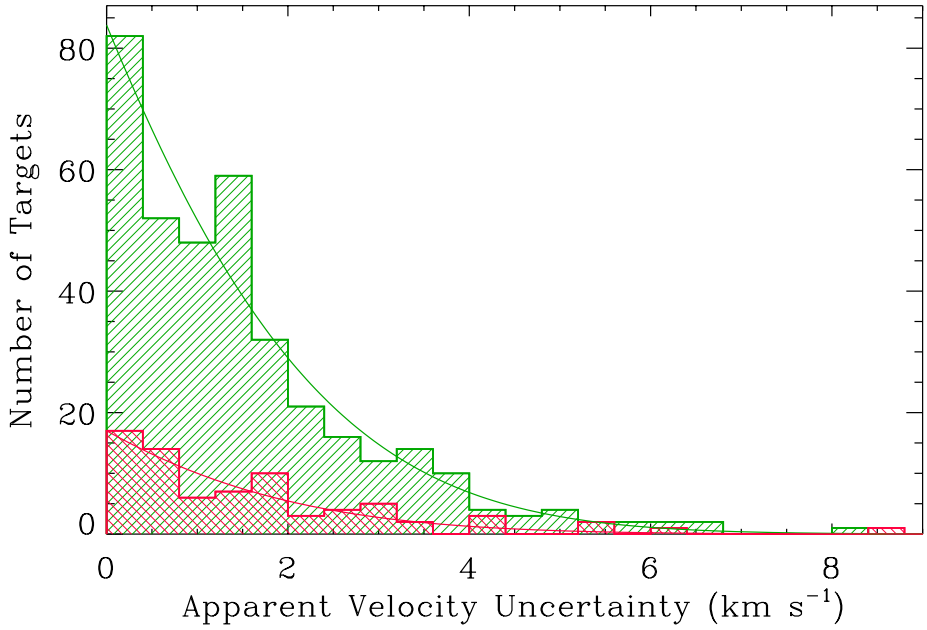

Figure 2.11 Similar to Figure 2.5 but corresponding to targets with $T_{\rm eff} > 12,000\,{\rm K}$ (green) and to targets with $12,000\,{\rm K} > T_{\rm eff} > 7000\,{\rm K}$ (pink).

and $\log g$, is $0.580 \pm 0.002\,M_{\odot}$, and if we restrict the comparison to 441 WDs in our sample, $\langle M \rangle = 0.575 \pm 0.002\,M_{\odot}$. Both values are significantly smaller than the mean mass we derive using the gravitational redshift method.

Using atmosphere models that implement the new Stark-broadened line profiles from Tremblay & Bergeron (2009) and an updated treatment of the microfield distribution, the SPY sample shows an increase of $\sim 0.03\,M_{\odot}$ in the mean mass (Koester, private communication), but this resulting mean mass is still significantly less than our value. In fact, our mean mass is significantly larger than the determinations from all the previous spectroscopic studies listed in Table 2.5 except that of

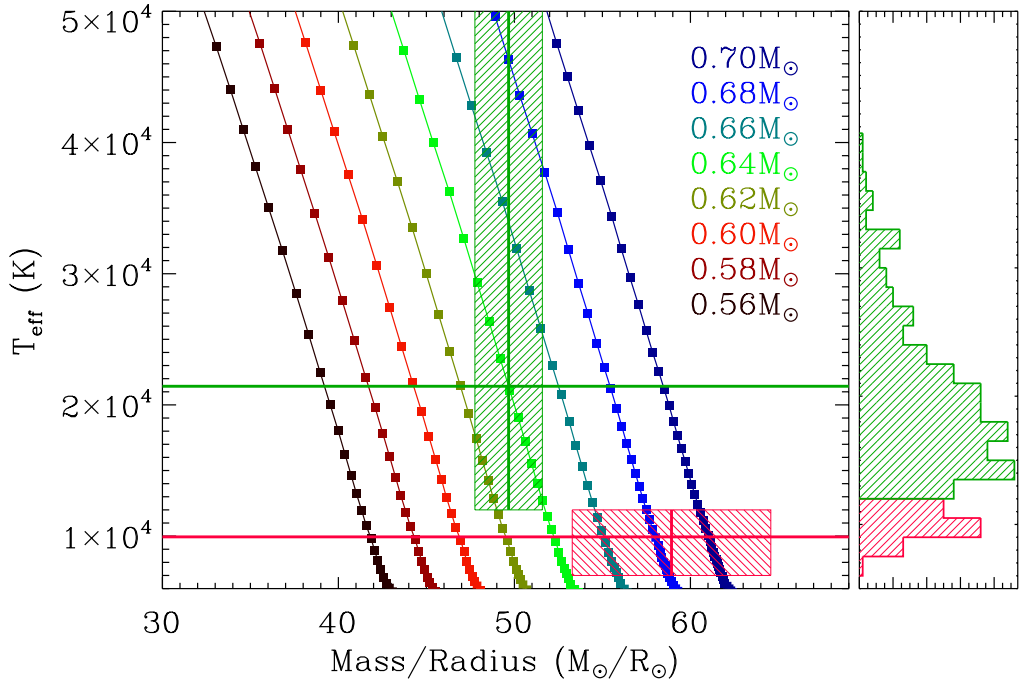

Figure 2.12 Same as Figure 2.6 but for targets with $T_{\rm eff} > 12,000\,{\rm K}$ (green) and with $12,000\,{\rm K} > T_{\rm eff} > 7000\,{\rm K}$ (pink). $\langle M \rangle^{\rm hot} = 0.640 \pm 0.014\,M_{\odot}$ and $\langle M \rangle^{\rm cool} = 0.686^{+0.035}_{-0.039}\,M_{\odot}$.

Tremblay & Bergeron (2009) and Gianninas et al. (2011).

The recent work of Tremblay & Bergeron (2009) uses atmosphere models with modified Stark broadening calculations to re-analyze the WDs from Liebert et al. (2005). They find a larger mean mass ($0.649\,M_{\odot}$) than previously determined for the Palomar-Green sample ($0.603\,M_{\odot}$). The mean mass we derive using the gravitational redshift method agrees well, thus providing independent observational evidence in support of these new atmosphere models.

Other studies incorporate the line profiles of Tremblay & Bergeron (2009).

Limoges & Bergeron (2010) find a smaller mean mass ($0.606\,M_{\odot}$) for WDs in the Kiso Schmidt ultraviolet excess survey. Tremblay et al. (2011a) re-analyze WDs from SDSS Data Release 4. Though they find a $0.02\,M_{\odot}$ increase in mean mass from that of Kepler et al. (2007), the value still remains less than ours. Gianninas et al. (2011) measure a large mean mass ($0.661\,M_{\odot}$), but when restricting their sample to WDs with $T_{\rm eff} > 13,000\,{\rm K}$, it agrees with ours at $\langle M \rangle = 0.638\,M_{\odot}$. The most recent SDSS Data Release 7 contains the largest number of WDs (3577). Kleinman et al. (2013) find a smaller mean mass including WDs with $T_{\rm eff} < 13,000\,{\rm K}$ ($0.623 \pm 0.002\,M_{\odot}$) or excluding them ($0.593 \pm 0.002\,M_{\odot}$).

It is necessary to keep in mind that these are the mean masses determined for each specific sample and that selection biases or subtle differences in the atmosphere models or analysis techniques likely introduce systematic differences from a true WD mean mass. Therefore the comparison with minimal systematic uncertainty is between our gravitational redshift determination and the spectroscopic mass determinations from the same SPY sample.

2.6 Conclusions

We show that the gravitational redshift method can be used to determine a mean mass of a sample of WDs whose dynamics are dominated by random stellar motions. For 449 non-binary thin disk normal DA WDs from SPY, we find $\langle v_{\rm g} \rangle = \langle v_{\rm app} \rangle = 32.57 \pm 1.16\,{\rm km\ s^{-1}}$. Using the mass-radius relation from evolutionary models, $\langle M \rangle = 0.647^{+0.013}_{-0.014}\,M_{\odot}$. This is in agreement with the results of previous gravitational redshift studies. It is significantly higher than all spectro-

scopic determinations prior to that of Tremblay & Bergeron (2009), with which it agrees well. Tremblay & Bergeron (2009) incorporate new calculations of Stark-broadened hydrogen line profiles and a different treatment of the microfield distribution into their atmosphere models. Though subsequent spectroscopic analyses use these new line profiles, only the mean mass from Gianninas et al. (2011) (in addition to Tremblay & Bergeron 2009) agrees with our determination.

We find that the targets in our sample move with respect to the kinematical LSR described by Standard Solar Motion (Kerr & Lynden-Bell 1986) with the following values: (U, V, W)=$(-1.62 \pm 3.35, +1.84 \pm 3.43, -1.67 \pm 3.37)$ km s^{-1}. *This is consistent with no movement relative to this LSR*.

Our results provide evidence that the mean mass of thick disk DAs is the same as for thin disk DAs within $0.005 \pm 0.119\, M_{\odot}$.

The gravitational redshift method is independent of spectroscopically determined surface gravity from atmosphere models and is insensitive to the $\log g$ upturn problem (Section 2.5.1). $\langle v_{\rm app} \rangle = 31.61 \pm 1.22$ and 37.50 ± 3.59 km s^{-1} for targets with $T_{\rm eff} > 12,000$ K and with $12,000$ K $> T_{\rm eff} > 7000$ K, respectively. This translates to $\langle M \rangle^{\rm hot} = 0.640 \pm 0.014\, M_{\odot}$ and $\langle M \rangle^{\rm cool} = 0.686^{+0.035}_{-0.039}\, M_{\odot}$, which disagrees with spectroscopic results prior to 3D modeling of convection in DA atmospheres by showing *no* significant change in the mean mass of DAs across a temperature split at $T_{\rm eff} = 12,000$ K. This confirms the results of Kepler et al. (2007) and Engelbrecht & Koester (2007), who find no $\log g$ increase in their photometric investigations.

Back in Don's office. It's a couple weeks or so since I darted out of this room salivating at the promise of a scientific idea. Now I slump down into a chair, enervated, intellectually detumescent.

"I'm sorry, Don."

"Sorry for what?"

"I got an answer for the mean mass, but it's way too large. I did something wrong. Or the method doesn't work. I don't know."

"What did you get?"

"Zero point six four nine solar masses." I state my number with staccato speech, I suppose, to reflect the measurement precision I had hoped to achieve. "There's no way the white dwarf mean mass is *that* far above 0.6 solar masses, right? I made a mistake."

I'm obviously disappointed. I see Don smirk, prompting me to raise an inquisitive eyebrow.

"Well, maybe not. I hear Pierre has a student who's doing some good work."

"Pierre?"

"University of Montreal. I think the student's name is Pier-Emmanuel. You should look up his work."

"Um...okay."

I trot out of Don's office. Maybe fifteen minutes later I fly back in.

"Don! Tremblay and Bergeron redid their atmosphere models! They re-analyzed the WDs from the PG survey and got a higher mean mass!"

"What'd they get?"

"0.649 solar masses!"

"See, maybe your method isn't wrong. Maybe you're onto something."

Chapter 3

Developing a Laboratory Experiment

At a lot of schools – I don't know, maybe most – the two are one. Here at the University of Texas, though, Astronomy and Physics are separate departments. They're in the same building, but they're not even on adjacent floors. Mathematicians provide a few-floor partition. (Astronomy occupies the top stories. I always found this fitting. That we're at least a little bit closer to the stars, albeit infinitesimally closer.) So I don't attend seminars in the Physics Department very often.

Today Don suggested I go to one. Okay. Sure.

I head downstairs with Mike and some undergrads. The speaker is a scientist visiting from Sandia National Labs. Never heard of it. Remember, I'm in Astronomy. We just don't get the exposure to that kind of career path.

This is the moment when my graduate experience becomes one quite unorthodox for students of astronomy.

Jim (Bailey, the speaker) tells us about the *Z* Facility. He tells us about his research. He tells us about how he's using *Z* to create iron plasmas at the same conditions (temperature, density) as the inside of the Sun.

I'm salivating. (There I go again.) An idea starts to…But if he can make a plasma with…Maybe we could…But surely…

I whip my head around and shout *Mike!* telepathically. He doesn't hear me. But I doubt he would have even if I had the gift. (Or if he had it. I'm not sure how it works. Do I need it? Does he? Do we both?) His mouth is ajar. Is that saliva I detect?

Oh, Don. Now I know why you sent me here.

The history of laboratory experiments relevant to white dwarf photospheres follows the progress of theoretical line shapes, particularly for Stark-broadened hydrogen. During the 1960s and early 1970s, the frequency of shock-heated (e.g., Berg et al. 1962; McLean & Ramsden 1965; Bengtson et al. 1969), pulsed discharge (e.g., Vujnović et al. 1962; Hill & Gerardo 1967; Morris & Krey 1968), and stabilized arc experiments (e.g., Wiese et al. 1963; Shumaker & Popenoe 1968; Wiese et al. 1972) was high, tracking with the dynamic advances in theory (e.g., Kolb & Griem 1958; Baranger 1958c,b,a; Griem et al. 1959, 1962; Kepple & Griem 1968; Smith et al. 1969). As time went on, improving the precision of diagnostic techniques contributed more to the experimental motivation (e.g., Baessler & Kock 1980; Helbig & Nick 1981) in addition to testing the latest theory (e.g., Vidal et al. 1973).

Astronomical observation frequently uses line shape theory – white dwarf

(WD) photospheres in particular are an ideal astrophysical environment for its application (e.g., Dimitrijević et al. 2011). Until now, however, this field has not been a significant motivator for experiments. With new advances in theory (e.g., Tremblay & Bergeron 2009; Santos & Kepler 2012), new experimental capabilities available at modern facilities, and a wealth of spectroscopic observations that did not exist much more than a decade ago (e.g., Kepler et al. 2007; Kleinman et al. 2013), this is changing.

3.1 Motivation

As we discuss in Chapter 2, the spectroscopic method is a widely used technique responsible for determining parameters for thousands of WDs (e.g., Kleinman et al. 2004; Liebert et al. 2005; Eisenstein et al. 2006; Kepler et al. 2007; Koester et al. 2009b; Limoges & Bergeron 2010; Castanheira et al. 2010; Kleinman et al. 2013). Atmospheric parameters form the foundation (and limit the ultimate accuracy) of many other research areas, such as determining the age of the Universe (Winget et al. 1987), using asteroseismology to study matter at high temperatures and densities in the deep interiors of WDs (e.g., Winget & Kepler 2008), constraining the mass of supernova progenitors (e.g., Williams et al. 2009), and probing properties of dark matter axions (Bischoff-Kim et al. 2008b).

While this method is powerful and precise ($\frac{\delta T_{\rm eff}}{T_{\rm eff}} \sim 5\,\%$ and $\frac{\delta \log g}{\log g} \sim 1\,\%$ are typical for a given star), its *accuracy* is suspect. In Chapter 2 we show that the mean mass of WDs determined from spectroscopic investigations disagrees with the mean mass determined from an alternate technique which uses gravitational

redshifts (Falcon et al. 2010b, 2012). The gravitational redshift technique is largely independent of atmosphere models and line-broadening theory. It is only relevant, however, to a large space-velocity averaged sample of nearby WDs where radial velocities relative to the Solar System can be averaged out, or the handful of bright WDs in binary systems where the gravitational redshifts can be disentangled from the stellar radial motion. Astronomers need a solution that applies to individual WDs – to all observed WDs, in all stellar populations and regions of the Galaxy. Astronomers need the spectroscopic method benchmarked.

WD atmosphere models are still advancing. The models currently being used by spectroscopists in the community incorporate the latest hydrogen line profiles of Tremblay & Bergeron (2009). In re-analyzing the hydrogen-atmosphere WDs from the Palomar-Green Survey (Liebert et al. 2005), the spectroscopic fits of Tremblay & Bergeron (2009) yield significant systematic increases in $T_{\rm eff} \sim 200$–$1000\,{\rm K}$ and in $\log g \sim 0.04$–0.1 compared to the previous analysis of the same sample of WDs which used the line profiles of Lemke (1997) following the theory of Vidal et al. (1973). This work demonstrates that modified hydrogen line profiles greatly impact the interpretation of WD spectroscopic observations. The experimental basis for the line profile theories, however, does not presently provide accurate enough constraints to discern which theoretical model is optimal, if any, and at which conditions. The ultimate arbiter of the differences in relative line shapes produced by different theoretical models can only be laboratory experiment.

3.1.1 The Laboratory Perspective

The differences in the new theory and the resulting impact on the WD atmospheric parameters motivate us to perform new experiments to measure hydrogen Balmer line shapes with which to compare theoretical ones. In this chapter we describe an experimental platform for creating hydrogen plasmas at WD photospheric conditions ($T_{\rm e} \sim 1\,{\rm eV}$[1], $n_{\rm e} \sim 10^{17}\,{\rm cm}^{-3}$) (Falcon et al. 2010a, 2013a). Using this platform we measure hydrogen Balmer line profiles in emission and in absorption. Not only are we the first to measure hydrogen line profiles in absorption at these conditions, but we are the first to measure spectral lines in emission and absorption *simultaneously*. This allows for the investigation of plasmas not in local thermodynamic equilibrium and their time evolution, which we list in Section 7.5.2 as a focus for future work. Our experiment is unique in that it uses a radiation-driven plasma source which offers some advantages over previous experiments. This is only possible given the x-ray capability of the *Z* Pulsed Power Facility (Matzen 1997; Spielman et al. 1998; Matzen et al. 2005) at Sandia National Laboratories.

3.2 Experimental Setup

A brief overview before elaborating in the following subsections: we place a gas cell assembly a distance away (324 mm) from an x-ray source along a radial line of sight (LOS). X-rays irradiate the gas cell, transmit through a thin ($1.44 \pm 0.02\,\mu$m) Mylar window, and are absorbed by a gold wall at the back of the cell cavity, heating

[1] When referring to temperature, we use units such that the Boltzmann constant $k_{\rm B} = 1$.

it to an electron temperature of a few eV. The gold re-emits as a continuum, heating the hydrogen through photoionization.

We observe the hydrogen plasma along lines of sight perpendicular to the x-ray radiation and parallel to the gold wall using lens-coupled optical fibers, which deliver the light to time-resolved spectrometer systems.

3.2.1 X-ray Source

Our experiment is part of the *Z* Astrophysical Plasma Properties (ZAPP) Collaboration (Rochau et al. 2014), a group of experiments conducted in coordination at the *Z* Pulsed Power Facility at Sandia National Laboratories. ZAPP experiments are performed simultaneously in a large ($> 60\,\mathrm{m}^3$) vacuum chamber each making use of the same x-ray source to initiate plasma formation.

The source of x-rays is a *z*-pinch dynamic hohlraum (e.g., Spielman et al. 1998; Nash et al. 1999; Stygar et al. 2001; Sanford et al. 2002; Slutz et al. 2003; Bailey et al. 2006; Rochau et al. 2007, 2008), located at the focal point of the *Z* Pulsed Power Accelerator (Stygar et al. 2007). The accelerator supplies $25.8\,\mathrm{MA}$ of current (Rochau et al. 2014) that passes through a nested array of tungsten wires (see, e.g., Deeney et al. 1998; Cuneo et al. 2005; Ampleford et al. 2012). 240 and 120 wires, each $11.4\,\mu\mathrm{m}$ in diameter, make up the outer (40-mm diameter) and inner (20-mm diameter) arrays, respectively. The magnetic pressure from the induced magnetic field (from the current) implodes the tungsten wire plasma onto the central (z) axis. Here the *z*-pinch stagnates (filled, red circle in Figure 3.1) and shock heats the tungsten plasma to temperatures around 200 eV (Sanford et al.

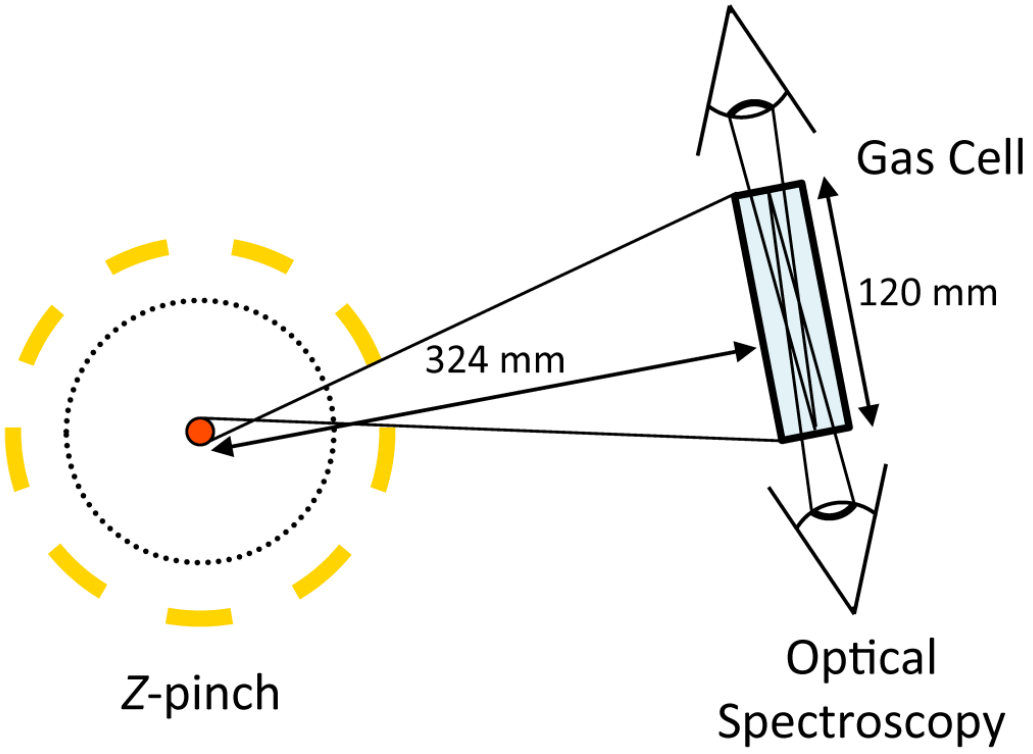

Figure 3.1 Top view schematic of the experimental setup inside the vacuum chamber. The gas cell sits 324 mm away from the z pinch. We observe the hydrogen plasma along lines of sight perpendicular to the x-rays. This figure is not drawn to scale.

2002). Since the tungsten is optically thick and has a high atomic number ($Z = 74$), it radiates nearly as a Planckian (Foord et al. 2004).

All this takes place within a current return canister whose cylindrical wall (segmented, gold annulus in Figure 3.1) contains nine rectangular apertures (11x13 mm) out of which x-ray radiation escapes. Our gas cell intercepts the x-rays leaving the z pinch along one of these radial lines of sight, as do two other ZAPP experiments along two other lines of sight (Mancini et al. 2009; Hall et al. 2009, 2010,

2011, 2014). One ZAPP experiment makes use of x-rays escaping in the upward axial direction (Bailey et al. 2007, 2009; Nagayama et al. 2012a, 2014a,b).

3.2.2 Plasma Formation

For the initial design of the experiment, we simulate the heating of the gas cell using the two-dimensional radiation-hydrodynamics code LASNEX (Zimmerman et al. 1978). In this simulation the radiation from the z pinch peaks at slightly below 230 eV and accounts for the time-dependent radius of the z pinch (Macfarlane et al. 2002; Rochau et al. 2005; Jones et al. 2006a). We take the start time of the simulations to be the time of interaction of the outer and inner wire arrays (see Deeney et al. 1998) in the z-pinch dynamic hohlraum occurring $\sim$32 ns before the maximum power of the radiation pulse. The radiation drive is launched in the simulations directly in front of the gas cell and is geometrically diluted to account for the distance from the source. The simulations include the Mylar window, the hydrogen gas fill, and the walls of the cell.

The results of these simulations draw out a qualitative picture of the plasma formation within our initial gas cell design. We supplement these results with the latest description of the z-pinch radiation for radial lines of sight (Loisel et al. 2014), which comes from measurements of the specific z-pinch dynamic hohlraum configuration (i.e., Marx capacitor bank charge, nine-slot current return canister) we employ. The maximum power and full-width-at-half-maximum of the z-pinch pulse (as measured by the total-energy-and-power diagnostic; Ives et al. 2006) are typically ~ 220 W and $\lesssim 4$ ns, respectively (Rochau et al. 2014). In Section 6.1, we quantify

this qualitative picture with measurements from experiments using matured gas cell designs (see Section 3.2.3 and Chapter 4).

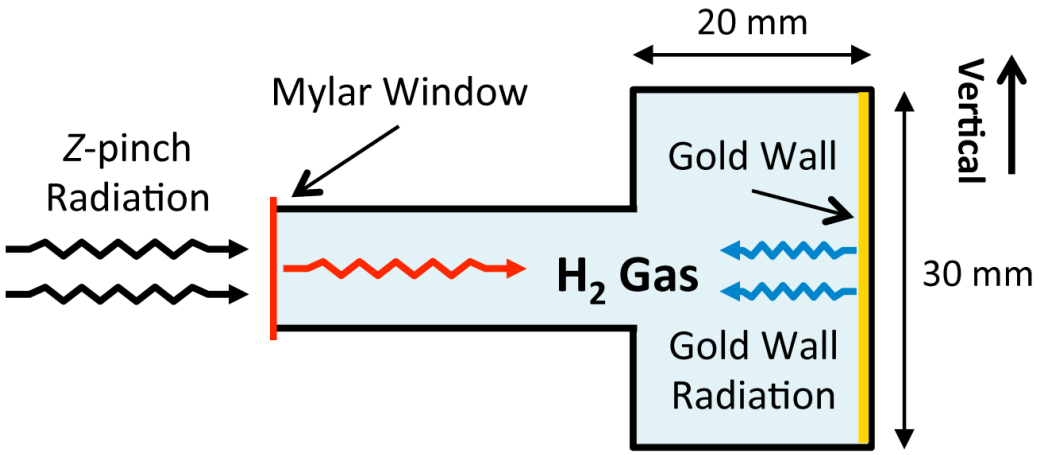

Figure 3.2 Observing LOS view (perpendicular to incident radiation) schematic of the gas cell cavity cross-section, drawn to scale. *Z*-pinch x-rays (black arrows) transmit through the Mylar window (red) and are absorbed by the gold wall at the back end of the cell cavity. The gold wall re-emits (blue) to heat the hydrogen gas.

The plasma formation picture: *z*-pinch photons are geometrically diluted as they travel the distance to the gas cell (black arrows in Figure 3.2; black curve in Figure 3.3 as determined by Loisel et al. 2014). The ~ 1.4-μm thick Mylar window attenuates the radiation as it enters the cell (red arrows; dashed, red curve assuming room-temperature x-ray transmission from Henke et al. 1993), eliminating all photons below ~ 70 eV. For photons at these high energies, the mean free path through hydrogen is large compared to the size of the gas cell. In other words, hydrogen is transparent to these photons, so they stream through the gas and do not directly contribute to the plasma heating. We illustrate this by plotting the absorption mean

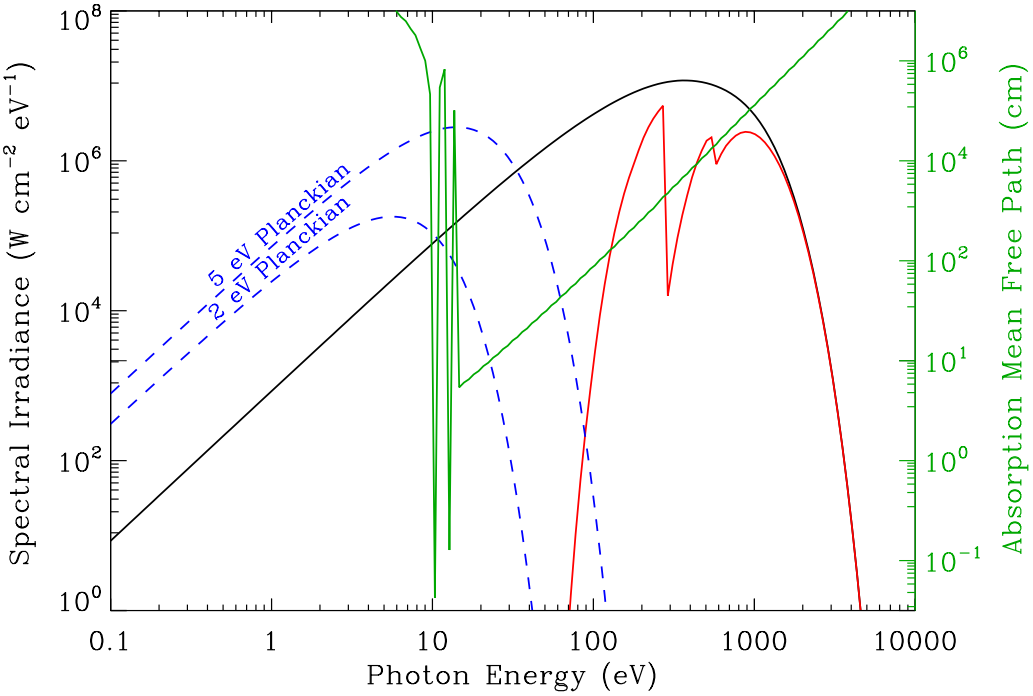

Figure 3.3 Radiation environment of the gas cell. The black curve is the spectral irradiance of the x-ray photons incident on the gas cell (Loisel et al. 2014). These photons transmit through the Mylar window as they enter the cell (red curve). They are absorbed by a gold wall, which re-emits as a continuum approximated as a $\sim$ few eV Planckian; we show two examples within our range of estimated temperatures (blue curves). The green curve is the absorption mean free path through hydrogen gas at room temperature and 10 Torr. The minima (the photon energies most easily absorbed) are within the photon energy range of the gold wall radiation.

free path of hydrogen gas at room temperature and 10 Torr (our typical initial conditions) as a function of photon energy (green curve). In the photon energy range of the attenuated x-rays, the mean free path is much larger than the width of the gas cell (2 cm in the direction perpendicular to the gold wall). The x-rays are instead absorbed by the gold wall and heat it to a $\sim$ few eV electron temperature. It then re-

emits as a continuum (blue arrows; blue curves in Figure 3.3 which we approximate as Planckian emission). The hydrogen is optically thick to the gold wall radiation; the minima values of the mean free path are in its photon energy range. This radiation photoionizes the hydrogen and is attenuated such that the radiation intensity and associated ionization fraction of the plasma decreases with increasing distance away from the gold wall. We confirm this qualitative picture in Section 3.4.1.

The plasma formation in our gas cell is similar to that in the boundary region of a Strömgren sphere (Strömgren 1939) surrounding a hot O star. Both plasmas are predominantly hydrogen, and both sources of ionizing radiation are approximated as Planckian emitters with $\sim$ few-eV temperatures, though the density in our gas cell ($\sim\ 10^{18}$ particles cm^{-3}) is significantly higher than that of the interstellar medium (e.g., Redfield & Falcon 2008) or a denser nebula (e.g., Osterbrock & Ferland 2006).

If we calculate an order-of-magnitude Strömgren "distance" from the gold wall, we find that this balance of photoionization and recombination should occur at ~ 10 mm, which is within the dimensions of our gas cell cavity. The plasma within the vicinity of a Strömgren sphere can also be approximated as isothermal, and, for a hot O star, an electron temperature $T_{\rm e} \sim 1$ eV is typical (Shu 1991; Osterbrock & Ferland 2006). The LASNEX simulations of the environment in our gas cell predict $T_{\rm e} \sim 1$ eV given a gas fill pressure of 15 Torr.

For an initial fill pressure of $\sim 10-15$ Torr, we require an ionization fraction $\gtrsim 10$ % to reach electron densities in our target range of $n_{\rm e} \gtrsim 10^{17}$ cm^{-3}. We revisit this point in Section 3.4.1.

3.2.3 Gas Cell

Oh! That's a good one! I quickly grab my notebook.

"Will you please repeat that, Greg?"

"Huh?"

"What you just said. About the Mylar puffing out 'cause the cell's pressurized. I'm totally gunna quote that somewhere. I want to make sure I got it down accurately."

I flip my notebook around to show him what I wrote:

`''We use x-rays to pop balloons!''  - GAR, 06.14.2012`

The pulsed power shot configuration for the ZAPP experiments requires a blast shield, which is used to mitigate debris within the the vacuum chamber resulting from the z pinch. Its nominal outer diameter is $\sim$ 625 mm at its base, and our gas cell assembly sits immediately outside this blast shield at a distance of 324 ± 2 mm from the z-pinch axis.

The gas cell design changes with time due to many factors, including: responding to lessons learned of experimental shortfalls, accommodating growing

and additional functionality, and improving reliability and efficiency. In this subsection we describe the culmination of many iterations and modifications of the design, our Absorption-Continuum-Emission (ACE) gas cell, named for its capability of observing the hydrogen plasma along three lines of sight. This is also the design generating most of the data we scrutinize for the scientific target of this work, investigating hydrogen Balmer line shapes relevant for WD atmosphere models. We take a closer look at the evolution of the gas cell (and our experimental methods) leading up to the ACE design in Chapter 4.

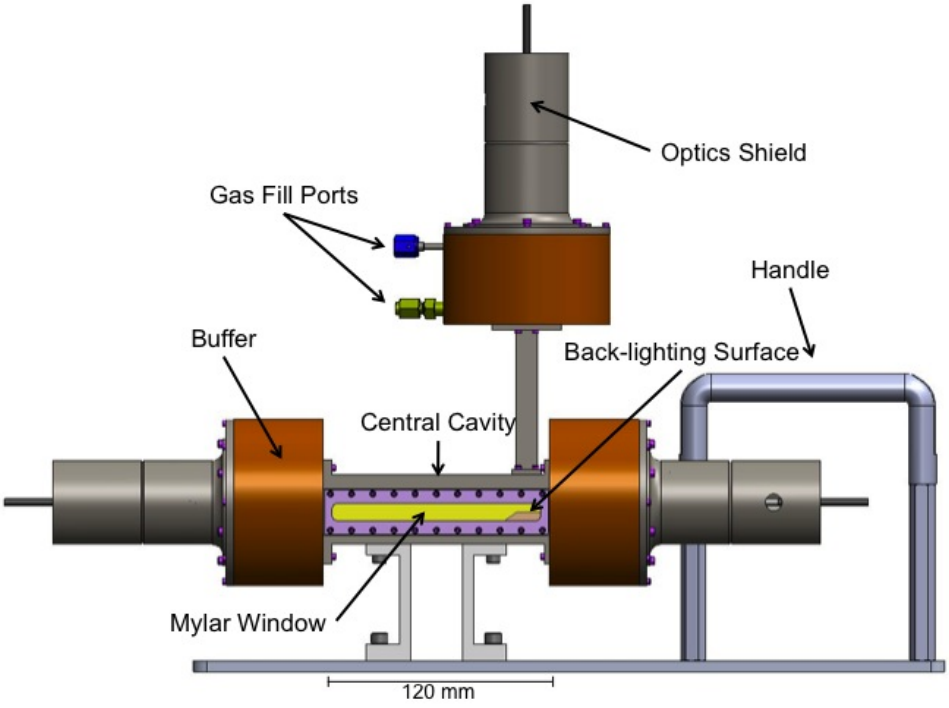

Figure 3.4 Front view drawing of the ACE gas cell design. Three lines of sight observe the plasma inside the central cavity.

Figure 3.4 shows a front view drawing of the ACE design. The plasma forms

inside a rectangular central cavity that is 120x30x20 mm. A Mylar window faces the z-pinch x-rays and interfaces between the vacuum chamber and the pressurized gas cell. This window is offset 30 mm in front of the central cavity (in the radial direction towards the z pinch; see Figure 3.2). This offset results in an extended lifetime (compared to initial experiments which had no offset) of the quasi-steady-state period of plasma conditions in our experiment (see Section 3.4.2) by delaying the arrival time of a shock (predicted by the LASNEX simulations) that propagates from the ionized Mylar into our observed LOS. A thin foil (not shown) partitions the cavity within the buffer (orange) from the central cavity. 5-mm diameter apertures in this foil open up both cavities to each other so that both are pressurized with the gas fill. The function of the buffer is to provide spatial separation between a fused silica window (interfaces between the vacuum chamber and the gas cell) and the hot plasma so that the window does not melt or become a plasma itself, thus interfering with our observation of the hydrogen. Inside the buffer cavity, we insert a black, apertured Delrin® disk to baffle light reflecting within the space.

For each LOS, a tubular, stainless steel shield protects the optics from radiation and debris. We look more closely at these optics in Figure 3.5. Light from the plasma exits the gas cell by passing through the fused silica window (Newport model 05QW40-30), tilted to stifle direct reflections, and a 3-mm diameter limiting aperture. An achromatic doublet lens (Thorlabs model AC060-010-A-ML) then focuses the light onto the end of a 100-μm diameter optical fiber. Figure 3.5 also shows the buffer end plate, to which the fused silica window couples, the optical fiber coupling hardware (purple component in Figure 3.5), and the lens mounting

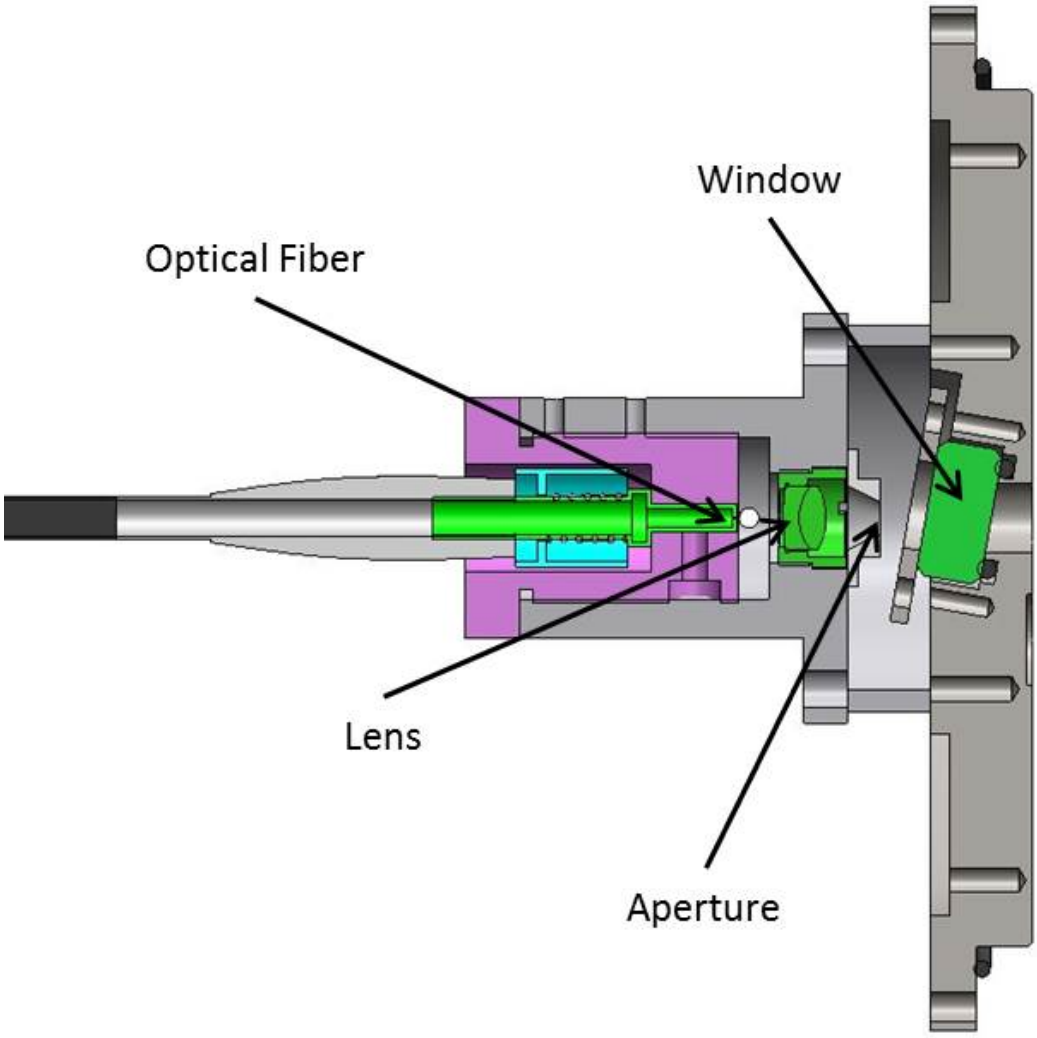

Figure 3.5 Optical setup at the end of our gas cell fiber. The fused silica window couples to the buffer end plate and interfaces between the pressurized gas cell (to the right; not shown) and a vacuum chamber housing the experiment. Light from the experiment passes through this window and a 3-mm diameter limiting aperture before focusing through an achromatic doublet lens onto the end of an optical fiber. We also show the adjacent hardware coupling these components. Screws are omitted for clarity.

hardware. Two screws connect the lens mounting hardware to the buffer end plate. We use these screws to align the optical LOS, and three additional set screws allow us to make fine adjustments to the alignment. We characterize our LOS collection beam in Section 5.3.3.

Inside the central cavity a stainless steel plate coated with 5 μm of gold lines the back wall. A polyhedral stainless steel block, also coated with 5 μm of gold, rests on one end. The surface of this block is tilted with respect to the plain normal to the z-pinch x-rays and pitched with respect to the horizontal plane. This allows the x-rays, the optics in one of the horizontal lines of sight, and the optics in the vertical LOS to each have a direct view of this surface. The x-rays heat up this gold surface just as they do the back wall, allowing it to function as a back-lighting surface for absorption measurements. An axial spacer placed between the central cavity and the vertical-LOS buffer fixes the distance separating the vertical-LOS optics from the back-lighting surface to equal that of the (horizontal) absorption-LOS optics from the back-lighting surface.

For ZAPP experiments, usually all the hardware installed inside the center section vacuum chamber is destroyed with each pulsed power shot. Ours is the first experiment performed at Z to reuse hardware. This is because it is the first experiment to place its hardware outside the blast shield. We place it so far from the z pinch in order for the x-rays to illuminate a large area (see Section 3.4.2). With newly manufactured hardware, the gas cell assembly is a shiny sight to see before the experiment (Figure 3.6). After the experiment, it is not (Figure 3.7).

Most of our gas cell components are constructed of type 306L stainless steel.

Figure 3.6 The experimenter with his ACE gas cell, both anticipating the upcoming visit of a chunk of white dwarf atmosphere to the terrestrial laboratory. Because we often reuse many hardware components, it is rare to see the assembly so pristine.

Only the central cavity, the thin apertured foil partitioning the central cavity and buffer cavity, the axial spacer, optical-fiber coupling hardware, and lens mounting hardware are constructed of type 6061-T6 aluminum. These first three are damaged beyond reuse each experiment (along with the gold-coated components). The latter two are protected by the optics shield. The components we reuse between experiments include the mounting hardware (platform base, legs, and handle), optics shields, and buffers (and buffer end plates).

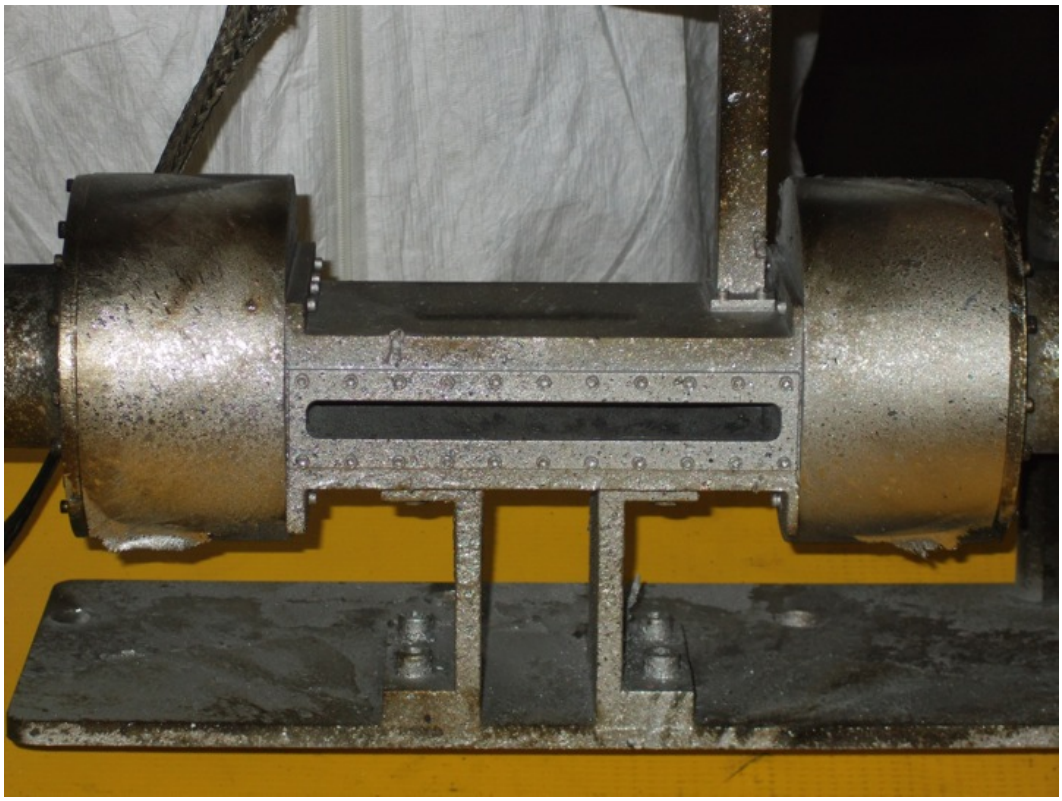

Figure 3.7 Debris and soot from the blast of the experiment humble the appearance of the gas cell. We thank it for serving as such a hospitable host to the visiting chunk of white dwarf atmosphere.

3.2.4 Gas Fill

The gas cell is evacuated ($\lesssim 5 \times 10^{-5}$ Torr) with the chamber. We then fill the cell with research-purity (99.9999 % or 1 part in 10^5) H_2 gas, making use of a fill and purge procedure repeated three times to rid the system of any lingering contaminants. Fill pressures range up to ~ 30 Torr, and we measure this pressure *in situ* using a piezoresistive pressure sensor (Omega Engineering, Inc. model PX72-1.5GV). We describe our method for determining the pressure in Appendix A.

Assuming the gas fill is at room temperature, the Ideal Gas Law gives us the total particle density. We assume no material escapes the gas cell volume on the time scale of our experiment ($< \frac{1}{2}\,\mu$s) so that the total atom density of the gas fill equals the sum of the neutral and ion (electron) densities of the created plasma.

3.3 Data

Chapter 5 contains a detailed account of our data acquisition, processing, and calibration procedures. Here we give a brief preview.

We record time-resolved optical spectra from the lines of sight traversing our gas cell using multiple spectrometer systems. Each LOS has its own independent system that collects light from the experiment using a lens-coupled optical fiber, transmitting the signal through additional fiber, through a spectrometer, and to a streak camera with a micro-channel plate intensifier. The setup is similar to that used previously at *Z* (Bailey et al. 1990, 1997, 2000; Dunham et al. 2004; Bailey et al. 2008; Falcon et al. 2010a, 2013a; Gomez et al. 2014a).

Figures 3.8 and 3.9 show example, uncalibrated time-resolved spectra (streak images) in false color of the hydrogen plasma from experiment z2484 in emission and absorption, respectively. We label the lasers, which we use as wavelength fiducials, the comb and impulse, which we use as timing fiducials, and the observed hydrogen Balmer spectral lines. In both streak images the hydrogen gas is invisible until the *z*-pinch x-rays arrive to heat the gold wall. For these images, we fix this time, the onset of the x-rays, at 1000 ns. The back-lighting continuum in the absorption data (Figure 3.9) decreases in time as the gold back-lighting surface cools.

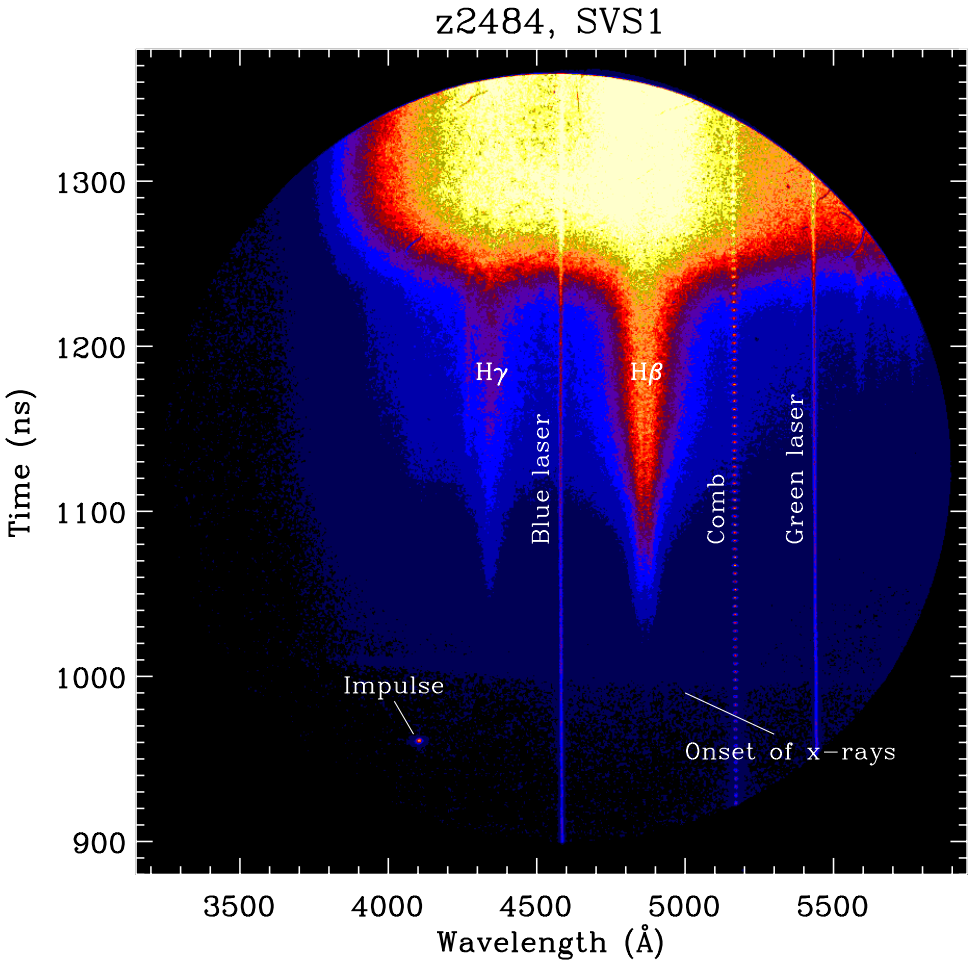

Figure 3.8 Uncalibrated, time-resolved spectrum in false color of hydrogen Balmer emission lines from experiment z2484 with the wavelength fiducials (lasers) and timing fiducials (comb, impulse) labeled.

It is important to note that the signal-to-noise (S/N) significantly increases when we observe the lines in absorption. This allows us to measure higher principal quantum number (of the upper electronic energy level), n, lines than in the emission case. It also allows us to observe transitions originating from the same lower en-

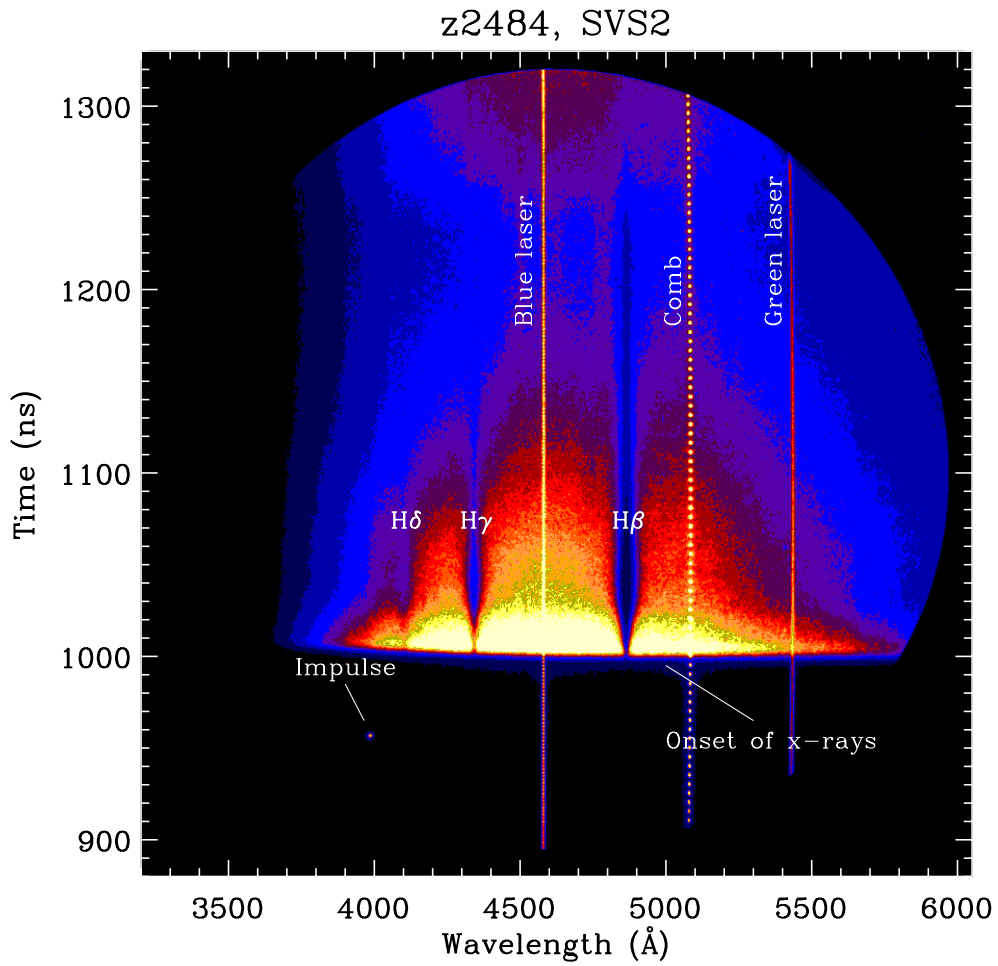

Figure 3.9 Uncalibrated, time-resolved spectrum in false color of hydrogen Balmer absorption lines from experiment z2484. We can observe higher n lines in absorption due to the increased S/N. The intensity of the back-lighting continuum decreases over the lifetime of the experiment as the gold back-lighting surface cools.

ergy level ($n = 2$), which simplifies the interpretation of our data and provides a unique perspective on relative line strengths (Sections 6.2.2.1 and 6.2.2.2).

3.4 Experimental Context

Besides the ability to observe our plasma in absorption, what distinguishes this experiment from others in the past that have investigated hydrogen Balmer line profiles in the range of conditions $T_{\mathrm{e}} \sim 1\,\mathrm{eV}$ and $n_{\mathrm{e}} \sim 10^{17}\,\mathrm{cm}^{-3}$ is the plasma source. Here it is radiation-driven. This decouples the heating source from the plasma we are studying in the sense that the initial conditions of the hydrogen gas (i.e., fill pressure) have a negligible effect on the radiation temperature of the gold wall. The gold temperature can be increased, for example, by moving the gas cell closer to the z pinch to decrease geometrical dilution of the incident radiation or by using a thinner Mylar window to decrease attenuation. This "decoupling" gives us potentially finer control of the experimental conditions as well as the ability to explore a broad range of plasma conditions.

3.4.1 Achievable Range of Electron Densities

We demonstrate that our plasma achieves the target electron density in Figure 3.10, which plots an Hβ emission line profile from experiment z2090 with the same line from the wall-stabilized arc experiment by Wiese et al. (1972). In Chapters 6 and 7, we further investigate the range of n_{e} our platform can achieve. This includes reaching higher densities than Wiese et al. (1972), which allows us to build upon the benchmark of their seminal work.

In Section 3.2.2 we use simulations to describe the formation of our hydrogen plasma as photoionization due to the gold wall radiation. We confirm this picture experimentally by using an alternate gas cell design, the "Dual Distance"

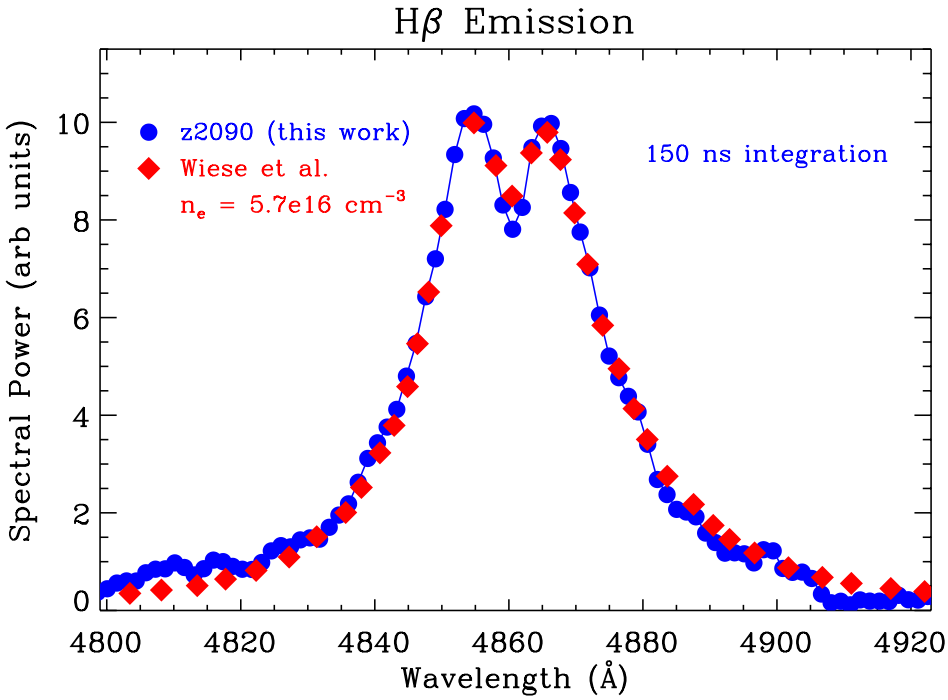

Figure 3.10 Hβ spectrum (filled, blue circles) integrated over a 150-ns quasi-steady-state period from experiment z2090. The filled, red diamonds are the data from the stabilized arc experiment of Wiese et al. (1972), which determines an electron density $n_e = 5.7 \times 10^{16}\,\mathrm{cm}^{-3}$. The qualitative agreement demonstrates that our plasma reaches the intended range of electron density.

gas cell (Section 4.1.2), to simultaneously measure our plasma along two lines of sight at different distances from the gold wall during a single experiment. In experiment z2300 we observe our plasma in absorption along lines of sight that are 5 and 10 mm away from the gold wall. In experiment z2302 the lines of sight are 10 and 15 mm away. Both experiments use the same nominal gas fill pressure of ~ 30 Torr. We estimate the electron density by fitting our observed Hβ spectral lines to the tabulated profiles from Lemke (1997), which follow the line broadening theory of

Vidal et al. (1973). We discuss our fitting methods, including how we convert our measured absorption data to transmission, in Section 6.2.1.

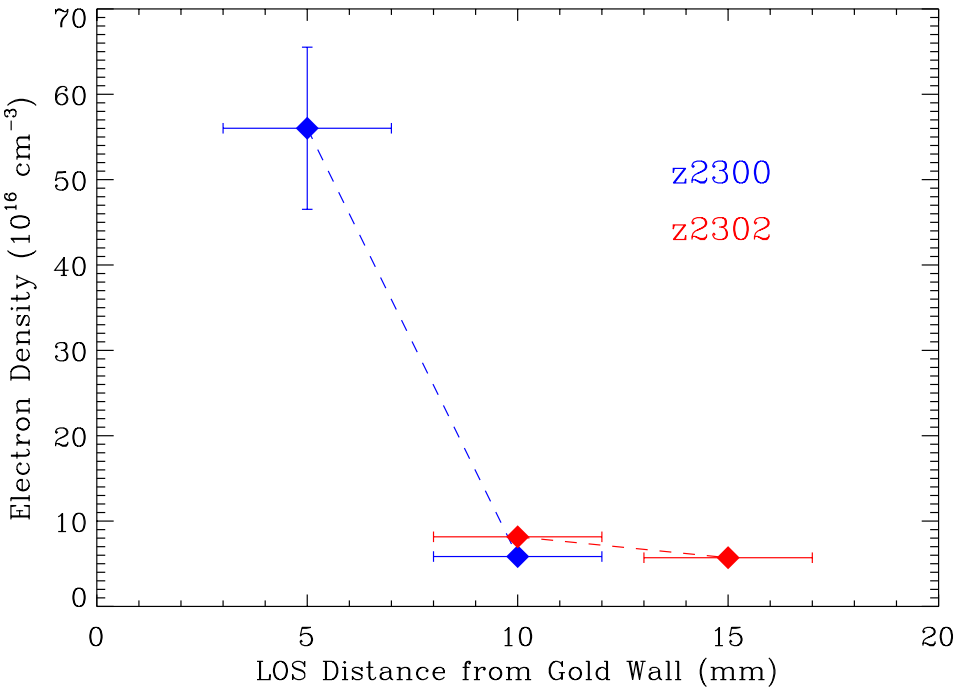

Figure 3.11 The electron density of our hydrogen plasma, estimated from Hβ transmission line fits, decreases with increasing distance from the gold wall. Dashed lines connect determinations from simultaneous observations of lines of sight 5 and 10 mm away from the gold wall from experiment z2300 (blue) and of lines of sight 10 and 15 mm away from the wall from experiment z2302 (red). Solid vertical lines show the standard deviations of n_e values inferred from 5-ns line-outs spanning 30–45 ns after the onset of x-rays. This vertical line is larger than the symbol size for only the data point corresponding to the LOS closest to the gold wall. Solid, horizontal lines represent the 4-mm nominal LOS beam diameters.

Figure 3.11 plots the inferred n_e as a function of LOS distance from the gold wall, showing the decrease with increasing distance. Dashed lines connect

values determined from the lines of sight that are 5 and 10 mm away from the gold wall from experiment z2300 (blue) and 10 and 15 mm away from the wall from experiment z2302 (red). Each data point is the mean $n_{\rm e}$ inferred from fits to three consecutive 5-ns line-outs (defined in Section 5.2.2) spanning 30–45 ns after the onset of x-rays. The solid, vertical lines represent the standard deviation of inferred $n_{\rm e}$ for these three line-outs. For the 10 and 15 mm points, the standard deviations are smaller than the symbol size. The solid, horizontal lines are the 4-mm nominal LOS beam diameters used for these experiments. We note that the extracted line transmissions we fit for these determinations do not include self-emission corrections (Section 6.2). Since this should result in overestimations of only $\sim$ few percent (Section 7.1.2), it does not change our qualitative results.

3.4.2 Comparison with other Experimental Platforms

Forming a hydrogen plasma using radiation requires a sufficient number of ionizing photons distributed over a relatively large surface area. This is only possible with a large input of energy to the experimental system, which, in our case, is supplied by the large amount of x-rays from a z-pinch dynamic hohlraum.

To understand how our radiation-driven plasma source compares with other plasma sources, we look to the discussions of Konjević & Roberts (1976); Konjević & Wiese (1976); Konjević (1999) and Konjević et al. (2002). Though these reviews do not include experiments investigating hydrogen specifically, they provide an excellent contextual description of the plasma sources, diagnostic methods, and experimental considerations pertinent for laboratory studies of Stark-broadened

spectral lines.

As pointed out in Wiese et al. (1972), the two most desirable properties of a plasma source are that it is stationary (in a steady state of plasma conditions) and homogeneous (in a uniform state of plasma conditions). None are truly stationary or homogeneous, but different sources can achieve either or both of these properties to some degree.

Shock-heated experiments (e.g., Doherty & Turner 1955; Berg et al. 1962; McLean & Ramsden 1965; Bengtson et al. 1969; Hey & Griem 1975; Okasaka et al. 1977; Djurović et al. 2005) observe a plasma in a shock front that travels through a tube. If the shock front is planar and the boundary layers negligible, then one achieves a homogeneous plasma by observing along a LOS that is tangential to the plane of the shock front. Since this plasma is not stationary, the temporal resolution of the observation must be sufficient. The experimental setup must also be highly reproducible to repeat the experiment many times to accumulate a satisfactory signal level. In the published literature, hydrogen has not always been the primary component of the gas fill. This means that some composition other than hydrogen was the focus of scientific inquiry and scrutinizing the subtleties associated with experimenting on hydrogen specifically may not have been a priority of the work.

One may also achieve homogeneity using pulsed discharges (e.g., Vujnović et al. 1962; Hill & Gerardo 1967; Morris & Krey 1968; Torres et al. 1984) by appropriately arranging the observing optics (i.e., by observing a discharge plasma "end-on" along its axis) and while paying special attention to the boundary layers. These plasmas are also not stationary and must be highly reproducible. Again,

hydrogen has not always been the primary component of the gas fill.

Stabilized arc experiments are stationary, which is advantageous for data collection and for achieving high S/N data. These plasmas are not radially homogeneous, so when they are observed "side-on" (perpendicular to the arc axis) (e.g., Wiese et al. 1963; Shumaker & Popenoe 1968; Wiese et al. 1972; Ershov-Pavlov et al. 1987), one must correct for the radial temperature distribution using, for example, an Abel inversion (Bockasten 1961). Some investigations observe the plasma "end-on" (e.g., Baessler & Kock 1980; Helbig & Nick 1981; Halenka & Musielok 1986; Djurović et al. 1988), but, like the pulsed discharge experiments, properly addressing the boundary layers in the plasma is a significant difficulty. Also, with the exception of Wiese et al. (1963, 1972) and Wiese et al. (1975), the experiments we list here operate arcs in gases that are mostly argon with only small amounts of hydrogen. The reason is for plasma diagnostics using Ar spectral lines as well as to observe the hydrogen at desired optical depths. However, the shapes of the hydrogen profiles are affected by Ar lines due to blending; removing these lines introduces a systematic uncertainty.

Our discussion does not include all possible plasma sources. We attempt to cover the ones most relevant to our investigation. For example, though experiments using radio frequency discharge plasmas (e.g., Schlüter & Avila 1966; Bengtson et al. 1970) observe many high n lines, the electron densities are too low for our interests. Laser-driven optical discharge plasmas (e.g., Carlhoff et al. 1986; Uhlenbusch & Viöl 1990) are stationary, but they are too high density, leaving only the lowest n Balmer lines separated (not overlapping) enough to be useful. Laser-

induced optical breakdown plasmas span a large range of conditions but are transient, inhomogeneous, and spatially small (Parigger et al. 1995, 2003).

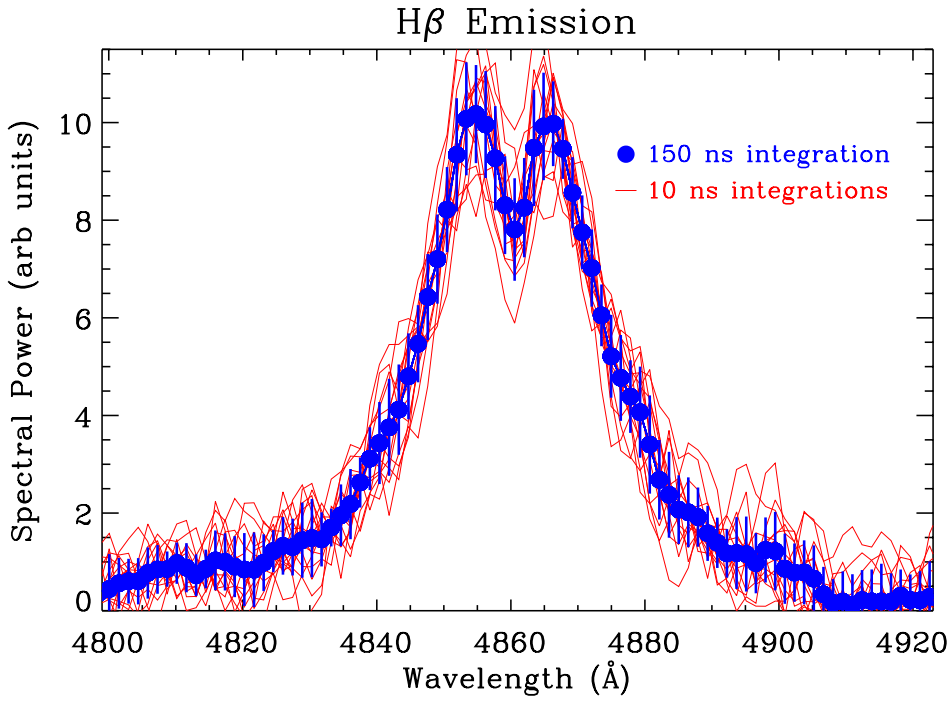

Figure 3.12 Hβ emission line profiles integrated over 10-ns durations (red curves) throughout a 150-ns quasi-steady-state period from experiment z2090 (the same integration we plot in Figure 3.10). The combined 150-ns integration curve (filled, blue circles) includes the standard deviation ($\sim 15\,\%$ at half of the maximum spectral power) of the shorter time integrations, illustrating the level to which they stay similar.

The plasma generated in our experiment is not quite stationary like the stabilized arc plasmas, but with our time-resolved measurements (Section 3.3) we monitor smooth changes in the plasma conditions (Section 7.1). In some experiments, our plasma can reach a quasi-steady-state where the Balmer line shapes remain rel-

atively constant for some time. We illustrate this in Figure 3.12, which plots 10-ns integrations of the Hβ emission line (red curves) throughout a 150-ns quasi-steady-state period from experiment z2090 (the same integration we plot in Figure 3.10). The standard deviation ($\sim$ 15 % at half of the maximum spectral power) of these red curves is a measure of the stability of the spectral line throughout time.

Our plasma is also heated by radiation coming off of a relatively large (120x10 mm) planar surface. This reduces the limitations of observation imposed by the localized heating that occurs with pulsed discharges or arcs. We are not concerned with accurately integrating our observed LOS over an arc or annulus of constant radius about an axis as is needed for "end-on" observations. Nor are we concerned with performing Abel inversions for "side-on" observations, which can yield erroneous emission measurements if the opacity of the plasma is not properly handled (Nagayama et al. 2008). We are free to change the distance of our LOS from the gold wall, thus probing different ionizations within the same plasma. The large heating surface allows us to observe longer path lengths than can be achieved in other plasma sources, and we can vary these lengths more readily. Observing longer path lengths means we can measure spectral lines that are more optically thin without having to increase the density or integrate over long exposure times. The large surface also aides us in achieving homogeneity (along lines of sight at a constant distance from the wall) by minimizing the sensitivity of the plasma heating to small inhomogeneities in the gold wall temperature. More importantly, the long path length minimizes the effect of boundary layer plasmas contributing to inhomogeneity (e.g., Bengtson & Chester 1976).

Perhaps the most distinguishing feature of our experiment is the ability to observe hydrogen Balmer lines in absorption in addition to emission. Just as x-rays from the z-pinch heat the gold wall at the back end of the gas cell cavity, they also heat another gold surface that is angled so as to have a clear line of sight to both the observing optics and the z-pinch radiation. The re-emission from the gold provides a bright, smooth continuum background useful for absorption measurements across our visible wavelength range (Iglesias 2006).

It is interesting to note that, because experiments have never before had such a back-lighter available that allowed for absorption measurements, there has never been a convention in line profile studies to specify emission versus absorption line profiles. "Line profile" has always implied "*emission* line profile". In fact, one must search the literature carefully in order to encounter this more precise jargon, but even then, it is used in a hybrid form in the context of self-absorption of an emission line (e.g., Burgess & Mahon 1972). We also point out that the spectral lines in WD observations, from which atmospheric parameters are determined, are all measured in absorption.

3.5 Conclusions

We describe an experimental platform to create hydrogen plasmas in the range of conditions that exist in white dwarf photospheres ($T_{\rm e} \sim 1\,{\rm eV}$, $n_{\rm e} \sim 10^{17}\,{\rm cm}^{-3}$). Here we measure hydrogen Balmer line profiles in emission and, for the first time, in absorption, and, also for the first time, in emission and absorption *simultaneously*. We will use these profiles to constrain the latest theoretical WD

atmosphere models, which, when used with the spectroscopic method, are responsible for determining fundamental parameters (i.e., effective temperature, mass) for thousands of WDs. We perform our experiment at the *Z* Pulsed Power Facility at Sandia National Laboratories, making use of its powerful x-ray capability to initiate plasma formation in a gas cell. Our plasma source is radiation-driven, which is unique compared to past experiments and which decouples the heating source from the plasma to be studied.

Chapter 4

Evolving a Laboratory Experiment

It's so backwards. This.

Being at the observatory seems so natural now. Staying awake is so easy. Innumerable stars gaze down upon you (condescending in the archaic definition), peeling back your eyelids with awe. Yes, it's solitary time, those nights, but aren't they so peaceful? Don't you feel like if you just sit there long enough, outside the telescope, on the cold metal of the catwalk in the dark, that you'll just *absorb* wisdom from those elders up above. Like Kubrick's/Clarke's man-apes acquiring knowledge from the mysterious monolith.

Oh, but the night. Yes, it's easy to stay up, to push the nocturnal envelope. I guess I'm just used to learning taking place in an intimate environment, beneath the cloak of night, in the absence of the brilliant Sun saturating the world with too many photons to count, life getting lost in the noise of television commercials, traffic lights, hallway gossip.

Here, it's different. Right now I'm encroaching upon the night from the wrong direction. It's 4:45 am! I'll be at the lab by 6:00 to start a really

long day (not night) punctuated by a shot experiment. There will be dozens of people bustling around, seemingly as many as stars lining the celestial sphere. The shot schedule will demand a constant sense of urgency. Walkie-talkie radio chatter will clog the ether.

The complete opposite. Is it even possible to gain knowledge by doing things this way?

Just you wait and see.

Similar to observatories in the astronomy realm, the *Z* Facility, for its fraction of time allocated to fundamental science, solicits proposals from principal investigators. For the accepted proposals, *Z* then schedules days for shot experiments. Because of the time needed to refurbish the facility between shot experiments, only one is conducted per day. An experimenter receives groups of a few subsequent days (a series) and at different times throughout the year. Our experiments, for example, may occur for one week – a series of five experiments in five days – for three series each separated by a couple or a few months.

Unlike at observatories, gathering data at *Z* means destroying much hardware. Some of this hardware, collectively called "load hardware", is responsible for coupling the impressively high current from the accelerator pulse through the wire array to create the *z*-pinch dynamic hohlraum. Other hardware, the "experiment hardware", consists of gas cells or targets for the ZAPP experiments (Rochau

et al. 2014). Some of our experiment hardware survives, as mentioned in Section 3.2.3. All hardware is custom-made, and some components require precise and delicate fabrication (i.e., assembling the wire arrays), which means a lead time of several weeks.

The facility, diagnostic instruments, and experiments also each operate and are maintained through the diligence of dozens of people in intricate coordination.

These three factors, as well as others, contribute to a unique environment in which we conduct our experiments. This results in a nonlinear evolution, most specifically for our gas cell design and experimental approach. The paucity and preciousness of each experiment limits how systematically we can investigate details of our experimental platform. We cannot afford to make a single modification at a time, assess, and move on to the next concern, as is good practice for thorough work. We must address multiple fronts in parallel in order to make reasonable progress, while keeping in consideration that lead times often mean that the hardware for the upcoming experiment series is already being manufactured before we receive results from the previous.

Table 4.1. Catalogue of Experiments

Experiment	Date	Cell Type	Fill Pressure (Torr)	SVS	Data Type	LOS Length (mm)	LOS Distance (mm)
z2084	04.14.2010		15		Emission	60	10
z2085	04.15.2010		0		Emission	60	10
z2086	04.16.2010		3		Emission	60	10
z2090	05.05.2010		15		Emission	60	10
z2091	05.07.2010		15		Emission	60	10
z2127	07.27.2010		15		Emission	60	10
z2128	07.28.2010		15		Emission	60	10
z2129	07.29.2010		15		Emission	60	10
z2153	01.18.2011		7.5		Emission	60	10
z2154	01.20.2011		7.5		Emission	60	10
z2155	01.21.2011		30		Emission	60	10
z2175	03.07.2011		15		Emission	60	10
z2176	03.08.2011	Short	30		Emission	30	10
z2218	06.27.2011		30		Emission	60	10
z2219	06.28.2011	Short	30		Emission	30	10
z2220	06.29.2011		0		Emission	60	10
z2221	06.30.2011	Long	30		Emission	120	10
z2222	07.01.2011	Long	30		Emission	120	10
z2242	08.17.2011	Transmission	15		Absorption	120	10
z2243	08.18.2011	Transmission	0		Absorption	120	10
z2244	08.19.2011	Transmission	15		Absorption	120	10
z2267	11.28.2011	Transmission	30	1	Absorption	110	10
				2	Continuum	10	10
z2268	11.30.2011	Transmission	0	1	Absorption	110	10
				2	Continuum	10	10
z2269	12.01.2011	Transmission	30	1	Absorption	70	10
				2	Continuum	10	10
z2270	12.02.2011	Transmission	0	1	Absorption	110	10
				2	Continuum	10	10
z2298	02.06.2012	Dual Distance	30	1	Absorption	110	10
				2	Absorption	110	5
z2299	02.07.2012	Dual Length	30	1	Absorption	30	10
				2	Absorption	70	10
z2300	02.08.2012	Dual Distance	30	1	Absorption	110	10
				2	Absorption	110	5
z2301	02.09.2012	Dual Length	15	1	Absorption	30	10
				2	Absorption	70	10
z2302	02.10.2012	Dual Distance	30	1	Absorption	110	10
				2	Absorption	110	15
z2308	02.28.2012	Dual Length	30	1	Absorption	30	10
				2	Absorption	70	10
z2309	02.29.2012	Dual Distance	30	1	Absorption	110	10
				2	Absorption	110	5
z2310	03.01.2012	Dual Distance	15	1	Absorption	110	10
				2	Absorption	110	5
z2363	06.11.2012	TEA	30	1	Emission	100	10
				2	Absorption	100	10

Table 4.1 (cont'd)

Experiment	Date	Cell Type	Fill Pressure (Torr)	SVS	Data Type	LOS Length (mm)	LOS Distance (mm)
				3	Continuum	10	10
z2364	06.12.2012	TEA	30	1	Emission	100	10
				2	Absorption	100	10
				3	Continuum	10	10
z2365	06.13.2012	TEA	30	1	Emission	100	10
				2	Absorption	100	10
				3	Continuum	10	10
z2366	06.14.2012	TEA	30	1	Emission	100	10
				2	Emission	100	10
				3	Continuum	10	10
z2367	06.15.2012	TEA	10	1	Emission	100	10
				2	Emission	100	10
				3	Continuum	10	10
z2388	07.31.2012	ACE	10	1	Absorption	120	10
				2	Emission	120	10
				3	Continuum	10	10
z2389	08.01.2012	ACE	10	1	Emission	120	10
				2	Absorption	120	10
				3	Continuum	10	10
z2409	09.17.2012	ACE	10	1	Emission	100	10
				2	Absorption	100	10
				3	Continuum	10	10
z2410	09.18.2012	ACE	10	1	Emission	100	5
				2	Absorption	100	5
				3	Continuum	10	10
z2411	09.19.2012	ACE	10	1	Emission	100	15
				2	Absorption	100	15
				3	Continuum	10	10
z2412	09.20.2012	ACE	20	1	Emission	100	5
				2	Absorption	100	5
				3	Continuum	10	10
z2413	09.21.2012	ACE	0	1	Emission	100	10
				2	Absorption	100	10
				3	Continuum	10	10
z2482	03.04.2013	ACE	10	1	Emission	120	10
				2	Absorption	120	10
				3	Continuum	10	10
z2483	03.05.2013	ACE	10	1	Emission	120	10
				2	Absorption	120	10
				3	Continuum	10	10
z2484	03.07.2013	ACE	10	1	Emission	120	10
				2	Absorption	120	10
				3	Continuum	10	10
z2552	09.24.2013	Dual Length	10	1	Absorption	70	10
				2	Absorption	30	10
z2553	09.25.2013	ACE	10	1	Emission	120	10
				2	Absorption	120	10

Table 4.1 (cont'd)

Experiment	Date	Cell Type	Fill Pressure (Torr)	SVS	Data Type	LOS Length (mm)	LOS Distance (mm)
z2554	09.27.2013	ACE	10	1	Continuum	10	10
				2	Absorption	120	10
				3	Emission	120	10
z2588	12.04.2013	ACE	10	1	Emission	120	10
				2	Absorption	120	10
				3	Continuum	10	10
z2589	12.06.2013	ACE	10	1	Emission	120	5
				2	Absorption	120	5
				3	Continuum	10	10
z2590	12.09.2013	ACE	10	1	Emission	120	10
				2	Absorption	120	10
				3	Continuum	10	10

Having described the critical features of the gas cell design and overall experimental approach in Chapter 3, we now document some of the modifications made during development and the reasoning behind them. We discuss this in the context of our catalogue of experiments, listed in Table 4.1. The gas fill pressure (Column 4) is the nominal or target value. Column 5 lists the SVS system used. The data type (Column 6) is the intent of the experiment. The LOS Length (Column 7) and LOS Distance (Column 8) are the nominal line-of-sight (LOS) lengths of plasma observed and line-of-sight distances away from the gold wall, respectively. We group experiments into series.

The most significant developments include observing the hydrogen plasma in absorption, which drastically improves the signal-to-noise ratio (S/N) of our data, allowing us to measure higher principal quantum number (n) lines. Another is the capability to observe multiple lines of sight simultaneously during a single experiment using multiple spectrometer systems.

4.1 Gas Cell Designs

4.1.1 Early Development

Our first two experiment series (z2084–6, z2090–1) in April and May 2010 fielded the cell design illustrated in Figure 4.1. We label the primary components, including the central cavity (gray), gas fill ports, Mylar window, tubular optics shield, and buffer (green), each of which serves the same function as described for the ACE gas cell in Section 3.2.3. Designed to observe the plasma in emission and along only one 60-mm LOS, the central cavity is cylindrical. Other differences

include the thin foil (not shown) separating the central cavity from the buffer; its aperture is 3 or 4 mm in diameter rather than 5 mm. The buffer diameter is also smaller at 40 mm, and no additional offset spaces the Mylar from the observed LOS. The fused silica window (not shown) is not yet tilted. We adhere a BK 7 bi-convex lens (Newport model KBX010AR.14) inside the lens mount (dark blue) with epoxy in line between the optical fiber and the fused silica window. Figure 4.1 also shows the mounting hardware that secures the assembly to the floor of the *Z* vacuum chamber and aligns the gas cell with the vertical plane of the *z* pinch.

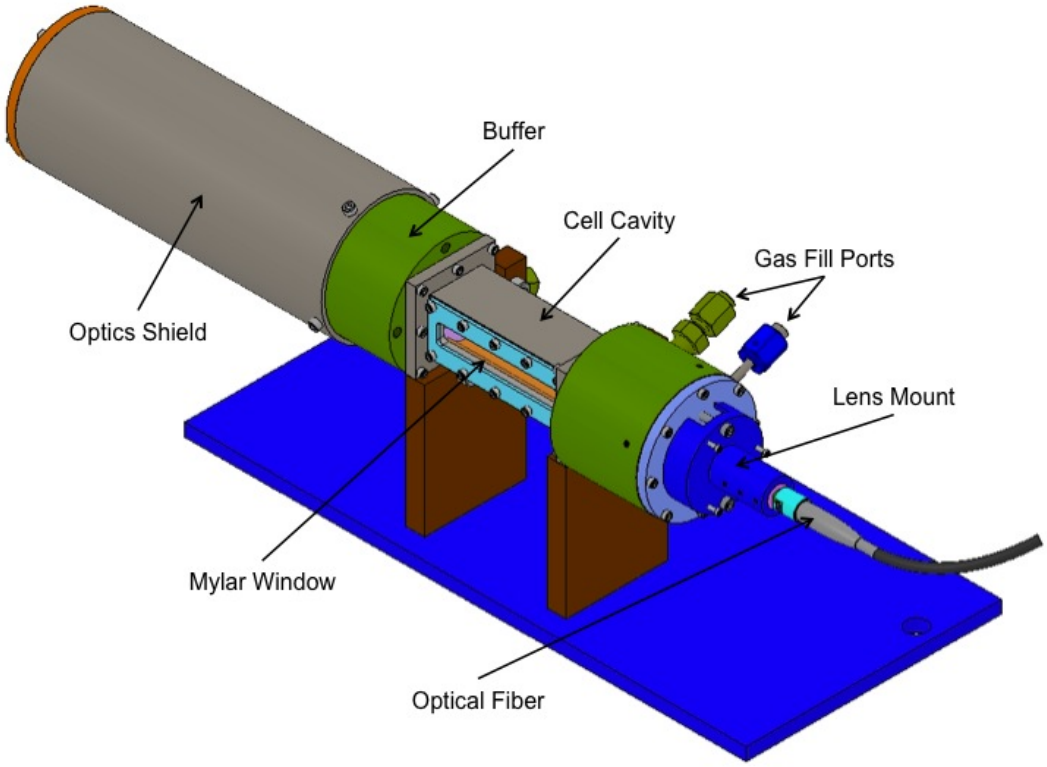

Figure 4.1 Isometric view of the initial gas cell design fielded April and May 2010.

By our third series (z2127–9), we made multiple modifications to the de-

sign. (1) We tilted the fused silica window so that its normal was not parallel with the LOS of the optics. This mitigates optical reflections along this LOS that may complicate our observed signal. (2) We doubled the diameter of the buffer cavity from 40 to 80 mm (see Figure 4.2). A larger cavity allows increased dilution of scattered light. (3) We inserted thin, black, apertured Delrin® disks into the buffer cavity. These disks provide baffling outside their apertures, which are centered along the optical LOS. Starting with experiment z2127, all following experiments incorporate the titled fused silica window and larger buffer. We used the Delrin® baffles for experiments z2127–9 and z2153. Starting with z2154, we stopped using them after observing contaminant (non-hydrogen) spectral features in our data and mistakenly concluding that the source was the Delrin®. We did not resume using these baffles until z2365.

In the measured emission data from the first two experiment series, we observed a drastic brightening of the signal to occur relatively late in time. (Recall that our data are time-resolved.) We attributed this to an ionization wave propagating from the Mylar, having been ionized from the z-pinch x-rays, and intersecting our observed LOS. To extend the lifetime of each experiment, (4) we modified the gas cell hardware to extend the distance of the Mylar window 30 mm closer to the z pinch and hence 30 mm farther from our observed LOS (starting with z2128), as we show in Figure 4.2. Before this modification, the Mylar window resided only 20 mm in front of the gold wall. The figure also points out a window cover, which we used for a few experiment series to minimize the chance of the Mylar window getting ruptured during the installation of the cell assembly into the Z vacuum chamber.

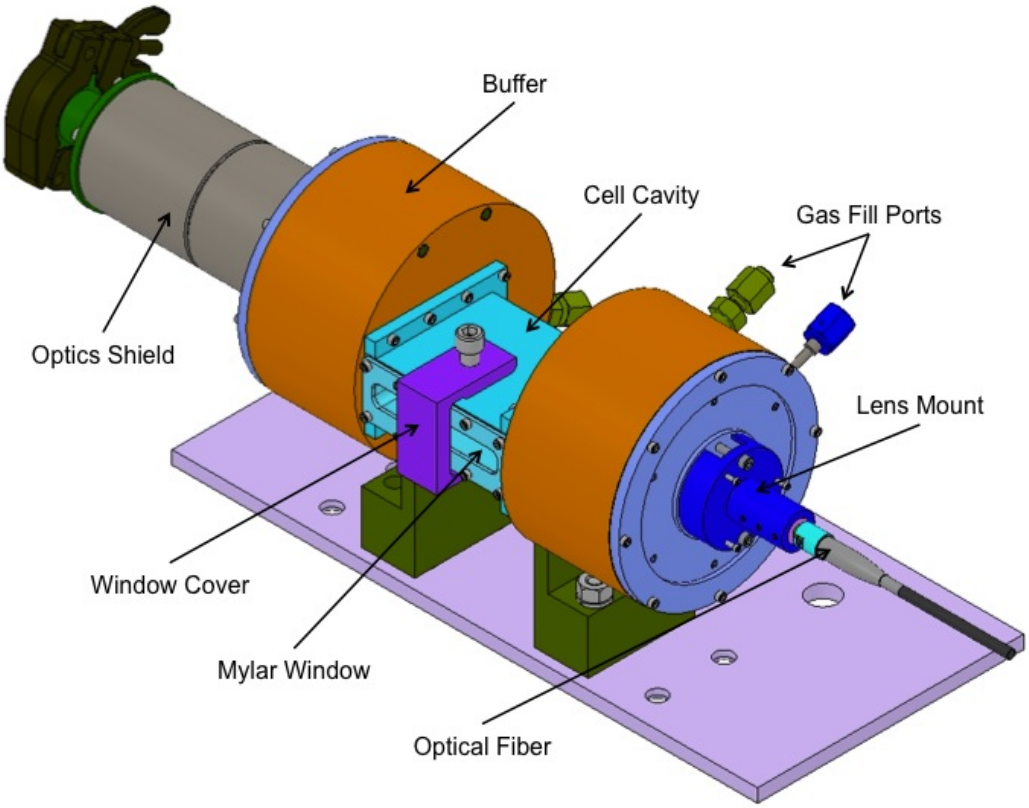

Figure 4.2 Isometric view of the modified gas cell design fielded July 2010.

We discuss the KF flange connected to the end of the optics shield in Section 4.1.4.

At this point, the gas cell has two lines of sight from which to observe the plasma. We couple an optical fiber to each lens mount but only use one to collect emitted light from the experiment and send to a spectrometer system. The other fiber projects laser light through the cell cavity. With the two fibers co-aligned, our collection LOS not only observes the plasma but also the laser simultaneously. We initially used this technique to confirm the lifetime of our optics. If the laser disappears from view at some time during the streak record, we may interpret that as

the fused silica window becoming opaque, optics becoming misaligned, apertures collapsing or closing off, or other scenarios. This was the configuration for the first two experiment series. Having confirmed the longevity of our observation, for z2127–9 and z2153–5 we removed the second optical fiber and replaced it with a "cave" – a tubular, black, rubber cavity (light trap) into which our collection LOS observes in order to minimize the background signal of our plasma emission measurement. Measuring no effect, we abandoned the "cave" after the January 2011 experiment series.

For the last experiment of the January 2011 series, z2155, we increased the diameter of the apertures in the thin foils partitioning the buffer from the central cavity from 3 or 4 mm to 6 mm. We did this to test the hypothesis that contaminant spectral features observed in our data originated from material ablating from these apertures and interloping our LOS. We used these larger diameter apertures through experiment z2270.

Experiment z2176 fielded a gas cell shortened from 60 to 30 mm. By observing weaker emission lines (using the same initial conditions) we confirmed that the emission came from the central cavity. Observing lines of equal strength means that the length of the central cavity makes no difference, which implies that the observed emission comes from elsewhere, such as from the buffer cavity or from the aperture between the buffer and the central cavity. This experiment also suggested that, by using a longer cell, we would increase our observed signal, which is critical for measuring higher n lines that are intrinsically weaker. Fielding a longer cell would require modifications to the load hardware (see Section 4.2) in addition to

our gas cell hardware.

The next series continued these modifications to field gas cells with three different lengths: z2218 at 60 mm, z2219 at 30 mm, z2220 again at 60 mm, and z2221–2 at 120 mm. Now needing to observe a longer LOS, we switched the lens coupled to the optical fiber to one with a longer effective focal length (Newport model KBX013AR.14) to achieve better collimation for our lines of sight.

The emission lines we observed using the "long" gas cell became more intense. The S/N of the higher n lines, however, still was not sufficient for our scientific goal: to measure the relative line shapes of hydrogen Balmer lines. Thus, a strategy emerged to use a gold wall as a back-lighting surface and observe the hydrogen in absorption.

4.1.2 Intermediate Development and Alternate Designs

The August 2011 series (z2242–4) introduced the "Transmission" gas cell design (Figure 4.3). It features a gold-coated back-lighting surface (not shown) inside the central cavity. This surface is angled so that it is visible to a horizontal LOS, a vertical LOS, and the z-pinch x-rays. The x-rays heat this surface just as they heat the gold wall at the back end of the cell cavity, creating a bright, continuum back-lighter useful for absorption measurements across a broad wavelength range. The "Transmission" gas cell was our first design to use two spectrometer systems to make two measurements during a single experiment (see Section 4.2), doing so in the last experiment series of 2011 (z2267–70). The cell uses the "long" gas cell size so that the plasma LOS is nominally 120 mm. z2269 fielded an intermediate

length cell with a plasma LOS $\sim 70\,\mathrm{mm}$.

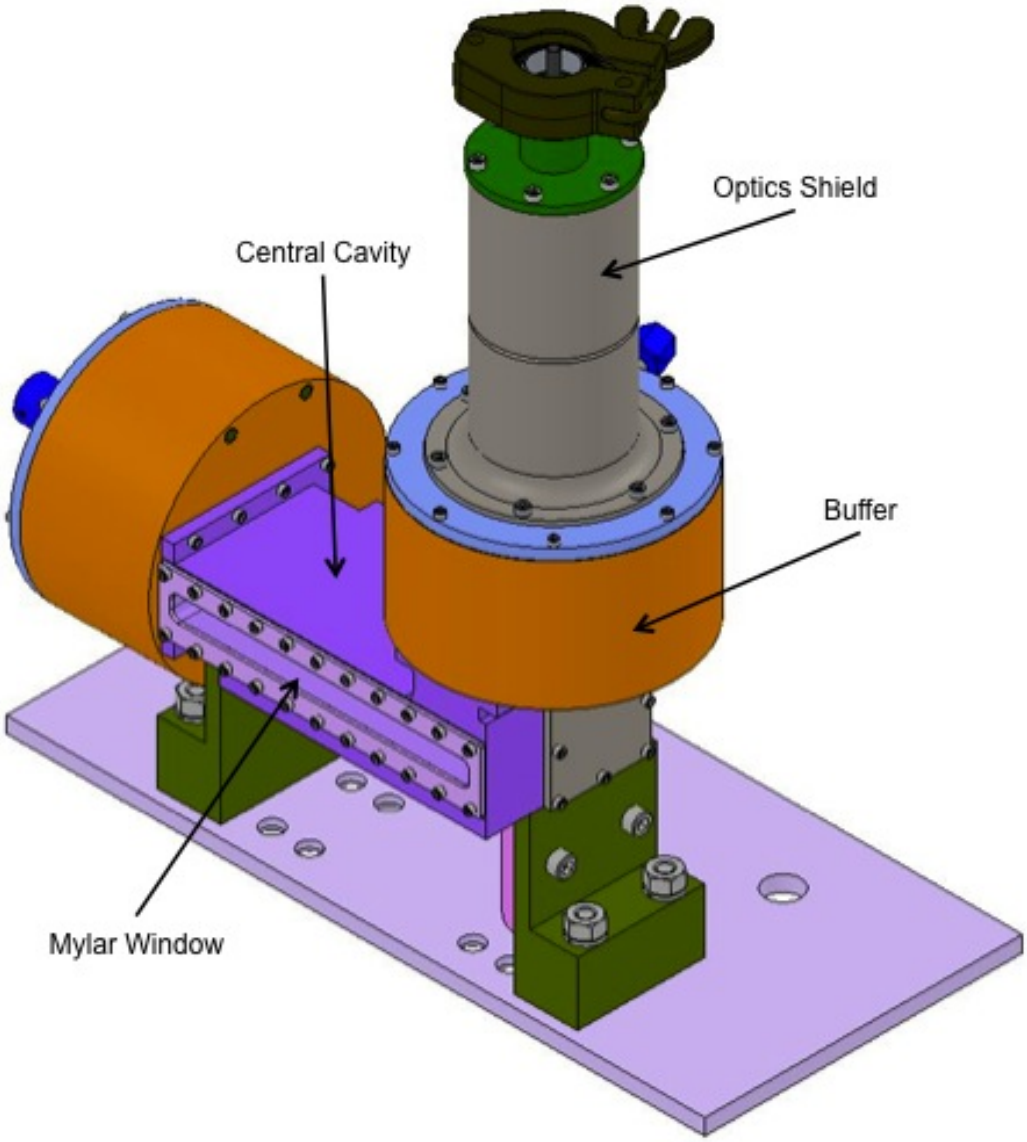

Figure 4.3 Isometric view of the "Transmission" gas cell design fielded August and November 2011.

Starting with z2267, we implemented some additional hardware external to

the gas cell assembly. We placed two limiting apertures at ~ 43 and ~ 58 mm away from the z-pinch axis and along the LOS to the cell. These apertures have rectangular holes. They serve us by attenuating radiation re-emitted from sources other than the z pinch (that become heated by the z pinch). This enhances experiment-to-experiment reproducibility of the radiation incident on the cell by ensuring that z-pinch radiation dominates. It does not, however, mitigate penumbra effects (e.g., Dawson et al. 1984; Wang et al. 2002) due to the finite size of the z pinch and aperture holes nor shape the intensity of the incident radiation to a uniform distribution across the length of the cell. A flattening filter may be used for this, but due to the time-dependent radius and emitted power of the pinch, its precise design may not be straightforward. We leave it for future work to investigate the dependence of the heating of the gold in the central cavity (and hence plasma formation) on the spatial distribution of the z-pinch radiation incident on the gas cell. Given those results, one may use a 3D view factor code such as VISRAD (MacFarlane 2003) with the z-pinch model from Loisel et al. (2014) to optimize a design for a flattening filter.

The two February 2012 experiment series unveiled two new designs, which we name "Dual Distance" and "Dual Length" in Table 4.1. The "Dual Distance" gas cell (Figure 4.4) boasts multiple configurations that allow two anti-parallel, horizontal lines of sight to observe the plasma at different distances from the gold wall. The "Dual Length" design (Figure 4.5) also has two anti-parallel, horizontal lines of sight but at the same distance from the gold wall. A triangular gold-coated wedge sits in the central cavity of the cell, forbidding the two lines of sight from meeting, and it is off-center so that each LOS traverses a different length.

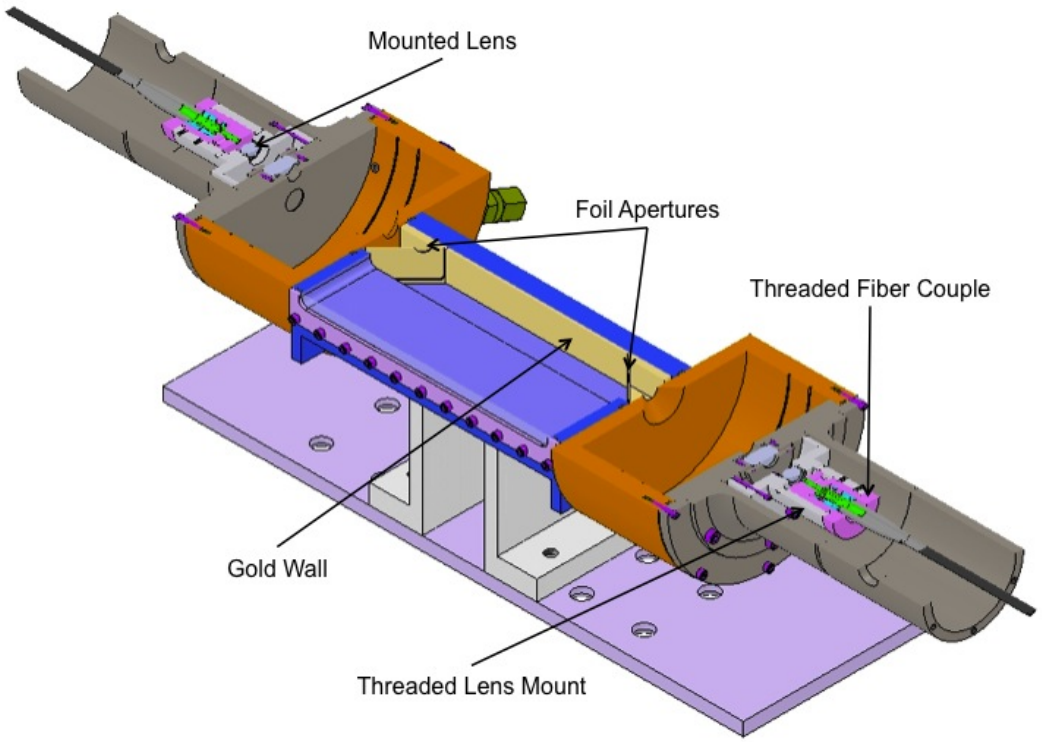

Figure 4.4 Isometric cross-section view of the "Dual Distance" gas cell design fielded February 2012. The apertures in the foils separating the central cavity from the buffer cavities allow lines of sight to observe different distances away from the gold wall.

For experiments z2298–302, we modified the interior of the central cavity, making it rectangular as illustrated in Figures 3.2, 4.4, and 4.5. Before z2298, the central cavity was cylindrical. A cylindrical cavity has only one preferred line of sight – in the center (zero radius). The rectangular cavity provides the flexibility to vertically translate a LOS (within some range) while observing the same nominal plasma conditions. Experiments z2308–10 fielded "Dual Distance" and "Dual Length" cells with cylindrical cavities, but all since (of any design) have rectangular

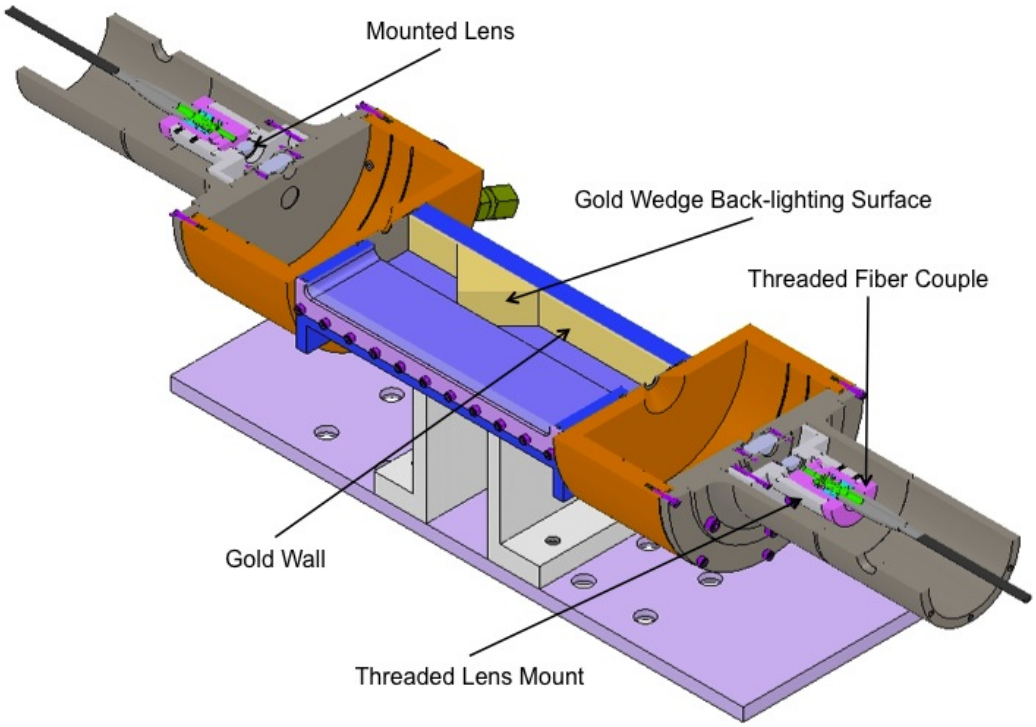

Figure 4.5 Isometric cross-section view of the "Dual Length" gas cell design fielded February 2012. The gold wedge back-lighting surface splits the central cavity into two unequal volumes, allowing two lines of sight to observe different lengths of plasma.

cavities.

Before the June 2012 experiment series, we modified the "fiber couple" (pink component in Figures 4.4 and 4.5) and "lens mount" (light gray component) hardware components so that the two couple together with a relatively fine thread. We use these for z2363 and all following experiments. Set screws fasten the optical fiber to the "fiber couple", and epoxy adheres the lens onto the "lens mount". To collimate the optic, we adjust the distance between the end of the optical fiber and

the lens. Before the threaded design, this adjustment was coarse as it only relied upon our ability to slide the cylindrical "fiber couple" within the "lens mount" along the direction of the optical LOS to optimize the position. The threaded components allow for fine adjustment of this collimation. Figure 3.5 shows a closer view of this optical setup.

The June 2012 experiment series (z2363–7) unveiled yet another cell design – a combination of the "Transmission" gas cell and the previous one used for emission measurements. We refer to this design as the "TEA" configuration, which stands for: Transmission–Emission–Absorption. This gas cell allows three lines of sight to record data. As designed, the "TEA" configuration suffers some shortfalls, which we now address.

4.1.3 Matured Development

For the next experiment series (z2388–9), we modified the "TEA" configuration gas cell to correct its shortfalls. We name this improved design the "ACE" configuration (Figure 3.4) not only to shed vestiges of its fallen progenitor but also to be more descriptive of the three lines of sight that define it: Absorption–Continuum–Emission. Both designs consist of slightly-angled, intersecting, horizontal lines of sight with which to observe the plasma in emission and absorption. As illustrated in Figure 4.6, the "TEA" configuration (top) exposes its apertures (in polyhedral blocks and not in thin foils) to the z-pinch x-rays while the apertures in the "ACE" configuration (bottom) are not visible to the x-rays, residing wide of the Mylar window and perpendicular to the observing lines of sight. The back-lighting

surface remains exposed. As discovered during the June 2012 experiment series, leaving the apertures exposed allows them to heat up from the incident x-rays, and the re-emission of the hot apertures interlopes our lines of sight, overwhelming our measurements with foreground and background continuum signal. For this same reason the "Dual Distance" design, too, is fundamentally flawed.

Also to mitigate undesired emission from the apertures and provide a larger tolerance, we modified these apertures again, settling at 5 mm in diameter. We use this size diameter since.

The ACE design incorporates the feature of the "Dual Length" cell that allows the horizontal (emission and absorption) lines of sight to observe at different distances from the gold wall. Unlike the "Dual Length" cell, though, the ACE cell cannot observe two different distances with two lines of sight simultaneously. Both horizontal lines of sight observe one of three positions: 5, 10, or 15 mm away from the gold wall. We illustrate how each of these positions probe our experimental plasma in Section 6.1.2.

Starting with z2389 we decreased the thickness of the gold coating of the interior components of the central cavity from 25 to 5 μm in order to decrease hardware expenses. Also to decrease expenses and because it serves no function now that they are shielded from the x-rays, from z2409 and on we abandoned coating the thin foils (with the apertures) with gold, leaving them as bare aluminum.

The September 2012 experiment series saw minor modifications to optimize the "ACE" configuration gas cell. We changed the lens coupled to the optical fiber

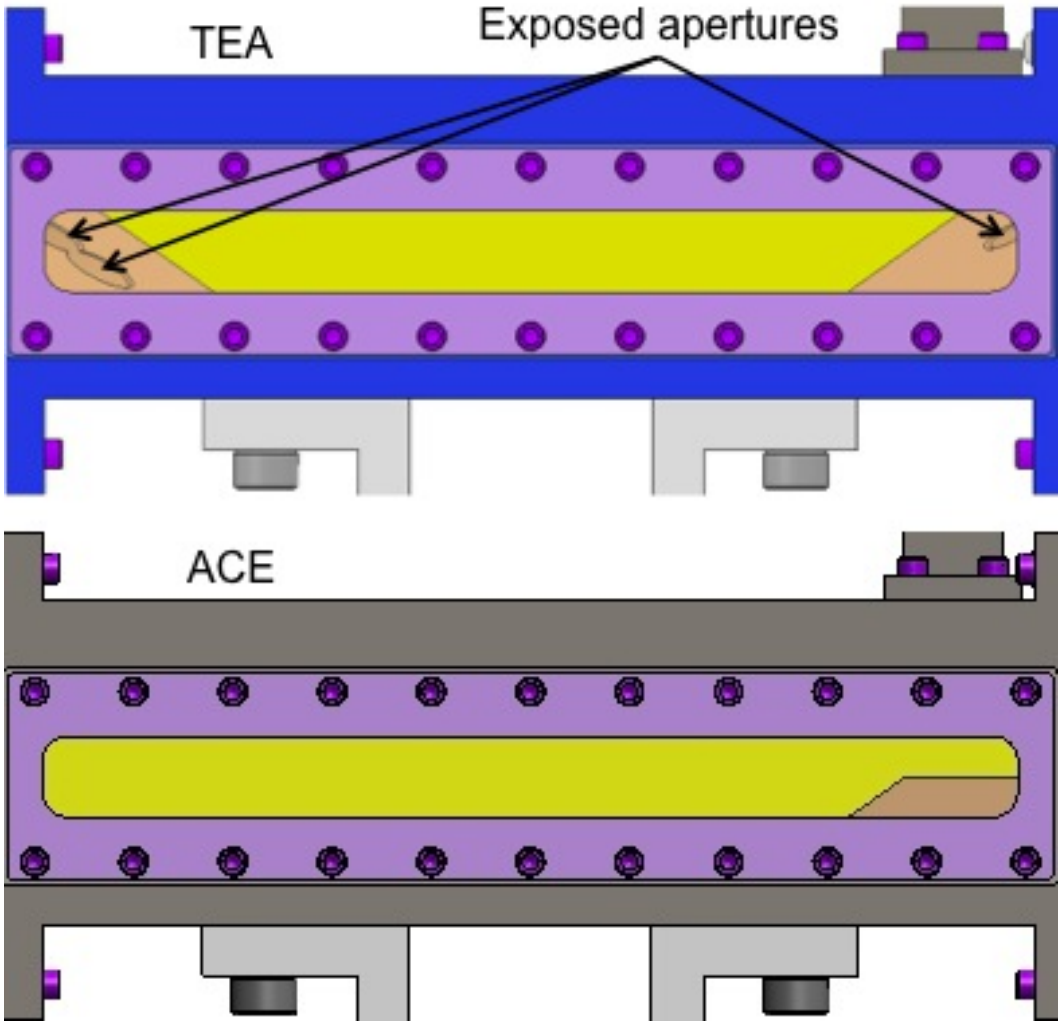

Figure 4.6 Front-view drawings of the central cavity for the "TEA" configuration gas cell (top) and the "ACE" configuration gas cell (bottom). For the former design, the apertures are exposed to the z-pinch x-rays.

to an achromatic doublet lens (Thorlabs model AC060-010-A-ML; shown in Figure 3.5) to reduce chromatic aberration across our observed spectral range. These lenses are also mounted inside a threaded hardware. We modified the "lens mount"

to couple with this thread. Not only is this more convenient than adhering an unmounted lens to the "lens mount" using epoxy, it prevents damage to the lens that may occur during handling, such as leaving residue on the lens, and it makes the optical fiber assemblies more uniform.

We implemented a 3-mm diameter limiting aperture (Figure 3.5) between the lens and the fused silica window. This reduces the size of our collection beam, granting more clearance of the aperture in the (now aluminum) thin foil between the buffer and central cavity. Combined with beam profiler measurements, the 3-mm limiting apertures make the collection beams of the optical fiber assemblies more uniform and more easily characterized, and characterizing the collection optics is an essential component of the calibration of our measurements (see Section 5.3).

We also revived the "cave" for the emission LOS by adhering a short ($\sim 2\,\mathrm{cm}$), ~ 1-cm diameter, black, rubber tube on the inside buffer wall opposite of the emission LOS at the end of its LOS. We used these tubular baffles for experiments z2409–13 but removed them for the March 2013 series (z2482–4) and on because they interfered with our calibration procedure.

4.1.4 Protecting the Gas Cell Fibers

A ~ 4-mm thick tubular, stainless steel shield protects the fused silica window, lens, and optical fiber end for each LOS where the fiber assembly couples to the gas cell. Its first function is to prevent x-rays from denaturing any of the optical components throughout the duration of the experiment ($< 0.5\,\mu\mathrm{s}$). This may include radiation-induced attenuation (e.g., Weiss 1992) or emission inside the op-

tical fiber. Its second function is to fend off debris from the z pinch (which arrives tens to hundreds of μs after the radiation and after our streak record) in the hope of preserving hardware for another experiment. With the debris, soot fills the gas cell cavities and cakes onto the inside surface of the fused silica window. We dispose of the window after each experiment but typically reuse the remaining optical components.

The optics shield is of finite length. Hence, the gas cell fiber extends beyond the jurisdiction of the shield, running ~ 1 m away from the z-pinch axis to a port in the wall of the chamber where its connects to the feed-through fiber (see Section 5.1). For this portion of the fiber, we need a solution to continue the functions of the optics shield while being sufficiently flexible to form to the path of the fiber to the feed-through port. Over the course of our experiments, we have implemented various strategies.

We first used bicycle brake cable housing (Jagwire part #90Y0026), which has coil-wound steel beneath its plastic liner. The inner diameter is perfectly sized to feed through the optical fiber once the fiber is stripped to its 125-μm plastic buffer. Though novel, fabricating gas cell fibers this way is tedious and time-consuming when several fibers are needed.

We next fed optical fibers through $\frac{3}{4}$-inch diameter stainless steel flexible vacuum roughing hose, saving the hassle of stripping fibers. The hose connects to the optics shield via a KF flange (Figures 4.2 and 4.3). Though the KF connection is convenient and the tubing sturdy, the assembly becomes awkward and cumbersome; the short length of fiber that extends past the end of the tubing is especially fragile

and prone to kinking.

Following the idea of the vacuum hose, we attempted a tin-plated copper grounding braid (McMaster-Carr part #6949K62) to encase the fiber like a sleeve. It is lighter, more flexible, and adjustable in length. It is also more difficult to feed optical fiber through this sleeve.

When procuring a type of shield for the fiber, one must consider the investment of resources. The requirement of flexibility inherently makes this shielding physically weaker than the rigid optics shield. This means it is more vulnerable to larger particles of debris or shrapnel that may strike our gas cell assembly on occasion. Though rare, we indeed witness punctured or even severed gas cell fibers reinforced with any of the types of shielding discussed. When this occurs, we question the investment and consider wholly foregoing shielding. Before committing such a rash rebuttal, we need an investigation of the radiation effects specific to our *z*-pinch environment on our collection optics, in particular the effects of transverse x-rays on our optical fibers.

4.2 Additional Notes on the Evolution of the Experiment

Starting with the January 2011 experiment series (z2153–5), the Marx generator charge voltage of the *Z* accelerator was increased from 80 to 85 kV as directed by the primary ZAPP experiment investigating the opacity of iron at the conditions of the solar interior (Bailey et al. 2007, 2009; Nagayama et al. 2012a, 2014a,b). Increased charge voltage leads to increased current through the wire array load which increases the ultimate x-ray yield.

For the experiments z2153–5 we filled the gas cells with helium rather than hydrogen to investigate the feasibility of exploring this composition in future work (Section 7.5.3; Falcon et al. 2013b). Similarly, experiment z2590 used carbon dioxide as the gas fill.

In the June 2011 series (z2218–22), we modified the current return canister of the load hardware to have nine slots instead of eighteen. This time it was our experiment that prompted a modification that affected all the ZAPP experiments. In this design, each slot is wider, allowing a broader x-ray LOS to escape the *z*-pinch dynamic hohlraum. This change coincided with and allowed for the implementation of our "long" (120 mm) gas cell design.

In the autumn of 2011, we moved the location of our spectrometer system from the floor below the *Z* accelerator, where the laser-triggered gas switches (Lechien et al. 2008, 2010) are operated and maintained, to the Laser Target Bay, one of the buildings housing the *Z*-Beamlet laser (Rambo et al. 2005). This permitted the space to incorporate an additional, duplicate spectrometer system, and then eventually a third system. Taken at face value, this increases our data acquisition by two- and three-fold. Upon implementing calibrations (see Section 5.3), however, it also increases the richness of our data set by providing powerful constraints to diagnose our plasma.

4.3 Summary

We elaborate on the development of our experimental platform to create hydrogen plasmas at white dwarf photospheric conditions, focusing on the gas cell

design. The gas cell evolves from observing the plasma in emission to observing it in absorption, significantly increasing the S/N of our data and allowing us to measure higher n lines. The cell also evolves from observing one to two to three lines of sight simultaneously during one pulsed power shot experiment, broadening our diagnostic capabilities.

Chapter 5

Data Acquisition, Processing, and Calibration

Phew. Gas cell is installed into the vacuum chamber. Lid's on. They're pumping down. Schedule's looking good. We have time for lunch (not guaranteed on shot days). How about a little levity? Something to spell my flow (Csikszentmihalyi 1991) for a short while before we get back to the final shot preparations. Nothing heavy.

Ah. Just this walk to the cafeteria is nice. I lift my face toward the sun, let the crisp, dry air imbibe my stress through my skin. Then turn to observe the three of us. We form quite the ambulatory spectacle. Well, I think so at least. It's no Reservoir Dogs. It's no "*the walk*". But we're in a line. Greg's tall, built like a linebacker. Don's optimism puts a slight skip in his step, almost an equestrian trot. And me – I feel the ambivalence in my gait as it struggles to assimilate the mannerisms of either mentor. I *feel* the antiphony. It's like a puppy dog darting back and forth between two people playing catch. I can only wonder if it's visible to others. And silly-looking.

We collect our food and sit down at a table. Greg starts up the conversation. "I'm concerned that we're not making enough progress. We get together for shots

and do a lot of work for that week. But then we step away and don't do much 'til the next shot series. Too much starting and stopping."

So much for something light.

"Yes, I agree." Don agrees.

"So I've been looking to hire a post-doc. Someone to be here at the lab full-time and focus on this project. I maybe had one candidate, but it fell through, and I haven't been able to find anyone else."

I'm listening, nodding.

Don lifts his chin, lifts his eyebrows even more, looks at Greg in a manner that conveys cahoots, "What about a grad student?"

My teeth suspend their incision into my cheeseburger, my nose settling directly above the warmth of the sesame bun. Don's suggesting…

"Not just any grad student," smiles Greg. He turns his head, squares up to address me. "Well, what do you think about coming in as a full-time intern?"

Um.

He continues. "That's what I did. That's how I finished up my grad school."

"I completely support it if you want to do that, Ross." Don's sold.

Um.

"I think we can make a lot of progress – if you're up for it."

"Um…move here?"

That evening I call up my best friend in Albuquerque, the guy with whom I hang out when I'm in town for experiments, a guy who also works at Sandia, a guy to whom Greg introduced me. "Hey, Nate. If I move to Albuquerque in, like, a couple weeks or sooner, can I live with you?"

The *Z* Pulsed Power Facility at Sandia National Laboratories employs a number of instruments to diagnose its range of experiments (e.g., Spielman et al. 1997; Sanford et al. 1997; Chandler et al. 1999; Spielman et al. 1999; Nash et al. 2001; Lake et al. 2004; Jones et al. 2006b; Ives et al. 2006; Sinars et al. 2011; Gomez et al. 2012). In our experiment, the primary diagnostic instrument we use is streaked visible spectroscopy (SVS). This chapter describes how we acquire time-resolved spectra using this diagnostic and process the data. We apply calibrations to measure absolute spectral radiance with our spectrometer systems (e.g., Dunham et al. 2004; Johnston et al. 2012), which aides us to measure spectral line profiles and constrain atomic energy level populations corresponding to those lines. It also allows us to implement optical pyrometric techniques (e.g., Foley 1970; Lyzenga & Ahrens 1979; Partouche-Sebban et al. 2002; Miller et al. 2007) to measure the Planckian temperature of the back-lighting surface in our gas cell used for spectral absorption measurements. Aside from absolute spectral radiance, our calibrations include correcting for the relative instrumental efficiency across wavelength, which is critical for transmission measurements (e.g., Bailey et al. 2009) as well as for studying line shapes (e.g., Wiese et al. 1972).

5.1 Collecting Light from the Experiment

Lens-coupled optical fibers attached to the gas cell assembly collect light emitted from the experiment and deliver it to time-resolved spectrometer systems. We use three systems, but here we focus our description on the first two. Each of these two consists of identical components.

A series of four optical fibers (three connections) link each line of sight (LOS) to its spectrometer. The first connects the gas cell to a vacuum feed-through port that interfaces between the vacuum chamber containing the ZAPP experiments (Rochau et al. 2014) and the LOS 110 diagnostic boat. This diagnostic boat is one of nine alcoves concentrically located immediately outside the vacuum chamber, smaller than the vacuum chamber, designated according to the azimuthal position with respect to other diagnostic radial lines of sight, and aptly named because they reside below the water level of the *Z* water section (see, e.g., Stygar et al. 2007). The feed-through fiber connects to a long (~ 41 m) transit fiber that leads out of the *Z* Facility high bay and into an adjacent building where the SVS diagnostic resides. This transit fiber finally connects to an optical fiber positioned at the input of the spectrometer. For optimal transmission at blue wavelengths, all optical fibers are high-OH silica core/clad step-index multimode fibers. The numerical aperture is 0.22 ± 0.02. All fibers also have a 100-μm core diameter to match the core diameter of the gas cell fiber. We choose its core diameter to function with the optics characterizing the LOS collection beam (Figure 3.5; Section 5.3.3).

The spectrometer is a 1-m focal length, $f/7$ aperture Czerny-Turner design (McPherson, Inc. model 2061). We use 150 groove mm^{-1} gratings in order

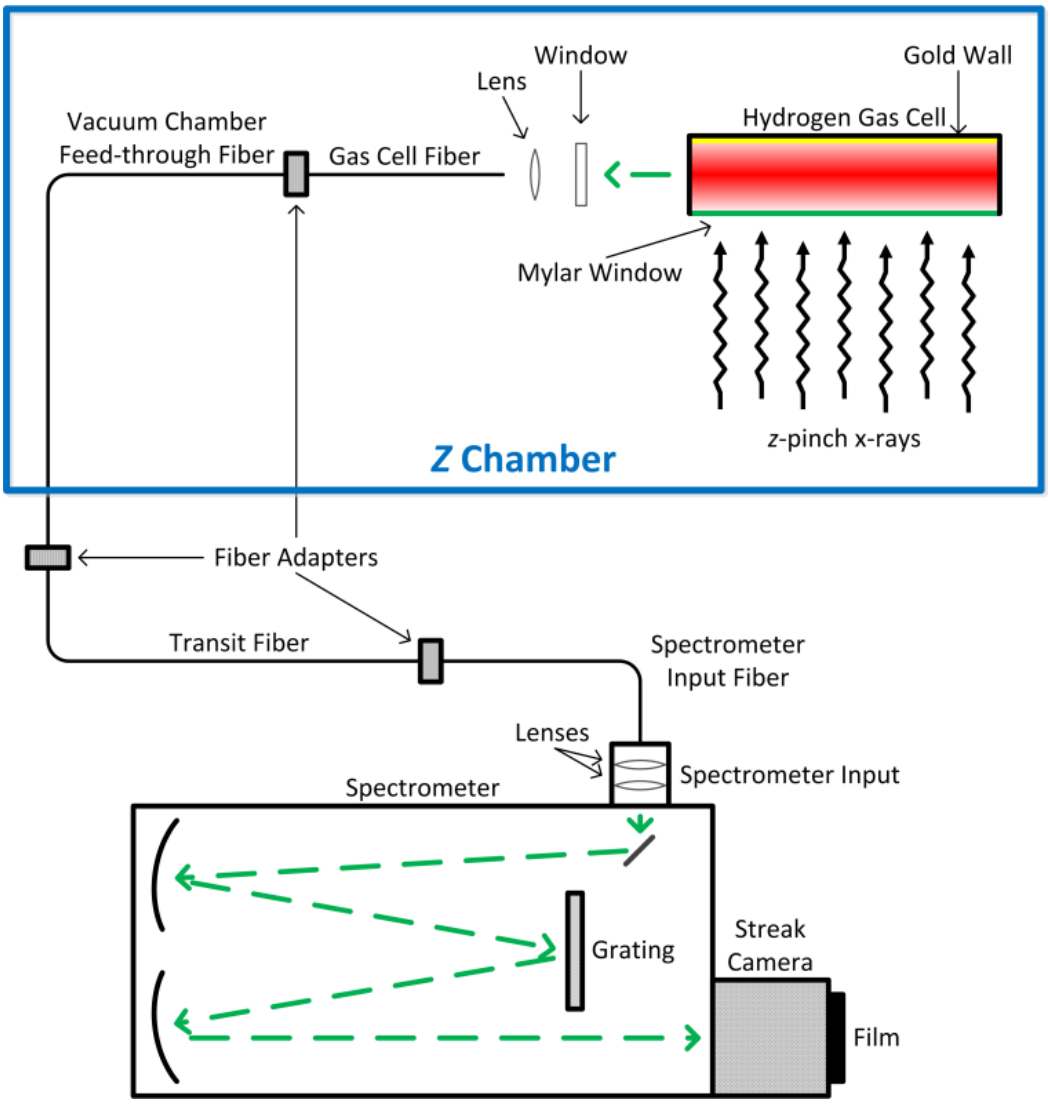

Figure 5.1 Schematic of the light travel path from the experiment through a series of optical fibers, the spectrometer, and the streak camera before depositing onto film for a single line of sight.

to capture a broad wavelength range. The streak camera (EG&G model L-CA-24; Olsen 1989), which includes an S20 multi-alkali photocathode (e.g., Varma

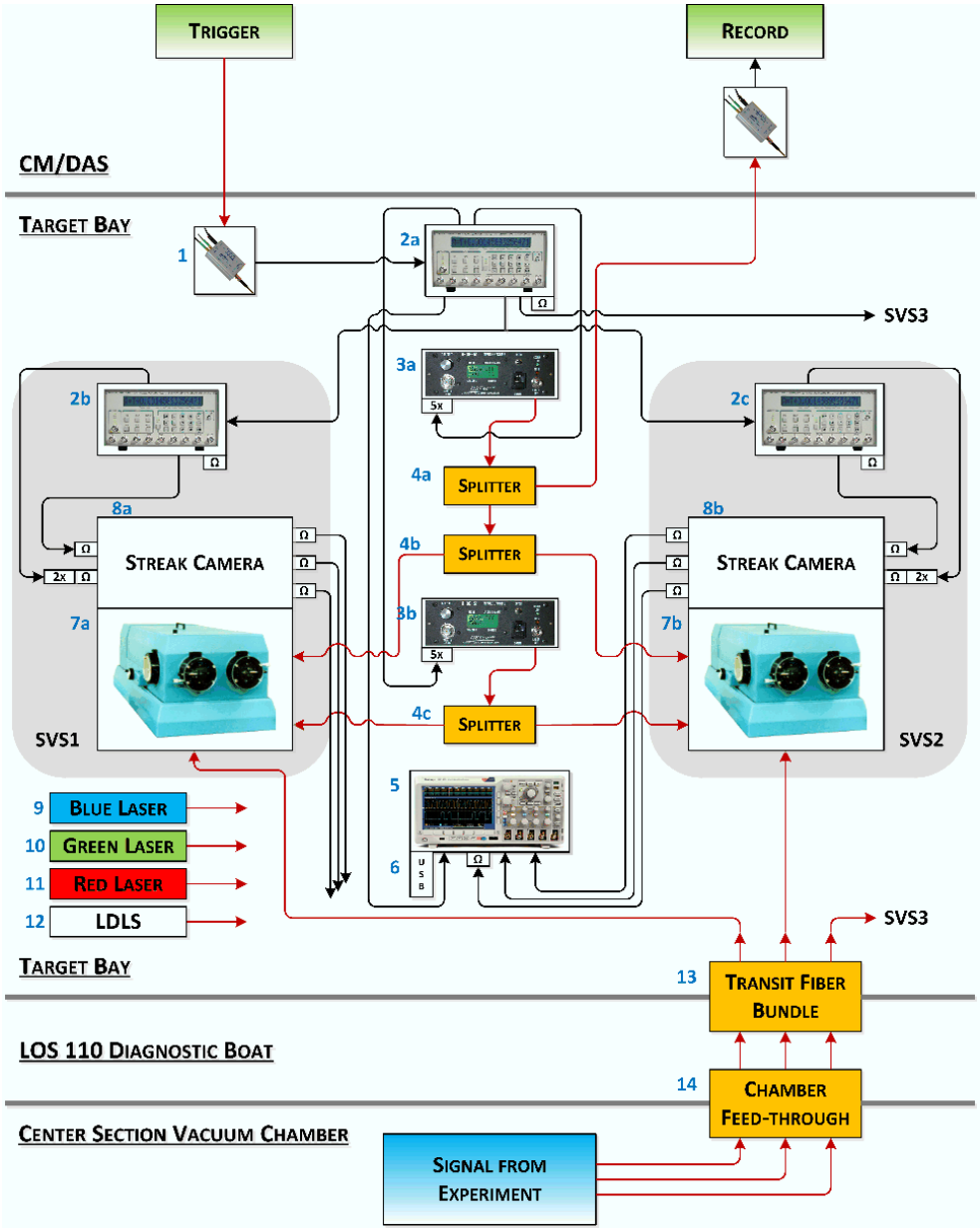

Figure 5.2 Schematic of the streaked visible spectroscopy diagnostic showing optical-fiber (red) and coaxial (black) connections. We list the details of the numbered components in Table 5.1

& Ghosh 1973; Hallensleben et al. 2000) and a P20 phosphor on an optical fiber output window, sweeps the spectrum over ~ 450 ns with $\sim$ 1–2 ns temporal resolution. A micro-channel plate intensifier (MCP; Ladislas Wiza 1979) amplifies the phosphor emittance exiting the camera, outputting to Kodak T-MAX 400 film. The entrance to each spectrometer is conveniently fiber-coupled and has a two-lens (Newport model APAC12, Thorlabs model AC254-050-A-ML) optical setup to optimize the fiber input to the numerical aperture of the spectrometer (e.g., Johnston et al. 2010). We use a 100-μm entrance slit. Figure 5.1 shows a schematic illustrating the path the light from the experiment travels to the film for a single LOS. We discuss the series of optical fibers as well as the optical setup at the end of the gas cell fiber observing the experimental plasma in Section 5.3.2. This SVS diagnostic setup is similar to that used in previous work at *Z* (Bailey et al. 1990, 1997, 2000; Dunham et al. 2004; Bailey et al. 2008; Falcon et al. 2010a, 2013a; Gomez et al. 2014a). Figure 5.2 further illustrates the SVS components, and Table 5.1 provides the details.

5.2 Reduction and Processing

Our time-resolved spectrum, or streak image, starts its life on T-MAX 400 film. A Perkin-Elmer microdensitometer digitizes the film data, and we convert the film density to units of radiant exposure (erg cm^{-2}) using a NIST-calibrated step wedge filter (see, e.g., Bland-Hawthorn et al. 1993; Knapp et al. 2012). We then translate the two position axes of the image into time and wavelength.

Table 5.1. Streaked Visible Spectroscopy Diagnostic Components

Number	SVS	Component	Vendor	Model
1		O/E Converter	Highland Technology	J730-1 Fiberoptic-to-Electrical Converter, 21A730.1B
2a		Master Delay Generator	Stanford Research Systems	DG535 Digital Delay Generator
2b	1	Camera Delay Generator	–	–
2c	2	–	–	–
3a		Impulse Generator	NSTec	H-OE-51 Time/Mark Impulse Generator 13
3b		Comb Generator	–	–
4a		Optical Fiber Splitter	Thorlabs	FCMM50-50A
4b		–	–	–
4c		–	–	–
5		Oscilloscope	Tektronix	DPO3054 Mixed Signal Oscilloscope
6		USB Flash Drive	Edge Tech	DiskGo Classic, 2 GB
7a	1	Spectrometer	McPherson, Inc.	2061 1 m focal length, $f/7$ Czerny-Turner Monochromator
7b	2	–	–	–
8a	1	Streak Camera	EG&G	L-CA-24 Streak Camera
8b	2	–	–	–
	1	Streak Camera Power Supply	EG&G	L-PS-36
	2	–	–	–
	1	Streak Camera Power Supply Monitor	EG&G	L-ME-5
	2	–	–	–
9		Blue Laser	Modu-Laser	Stellar-Por 457/4.5 Argon Ion Laser
10		Green Laser	CVI Melles Griot	05-LGR-193 Green Cylindrical Helium Neon Laser
		Green Laser Power Supply	CVI Melles Griot	05-LPL-903-065 Laboratory Helium Neon Laser Power Supply
11		Red Laser	JDS Uniphase	1122 Helium Neon Laser Head
		Red Laser Power Supply	–	1202-1 HeNe Laser Power Supply
12		LDLS	Energetiq Technology, Inc.	
13		Transit Fiber Bundle		
14		Chamber Feed-Through		

5.2.1 Applying the Temporal Dispersion

We set the scale of the temporal axis using a stream of equally-spaced laser pulses (comb) exposed onto the film during the experiment. By measuring the apparent comb spacing as a function of position across the streak image and fitting a 2^{nd}-order polynomial, we correct for a smoothly and relatively slowly varying sweep rate. We use a single laser pulse (impulse) as a timing fiducial to establish the relative time between data recorded with each spectrometer system (SVS1 and SVS2). Separate units supply the comb and impulse (component numbers 3b and 3a, respectively, in Figure 5.2 and Table 5.1), and we use optical fiber splitters to deliver the same comb (4c) and impulse (4b) to both spectrometers (7a,b) simultaneously.

5.2.2 Applying the Spectral Dispersion

Before setting the spectral axis, we slice the streak image into a sequence of spectra each integrated over some short (few ns out of the few hundred ns streak duration) time interval, which we refer to as line-outs. Streaked lasers exposed onto the film prior to the experiment provide absolute wavelength fiducials throughout time. Our observed wavelength range encompasses two lasers at 4579 Å (blue; component 9 in Table 5.1) and 5435 Å (green; component 10). For each line-out, we use these lasers to measure and apply a linear spectral dispersion. By applying the dispersion in time steps rather than to the image as a whole, we correct for subtle warping of the image in the spectral direction. Similarly, by measuring the comb spacing at a single spectral position[2] in Section 5.2.1, we neglect any warping

corresponding to the temporal direction.

Since the lasers are highly monochromatic ($\Delta\lambda \sim 0.02$–0.03 Å), we recover instrumental broadening by measuring the laser profiles, which are best described as Voigt functions. Using the 150 groove mm^{-1} grating, the measured Voigt full-width-at-half-maximum, which we adopt as the instrumental resolution, is ~ 10 Å. We approximate this Voigt width as

$$f_{\rm V} \approx 0.5346 f_{\rm L} + \sqrt{0.2166 f_{\rm L}^2 + f_{\rm G}^2}, \tag{5.1}$$

where $f_{\rm L}$ and $f_{\rm G}$ are the full-widths-at-half-maxima of Lorentzian and Gaussian profiles, respectively (Olivero 1977).

5.2.3 Correcting for Transit Time Delay

Following the results of Cochrane et al. (2001), we correct our data for the wavelength-dependent optical fiber transit time delay given our total measured fiber length of 55 m. This delay manifests as bluer photons exiting a fiber after redder photons that enter the fiber at the same time. Therefore this correction is crucial for extracting line-outs that sample a unique time interval.

[2]The optical fiber(s) delivering the comb (and impulse) enters the spectrometer near its exit slit so as to pass into the streak camera without encountering the grating. Therefore, technically, a "spectral" position of the comb has no meaning, but we use this simplified terminology since that axis becomes the spectral axis.

5.3 Calibrations

"Greg, absolute calibrations are really hard."

I'm stuck in my own head, shuffling my thoughts in preparation for our meeting. He ricochets a response quickly. As if he's had this one primed for some time.

"Yeah, absolutely!" Immediately followed by: "Get it?"

My jaw slacks. His grin glistens. Yes, Greg. I get it.

Our data are now a sequence of line-outs in units proportional to spectral power (erg s^{-1} $Å^{-1}$). To properly compare data from SVS1 and SVS2 (and amongst experiments), we perform additional processing, including correcting for (1) the wavelength-dependent instrumental efficiency of the SVS system, (2) light attenuation through the optical path from the experiment to the spectrometer, and (3) the geometry or collection efficiency of the observed LOS in the experimental platform. We represent this as

$$L(\lambda) = \frac{L_{\text{un}}(\lambda) E_{\text{inst}}(\lambda)}{T_{\text{link}}(\lambda) A \Omega}, \tag{5.2}$$

where $L(\lambda)$ is our absolutely-calibrated spectral radiance as a function of wavelength λ in units of erg s^{-1} sr^{-1} cm^{-2} $Å^{-1}$, $L_{\text{un}}(\lambda)$ is the uncalibrated spectrum, $E_{\text{inst}}(\lambda)$ is the unitless absolute instrumental efficiency of the SVS system, $T_{\text{link}}(\lambda)$

is the transmission of the transit fiber link, A is the observed area, and Ω is the observed solid angle.

We divide our calibration procedure into components to achieve suitable signal-to-noise (S/N) from a continuum light source when needed (see Section 5.3.1), to accommodate the logistics of the experimental setup, which spans $\gtrsim 50\,\mathrm{m}$ across two buildings, and, most practically, to coordinate activities within a large, highly-subscribed facility such as *Z*. Calibrating components also enables us to evaluate which ingredients may limit performance (Section 5.3.4.2). For the component of our calibration described in Section 5.3.3, we employ a technique to determine the observed area and observed solid angle of our plasma which we observe along an extended ($\sim 120\,\mathrm{mm}$ long, $\sim 3\,\mathrm{mm}$ in diameter) line of sight. Our methods may be applied to a number of experiments performed at the *Z* Facility using the SVS diagnostic.

In this section, we follow the specific experiment z2553, for which one line of sight (LOS) observes the plasma in emission, and the other observes in absorption using a gold wall, irradiated by x-rays, as a back-lighting source.

5.3.1 Instrumental Efficiency

Multiple components within the spectrometer system attenuate the light and its spectral shape between entering the fiber-coupled input of the spectrometer and ultimately recording onto film. To measure this instrumental efficiency, we observe a continuum light source before it enters the spectrometer and as it appears on the film having passed through the instrument. The ratio of these spectra is the

relative instrumental efficiency across wavelength. We then place the data onto an absolute scale using lasers as absolute power fiducials. After applying this two-part correction, we have absolute spectral radiance as a function of wavelength at the spectrometer entrance.

5.3.1.1 Relative Efficiency Versus Wavelength

Our continuum light source is a laser-driven light source (LDLS; Energetiq Technology LDLS EQ-99FC). We choose this light source because its spectral shape is relatively smooth over our wavelength range of interest and because this shape is temporally stable (Zhu et al. 2012). Since we make optical fiber connections to spectrometers and other fibers, our definition for light source includes the LDLS plus an additional length of optical fiber. The light exits our light source (the fiber end) at a range of angles up to the maximum angle allowed by its numerical aperture; we assume that, when connected to the spectrometer (and to the fiber link in Section 5.3.2) for calibrations, we recreate the mode-filling conditions that exist during the experiment. Figure 5.3 shows the spectral power (colored diamonds) measured with an absolutely calibrated power meter (Thorlabs S120VC) by passing the light source through absolutely calibrated band-pass filters (blue for Oriel; black for Melles Griot). The vertical lines are the absolute measurement uncertainties. The full-width-at-half-maximum of each filter, whose profiles are nearly (but not quite) Gaussian, is smaller than the symbol size. We fit the spectrum with a 5^{th}-order polynomial (green curve) to obtain a smooth function with which to divide with the light source spectrum on film later in this section. We use the mean of

the deviations between measured and fitted values as the uncertainty (dashed, green curve).

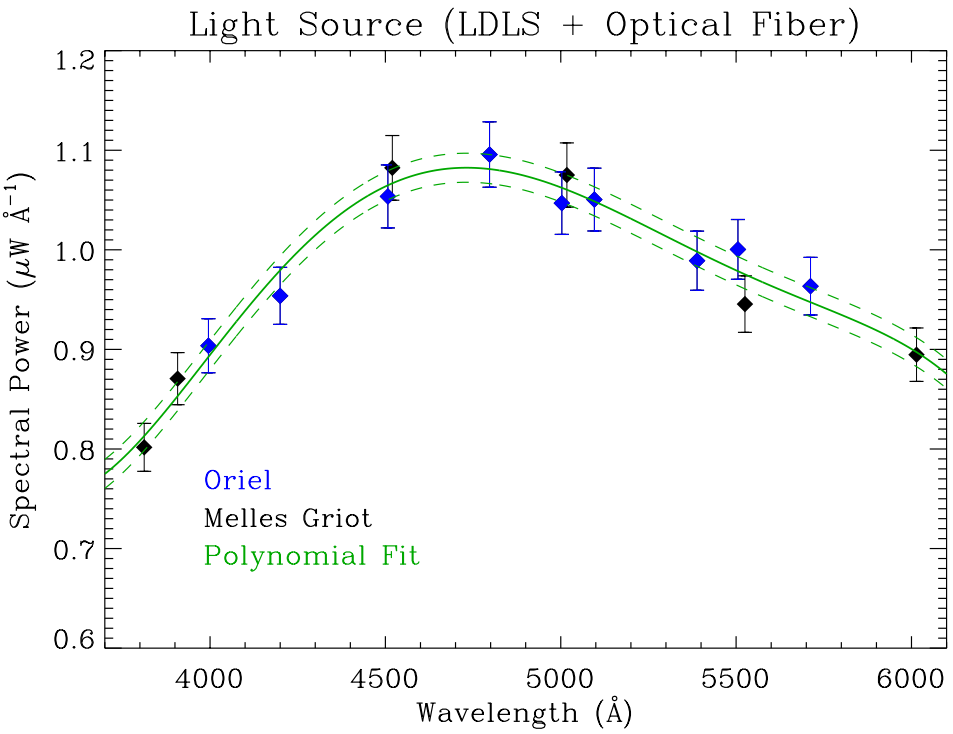

Figure 5.3 Power spectrum of our continuum light source, a laser-driven light source plus additional optical fiber, measured using absolutely-calibrated band-pass filters (diamonds). We show absolute measurement uncertainties (vertical lines). The full-with-at-half-maximum of each filter is smaller than the symbol size. A 5^{th}-order polynomial fit (solid, green curve) overlays the data. For its uncertainties (dashed, green curves) we use the mean of the deviations between measured and fitted values.

Now we pass this light source through the spectrometer system (spectrometer plus streak camera) to collect a streaked spectrum on film. We divide the reduced image into a sequence of 5-ns line-outs. At each spectral element we define

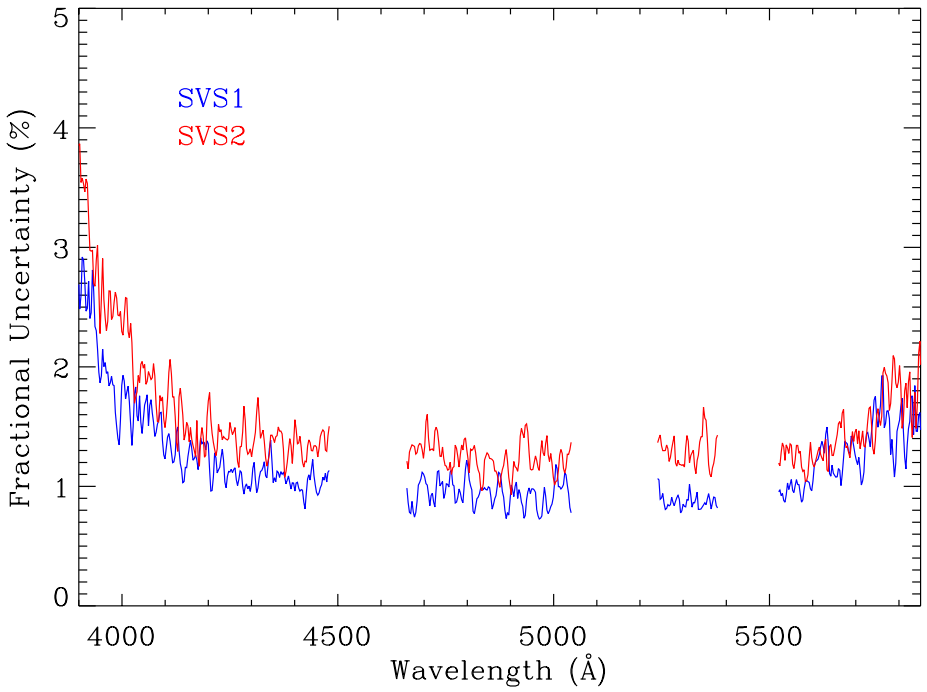

Figure 5.4 Wavelength-dependent fractional uncertainty of the measured spectral power due to the streak determined using the standard deviation of a sequence of line-outs. The elevating values at the blue boundary are due to low signal levels because of the decreasing instrumental sensitivity. We omit the spectral regions containing the lasers and comb. Throughout most of our wavelength range of interest, the spectra remain constant within $< 2\,\%$ for both SVS systems.

the fractional uncertainty due to the streak as

$$\sigma_{\text{streak}}(\lambda) = \frac{\sigma_P(\lambda)}{\langle P(\lambda)\rangle\sqrt{N}}, \tag{5.3}$$

where $\sigma_P(\lambda)$ is the standard deviation of the spectral power P at wavelength λ over N line-outs, and $\langle P(\lambda)\rangle$ is the mean of the spectral power at wavelength λ over those N line-outs. Figure 5.4 plots $\sigma_{\text{streak}}(\lambda)$ as a function of wavelength. We find

that the spectral power, and hence shape, remains constant within $< 2\,\%$ throughout most of our wavelength range for both SVS systems. We therefore use $\langle P(\lambda) \rangle$ as the wavelength-dependent spectral power of our continuum light source on film (Figure 5.5). The green curves are these spectra passed through a Butterworth filter (Butterworth 1930) to remove high-frequency noise; the uncertainties (dashed, green curves) reflect $\sigma_{\rm streak}(\lambda)$.

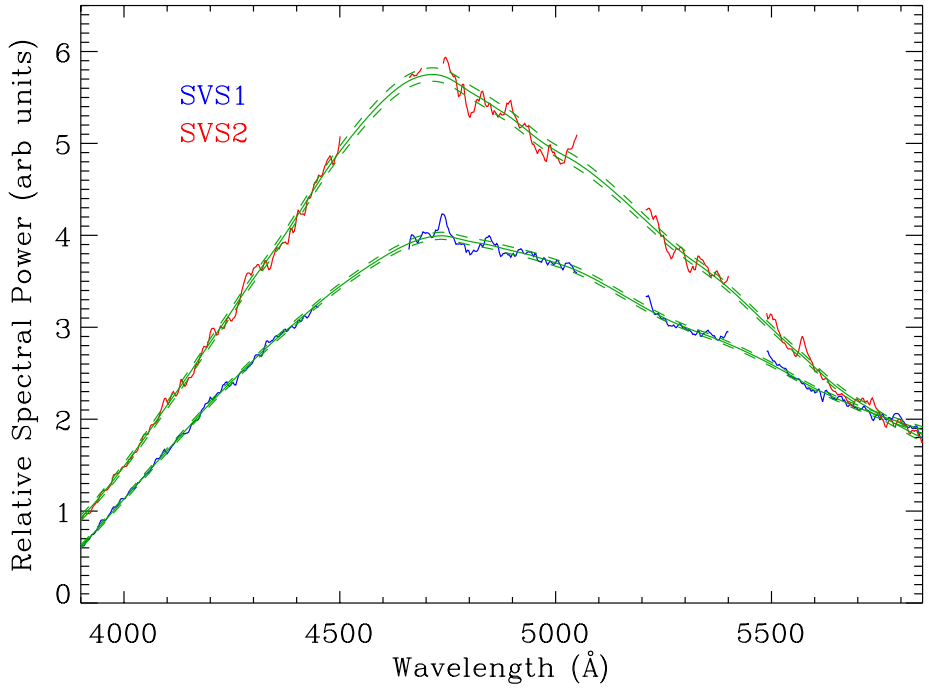

Figure 5.5 Spectral power as a function of wavelength of our continuum light source going through SVS1 (blue) and SVS2 (red). We pass the spectrum through a Butterworth filter (solid, green curves) and show the uncertainties due to the streak (dashed, green curves). The gaps in each spectrum are the regions containing the laser fiducials and comb.

To extract the relative instrumental efficiency for each SVS system (Fig-

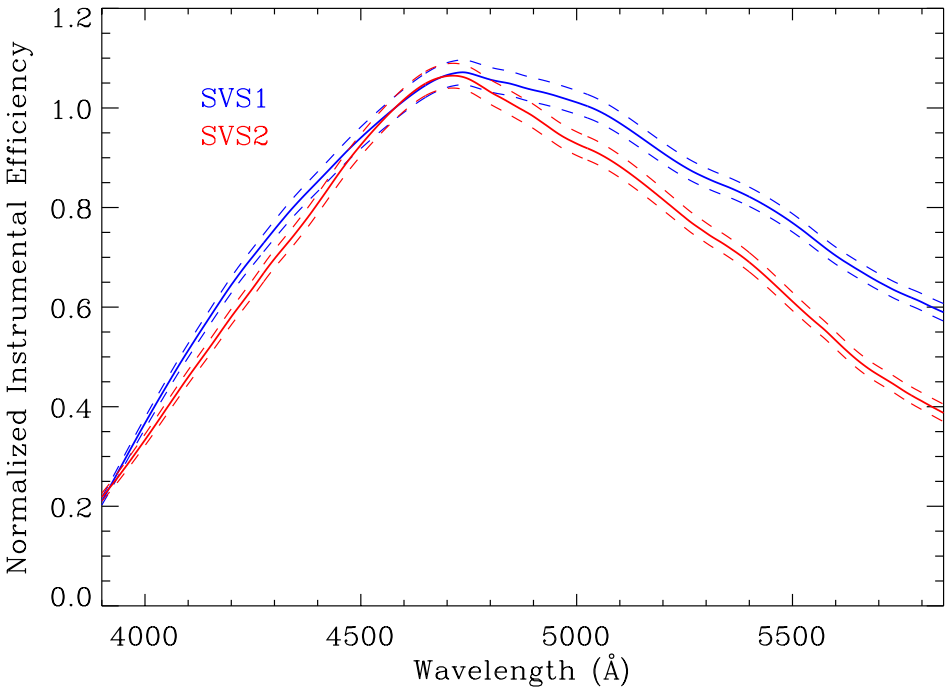

Figure 5.6 Relative instrumental efficiency for SVS1 (solid, blue) and SVS2 (solid, red) with uncertainties (dashed). Each curve is normalized to unity at the blue laser wavelength (4579 Å).

ure 5.6), we divide this light source spectrum recorded on film by the light source spectrum measured using the power meter and band-pass filters; we use the filtered curves and polynomial fit, respectively. Next we place each efficiency curve onto an absolute scale.

5.3.1.2 Absolute Efficiency Versus Wavelength

We use our two lasers as absolute power fiducials in addition to using them as wavelength fiducials. Like we do for the continuum light source, we make power

measurements of the lasers before they enter the spectrometer using an absolutely-calibrated power meter. Then we pass the lasers through the spectrometer system, recording the light onto film. As we mention in Section 5.2.2, we recover instrumental broadening by measuring the laser profiles from the line-outs we extract from the streak data. We integrate these profiles over wavelength to get the laser energy on the film at this time in the streak. By dividing the laser energy we measure before it enters the spectrometer (measured power multiplied by the duration of time integration) by this energy on film, we get the scaling factor to absolute units. This maps how energy on the film translates to energy as it enters the SVS system.

Since we measure precise integrations of the laser profiles, we avoid ambiguous determinations due to the changing signal in time from the experimental data, such as the back-lighter continuum, by performing this measurement on different film than the experimental film. Figure 5.7 plots our determined absolute scaling factors through time, as an example, for the green laser passed through SVS2. This includes four exposures on different film each time (different colors). The absolute scale of the time axis is arbitrary; we only require the relative scale for this exercise. For individual trials we find no significant trend throughout the streak; the standard deviations are similar with a mean standard deviation of 4.8 % of each respective mean. Between films, however, we can see systematic shifts such that the standard deviation of the means is 8.6 %. We find similar results for the other cases (i.e., blue and green lasers through SVS1 and blue laser through SVS2). Despite these shifts, we find agreement between absolute scaling factors determined using

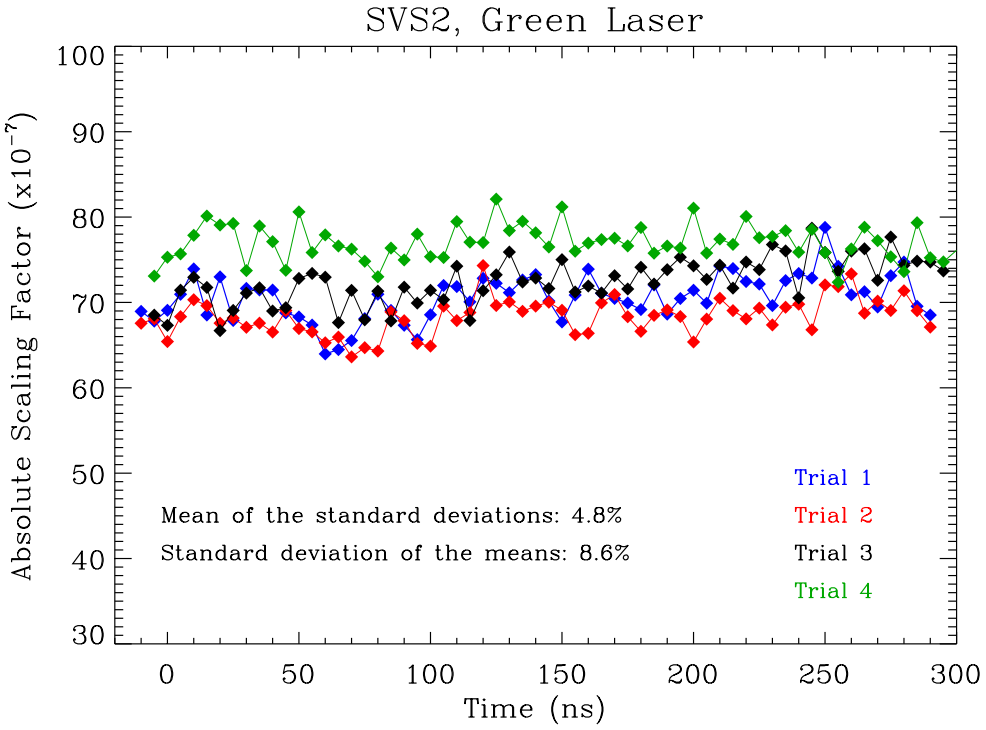

Figure 5.7 Examples of absolute scaling factors determined from lasers recorded onto film prior to the experiment. Different colors correspond to different film exposures. Individual trials show similar stability throughout the time of the streak; the mean of the standard deviations is 4.8 % of the respective means. Different film exposures, however, may show systematic trends.

the experimental film and the film exposed prior to the experiment. Therefore we attribute the shifts to a random uncertainty potentially due to the film processing or a streak camera voltage instability.

We use the mean of these measurements over all films as our absolute scaling factor for each laser with the standard deviation as the uncertainty. Dividing these absolute scaling factors from each laser, weighted by their uncertainties, by

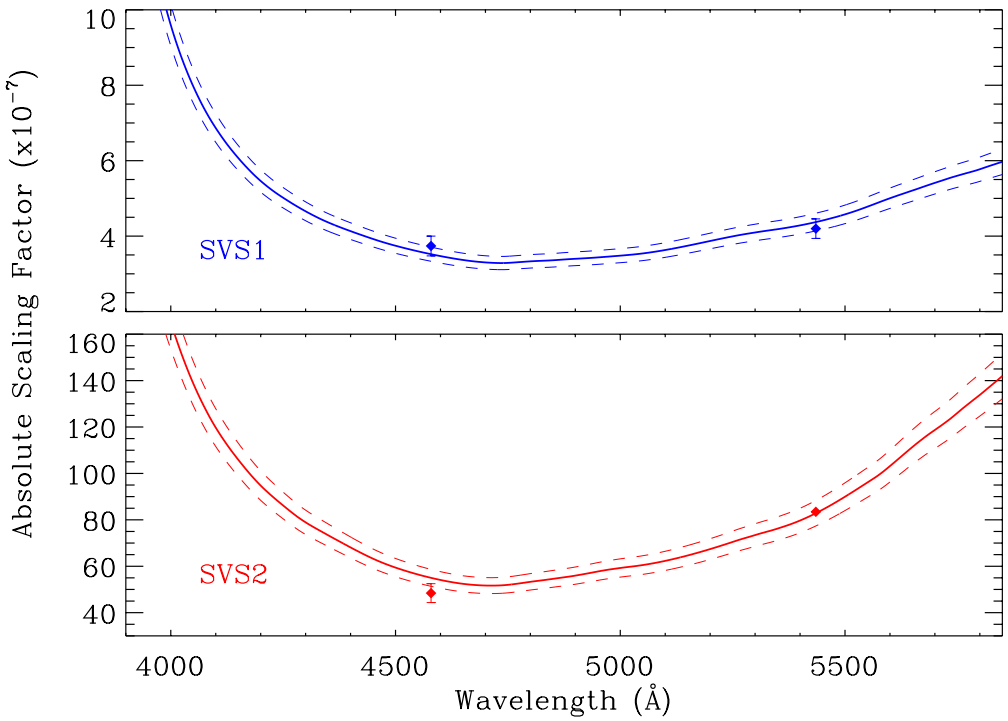

Figure 5.8 Absolute scaling factor curves for experiment z2553 for SVS1 (solid, blue) and for SVS2 (solid, red) with uncertainties (dashed). The difference in scale between the two curves is due to the different MCP gain voltages used for each spectrometer system.

the relative instrumental efficiency from Section 5.3.1.1 gives us an absolute scaling factor curve or absolute instrumental efficiency, $E_{\mathrm{inst}}(\lambda)$. Multiplying the data by $E_{\mathrm{inst}}(\lambda)$ thus gives us the wavelength-dependent absolute spectral energy as it enters the spectrometer. Figure 5.8 shows the absolute scaling factor curves for experiment z2553 for SVS1 (solid, blue) and for SVS2 (solid, red) at the spectrometer settings we use during the experiment (i.e., grating position, MCP gain voltage, et cetera). The dashed curves are the uncertainties. Since we measure the lasers (dia-

monds) independently from the relative efficiency determination, the corresponding absolute scaling factors provide additional validation of the relative shapes of the curves. We plot the two curves on different vertical scales. Since SVS1 observes our plasma in emission, the incoming signal is intrinsically lower than that of the absorption LOS, so we use a higher MCP gain voltage which results in a decreased $E_{\mathrm{inst}}(\lambda)$.

5.3.2 Light Attenuation During Optical Path from the Experiment

Continuing to move out from the spectrometer system and toward the gas cell, the next step corrects for light attenuation through the optical path from the experiment to the spectrometer. Light exits the gas cell by passing through the gas cell fiber ($\sim$ 2.2 m). This includes a fused silica window (Newport model 05QW40-30), a 3-mm diameter limiting aperture, and an achromatic doublet lens (Thorlabs model AC060-010-A-ML). Figure 3.5 illustrates this optical setup. The gas cell fiber couples to three other optical fibers in series – a vacuum chamber feed-through fiber (~ 5.1 m), a long (~ 41 m) transit fiber, and a spectrometer input fiber (~ 6.7 m), as shown in Figure 5.1.

We determine the absolute spectral transmission of this fiber link by measuring the ratio of the spectral powers of our continuum light source passing through the entire link and through the light source only. We use a small, concave grating spectrometer (StellarNet Inc. BLACK-Comet-HR) to measure this; since we want to recover a ratio, it is not necessary that this spectrometer be relatively calibrated across wavelength nor absolutely calibrated as the instrumental efficiency will can-

cel out. When measuring the light passing through the fiber link, we capture the entire emergent beam. This is a critical point for Section 5.3.3.

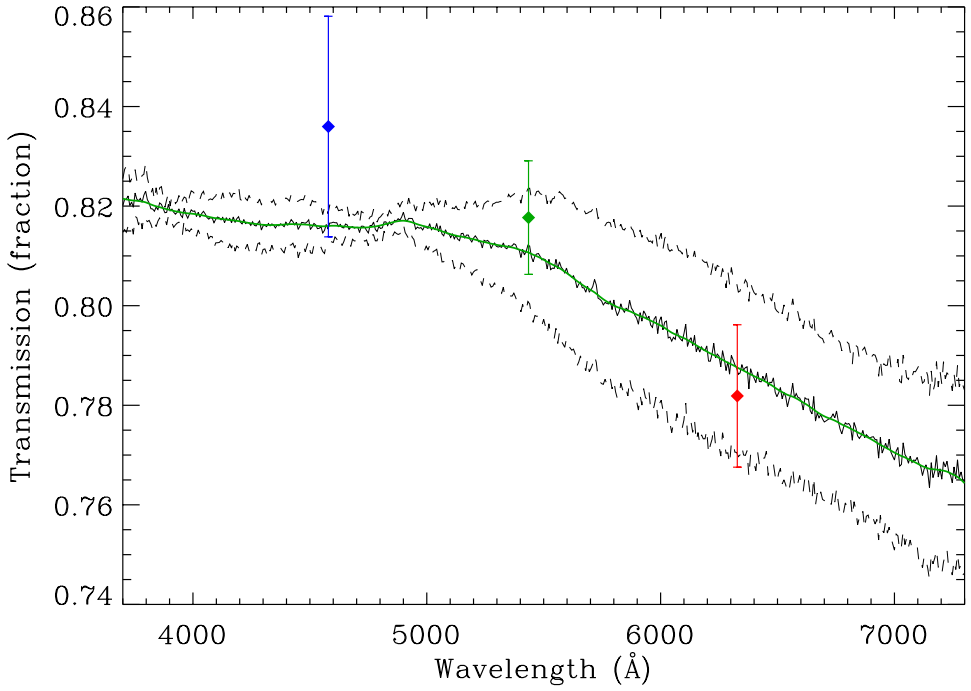

Figure 5.9 Measured absolute spectral transmission for an optical fiber coupler (solid) with absolute uncertainty (dashed). We remove high-frequency noise using a Butterworth filter (green curve). As an independent measure of wavelength-dependent transmission, we also determine transmissions of three lasers using a power meter (colored diamonds). It is necessary to account for the transmission of this component when determining the transmission of the transit fiber link.

This ratio, however, does not yet quite recover the attenuation of the fiber link for which we need to correct for our experiment. It includes the attenuation due to one too many ST®-female/ST®-female optical fiber couplers (e.g., Pasternack model PE900002), which comes from connecting our light source to the fiber link.

We measure the spectral transmission of a single coupler using this same "ratio" technique. The two configurations are (a) light source plus optical fiber and (b) light source plus two optical fibers, where the combined length of the two fibers in the latter configuration equals the length of the single fiber in the former. Therefore the only component that differs between the configurations is a single coupler. Figure 5.9 plots our measured spectral transmission for an optical fiber coupler. The green curve is the measured transmission passed through a Butterworth filter. As an independent check, we also include transmissions determined for three lasers each passed through the fiber configurations and measured with a power meter. Not only is it important to account for the transmission of this component for the sake of an ultimate absolute radiance level, but Figure 5.9 reveals a measurable dependence on wavelength.

The throughput of couplers depends on the mating surfaces between fiber ends. We ensure the ends are polished and perform wipes during disconnects since anything causing gaps of even a few μm will result in transmission losses (e.g., Wagner & Sandahl 1982; Tomita 1982; van Etten et al. 1985). The best practice is to minimize disconnects and junctions. Our transmission measurements may also depend upon the specific optical fiber used, particularly on the concentricity of the fiber core with respect to the cladding, buffer, and jacket. Since all the fiber we use throughout our experiment originates from the same batch, we neglect any such dependence. We assume our measurement is characteristic for any coupler within our system and remove its contribution to attenuation (transmission) before arriving at Figure 5.10. This plots the spectral transmission, $T_{\rm link}(\lambda)$, for the transit fiber link

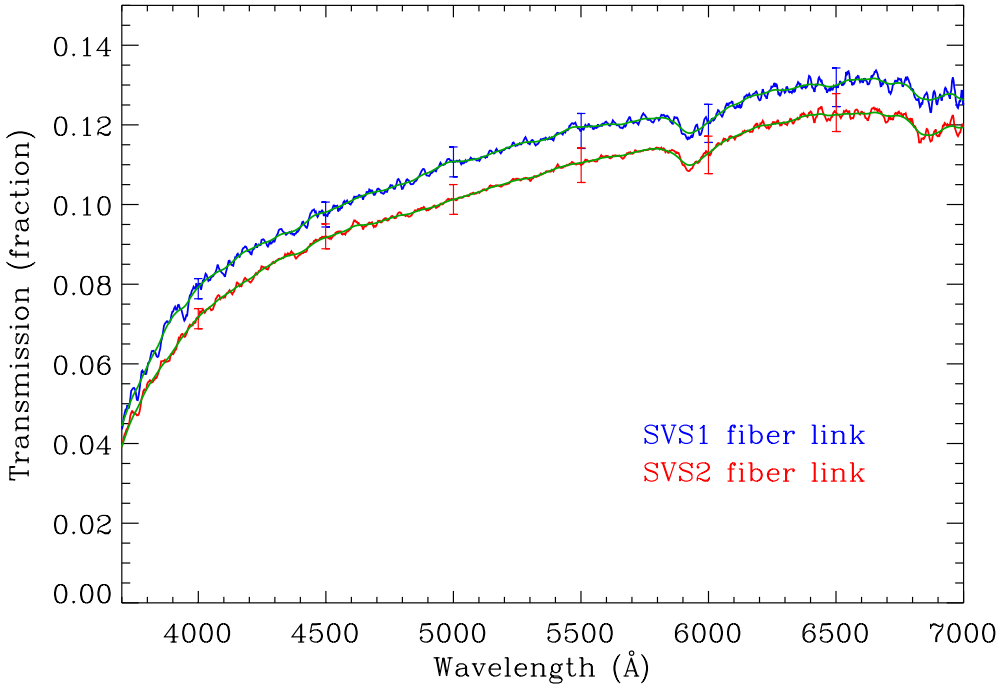

Figure 5.10 Measured absolute spectral transmissions for the transit fiber link going to SVS1 (solid, blue) and to SVS2 (solid, red) with their corresponding uncertainties (vertical lines). We remove high-frequency noise using a Butterworth filtering technique and plot the resulting (green) curves.

going to each SVS system (colored curves) with the corresponding uncertainties (vertical lines). This uncertainty includes an estimate of that due to disconnecting and reconnecting fibers (3 %; Dunham et al. 2004) since one connection (transit fiber to chamber feed-through fiber) is broken between calibration measurements and gas cell installation into the *Z* chamber. This estimate may encompass the variability of the gap distance between fiber ends inside the coupler. The green curves are, again, the measured transmissions passed through a Butterworth filter.

Dividing the data (after multiplying by the absolute scaling factor curve, $E_{\mathrm{inst}}(\lambda)$) by the high-frequency-filtered spectral transmission curve, $T_{\mathrm{link}}(\lambda)$, recovers the photons lost during the optical path from the experiment.

5.3.3 Geometry

At this point our data are in units of spectral power (erg s^{-1} $\mathrm{\AA}^{-1}$). The final step converts this to spectral radiance (erg s^{-1} sr^{-1} cm^{-2} $\mathrm{\AA}^{-1}$) by dividing by the emitting source area, A, and by the emitting source solid angle, Ω, that we observe. To determine these quantities, we must characterize our LOS collection beam.

5.3.3.1 Observed Beam Area

We illuminate the gas cell fiber with broadband light using the light source described in Section 5.3.1.1, taking care to overfill the acceptance cone of the optical fiber, and image the two-dimensional (2D) beam spot onto a CCD camera beam profiler (Thorlabs model BC106-VIS). The path the light follows includes the achromatic doublet lens and the 3-mm diameter limiting aperture. Figure 5.11 plots the azimuthally averaged and normalized beam profile at five distances along the collection beam LOS for the two gas cell fibers initiating the feed for each SVS system. Both beams are quite similar. The profile shape changes throughout the length of the beam, morphing from nearly flat-top (uniform) to nearly Gaussian to flatter again.

Recall that, in our measurements of the attenuation of the transit fiber link in Section 5.3.2, we pass the light source through the link and capture the entire

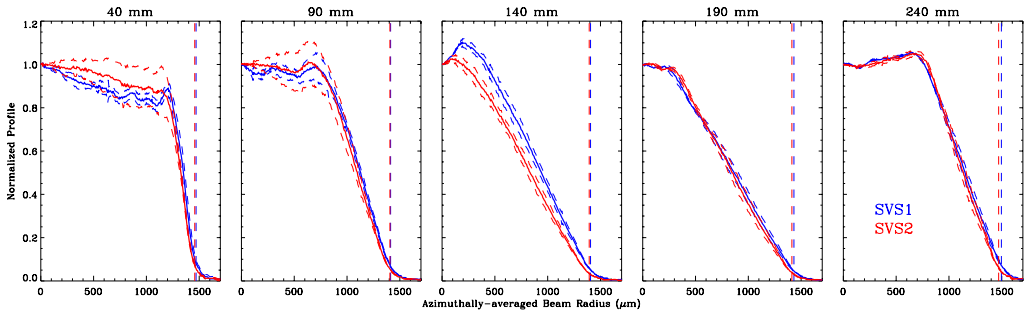

Figure 5.11 Gas cell fiber collection beam profile (solid curves) and uncertainties (dashed curves) determined from measured 2D beam spot images. We average over all azimuths and normalize the profile to its value at zero radius. A broadband light source illuminates the gas cell fibers corresponding to SVS1 (blue) and SVS2 (red). We measure the profiles at five LOS distances. We also plot our determined beam radius (dashed, vertical lines), which captures the entire emergent beam.

emergent beam. This means that our definition of beam area or diameter when measured with the beam profiler must also capture the entire beam. A Gaussian width, for example, does not satisfy this definition. We instead define the beam diameter as the difference between the locations in the wings of the profile that immediately rise above the noise level, which, in our case using the beam profiler, are only a few counts above the steady median dark level of three counts. The dashed, vertical lines in Figure 5.11 show our adopted beam radii. We account for the spatial sensitivity (the relative sensitivity across the area) of our collection beam in our determination of the observed solid angle in Section 5.3.3.2.

Figure 5.12 plots our measured beam diameters (colored diamonds) as a function of LOS distance; the uncertainties (solid, vertical lines) result from averaging the profile over azimuths or, in other words, the eccentricity of the 2D beam spot. Since the gas cell fiber optics include an achromatic lens as well as a 3-mm

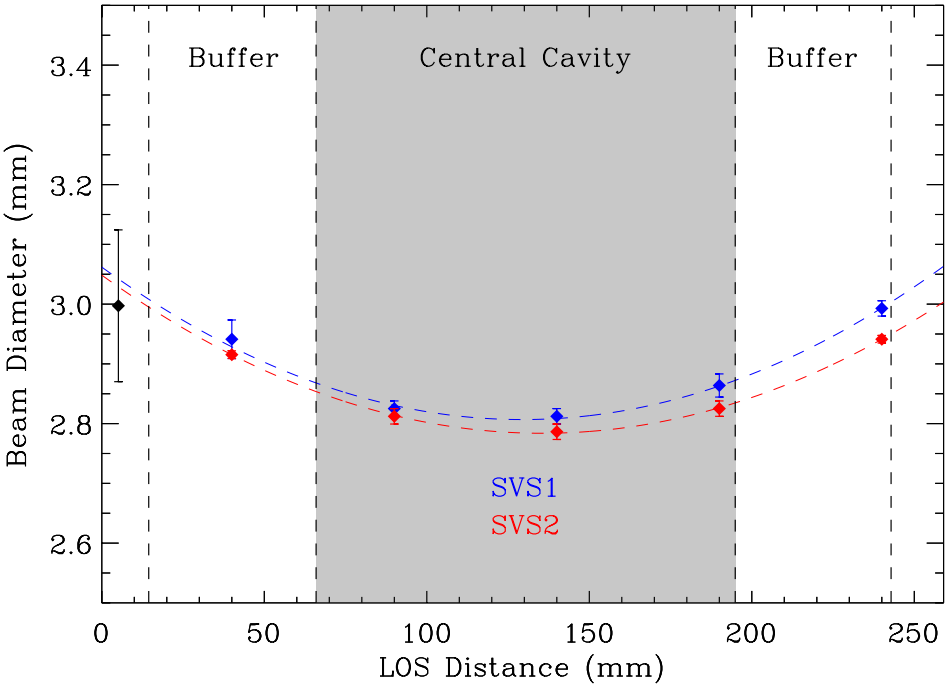

Figure 5.12 Measured collection beam diameters along the LOS for the gas cell fibers feeding SVS1 (blue diamonds) and SVS2 (red diamonds). The black diamond is the 3-mm diameter limiting aperture at the end of the gas cell fiber. The zoomed-in scale reveals that the subtle changes in beam diameters with LOS distance can be described with 2^{nd}-order polynomials (dashes, colored curves). We shade the distances corresponding to the central cavity of the gas cell – where we observe our experimental plasma – as well as the adjacent buffer cavities.

diameter limiting aperture, we neglect any dependence of the beam diameter on wavelength. The plot shows the limiting aperture (black diamond). Its uncertainty comes from the machine tolerance specified in the hardware drawing. A 2^{nd}-order polynomial (dashed, colored curve) describes how the beam diameter of each gas cell fiber changes with distance. Over the distances corresponding to our region of

interest, the central cavity of the gas cell (shaded region), the differences between the beam diameter extrema are merely 1.9 and 2.2 %, for the emission (SVS1) and absorption (SVS2) lines of sight, respectively. We also illustrate the distances corresponding to the gas cell buffers flanking the central cavity.

Using the polynomial fits of the beam diameter as a function of LOS distance, we can now recover the beam area, A, at any distance along each LOS, assuming axial symmetry. Now we must consider the physical source of emitted light we observe for each LOS. For the emission LOS, the emitted light comes from an extended volume of plasma inside the central cavity of our gas cell. Throughout the LOS distance that traverses this observed region ($\sim$ 69–189 mm from the lens), the collection beam area changes very little since the beam is quite nearly collimated. We therefore approximate a single value and use the mean area throughout this region, arriving at $A^{\mathrm{em}} = 0.0627 \pm 0.0007\,\mathrm{cm}^2$, where the uncertainty is the standard deviation of A. For the absorption LOS, the emitted light predominantly comes from the back-lighting surface, so we use the beam area corresponding to this distance (~ 183 mm from the lens), $A^{\mathrm{abs}} = 0.0623 \pm 0.0005\,\mathrm{cm}^2$. For this uncertainty, we use the mean uncertainty of the beam areas measured at the five different LOS distances for this gas cell fiber.

5.3.3.2 Observed Solid Angle

Because we know the geometry of the optical setup at the end of the gas cell fiber (i.e., fiber end numerical aperture and diameter, limiting aperture diameter, achromatic lens specifications, relative distances of the components) so precisely,

we can ray-trace (e.g., Spencer & Murty 1962) the angles of emission from a theoretical source at any position from the lens such that the emitted ray enters the fiber within its acceptance cone. Therefore we determine an observed solid angle, Ω, assuming axial symmetry. Since the collection beam has finite size, we model two cases: on-axis ($\Omega_{\rm on}$), which centers on the optical axis of the lens, and off-axis ($\Omega_{\rm off}$), which perpendicularly extends 1.5 mm (the nominal beam radius) from the LOS axis. Figure 5.13 plots our inferred solid angles as blue diamonds and squares, respectively. We use a beam area-weighted linear interpolation of these results to obtain an effective solid angle, $\Omega_{\rm eff}$, for an emitting surface perpendicular to the LOS axis for a given LOS distance (green triangles). The area-weighting includes the relative spatial sensitivity apparent in the measured beam profiles (Figure 5.11) by assuming that these profiles, which describe light emerging from the gas cell fiber, also describe the collection of light, relative across the beam area, propagating in the opposite direction. We define our effective solid angle as the integral over the beam radius, r, such that

$$\Omega_{\rm eff} = \frac{2}{R_{\rm max}^2} \int_{r=0}^{r=R_{\rm max}} r \Omega_{\rm int}(r) Y(r) {\rm d}r. \tag{5.4}$$

$R_{\rm max}$ is the maximum beam radius (dashed, vertical lines in Figure 5.11), $\Omega_{\rm int}(r)$ is the solid angle linearly interpolated between the on-axis and off-axis solid angles ($\Omega_{\rm int} = (\Omega_{\rm off} - \Omega_{\rm on})\frac{r}{R_{\rm max}} + \Omega_{\rm on}$), and $Y(r)$is the area-normalized beam profile:

$$Y(r) = \frac{\phi_{\rm beam}(r)}{\frac{2}{R_{\rm max}^2} \int_{r=0}^{r=R_{\rm max}} r \phi_{\rm beam}(r) {\rm d}r}, \tag{5.5}$$

which uses the (peak-) normalized measured beam profile $\phi_{\rm beam}(r)$ from Figure 5.11.

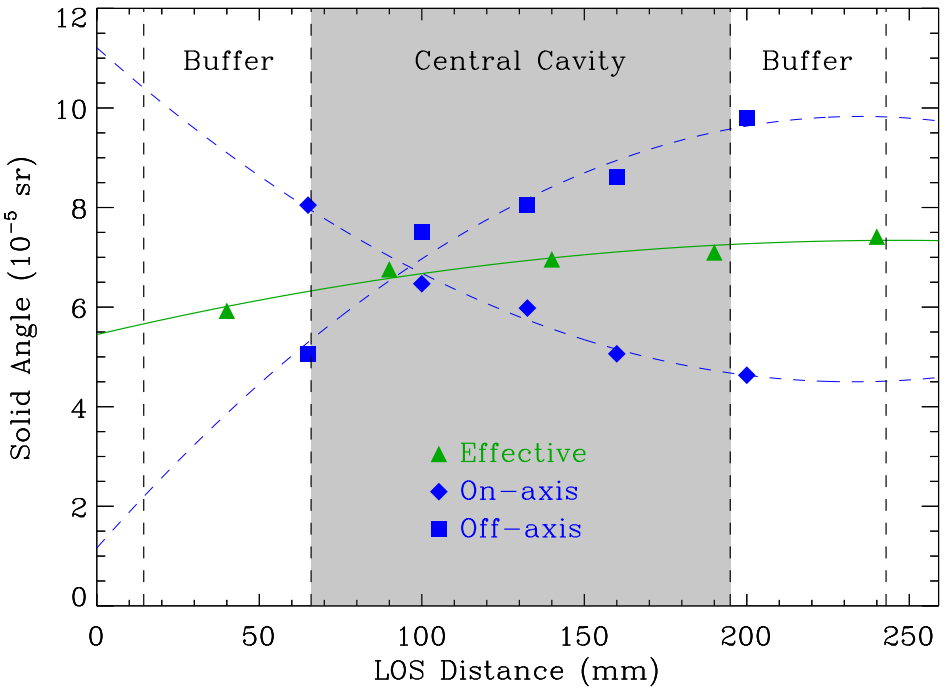

Figure 5.13 Observed solid angles for an emitting surface perpendicular to the optical axis along the LOS determined by ray-tracing. We use 2^{nd}-order polynomial fits (dashed curves) to the on-axis (blue diamonds) and off-axis (blue squares) ray-tracing results to interpolate across the LOS distance. A beam area-weighted linear interpolation supplies the effective solid angles (green triangles). For clarity we only plot values for the optical fiber corresponding to SVS1.

As with the observed area, A, to approximate single values we treat the emission and absorption lines of sight differently. For the emission LOS, we use the mean Ω_{eff} throughout the observed (emitting) region of the plasma to get $\Omega_{\text{eff}}^{\text{em}} = (6.87 \pm 0.29) \times 10^{-5}$ sr. The uncertainty has two components added in quadrature: the standard deviation of Ω_{eff} throughout the emitting region and the mean of the uncertainties at each distance of the 2^{nd}-order polynomial fit to the de-

termined Ω_{eff} values. The absorption LOS uses Ω_{eff} at the back-lighter distance and, as the uncertainty, the latter component used for the emission LOS. We get $\Omega_{\text{eff}}^{\text{abs}} = (7.21 \pm 0.19) \times 10^{-5}$ sr.

5.3.4 Results

We now have fully processed spectra, $L(\lambda)$, from both spectrometer systems. Figure 5.14 shows an example of emission data from SVS1 (blue) and absorption data from SVS2 (red), both produced from a photoionized hydrogen plasma during experiment z2553 at some particular 20-ns line-out within the streak. Vertical lines show the absolute uncertainties, σ, at selected wavelengths. The continuum in the SVS2 data is emitted from a gold back-lighter. On the top and bottom panels we plot the vertical axis of these data on a linear and logarithmic scale, respectively.

5.3.4.1 Validation

In the subsequent experiment, z2554, we configure SVS1 to observe the same physical area on the back-lighting surface[3] as SVS2 but through a minimal length ($\sim$ few mm) of intervening hydrogen plasma. Therefore, the absolute spectral radiance of the back-lighter emission measured from two independent spectrometer systems should agree, especially in the redward spectral regions where line (bound-bound) absorption and bound-free continuum absorption are minimal.

[3]Recall that the normal of the back-lighting surface is not parallel to the observing lines of sight but is twice-angled with respect to two orthogonal planes. This forbids the projected LOS beam spots from congruently overlapping, but they do indeed overlap for more than half of their projected areas.

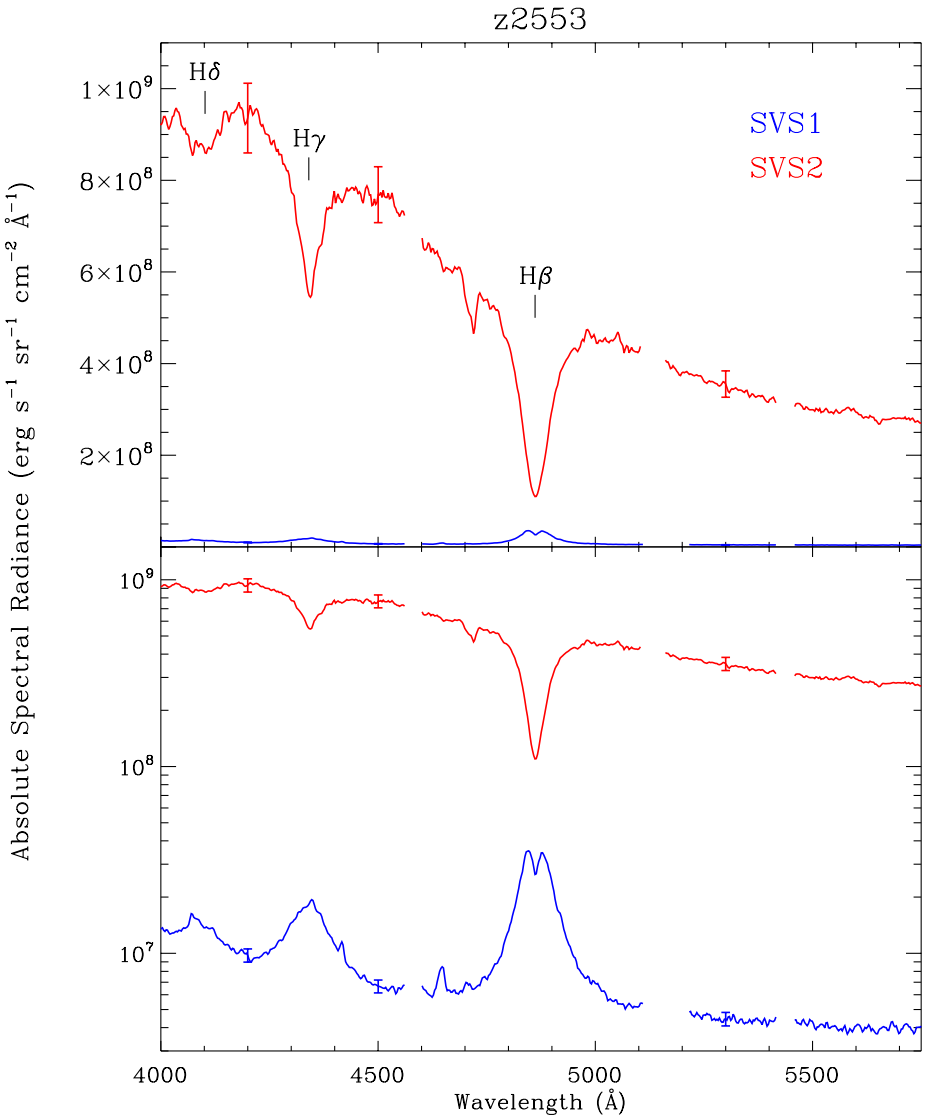

Figure 5.14 Example 20-ns line-out absolute radiance spectra from SVS1 (blue) and SVS2 (red) from experiment z2553 of a photoionized hydrogen plasma in emission and in absorption with a continuum back-lighter, respectively. Vertical lines illustrate the uncertainties at selected wavelengths. The gaps in the data are the regions where the wavelength fiducials and comb reside. The top and bottom panels plot the data with the vertical axis on a linear and logarithmic scale, respectively.

We apply our calibrations to the SVS data recorded from z2554. This uses the same normalized instrumental efficiency (Figure 5.6) as used for z2553 since the configuration of the SVS system remained undisturbed throughout the experiment series. The absolute scaling factor curve (Figure 5.8) differs for SVS1 because of the change in MCP gain voltage (to accommodate the back-lighter emission, which is much brighter than the hydrogen plasma emission from the previous experiment). The curve is nominally the same for SVS2, but we perform new measurements of the laser powers to use as absolute power fiducials. We also repeat the fiber link transmission measurement (Figure 5.10) after cleaning the fiber ends at the junctions that are disconnected in the process of installing new hardware between experiments. We reuse the same gas cell fibers used for z2553. The fiber corresponding to SVS2 observes the same LOS for both experiments, so the observed area and observed solid angle are both the same. The SVS1 fiber now observes the back-lighter (instead of the hydrogen plasma in emission) at $\sim 176\,\mathrm{mm}$ from its lens, which is similar to the distance at which SVS2 observes ($\sim 183\,\mathrm{mm}$).

Figure 5.15 plots the absolute radiance spectra, revealing a discrepancy between the data obtained from each SVS system. Redward of Hβ at 5300 Å, the two observed back-lighter continua differ by $33.7 \pm 12.7\,\%$ ($\frac{|L^{\mathrm{SVS2}} - L^{\mathrm{SVS1}}|}{\langle L \rangle}$). This may be due to one or more of the following: (1) we are underestimating our uncertainties, (2) an additional systematic uncertainty plagues the calibrated data betwen the two SVS systems, such as a poor optical fiber connection, or (3) the two lines of sight are not observing the same emission.

Since the components in Equation 5.2 are multiplicative and independent of

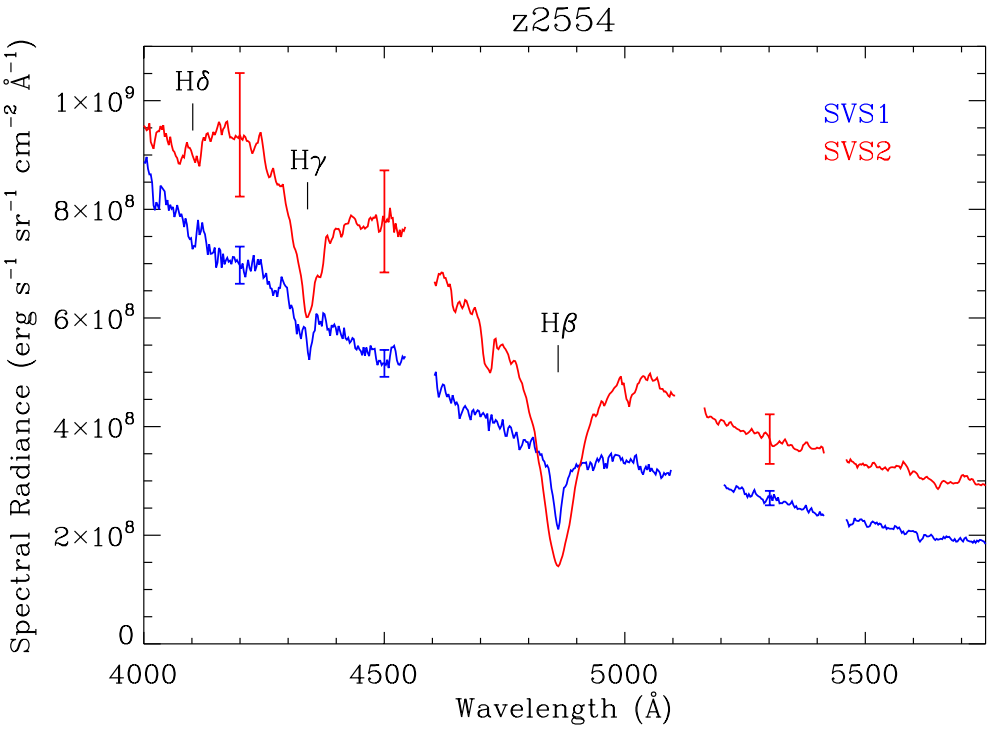

Figure 5.15 Similar to the top panel of Figure 5.14 but for experiment z2554. SVS1 (blue) and SVS2 (red) are absolute radiance spectra observing through a short ($\sim$ 7 mm) and a long ($\sim$ 114 mm) length of absorbing hydrogen plasma, respectively. At 5300 Å, the spectra differ by 33.7 ± 12.7 %.

time, an uncertainty in the calibration means that the fractional discrepancy apparent in Figure 5.15 will apply to all line-outs. If the two lines of sight observe the same emission, for all times we can match the continua levels from each SVS with a single scaling factor. Figure 5.16 plots the observed spectral radiance at a particular wavelength, 5300 Å, throughout time for SVS1 (blue) and SVS2 (red). We indeed find such a factor that scales the SVS2 data (green) to match those of SVS1. Performing this exercise at multiple wavelengths covering 4440–4530, 5170–5400,

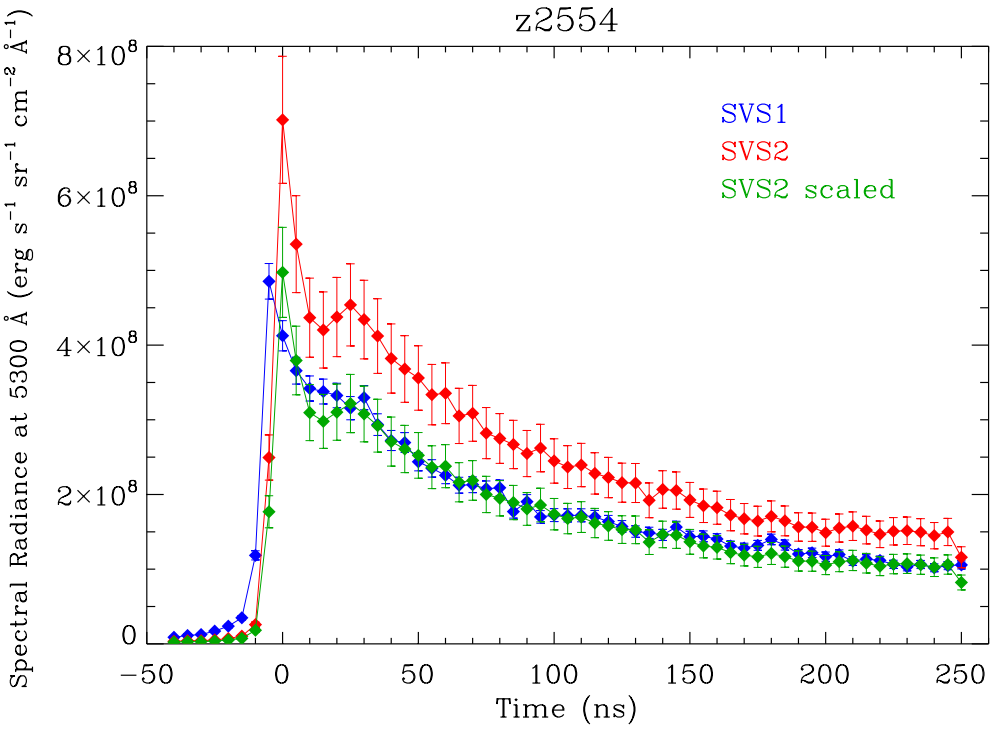

Figure 5.16 Observed spectral radiance at 5300 Å obtained with SVS1 (blue) and SVS2 (red) from experiment z2554. That these curves differ by a scaling factor (green) gives evidence that the discrepancy apparent in Figure 5.15 is due to an uncertainty in the calibration.

and 5470–5630 Å to include shared spectral regions between both SVS spectra that avoid absorption lines, fiducials, and artifacts, we find a mean scaling factor of 0.711 ± 0.017 where the uncertainty is the standard deviation of the factors found at different wavelengths.

We are confident that the discrepancy is due to an uncertainty in the calibration and that the two lines of sight both observe the back-lighter as intended. To determine whether this uncertainty is random (isolated) or systematic, we turn to

experiment z2552, which uses the "Dual Length" cell design (see Section 4.1.2) to simultaneously observe two different lengths of our hydrogen plasma in absorption. In this geometry, both lines of sight observe a back-lighting surface but a different one. However, each should be heated the same way from the z-pinch dynamic hohlraum radiation.

As with z2554, experiment z2552 uses the same normalized instrumental efficiency. The absolute scaling factor curves are nominally the same as for z2554 and include independent measurements of the laser powers to use as absolute power fiducials. The fiber link transmission measurements are also independent. We use different gas cell fibers. The distances of the back-lighting surfaces from the lenses in the gas cell fibers are ~ 141 and ~ 101 mm for SVS1 and SVS2, respectively. We again see the SVS2 spectra at higher levels than those of SVS1; we find a mean scaling factor of 0.733 ± 0.023. The agreement with that found for experiment z2554 gives evidence that the discrepancy in question is systematic and not random.

Without an independent validation for our absolute calibration, we cannot say whether or not we are underestimating our uncertainties. We also cannot identify the source of the vexatious systematic discrepancy nor the scaling factor to correct our data to the true absolute level. In Section 6.1 we further investigate strategies to determine this elusive scaling factor.

Setting this unidentified systematic uncertainty aside, we continue on to describe our random uncertainties under the assumption that they remain independent and will only scale with the same factor that will correct our data to the true absolute level.

Table 5.2. Absolute and Relative Uncertainties of our Calibrated Data

Experiment	SVS	σ (%)	σ^{rel} (%)
z2552	1	5.1	3.6
	2	9.0	3.5
z2553	1	7.6	3.9
	2	8.2	4.2
z2554	1	5.1	3.7
	2	12.1	4.2
z2588	1	12.8	3.7
	2	7.5	3.7

5.3.4.2 Uncertainties

The ultimate absolute uncertainties, σ, (vertical lines) plotted in Figures 5.14 and 5.15 result from a propagation throughout all the steps of the calibration procedure outlined in Equation 5.2. We define the relative uncertainty, σ^{rel}, (not plotted for clarity), or the uncertainty in the shape of our spectra, as that coming from the normalized instrumental efficiency and the transmission during the transit from the experiment; the other calibration components contribute uncertainty that does not depend on wavelength as we determine them.

Table 5.2 lists absolute (σ) and relative (σ^{rel}) uncertainties for the calibrated SVS data from selected experiments. These are averages over wavelength (the same spectral regions we use in Section 5.3.4.1) and over time (10–210 ns, where 0 ns is the onset of *z*-pinch x-rays and back-lighter emission) since the values remain constant over these abscissae. Between instruments and between the experiments we

Table 5.3. Uncertainty of Each Component of the Calibration Procedure

Experiment	SVS	$\sigma_{L_{\rm un}}$ (%)	$\sigma_{E_{\rm inst}}$ (%)	$\sigma_{T_{\rm link}}$ (%)	σ_A (%)	σ_Ω (%)
z2552	1	$0.7^{1.3}_{0.2}$	2.1	3.2	0.9	3.2
	2	$0.7^{1.5}_{0.4}$	8.4	2.9	0.9	1.0
z2553	1	$2.4^{8.5}_{0.6}$	5.4	3.5	1.2	2.5
	2	$0.9^{2.0}_{0.4}$	6.6	3.8	0.8	2.6
z2554	1	$1.2^{2.3}_{0.5}$	3.6	3.2	1.0	0.3
	2	$0.5^{1.0}_{0.2}$	11.2	3.7	0.8	2.6
z2588	1	$1.9^{5.8}_{0.8}$	1.7	3.3	2.6	11.7
	2	$0.7^{1.3}_{0.3}$	5.0	3.3	0.9	4.3
z2589	1	$\cdots$	1.9	3.2	1.2	2.5
	2	$1.5^{1.8}_{0.9}$	2.2	3.2	0.8	2.6

list in Table 5.2 the absolute uncertainty varies within the $\sim$ 5–13 % range. Again, this is the random uncertainty excluding the unidentified systematic discrepancy between SVS systems. The relative uncertainty is consistently $\sim 4\,\%$.

Table 5.3 lists the uncertainty of each component of the calibration procedure (i.e., $L_{\rm un}$, $E_{\rm inst}$, $T_{\rm link}$, A, and Ω from Equation 5.2) for selected experiments. As with Table 5.2, the values in Table 5.3 are averages over wavelength. Only $\sigma_{L_{\rm un}}$ has any dependence on time, which comes from using the comb to set the scale of the temporal axis (Section 5.2.1). We list the mean along with the minimum (subscript) and maximum (superscript) values over the 200-ns range. $\sigma_{L_{\rm un}}$ does not include the uncertainty due to the film processing. As it is, the uncertainties for this component and for the observed area, A, are the smallest across experiments, and $\sigma_{T_{\rm link}}$ is the most consistent. We note that the Ω component is the only component

whose uncertainty we determine through modeling as opposed to measurement.

For experiment z2588, σ_A and σ_Ω conspicuously differ from those of the other experiments. The culprit is the particular gas cell fiber we use. It happens to be the most poorly collimated of the bunch. Furthermore, SVS1 observes the emission LOS for this experiment. Recall that for the uncertainties in the observed area and observed solid angle for emission lines of sight, we use the standard deviations of the inferred A and Ω_{eff}, respectively, throughout the LOS distances. These LOS distances traverse the entire length of the plasma (Section 5.3.3.2). Consequently, these uncertainties are relatively large.

5.4 Conclusions

What begins as an ensemble of optical photons generated inside our gas cell ends up as a collection of calibrated spectra ripe for analysis and physical interpretation. We illustrate the light travel path of photons from the experiment and detail the processing of our time-resolved data acquired using the Streaked Visible Spectroscopy diagnostic at *Z*, emphasizing our calibration methods.

We fall short of validating the accuracy of our absolute calibration, finding a systematic uncertainty between the data from each SVS system. However, what is most critical for our purpose of measuring relative line shapes, especially for measuring in absorption or transmission, is the relative calibration across wavelength. We apply calibrations to our data and determine the uncertainties.

Chapter 6

Analyzing a Laboratory Experiment

Dark skies. Pristine view of the stars. And Earthward, blackness. I know somewhere down there – *way* down there – the Atlantic ripples with memories long-descended from the historic wakes of the Niña, the Pinta, and the Santa María. No. I'm not headed to Spain. Sorry to fake you out. I'm on my way to Poland. Krakow to be more precise. Time for another installment of the European White Dwarf Workshop.

I'll be a day late. Couldn't miss Emma's birthday party yesterday. The big 2! Jirod snapped some great photos of her running around the park with all her toddler friends, dancing around the water sprinkler, opening gifts. And a timeless one of her kissing me on the cheek. Sweet daughter.

I pull out my laptop, ready to put together slides for my talk later in the week. I've got a nice starting point – the talk I gave three months ago in Tallahassee for the International Conference on High Energy Density Laboratory Astrophysics.

Okay…let's see here…change the date…change the name of the conference…and…and…hmmm…

After nineteen and a half minutes or so (the time it takes to listen to the first four tracks of Diorama by Silverchair) I decide that I don't need to add any new slides. I'll perhaps hide one, but that's about it. I'll essentially *show* the same talk I gave in Florida, but the presentation will be utterly different. Because of my audience. The previous one consisted of experimental physicists, laboratory folk. This one'll be astronomers. Yeah yeah, it doesn't seem like much of a shift, but the mindset is quite different. The scientific interests are different. The experience and dynamic of the community are different.

My job with this talk is not only to share the work we've been doing and receive feedback. It's to inform members of the white dwarf community, particularly those who study stellar atmospheres, that we are no longer bound by our planet's gravity to observe the objects of our interest from afar. We can reach out and manipulate these objects. We can create extreme astrophysical environments. Here. **On Earth.** Address a whole new tome of scientific puzzles in a whole new way.

When I put it like that...

I need to rehearse.

The observing lines of sight traversing our gas cell deliver three kinds of data, from each of which we can use spectral fitting procedures to extract different, complementary information about our plasma. We preview the three kinds of data before elaborating throughout this chapter.

Heated by radiation from the z-pinch dynamic hohlraum, the gold surfaces within our cell re-emit *continuum* ($L_\lambda^{\rm cont}$). As we describe in Chapter 3, the gold surfaces serve two functions. The first is to form the hydrogen plasma through photo-ionization. The second (which developed during the evolution of our experiments; see Section 4.1.2) is to provide a back-lighter for absorption measurements. From these data we measure the emission from our gold, and, assuming it emits as a Planckian in our observed wavelength range, we extract the temperature, $T_{\rm rad}$, describing this radiation that heats the plasma.

Adding in foreground plasma transforms the *continuum* data into *absorption* data ($L_\lambda^{\rm abs}$). As such, all absorption data contain the information of continuum data, albeit obscured to some degree. This depends upon the kind of absorption. For our plasma and in our wavelength range, this is mostly line absorption due to electronic transitions between bound-bound energy levels, and, when the electron density is high, absorption lines may significantly obfuscate the back-light. Dividing the absorption data by their continua yields *transmission* data. We use the shapes of transmission lines to extract the electron density, $n_{\rm e}$, of our plasma. We also measure the population of the lower electronic energy level, n_1, associated with each line, which, for our case, is from the Balmer series, meaning $n = 2$ (we use n to describe both number density and principal quantum number, though we include a subscript with the former).

Removing the back-light leaves *emission* ($L_\lambda^{\rm em}$) from only the plasma itself. (This implies that the absorption data contain a component of self-emission. We discuss this in Section 6.2.) These data can also provide us with $n_{\rm e}$, as well as n_2

and the upper level population n_{u}.

For the scope of this work, we focus on the absorption data and use the emission data only en route to extracting transmission data for spectral fitting. We discuss future work utilizing the emission data in Sections 7.5.1 and 7.5.2.

6.1 Back-lighting Continuum

Our initial LASNEX (Zimmerman et al. 1978) simulations of the plasma formation in the gas cell (Section 3.2.2) opine that the gold, having absorbed z-pinch x-rays, heats to an electron temperature of a $\sim$ few eV and then cools off with time. More detailed simulations using, as input, the most up-to-date description of the z-pinch dynamic hohlraum radiation incident on our gas cell (Loisel et al. 2014) will better constrain the precise behavior of the gold.

Since gold possesses many electrons, we expect it to emit continua when sufficiently heated, and indeed we observe continuum emission from our back-lighting surface (Figures 3.9, 5.14, and 5.15) that decreases with time (Figure 5.16). Let us *assume* this gold emission is Planckian in the wavelength range we observe so that we may fit our measured continua spectra accordingly. The fitting model is:

$$L_{\lambda}^{\mathrm{cont}} = B_{\lambda}(T_{\mathrm{rad}})C_1 + C_2, \tag{6.1}$$

where $B_{\lambda}(T_{\mathrm{rad}})$ is the Planckian emission function at temperature T_{rad}, C_1 is a scaling factor, and C_2 is an additional, constant background level. Notice that, with respect to Chapter 5, we now move the wavelength λ out of the parentheses to the subscript.

This fit strongly relies on the accuracy of the absolute calibration. In Section 5.3.4.1 we show that this calibration is suspect and suggest that a scaling factor exists that will correct our data to the true absolute value. We include C_1 in our fitting model in anticipation of this factor. Similarly we also add C_2 for any scenario in which our measurement deviates from Planckian emission.

6.1.1 Measurements

We inspect the SVS1 data from experiment z2554 which uses the vertical LOS of the ACE gas cell (Figure 3.4) to observe a back-lighting surface through a minimal (~ 7 mm) length of hydrogen plasma.

Figure 6.1 plots our continuum fits to 10-ns line-outs beginning at 20, 40, 60, 80, 100, and 120 ns after the onset of x-rays (the z pinch). The solid, black curves are the spectral regions included in the fitting. We omit the regions where the laser fiducials and comb reside, and we exclude the Hβ and Hγ absorption lines (dotted, black curves) from the fit. We show three cases: (A; solid, red curves) fixing the scaling factor $C_1 = 1$ and the constant $C_2 = 0$; (B; solid, blue curves) fixing $C_1 = 1$ while allowing the constant C_2 (horizontal, dashed, blue lines) to be a free parameter; and (C; solid, green curves) allowing C_1 to be a free parameter while fixing $C_2 = 0$. Notice that we decrease the scale of the vertical axis with each row. Also, in successive frames we see the red cut-off (dotted) of each spectrum pushing redward. This is a manifestation of the circular format of the streak image; earlier in time corresponds to closer to the edge of the image.

Figure 6.2 shows the best-fit Planckian temperatures, $T_{\rm rad}$, for the sequence

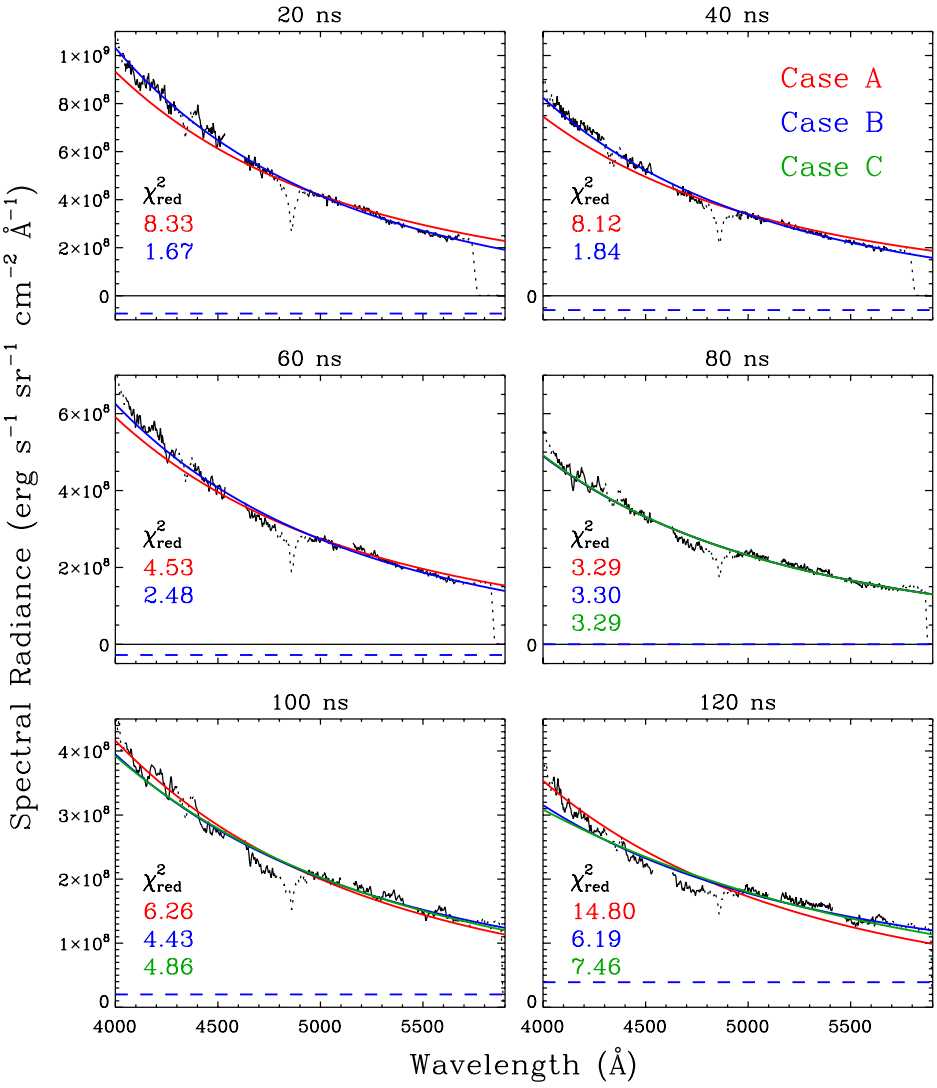

Figure 6.1 Continuum fits to selected line-outs of the gold back-lighter emission obtained with SVS1 from experiment z2554. The three fitting cases are (A; solid, red curves) solely Planckian emission, (B; solid, blue curves) Planckian emission with a constant background (horizontal, dashed, blue lines), and (C; solid, green curves) Planckian emission with a scaling factor. We give the fit parameters in Figure 6.3

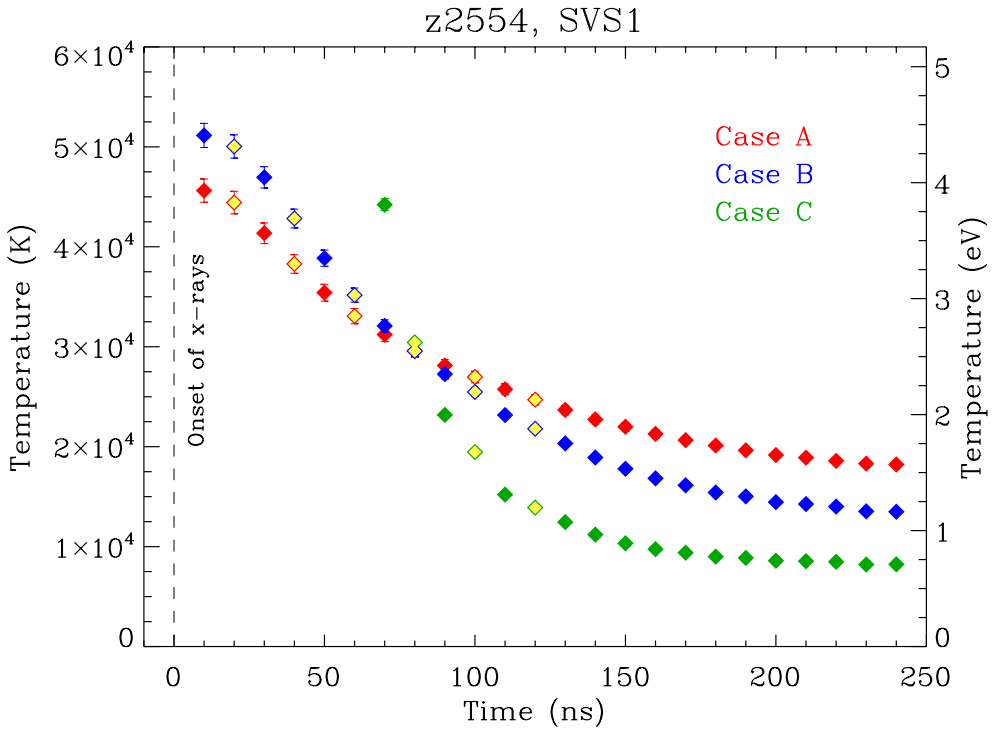

Figure 6.2 Planckian temperatures, $T_{\rm rad}$, determined from fitting 10-ns continuum line-outs measured using SVS1 from experiment z2554. We plot the results from the fitting cases described in the text, case A (red), case B (blue), and case C (green).

of 10-ns continuum line-outs throughout the streak for fitting case A (red), case B (blue), and case C (green). The uncertainties (solid, vertical lines) come from fitting our $+\sigma$ and $-\sigma$ absolute uncertainty spectra. We highlight (yellow) the fits plotted in Figure 6.1.

Case B produces fits with lower $\chi^2_{\rm red}$ than case A. The additional constant background C_2, which monotonically increases with time (Figure 6.3), does well to match the measured emission. However, C_2 is negative early in time, crosses zero at

~ 80 ns, and asymptotes to a positive value late in time. Assuming the back-lighter emission is Planckian, the behavior of C_2 cannot be explained by, say, scattered light in the gas cell, which would be positive at all times.

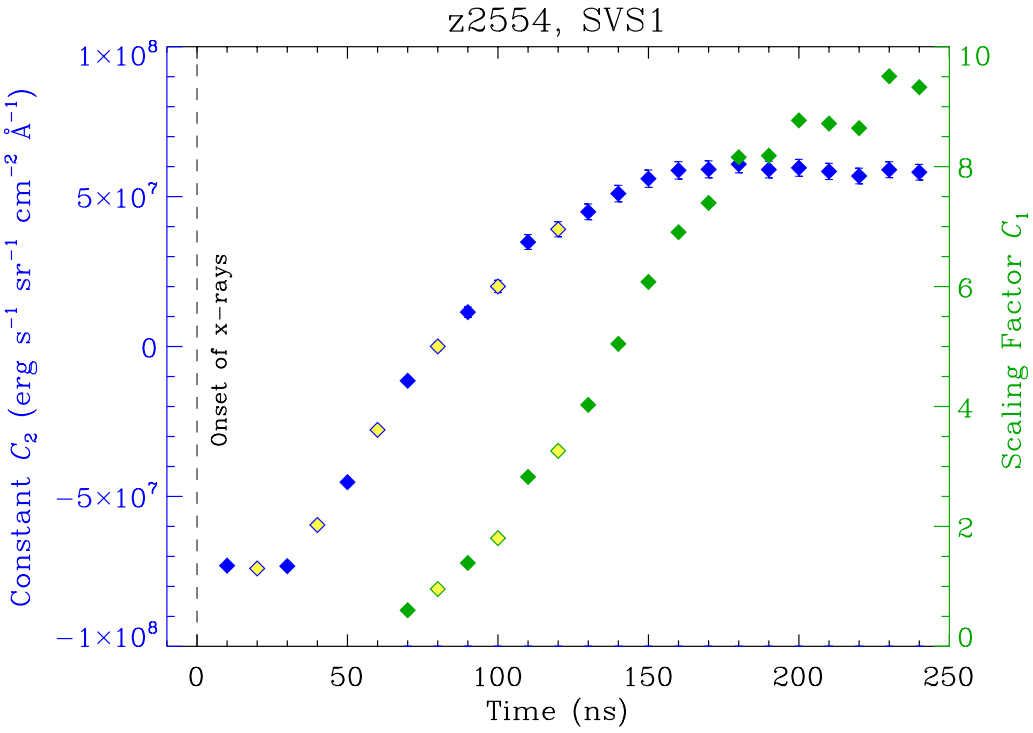

Figure 6.3 Constant C_2 values (blue) determined from case B fits and scaling factor C_1 values (green) determined from case C fits to continua measured using SVS1 from experiment z2554.

Since we believe our absolute calibration to be inaccurate by some scaling factor, case C should reveal this factor. Early in time, though, fits for this case C fail to converge. In this wavelength range and at these temperatures, the *shape* of the continuum is not sufficient to uniquely constrain a Planckian temperature. As with C_2 from case B, C_1 monotonically increases with time. We plot these values

in Figure 6.3, highlighting (yellow) the fits shown in Figure 6.1. The left and right axes correspond to the constant C_2 and the scaling factor C_1 from cases B (blue) and C (green), respectively.

6.1.2 Revisiting the Simulations of our Plasma Formation

Our LASNEX simulations begin by modeling the z pinch. Its radiation deposits energy into the gold wall inside our gas cell cavity. Then the gold re-emits to heat the hydrogen gas fill. Equipped with *measurements* of the gold emission, we can now bypass the first steps in the LASNEX simulations, which depend on the accuracy of the z-pinch radiation model (Rochau et al. 2008; Loisel et al. 2014) and of the energy conversion in the gold, and begin a simulation with the radiation that drives our hydrogen plasma formation. This subsection presents a preliminary investigation into this simulation primarily to demonstrate this application of the back-lighter emission measurements but also to further describe the behavior of the plasma. For this investigation we assume our measured back-lighter emission is the same as the gold wall emission. We are currently assessing how the hardware geometry and potential issues with heat transfer within the gold affect this assumption.

We use the one-dimensional radiation-magnetohydrodynamics code Helios-CR (Macfarlane et al. 2006). The simulation sets up a planar geometry with 20 mm of hydrogen gas, corresponding to the dimensions of our gas cell cavity. For the initial conditions, we use a static (no bulk motion) gas with a pressure of 10 Torr at room temperature. On one side of the hydrogen (corresponding to the gold wall),

we irradiate the gas with time-dependent Planckian emission described by our inferred radiation temperatures, $T_{\rm rad}$, from the SVS1 data from experiment z2554 (Section 6.1.1). This side of the hydrogen is fixed while the opposite side is free to expand. The simulation does not include the motion of the gold wall, which is likely to affect the conditions within a few mm of the wall. The code solves Navier-Stokes, Maxwell's, and energy conservation equations for separate electron and ion temperatures in a Lagrangian reference frame. It uses the Spitzer model (Spitzer & Härm 1953) for the electron thermal conductivity. We choose a multi-angle model with two angles with which the code computes the radiation transport for multiple photon energy groups. The collisional-radiative modeling includes collisional processes such as collisional ionization, recombination, excitation and de-excitation, as well as radiative processes such as photoionization, stimulated emission, spontaneous decay, radiative recombination, dielectronic recombination, autoionization, and electron capture. See Macfarlane et al. (2006) for more details about Helios-CR, including sources for atomic data.

For computational efficiency, we perform the simulation in a mode that determines level populations assuming local thermodynamic equilibrium (LTE) and uses pre-calculated opacity tables. With more patience the simulation can calculate populations and opacities in-line (NLTE) and use a detailed configuration accounting (e.g., Hansen et al. 2006) for the atomic energy level structure. This is the more appropriate strategy since our plasma is radiation-driven and therefore will depart from LTE. We leave NLTE simulations for future investigation.

Figures 6.4, 6.5, and 6.6 plot simulated electron temperature, $T_{\rm e}$, electron

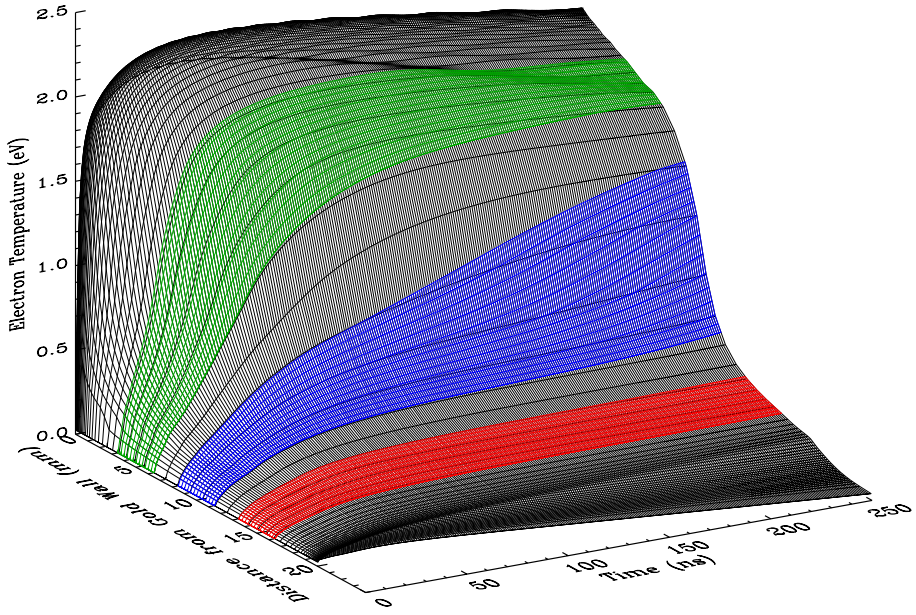

Figure 6.4 Helios-CR simulation in LTE mode of electron temperature as a function of distance from the gold wall and of time. We highlight our three possible LOS positions: 5 (green), 10 (blue), and 15 mm (red) away from the gold wall. Each is 3 mm in diameter. Closer to the wall the plasma heats up more quickly and to hotter temperatures than farther from the wall.

density, n_{e}, and ionization, respectively, as a function of distance from the gold wall and of time. We highlight the three possible LOS positions available with the ACE gas cell (Section 4.1.3). These are 5 (green), 10 (blue), and 15 mm (red) away from the gold wall, and each uses our nominal LOS beam diameter of 3 mm (Section 5.3.3.1). The plasma is hottest, densest, and most ionized closest to the wall where it rises to relatively stable conditions within a few tens of ns. Farther from the wall, the time to reach quasi-stable conditions elongates. The figures also show the

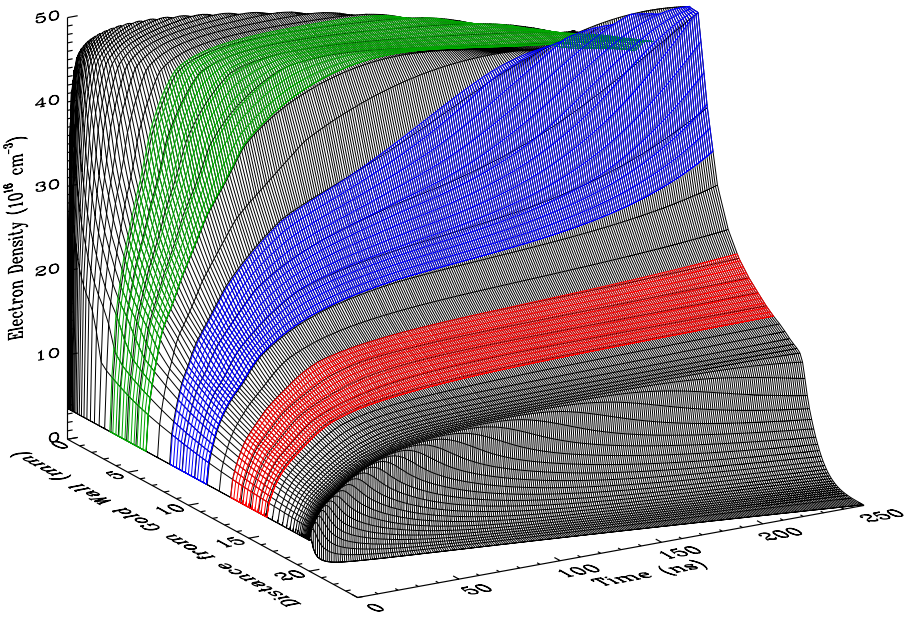

Figure 6.5 Helios-CR simulation in LTE mode of electron density as a function of distance from the gold wall and of time. Across space and time the plasma experiences electron densities ranging an order of magnitude.

plasma slowly expanding beyond its 20-mm initial size.

In Figure 6.7 we look more closely at $T_{\rm e}$ (top panel), $n_{\rm e}$ (middle panel), and ionization (bottom panel) for distances from the gold wall corresponding to our 5 (green), 10 (blue), and 15 mm (red) observing lines of sight. The dotted, solid, and dashed lines are the inner, central, and outer distances, respectively, of the lines of sight where "inner" is closest to the gold wall. This shows the range of plasma conditions probed by each LOS. At 100 ns, for example, the difference between $T_{\rm e}$ at the inner and outer boundaries of the LOS are 26, 77, and 35 % of $T_{\rm e}$

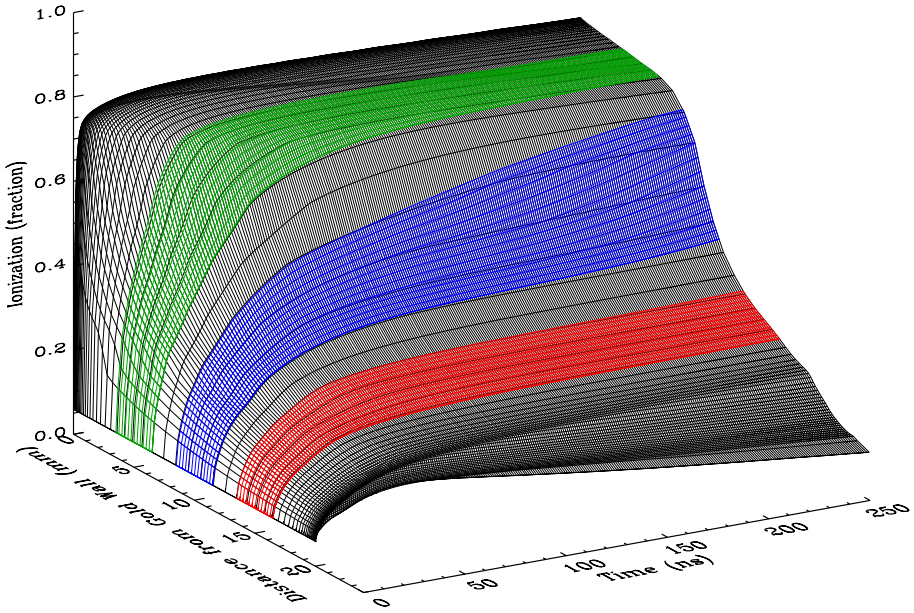

Figure 6.6 Helios-CR simulation in LTE mode of ionization (electron density divided by total particle density) as a function of distance from the gold wall and of time. The behavior follows from that illustrated Figure 6.4.

at the center of the LOS for the 5, 10, and 15 mm positions, respectively. For n_e the corresponding values are 6, 40, and 21 %, and for the ionization they are 8, 37, and 21 %. Aside from an ionization wave apparent in Figure 6.5, conditions decrease with increasing distance from the gold wall.

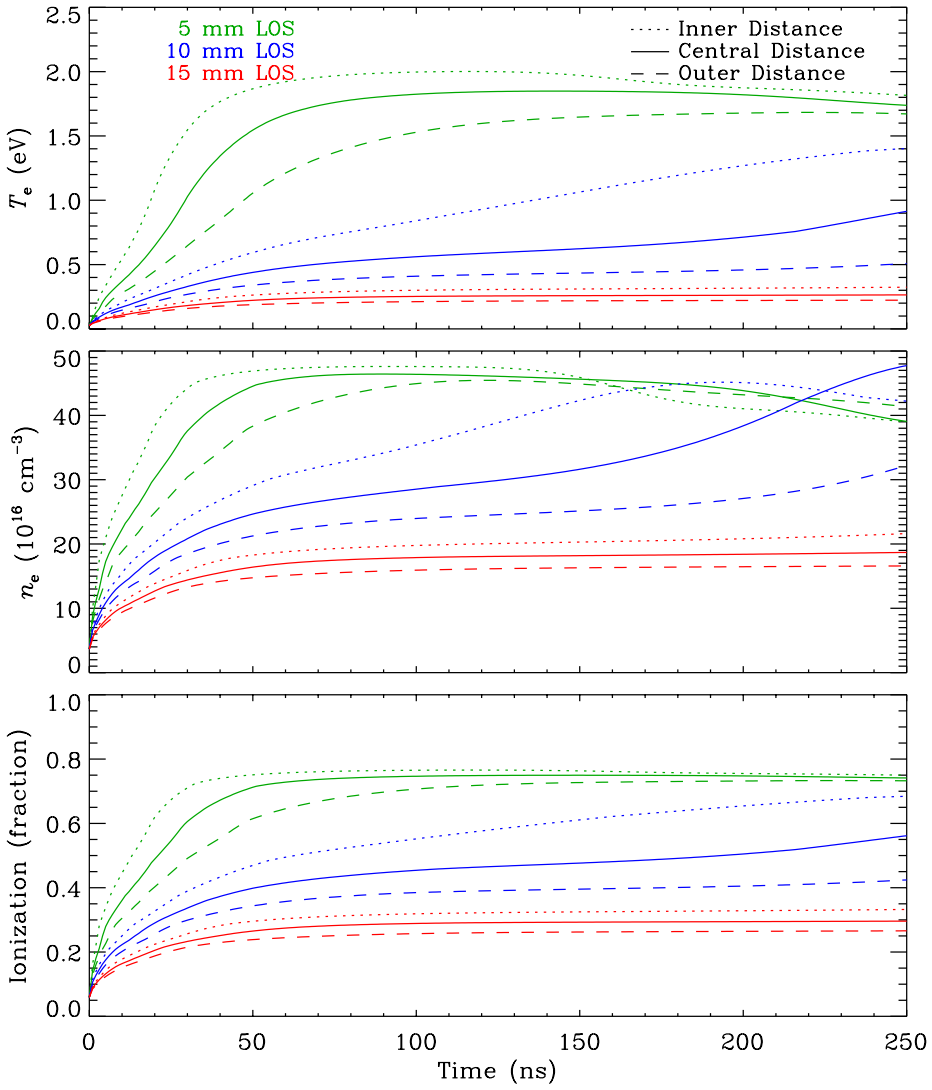

Figure 6.7 Simulated electron temperature (top panel), electron density (middle panel), and ionization (bottom panel) for lines of sight that are 5 (green), 10 (blue), and 15 mm (red) away from the gold wall. This shows the range of plasma conditions that span the nominal 3 mm diameter of the LOS. In general the conditions decrease from the boundary closest (dotted) to the gold wall through the central axis (solid) to farthest (dashed) from the gold wall.

6.2 Absorption

Our plasma emits because it is hot. Observing it when it is back-lit by an emission source that is even hotter (brighter) yields absorption spectra. Thus, absorption spectra contain three components:

$$L_\lambda^{\rm abs} = L_\lambda^{\rm cont} T_\lambda + L_\lambda^{\rm em}. \tag{6.2}$$

$L_\lambda^{\rm cont}$ describes the back-lighter (Section 6.1). T_λ and $L_\lambda^{\rm em}$ both describe our experimental plasma but in different ways. These are separable if on the same relative scale.

Figure 5.14 shows an example of our simultaneously measured emission ($L_\lambda^{\rm em}$) and absorption ($L_\lambda^{\rm abs}$) data, but it does not yet illustrate the relative levels of the two because of the systematic uncertainty in absolute scaling between data obtained with each SVS system we discover in Section 5.3.4.1. We find, however, that for the previous and subsequent experiments, z2552 and z2554, the absolute levels of the SVS1 data consistently differ from that of the SVS2 data by scaling factors of 0.711 ± 0.017 and 0.733 ± 0.023, respectively. We assume this systematic holds throughout this experiment series so that we may correct the SVS1 data from z2553 to place it on the same relative scale as the SVS2 data. Figure 6.8 shows the relative levels of emission (blue) and absorption (red) spectra from z2553 once we apply this scaling for 10-ns line-outs beginning at 50 (solid), 90 (dotted), and 130 ns (dashed) after the onset of x-rays. For the scaling, we use the mean of the values from z2552 and z2554, 0.722 ± 0.014. At Hβ the emission is always a significant fraction of the absorption level. Elsewhere it is not. Notice, though, that as the back-

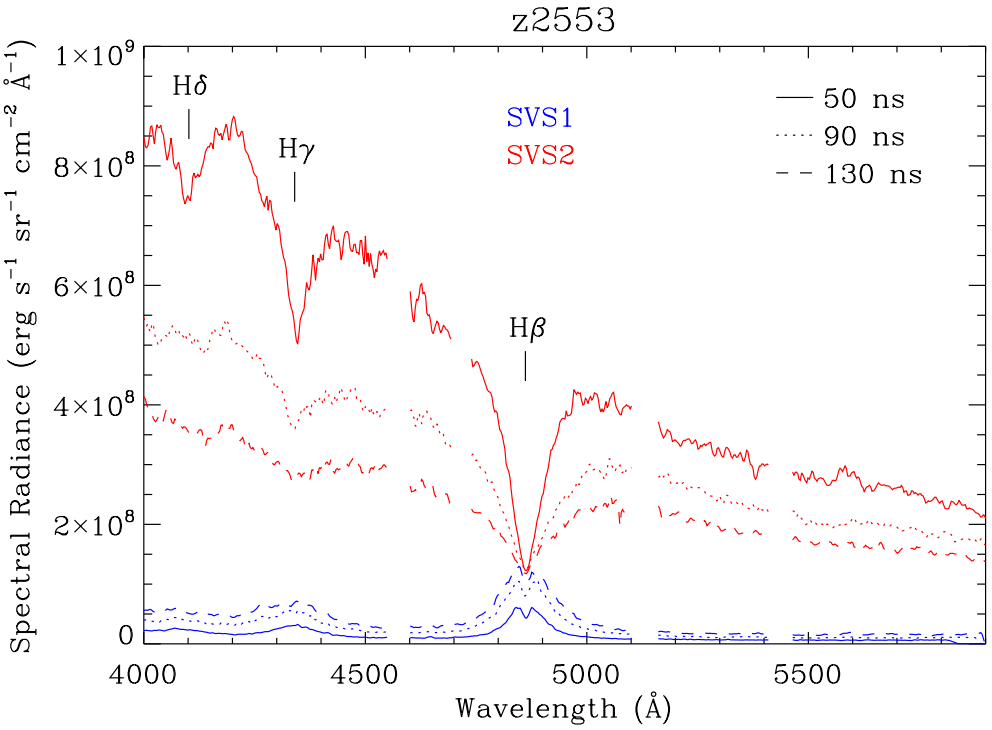

Figure 6.8 Spectral radiance line-outs from experiment z2553 acquired with SVS1 (blue) corrected to the same absolute scale as those acquired with SVS2 (red). The line-outs each span 10 ns and begin at 50 (solid), 90 (dotted), and 130 ns (dashed) after the onset of x-rays. The plasma emission increases with time as the back-lighter emission decreases, diminishing the contrast between the two. For clarity, we omit the uncertainties of the spectral levels.

lighter cools with time (as its emission decreases) the emission from the hydrogen plasma increases, worsening the contrast between the competing emissions. At 5300 Å, for example, the spectral radiance of the emission data is 2.1 ± 0.2, 3.8 ± 0.3, and 8.5 ± 0.7 % of that of the absorption data at 50, 90, and 130 ns, respectively. Figure 6.9 shows the emission level at 4500 Å (blue diamonds) and at 5300 Å (red diamonds) increase with time with respect to the absorption level for the data from

experiment z2553. We highlight (yellow) the line-outs plotted in Figure 6.8.

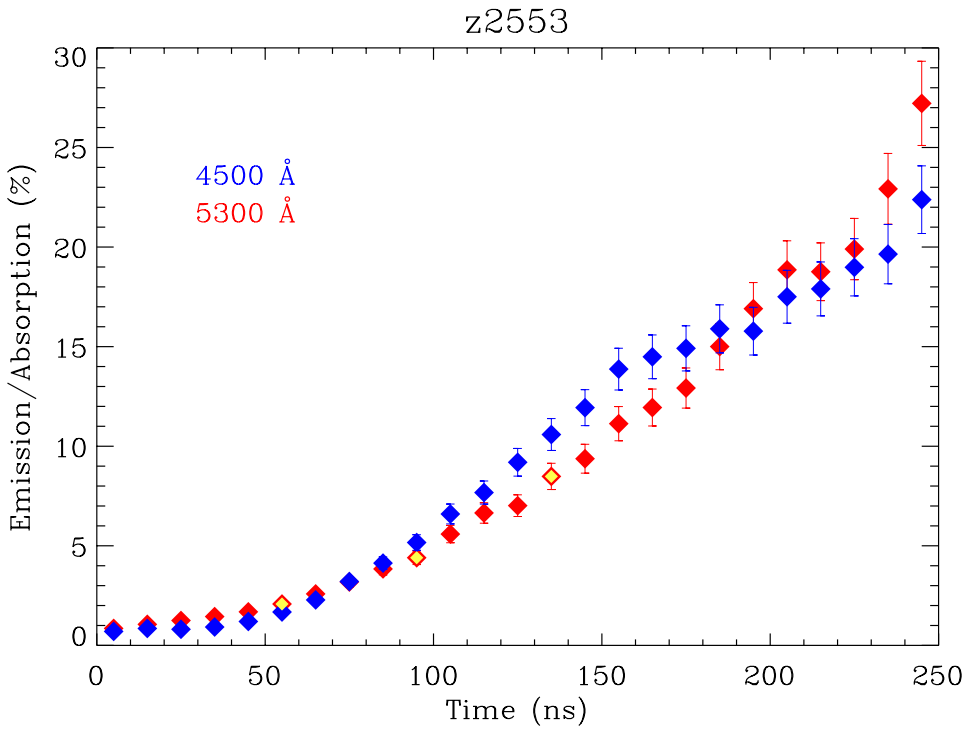

Figure 6.9 The emission level at 4500 Å (blue diamonds) and at 5300 Å (red diamonds) increases with time as a percentage of the absorption level, diminishing the contrast between the two and increasing the significance of the emission subtraction. We highlight (yellow) the line-outs plotted in Figure 6.8.

By making some assumptions and approximations, we can now remove the plasma self-emission from the absorption data to get emission-subtracted absorption or corrected absorption data:

$$L_\lambda^{\mathrm{abs,cor}} = L_\lambda^{\mathrm{abs}} - L_\lambda^{\mathrm{em}} = L_\lambda^{\mathrm{cont}} T_\lambda. \tag{6.3}$$

We first assume that, for experiment z2553, we may adjust the SVS1 data, according to the scaling factors determined from z2552 and z2554, to place it on the same

scale as the SVS2 data. We then approximate the length of plasma the emission LOS observes ($\sim$ 120 mm) to equal that of the absorption LOS ($\sim$ 114 mm); the two differ by $\sim$ 5 %. We also approximate the nature of the emission from each LOS to be the same, though the absorption LOS includes a $\sim$ few mm region adjacent to a gold back-lighting surface that the emission LOS does not. Figure 6.10 shows an example emission-subtracted absorption spectrum (solid, red) for the region surrounding the hydrogen Balmer lines versus its raw spectrum (dotted, red) for a 10-ns line-out from experiment z2553. Recall that early in time the emission is small compared to the absorption at all wavelengths and less so later in time. This plots an intermediate case at 80 ns. The subtracted emission (dotted, blue) is most significant at Hβ. and has a major effect on the shape of the center of the line.

The usual strategy to address plasma self-emission for absorption measurements is to require a back-lighter that is sufficiently bright to overwhelm self-emission (e.g., Perry et al. 1996; Bailey et al. 2009; Nagayama et al. 2014a). Our simultaneous emission and absorption measurements allow us to remove the former from the latter, and, to our knowledge, we are the first to do so for the study of line profiles. Consequently, this technique, and in particular the approximations we list, deserve further investigation for sensitivity and soundness.

6.2.1 Transmission

The corrected absorption spectra leave us one step away from transmission spectra (Equation 6.3): dividing by a continuum. Since our focus is line shapes, we choose an approach where we draw a continuum in the spectral vicinity of each

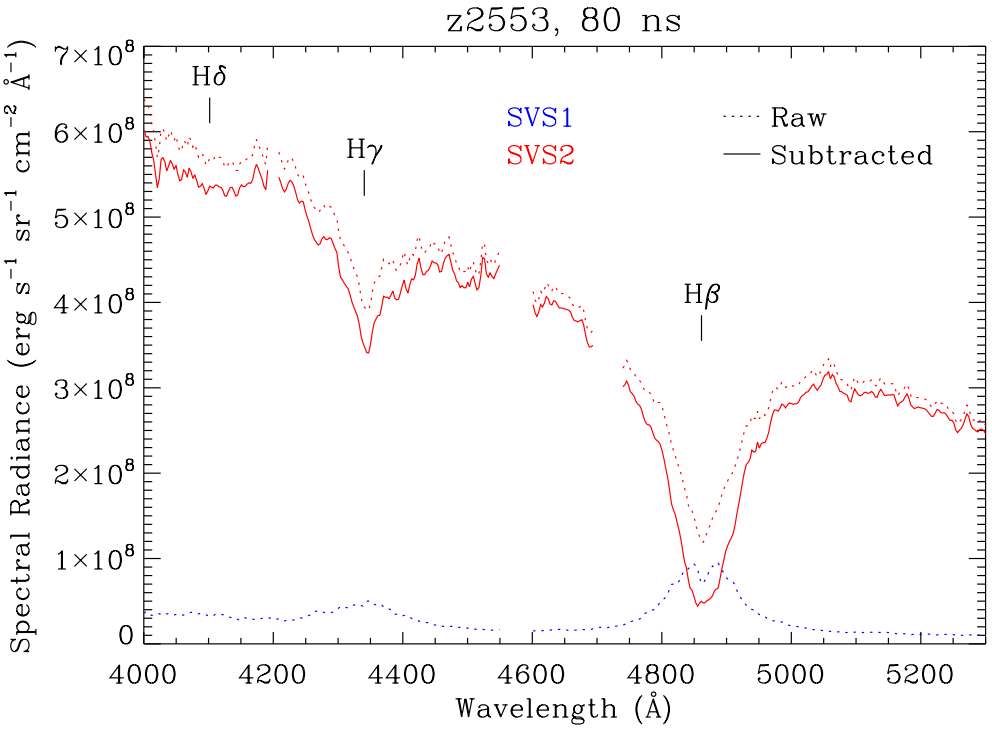

Figure 6.10 Example emission-subtracted absorption spectrum (solid, red) plotted with its raw absorption (dotted, red) and with the subtracted emission (dotted, blue). These 10-ns line-outs begin at 80 ns after the onset of x-rays from experiment z2553. The subtraction is most significant at the Hβ spectral region.

absorption line – a method employed in both the astronomy (e.g., Bergeron et al. 1992) and high energy density physics (e.g., Nagayama et al. 2014a) communities. This circumvents the need to explicitly include in our fitting model additional continuous opacity sources, namely, that due to the bound-free continuum (e.g., Däppen et al. 1987) and the H^- ion (e.g., Griem 1997). This sufficiently diagnoses the plasma when using the transmission of Hβ and/or Hγ. The line transmission of Hδ, however, is quite weak. As n_e of our observations increases we witness this

line disappear into the continuum (Section 7.3.2).

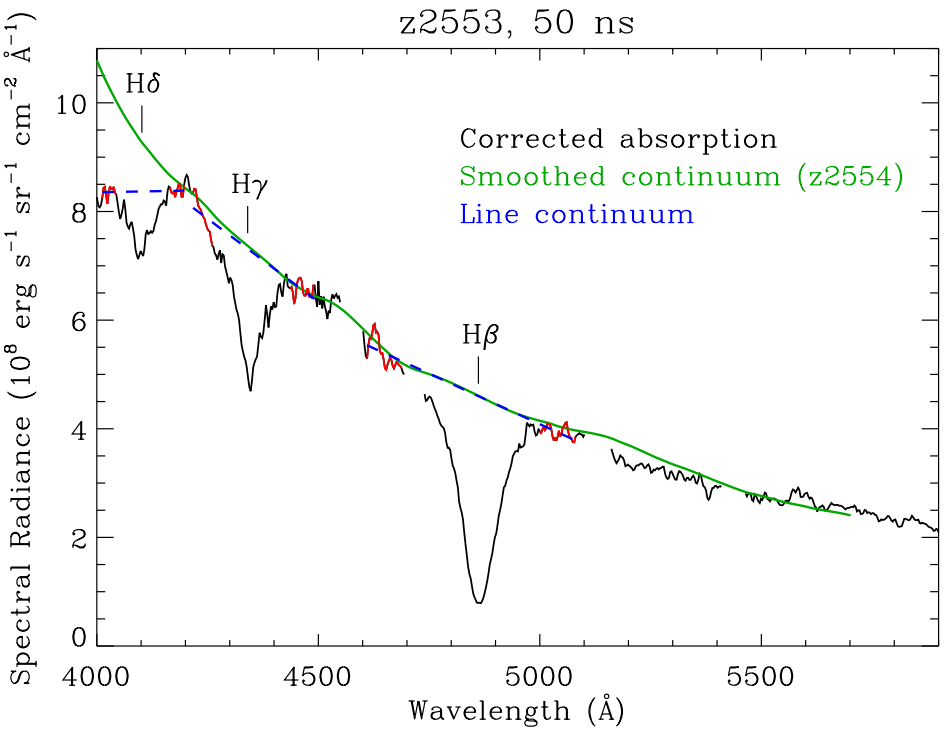

Figure 6.11 Example 10-ns corrected absorption line-out (black curve) beginning at 50 ns after the onset of x-rays from experiment z2553. We determine straight-line continua (dashed blue) to determine line transmission by fitting 1st-order polynomials to the spectral regions (red) surrounding the H Balmer lines. The green curve is the measured back-lighter continuum from experiment z2554; we scale it to match the absolute level of the black curve.

Figure 6.11 shows an example corrected absorption spectrum (black curve) with the straight-line continua (dashed blue) used to obtain line transmission for Hβ, Hγ, and Hδ. We determine these straight lines by fitting a 1st-order polynomial (straight line) to the spectral regions (red) flanking the absorption line. This spectrum is from a 10-ns line-out beginning at 50 ns after the onset of x-rays from

experiment z2553. We also plot the back-lighter continuum measured using SVS1 from experiment z2554. We scale this continuum to match the absolute level of the corrected absorption spectrum in the 4476–4560 Å (2.735–2.77 eV) spectral region. Note that for Hβ and for Hγ, the straight-line approximation of the local continuum is quite similar to the measured shape of the green curve. For Hδ, however, the presence of the bound-free continuum becomes obvious as the blue wing of this line merges with the red wing of Hϵ (beyond the plot window), thus significantly lowering the spectrum below the unattenuated continuum (green).

We fit the transmission due to bound-bound absorption of each hydrogen Balmer line for a homogeneous (single $T_{\rm e}$, $n_{\rm e}$, and $n_{\rm l}$) plasma:

$$T_\lambda^{\rm line} = \psi * {\rm EXP}\left\{-\kappa_\lambda^{\rm line} R\right\}, \tag{6.4}$$

where ψ is the measured instrumental broadening from Section 5.2.2, $\kappa_\lambda^{\rm line}$ is the opacity due to photoexcitation for a given bound-bound transition while neglecting stimulated emission (e.g., Mihalas 1978; Rybicki & Lightman 1979), and R is the length of the observed plasma[4].

For this case we express the opacity as

$$\kappa_\lambda^{\rm line} = \frac{\pi e^2}{m_{\rm e} c} f_{\rm l\to u} n_{\rm l} w_{\rm u}(n_{\rm e}) \phi_\lambda^{\rm line}(T_{\rm e}, n_{\rm e}), \tag{6.5}$$

where e is the charge of the electron, $m_{\rm e}$ is the mass of the electron, c is the speed of light, $f_{\rm l\to u}$ is the oscillator strength of the transition from the lower to upper energy level, and $n_{\rm l}$ is the population of the lower energy level. The reduction factor of

[4]Do not confuse this length R with the stellar radius from Equation 2.2.

the upper energy level $w_{\rm u}(n_{\rm e})$ is a function of electron density $n_{\rm e}$. It describes the lowering of the ionization potential (e.g., Unsöld 1948) or occupation probability (Däppen et al. 1987; Hummer & Mihalas 1988) of this level. The hydrogen line profile $\phi_\lambda^{\rm line}(T_{\rm e}, n_{\rm e})$ is a function of electron temperature $T_{\rm e}$ and electron density $n_{\rm e}$. Since it depends relatively weakly on $T_{\rm e}$ and dominantly on $n_{\rm e}$, we approximate ϕ to depend only on the latter. We explore this approximation in Section 6.3.1. Combining the physical constants into a single factor, C_κ, Equation 6.4 becomes

$$T_\lambda^{\rm line} = \psi * {\rm EXP}\left\{C_\kappa f_{\rm l\rightarrow u} n_{\rm l} w_{\rm u} \phi_\lambda^{\rm line}(n_{\rm e}) R\right\}. \tag{6.6}$$

The values of the oscillator strengths we incorporate into our fits come from Baker (2008), which are reported to high precision ($< 0.3\,\%$ uncertainty). We fix the LOS length R according to the dimensions of our gas cell design. This leaves $n_{\rm l}$, $w_{\rm u}(n_{\rm e})$, and $\phi_\lambda^{\rm line}(n_{\rm e})$ as free parameters.

6.2.2 Spectral Fitting Strategy

These first two, $n_{\rm l}$ and $w_{\rm u}$, are both factors. They manifest as the *depth* or *strength* of the absorption line. The line profile ϕ is area-normalized, so it describes the *shape* of the line. We first look at ϕ.

6.2.2.1 Line Shape

This is the focus of our study. Theoretical Stark-broadened line profiles can be calculated using different techniques that address plasma effects in different ways (e.g., Griem et al. 1959; Kepple & Griem 1968; Brissaud & Frisch 1971; Vidal

et al. 1973; Stamm et al. 1984). White dwarf atmosphere models incorporate these line profiles to produce synthetic spectra with which to compare observed spectra to determine atmospheric parameters. The choice or treatment of the profiles significantly affects the inferred atmospheric conditions (Tremblay & Bergeron 2009).

To discern which line profile model is most accurate, we compare out measured line shapes with the theoretical ones, which are nearly identical for lines with low ($n \leq 2$) principal quantum number, n, but deviate more with increasing n. Higher electron density exacerbates the discrepancy.

The Hβ line has a sufficiently low upper level ($n = 4$) for different theories to produce a similar line shape. Thus we fit Hβ to diagnose the plasma conditions, $n_{\rm e}$ and $n_{\rm l}$ (Section 7.1). We investigate using Hγ as a plasma diagnostic in Section 7.1.3. With these parameters in hand, we force calculated lines transmissions (Equation 6.4) onto the measured higher n lines, Hγ and Hδ, and compare the goodness of fit amongst line profile theories. Although our interest is in the line shape, this area-normalized profile possesses an intrinsic depth. Therefore it is necessary to constrain relative line strengths when comparing relative line shapes.

In the scope of this work, we are not interested in the line shift, so our fits also allow an additional free parameter, a small translation of the position of the line in photon energy or wavelength, to account for any systematic uncertainty in our wavelength calibration. This shift is always small. Median values from Hβ (and Hγ) transmission fits to the z2553 data are $\lesssim -0.0015$ eV. This magnitude is equal to the photon energy spacing between spectral elements at Hβ.

6.2.2.2 Reduction Factor

Two factors, $n_{\rm l}$ and $w_{\rm u}$, comprise the line strength we fit for each of the Balmer lines. These factors are indistinguishable without an additional constraint. We have two.

(1) These absorption lines share the same lower level population, $n_{\rm l}$. (2) Theory describes the reduction factor, w, for each line. It is ≤ 1, and it decreases with increasing n and with increasing $n_{\rm e}$. We discuss the physical meaning of w in Section 7.3.

As with line profiles, different theories approach w in different ways. Therefore we can use our measurements to discriminate between theories. For each theory, we use the calculated w_4 (which is nearly if not unity) in the Hβ transmission fit to determine $n_{\rm l}$. Then we fix $n_{\rm l}$ for the line strengths of Hγ and Hδ to fit for w_5 and w_6, respectively.

6.3 Diagnostic Sensitivity

We fit data that possess noise and measurement uncertainty. This limits the accuracy to which we determine fit parameters. We also approximate the line profile, ϕ, to have a negligible dependence on electron temperature, $T_{\rm e}$, and therefore depend solely on electron density, $n_{\rm e}$. Furthermore, our fitting model assumes that our experimental plasma either (1) is homogeneous and exists at a single plasma condition or (2) can be sufficiently and uniquely described by a homogeneous plasma. We leave it for future work to further measure or constrain the inhomo-

geneity present in our plasma transverse to (Figures 3.11 and 6.7) and along our observing lines of sight and to assess its affect on our results.

To investigate the sensitivity of our spectral fitting technique to the aforementioned factors, we perform a synthetic data analysis (e.g., Nagayama et al. 2012b,a) of our diagnostic transmission line, Hβ.

We create synthetic Hβ transmission data for a range of electron density, n_{e}, and lower level population, n_2. We simulate random noise (S/N $= 50$) and convolve instrumental resolution (Voigt profile with $\sim$ 10 Å full-width-at-half-maximum) typical of our experimental data. For these synthetic data we choose to use the tabulated Stark-broadened line profiles from Lemke (1997), which follow the theory of Vidal et al. (1973), and the reduction factor (as a function of n_{e}) for Hβ prescribed by Seaton (1990). Since we use the same ϕ and w_4 to synthesize and fit the data, our analysis is insensitive to these choices.

Figure 6.12 shows the results from fitting our synthetic data using the model described by Equation 6.6. For this parameter space, the values recovered from the fits (red diamonds) agree within uncertainties (red, horizontal and vertical lines) with the parameters we use to create the synthetic data (black diamonds). These fit uncertainties are random uncertainties and are most sensitive to noise (see Section 7.1.1). They are largest in the lower right-hand corner of the plot where the Hβ lines are narrower (decreasing n_{e}) and deeper (increasing n_2).

For these synthetic data, we use theoretical line profiles calculated for an electron temperature $T_{\mathrm{e}} = 1.00$ eV. Recall that we simplify our fitting model by

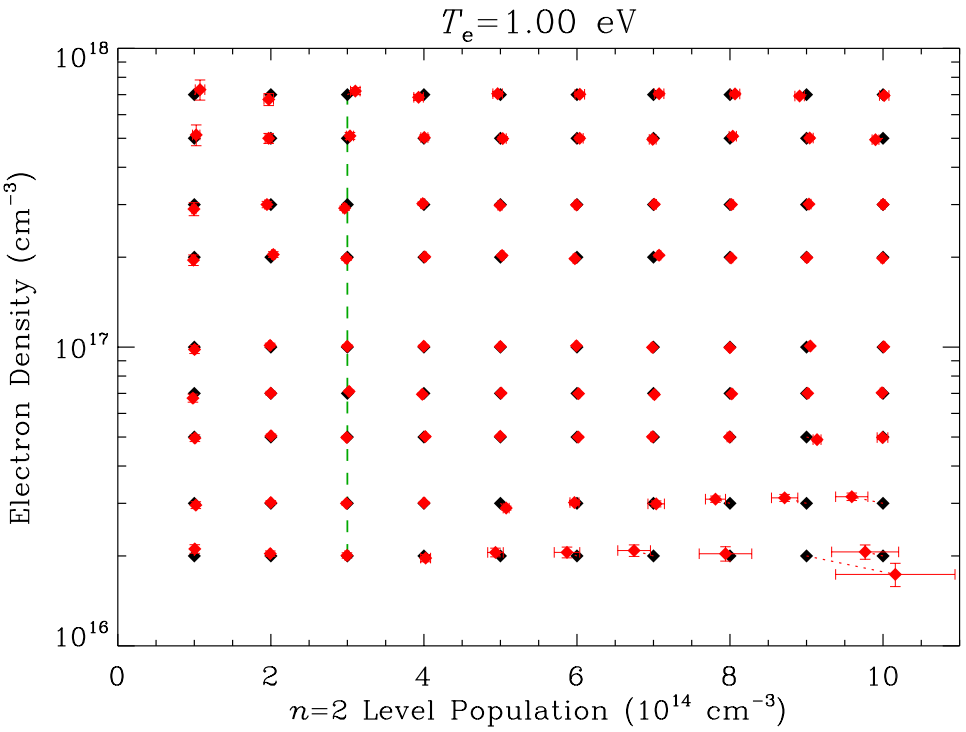

Figure 6.12 Recovered n_e and n_2 (red) from fits to synthetic Hβ transmission data (black) using the model described by Equation 6.6. The green, dashed, vertical line shows synthetic data points also plotted in Figure 6.15. Agreement within fit uncertainties (red, horizontal and vertical lines) shows that our fitting model successfully determines parameters in this range for a homogeneous plasma with $T_e = 1.00$ eV from data with our typical S/N and instrumental resolution.

neglecting the dependence of ϕ on T_e (Equation 6.6). Operationally, this means that we fit using profiles calculated for $T_e = 1.00$ eV. In other words, we assume that the electron temperature of our experimental plasma is 1.00 eV. We now test this approximation by repeating this exercise – by using the same fitting model with ϕ corresponding to $T_e = 1.00$ eV – to fit data synthesized at different T_e.

6.3.1 Line Profile Dependence on Electron Temperature

Figures 6.13 and 6.14 show the results of our fits of synthetic data created using line profiles corresponding to $T_e = 0.50\,\text{eV}$ and $T_e = 2.00\,\text{eV}$, respectively. We tether fits (red) to synthetic data (black) with red, dotted lines to illustrate the direction of discrepancy in parameter space.

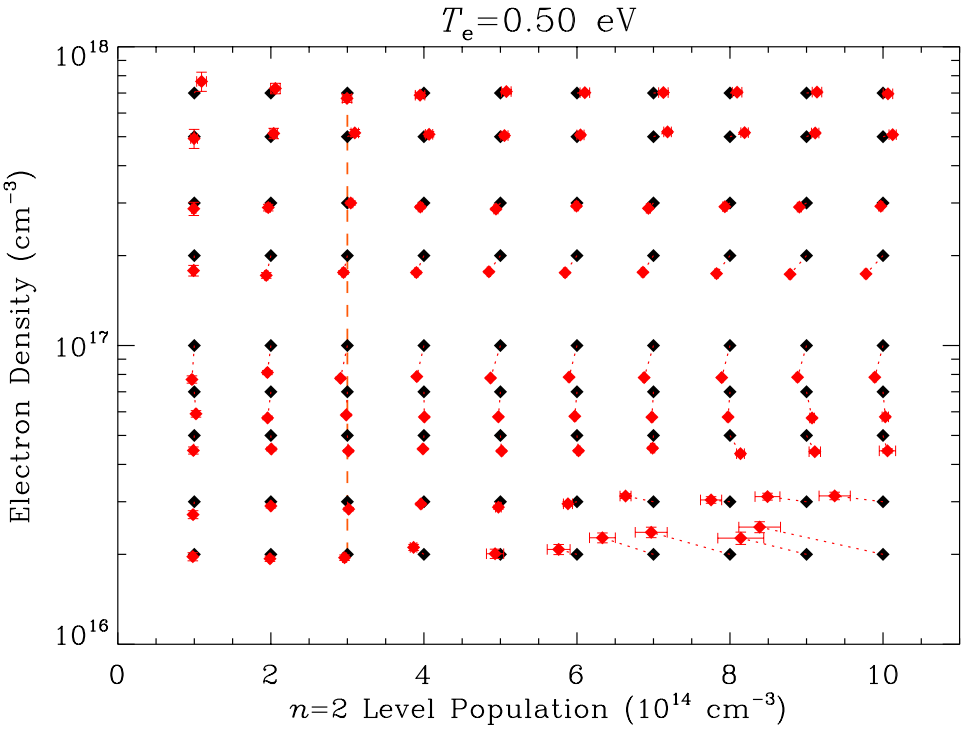

Figure 6.13 Same as Figure 6.12 but fitting synthetic data created using theoretical line profiles calculated for $T_e = 0.50\,\text{eV}$. The orange, dashed, vertical line shows synthetic data points also plotted in Figure 6.15. Even though the fitting model assumes $T_e = 1.00\,\text{eV}$, it successfully recovers n_2 for most of the parameter space, struggling for lines with low n_e and high n_2. The fits underestimate intermediate n_e values at all n_2.

For $T_e < 1.00\,\text{eV}$ (less than that corresponding to ϕ in our fitting model) the

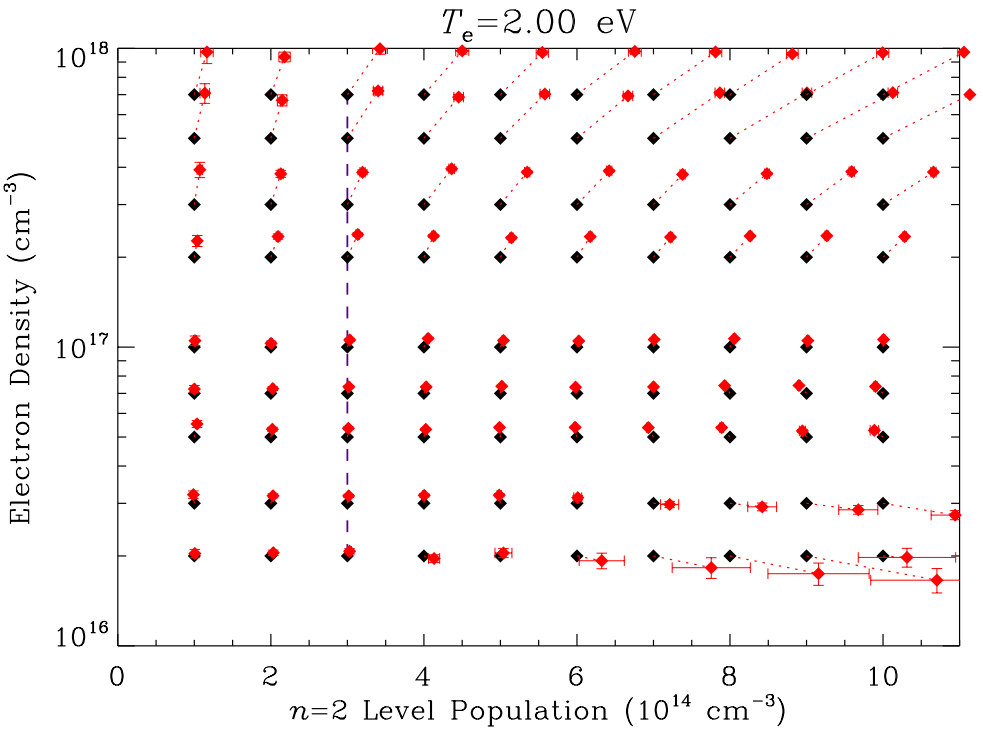

Figure 6.14 Same as Figure 6.12 but fitting synthetic data created using theoretical line profiles calculated for $T_e = 2.00$ eV. The purple, dashed, vertical line shows synthetic data points also plotted in Figure 6.15. For high n_e the fits systematically overestimate n_e and n_2. The overestimate of n_e increases with increasing n_2.

fits are successful at recovering n_2 except for lines with low n_e and high n_2. We recover the highest n_e values and underestimate the intermediate ones. For $T_e > 1.00$ eV (greater than that corresponding to ϕ in our fitting model) we overestimate n_e and n_2 at their highest values.

In Figure 6.15 we focus on the dependence on electron temperature by plotting the synthetic test results for determining n_e at a fixed n_2 (6×10^{14} cm^{-3}) versus T_e. The results of our Helios-CR simulation (Figure 6.4) motivate the range of elec-

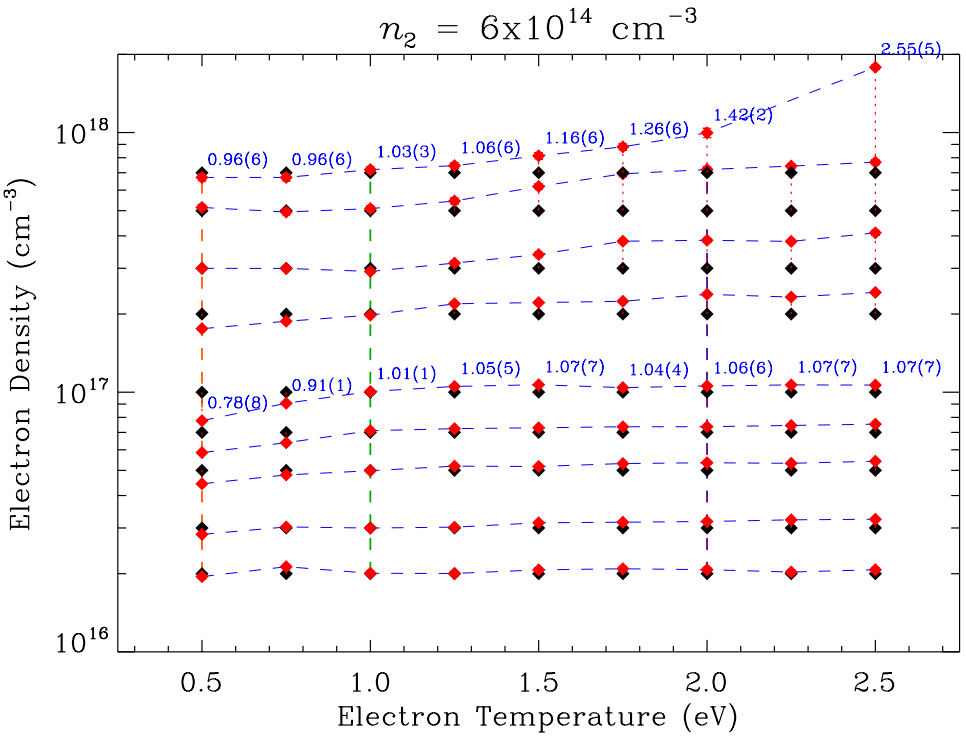

Figure 6.15 Recovered n_e (red) from fits to synthetic Hβ transmission data at a single n_2 value ($6 \times 10^{14}\,\mathrm{cm}^{-3}$) for a range of T_e. The fits assume $T_e = 1.00\,\mathrm{eV}$. Dashed, vertical lines show the plasma conditions corresponding to $T_e = 1.00\,\mathrm{eV}$ from Figure 6.12 (green), $T_e = 0.50\,\mathrm{eV}$ from Figure 6.13 (orange), and $T_e = 2.00\,\mathrm{eV}$ from Figure 6.14 (purple). Blue, dashed, horizontal lines connect fits to synthetic data created at the same n_e. For two rows of n_e we print the ratio of fit to synthetic value to illustrate the trend with respect to T_e.

tron temperatures we explore. Dashed, vertical lines point out the plasma conditions coinciding with $T_e = 1.00\,\mathrm{eV}$ from Figure 6.12 (green), $T_e = 0.50\,\mathrm{eV}$ from Figure 6.13 (orange), and $T_e = 2.00\,\mathrm{eV}$ from Figure 6.14 (purple). To illustrate trends as a function of T_e, we connect fits to data synthesized at the same n_e with blue, dashed, horizontal lines. For two cases, $n_e = 1 \times 10^{17}\,\mathrm{cm}^{-3}$ and $n_e = 7 \times 10^{17}\,\mathrm{cm}^{-3}$, we

print the ratio of the fit value to the synthetic value for all $T_{\rm e}$. The uncertainty of the last digit is in parentheses.

6.4 Conclusions

Of the three kinds of data we simultaneously measure from the three lines of sight observing our experiment, we use the first, *continuum* data, to further describe our experimental platform. Assuming the gold back-lighter emits as a Planckian in our observed wavelength range, we fit for its temperature, $T_{\rm rad}$, as it cools with time. We then feed these measurements into a Helios-CR (Macfarlane et al. 2006) simulation to investigate the dynamics of the plasma formation and temporal behavior.

We correct our *absorption* data for plasma self-emission by subtracting our measured *emission* data. Once we divide by a continuum in the spectral vicinity of each absorption line, we extract *transmission* data. Fitting the Hβ transmission line yields our plasma conditions ($n_{\rm e}$ and $n_{\rm l}$). We describe our strategy for comparing theoretical line shapes against our measured line shapes as well as theoretical reduction factors for absorption lines against our measured reduction factors.

We conduct a synthetic investigation to quantify the accuracy to which we can determine our plasma conditions, over some range of $n_{\rm e}$ and n_2, from fitting Hβ. This accounts for noise in our measured spectra and instrumental resolution. We also test our approximation that the line shape ϕ has a negligible dependence on electron temperature, $T_{\rm e}$, by using line profiles calculated for $T_{\rm e} = 1.00\,$eV to fit data synthesized using line profiles corresponding to the range of $T_{\rm e} = 0.5$–$2.50\,$eV.

We find that, in general, we systematically underestimate $n_{\rm e}$ when $T_{\rm e} < 1.00$ eV and overestimate $n_{\rm e}$ when $T_{\rm e} > 1.00$ eV. The level of discrepancy depends on the region in parameter space, but for an intermediate n_2 (6×10^{14} cm^{-3}), the underestimation at low $T_{\rm e}$ can be $\gtrsim 20\,\%$ but only at intermediate $n_{\rm e}$. The overestimation at higher $T_{\rm e}$ can be up to $\sim 40\,\%$ for the highest $T_{\rm e}$ and $n_{\rm e}$.

Chapter 7

Results, Summary, and Future Directions

"10 kV."

The tinny intercom speaks, voicing yet another way in which this life is backwards from astronomy. (Okay, for this one, I'm wrangling in space exploration and placing it under the astronomy umbrella. I appreciate your patience.) I'm used to TV counting *down* for a space shuttle launch, but…

"20 kV."

…here it's a count *up*. This is when they charge the Marx capacitor banks, storing up voltage in preparation for the pulsed power shot.

"30 kV."

Jim paces about in the north hallway of Building 983, home of *Z*.

"40 kV."

Down the hall, Don's giddy. Waiting outside the doors to the *Z* high-bay so he can see the blue and/or yellow flash of leaked electrical charge out of the water section.

"50 kV."

Alan and I stand next to the SVS systems in the next building, double-checking triple-checking quadruple-checking our checklist and our notes. We didn't forget anything, did we, Alan?

"60 kV."

Taisuke sits at his desk in his office in Building 970, maybe 100 yards away.

"70 kV."

Getting close.

"80 kV."

The town holds its breath.

"85 kV. *Z* is arming to fire."

BOOM!!!

Or maybe it's

BANG!!!

I haven't yet decided which best describes it. But it jolts us. Jim lets out a sigh of relief. Don leaps into the air in joy. Alan and I pull the film and shut down the SVS systems. Taisuke's office shudders. He turns to the window, smiles. Albuquerque continues with its day. After you, ma'am. Don't forget to pick up Suzie from day care. I'll just have a Caesar salad. Keep the change. Two adult tickets for the new Robert Rodriguez, please.

I hope we got data.

Let us consider the current state of theoretical line profiles used in white dwarf (WD) atmosphere models. Tremblay & Bergeron (2009) (hereafter TB) revamped WD atmosphere models by modifying line profiles calculated using the unified theory of Stark broadening of Vidal et al. (1973) (hereafter VCS) to account for the loss of upper energy level transitions due to high electric microfields. They do this by following the lead of Seaton (1990) to incorporate the occupation probability formalism of Hummer & Mihalas (1988) into the line profile calculation. When put into an atmosphere model this significantly improves the consistency of atmospheric parameters (i.e., effective temperature, $T_{\rm eff}$, and surface gravity, $\log g$) inferred from different hydrogen Balmer lines, observed spectroscopically. Additionally, it results in a systematic increase in these inferred parameters.

For DA WDs from the Palomar-Green Survey (Liebert et al. 2005), TB use their modified line profiles to determine an increased mean mass of $\langle M \rangle = 0.649\,M_{\odot}$. We use gravitational redshifts – a method independent of theoretical line profiles – to determine the mean mass of DA WDs in the solar neighborhood. We find $\langle M \rangle = 0.647^{+0.013}_{-0.014}\,M_{\odot}$ (Chapter 2; Falcon et al. 2010b). This is in excellent agreement with TB. Subsequent spectroscopic studies incorporating TB line profiles, however, do not find mean masses that agree with that determined from the gravitational redshift method. These include Limoges & Bergeron (2010), Tremblay et al. (2011a), and Kleinman et al. (2013), who find $\langle M \rangle = 0.606, 0.613$, and

$0.623\,M_{\odot}$, respectively.

This prompts us to look more deeply into WD atmosphere models, and since such a relatively subtle change makes a significant impact in the interpretation of observed WD spectra, we turn our focus to the theoretical line profiles. For the WD astronomy community, TB profiles now replace VCS profiles as tabulated by Lemke (1997). TB compare their profiles as well as VCS profiles with laboratory data from the wall-stabilized arc experiment of Wiese et al. (1972), which provides a sequence of relevant emission lines (hydrogen Balmer series) at relevant conditions ($n_{\rm e} = 1.5$ to $10 \times 10^{16}\,{\rm cm}^{-3}$). They choose to consider the experiments with the lowest and highest electron density, $n_{\rm e}$. For the former, the experimental data favor TB profiles over VCS profiles. For the latter, they cannot draw a stringent conclusion, finding difficulty in fitting either flavor of profiles at the reported plasma conditions.

This higher $n_{\rm e}$ regime is clearly interesting for the purpose of discriminating between theoretical line profile models. However, few laboratory experiments push into high $n_{\rm e}$ ($\gtrsim 10^{17}\,{\rm cm}^{-3}$) for the investigation of hydrogen Balmer line shapes, and for the ones that do, none besides Wiese et al. (1972) and Wiese et al. (1975) measure multiple lines. As TB show, the difference in line shape between their profiles and those determined using VCS increases with increasing principal quantum number (of the upper energy level of the transition), n. Therefore, leveraging multiple lines in an experiment is critical, *especially* when plasma diagnostics that are independent from line shapes are not available.

7.1 The Hydrogen Balmer β Line as a Plasma Diagnostic

We design our experiment to reach these high electron densities and to observe multiple Balmer lines (Chapters 3 and 4; Falcon et al. 2010b, 2013a). Hence, we provide new laboratory data at these plasma conditions using a fundamentally different experimental approach. Then we extend to higher $n_{\rm e}$ to conduct the first investigation in this regime of multiple hydrogen Balmer line shapes measured simultaneously. Furthermore, this extension is continuous; we measure the range of $n_{\rm e}$ in a single experiment and in the same plasma through time-resolved spectroscopic measurements. As we mention in Section 6.2.2.1, we use the Hβ line to diagnose our plasma conditions ($n_{\rm e}$ and $n_{\rm l}$) since we expect the discrepancy between line profile theories (VCS and TB) to be negligible here.

Figures 7.1, 7.2, and 7.3 show fits, using Equation 6.6 with a Levenberg-Marquardt minimization (Levenberg 1944; Marquardt 1963), of our measured Hβ line transmission from 10-ns line-outs beginning at 10, 50, and 100 ns, respectively, after the onset of x-rays from experiment z2553. We perform the fits using different theoretical line profiles; for each we display the goodness-of-fit expressed by the reduced chi squared, $\chi^2_{\rm red}$, and the best-fit electron density, $n_{\rm e}$, and lower level ($n = 2$) population, n_2. For these fits we use the reduction factor for Hβ, $w_4(n_{\rm e})$, as formulated by Seaton (1990). For this work and for the purpose of comparing the line shapes used in WD atmosphere models, this is the most appropriate choice, because this is the formalism used in the community (e.g., Bergeron et al. 1991; Tremblay & Bergeron 2009). Despite that, using other theoretical prescriptions make a negligible ($\lesssim 0.02\,\%$) difference for the $n_{\rm e}$ determination. Although among theories w_4 is

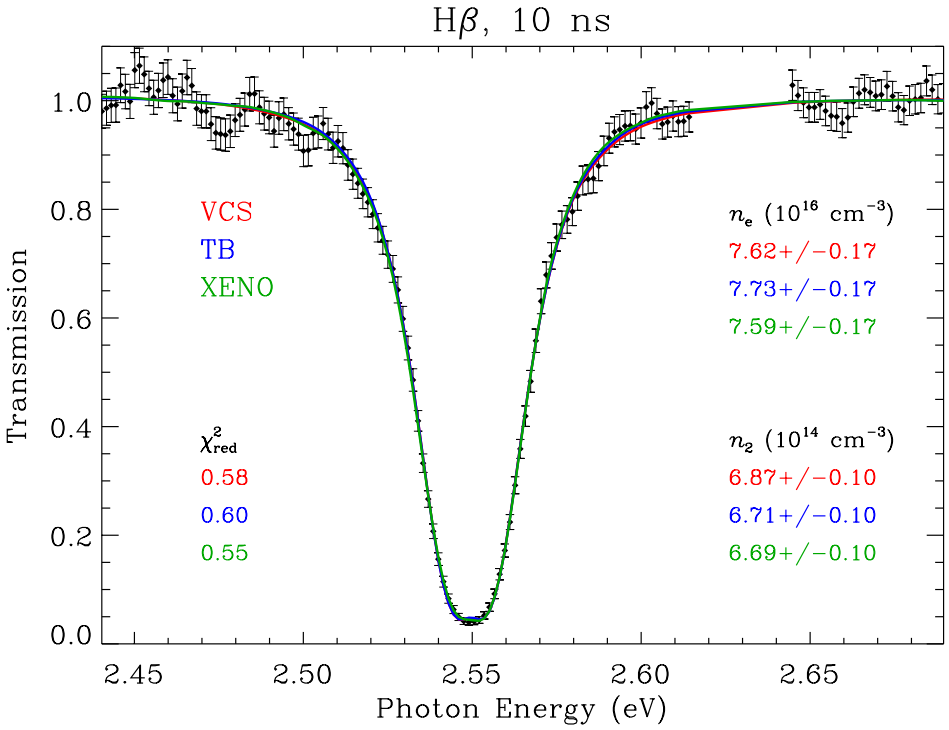

Figure 7.1 Measured Hβ transmission line-out (black diamonds) of our hydrogen plasma from 10–20 ns after the onset of x-rays from experiment z2553. The uncertainties (black, vertical lines) represent the S/N. We show fits using Vidal et al. (1973) (VCS; red), Tremblay & Bergeron (2009) (TB; blue), and Xenomorph (XENO; green; Gomez et al. 2014b) line profiles and print the corresponding $\chi^2_{\rm red}$, $n_{\rm e}$, and n_2 values.

within a $\sim$ few % of unity, at $n_{\rm e} = 1 \times 10^{17}$ cm^{-3} the description of Seaton (1990) is ~ 2 % less than w_4 as determined using the ionization depression of Ecker & Kröll (1963), for example. At $n_{\rm e} = 4 \times 10^{17}$ cm^{-3} this difference increases to $\gtrsim 6$ %, so the choice of reduction factor introduces a measurable systematic difference in the determined n_2. This manifests as, on average, a ~ 3 % higher inferred n_2 from Hβ when using w_4 derived from Seaton (1990) compared to that derived from Ecker &

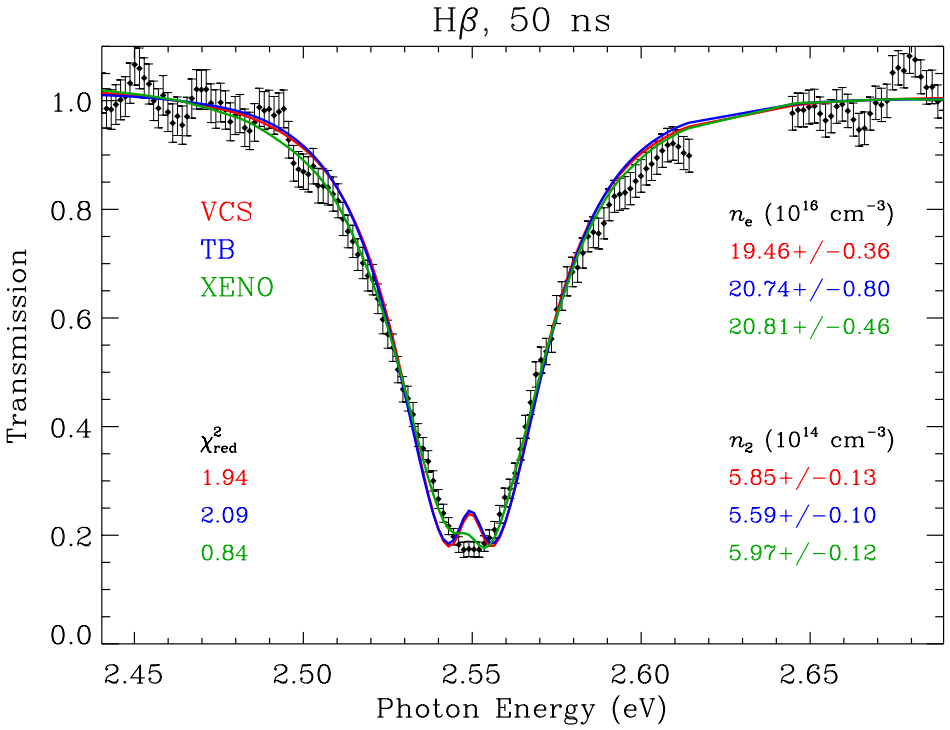

Figure 7.2 Same as Figure 7.1 but for a 10-ns line-out beginning at 50 ns after the onset of x-rays.

Kröll (1963).

Using VCS (red) and TB (blue) line profiles provide relatively good (low $\chi^2_{\rm red}$) fits early in time when $n_{\rm e}$ is lowest, but as the Hβ line widens with time, the fits are poorer (Figure 7.4), predicting more structure in the line center than observed as well as narrower line wings. Then after $\sim$ 110 ns, the fits are extremely poor. Before this time, though, the increasing, but still intermediate, poorness of fit is either due to our data or our fitting model. Systematic uncertainties, such as the plasma self-emission subtraction (Section 6.2), may be compromising the integrity

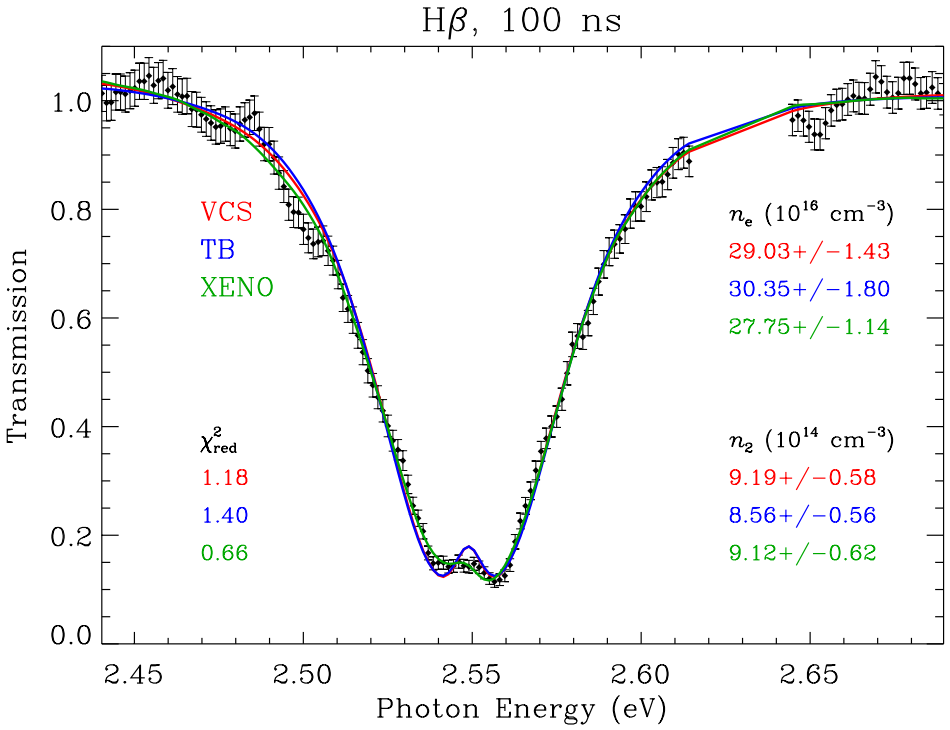

Figure 7.3 Same as Figures 7.1 and 7.2 but for a 10-ns line-out beginning at 100 ns after the onset of x-rays.

of our data. Let us assume this is not the case and consider a folly in our fitting model. An invalid assumption about our plasma, such as its homogeneity along our observed LOS, could harm the fit (we review our experimental assumptions in Section 7.4.1). Our choice of line profile could also be insufficient.

VCS profiles are not state-of-the-art for the plasma conditions of our experiment so their use as a plasma diagnostic may be suspect. WD astronomers use them because the works of Schoning (1994) and Napiwotzki & Rauch (1994) show that, once incorporated into a WD atmosphere model, whose radiation traverses plasmas

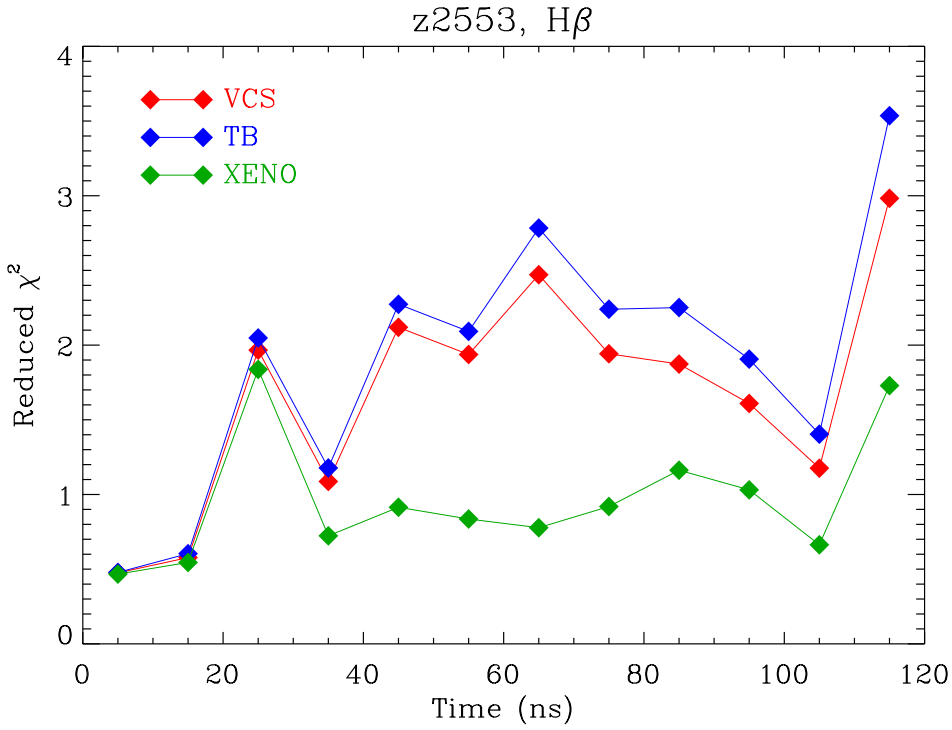

Figure 7.4 Goodness-of-fit versus time expressed by the reduced chi squared, $\chi^2_{\rm red}$, for fits to Hβ line transmission data measured from z2553 using VCS (red), TB (blue), and Xenomorph (green) line profiles. This includes $\chi^2_{\rm red}$ values for the fits plotted in Figures 7.1, 7.2, and 7.3. We plot times through 110 ns after the onset of x-rays. Defined this way, Xenomorph profiles provide the best fits.

with a range of $T_{\rm e}$ and $n_{\rm e}$, the subtleties of theoretical line shapes vanish. Since then, line profile calculations have improved. Those following the Model Microfield Method (Brissaud & Frisch 1971; Seidel 1977; Stehlé 1994; Stehlé & Hutcheon 1999), generalized theory of Stark broadening (Ispolatov & Oks 1994; Oks et al. 1995; Touma et al. 2000), and computer simulation method (CSM; e.g., Stamm et al. 1984; Cardeñoso & Gigosos 1989; Stambulchik & Maron 2006) produce line profiles in better agreement with laboratory data, particularly those from the exper-

iments of Wiese et al. (1975), Grützmacher & Wende (1977), and Grützmacher & Wende (1978), because these calculations include more sophisticated atomic kinetic effects, namely those from non-stationary ions (ion dynamics). Indeed, Gigosos & Cardeñoso (1996) and Gigosos et al. (2003) specifically designate their CSM profiles for plasma diagnosis.

VCS profiles, as tabulated by Lemke (1997), also do not account for asymmetries. Neither do TB profiles, and although laboratory studies have measured asymmetric line shapes for some time (e.g., Kudrin & Sholin 1963; Halenka 1988; Djurović et al. 2005), only recently has significant progress been made with CSM theory to address this phenomenon (e.g., Olchawa 2002; Stambulchik et al. 2007; Djurović et al. 2009). This progress, however, is only for the first two Balmer lines, Hα and Hβ.

In addition to fitting our data with VCS and TB profiles, we fit them with Xenomorph (Gomez et al. 2014b) line profiles (XENO; green curves in Figures 7.1, 7.2, and 7.3). These are CSM calculations. Figure 7.4 reveals that using these results in fits with smaller $\chi^2_{\rm red}$ than that of VCS or TB. This is because, besides including more sophisticated physics, these calculations handle asymmetries in a physically self-consistent way (Gomez et al. 2014b). This subtlety is most evident in the line center and red wing of the fitted Hβ transmission line in Figure 7.3. For all cases, the fits become poor after $\sim$ 110 ns, primarily due to decreasing signal level (Figure 6.10).

Through fits to our measured Hβ line transmission, we observe the electron density of our plasma increase throughout the first 90 ns after the onset of x-rays

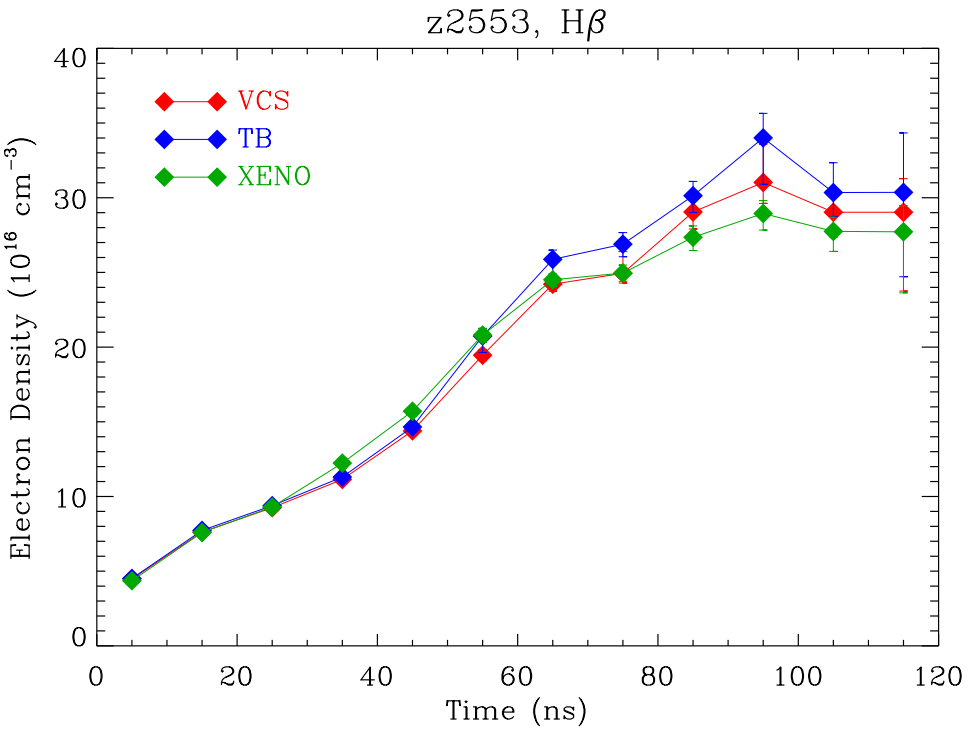

Figure 7.5 Electron density versus time determined from fits to Hβ line transmission data measured from z2553 using VCS (red), TB (blue), and Xenomorph (green) line profiles. The uncertainties (vertical lines) are the fit uncertainties (due to noise) and those due to calibration added in quadrature.

from the z pinch and then plateau (Figure 7.5). Throughout these plotted times we match the n_e range observed by Wiese et al. (1972) and then exceed it by approximately a factor of three. With other data, beyond the scope of this work, we infer electron densities up to nearly $n_e \sim 10^{18}\,\mathrm{cm}^{-3}$. Though different theoretical line shapes provide different goodness-of-fit (Figure 7.4), they infer electron densities in general agreement. Including up to the line-out beginning at 110 ns after the onset of x-rays, the mean of the maximum difference between n_e inferred using the

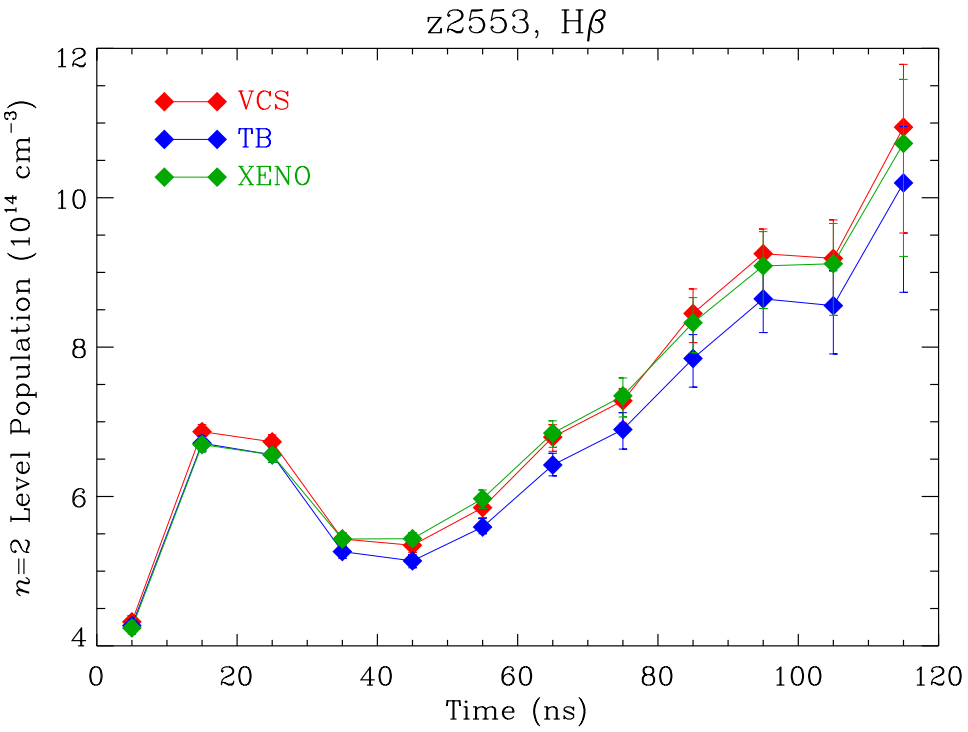

Figure 7.6 Lower level ($n = 2$) population versus time determined from fits to Hβ line transmission data measured from z2553 using VCS (red), TB (blue), and Xenomorph (green) line profiles and the reduction factor w_4 derived from Seaton (1990). The uncertainties (vertical lines) are the fit uncertainties (due to noise) and those due to calibration added in quadrature.

different theoretical line shapes for each line-out is $\sim 7\,\%$, and the mean of the standard deviations for each line-out is $\langle\sigma\rangle \sim 4\,\%$. For n_2 we see a spike soon ($\sim$ 10–20 ns) after the onset of x-rays followed by a gradual increase with time (Figure 7.6). Again, the different theoretical line shapes infer n_2 in general agreement; the mean maximum difference between inferred n_2 is $\sim 5\,\%$, and $\langle\sigma\rangle \sim 3\,\%$. We discuss the uncertainties (vertical lines) in Section 7.1.1.

Experiment z2553 is not an oddball case. Other independent experiments (z2554 and z2588) which have similar initial conditions also yield Hβ transmission line fits with similar $\chi^2_{\rm red}$. We infer similar $n_{\rm e}$ values that smoothly increase throughout the first ~ 100 ns after the onset of x-rays (Section 7.1.4) and increasing n_2 with a spike at $\sim$ 10–20 ns.

7.1.1 Uncertainties

For each line-out the uncertainties for the transmission data points (black, vertical lines in Figures 7.1, 7.2, and 7.3) represent the S/N. These are most appropriate to consider when fitting to models, because along with the best-fit parameters, the fitting should also determine the random uncertainties $\sigma^{\rm fit}$ of these parameters. Such fitting does not handle systematic uncertainties, so it is not appropriate to include $\sigma^{\rm rel}$ (defined in Section 5.3.4.2) for instance.

We estimate the noise level for each transmission line when fitting the adjacent spectral regions (red in Figure 6.11) for the straight line (dashed blue in Figure 6.11) used to convert the corrected absorption $L_\lambda^{\rm abs,cor}$ to transmission T_λ; the standard deviation of the red spectral points about the dashed, blue straight line becomes the noise level.

To determine the uncertainties due to the calibration $\sigma^{\rm cal}$, we perform two additional fits. These are fits to line transmissions determined from the ± 1-σ cases of the corrected absorption (i.e., $T^{\pm\sigma} = \frac{L^{\rm abs,cor} \pm \sigma}{L^{\rm cont}}$, where σ is the absolute uncertainty defined in Section 5.3.4.2). The differences of the fit parameters compared to the original (0-σ) case are the uncertainties due to calibration.

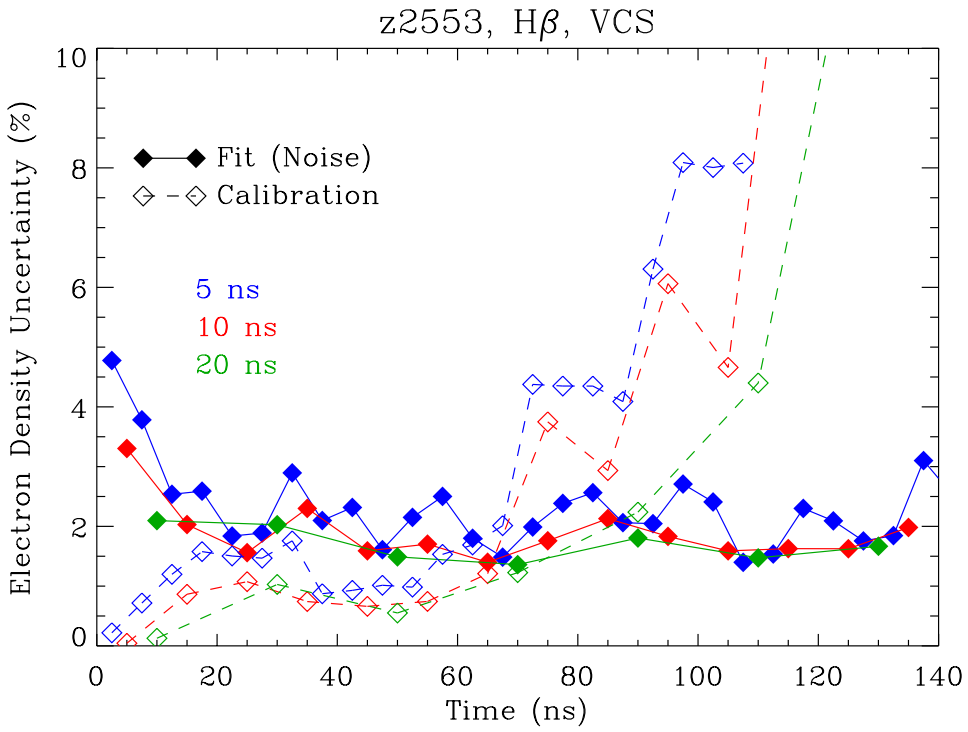

Figure 7.7 Uncertainties in n_e due to the fit or noise (filled diamonds with solid lines) and the calibration (open diamonds with dashed lines) for Hβ transmission line fits throughout time from experiment z2553. For simplicity we only show fits using VCS line profiles since fits using all line profiles exhibit the same qualitative trends. Fit uncertainties remain constant and calibration uncertainties decrease when using line-outs of 5 (blue), 10 (red), or 20 (green) ns durations.

Figures 7.7 and 7.8 show the fit (filled diamonds with solid lines) and calibration (open diamonds with dashed lines) uncertainties for the inferred n_e and n_2, respectively, from Hβ transmission line fits throughout time from experiment z2553. The calibration uncertainties are not necessarily symmetric ($|+\sigma^{cal}| \neq |-\sigma^{cal}|$), so for simplicity we plot the mean of the $\pm\sigma$ cases. All these uncertainties correspond to fits using VCS line profiles; the following qualitative trends do

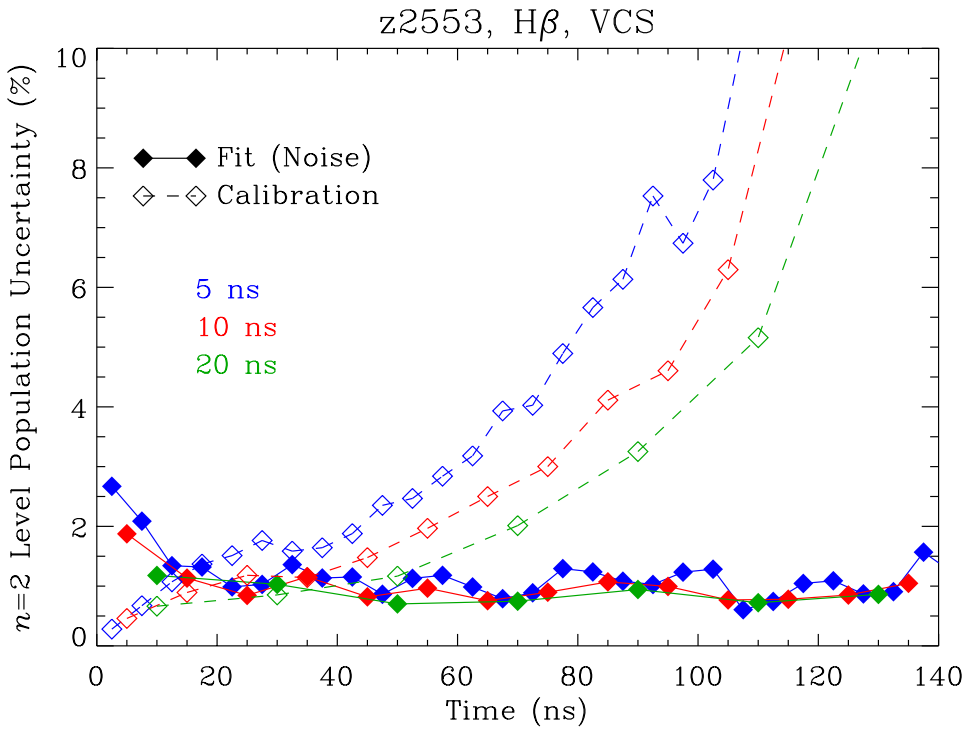

Figure 7.8 Same as Figure 7.7 but for best-fit n_2. The qualitative trend is the same as the fit uncertainties remain constant and calibration uncertainties decrease when using line-outs of 5 (blue), 10 (red), or 20 (green) ns durations.

not depend upon the choice of the theoretical line shape model. For n_e the calibration uncertainties are less than the fit uncertainties until $\gtrsim 60$ ns when they swap. For n_2 the fit uncertainties are, in general, less than the calibration uncertainties. The fit uncertainties are also nearly constant throughout time at ~ 2 and ~ 1 % for n_e and n_2, respectively. The calibration uncertainties increase with time. This is because the emission subtraction increases with time, which means that the uncertainty due to the subtraction increases as well. The adopted uncertainties printed in Figures 7.1, 7.2, and 7.3 and plotted in Figures 7.5 and 7.6 are the fit and calibration

uncertaintties added in quadrature (i.e., $\sigma^{\mathrm{adopt}} = \sqrt{(\sigma^{\mathrm{fit}})^2 + (\sigma^{\mathrm{cal}})^2}$).

We use these figures along with Figure 7.4 to motivate our choice to focus our analysis on the first ~ 110 ns after the onset of x-rays for the scope of this work.

We also show the difference in these uncertainties when fitting line-outs of different durations: 5 (blue), 10 (red), and 20 (green) ns. The line-out duration does not affect the fit uncertainties. In general the calibration uncertainties decrease with longer line-outs because longer line-outs have less noise. This results in more certain determinations of the straight-line continua (dashed, blue lines in Figure 6.11) used to extract line transmission. Therefore, as a compromise between minimizing calibration uncertainties and maintaining temporal resolution of the changing conditions of our plasma, we choose 10 ns as our nominal line-out duration.

7.1.2 Exploring the Emission Correction

We show in Figure 6.9 that the emission subtraction is increasingly important in time for the transmission extraction. With Figures 7.9 and 7.10 we quantify this importance for the determination of n_{e} and n_2, respectively, by comparing these parameters inferred from fitting emission-corrected transmission (the normal case from corrected absorption $L_{\lambda}^{\mathrm{abs,cor}}$) versus transmission from measured absorption with no emission correction (subtraction). Neglecting the emission subtraction in the transmission extraction results in overestimating n_{e} and underestimating n_2 from spectral fitting for all theoretical line shapes. The overestimate in n_{e} is roughly a few percent for early in time; after ~ 70 ns when the relative levels of the measured emission become a significant fraction of the measured absorption (Figure

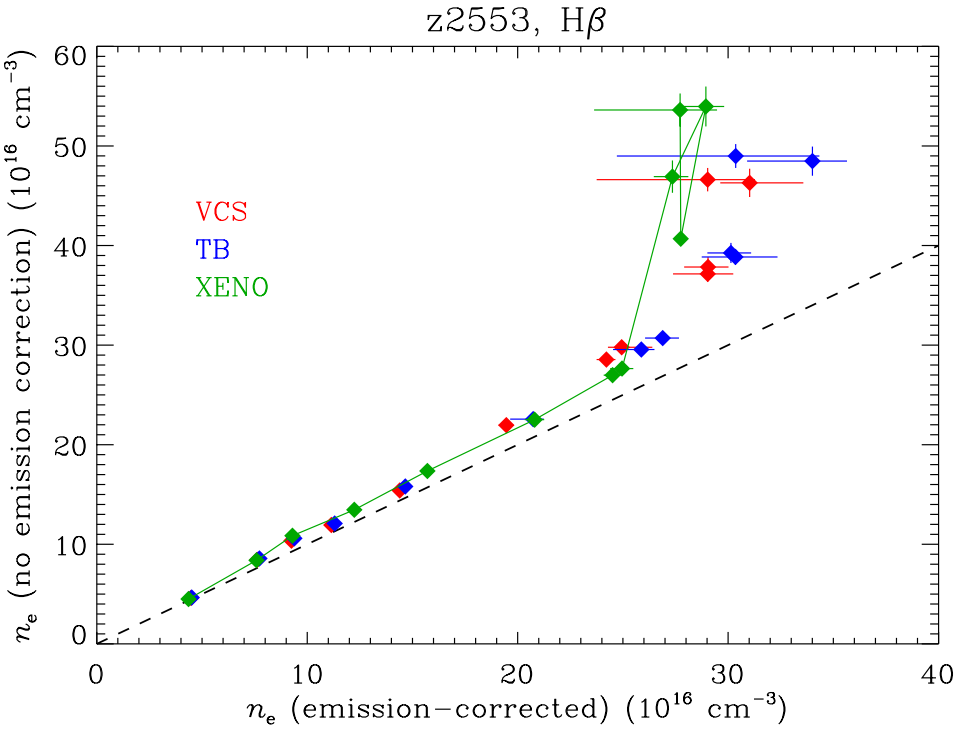

Figure 7.9 Inferred n_e from fits to transmission extracted from emission-corrected absorption versus that from fits to transmission extracted from absorption with no emission correction. The latter case overestimates n_e, especially for the highest values. We plot the unity line (dashed). Straight line segments connect the points chronologically for one fitting case, Xenomorph (green), where time begins in the bottom left of the plot window.

6.9), it increases to more than tens of percent.

To illustrate the time evolution we connect the data points (filled diamonds) with straight line segments. Since the inferred parameters follow the same qualitative trends for all line shapes (Figures 7.5 and 7.6), we connect the points only for the fits using Xenomorph (green) for clarity, where earlier in time corresponds to the lowest values in the bottom left of the plots. This evolution is nearly monotonic

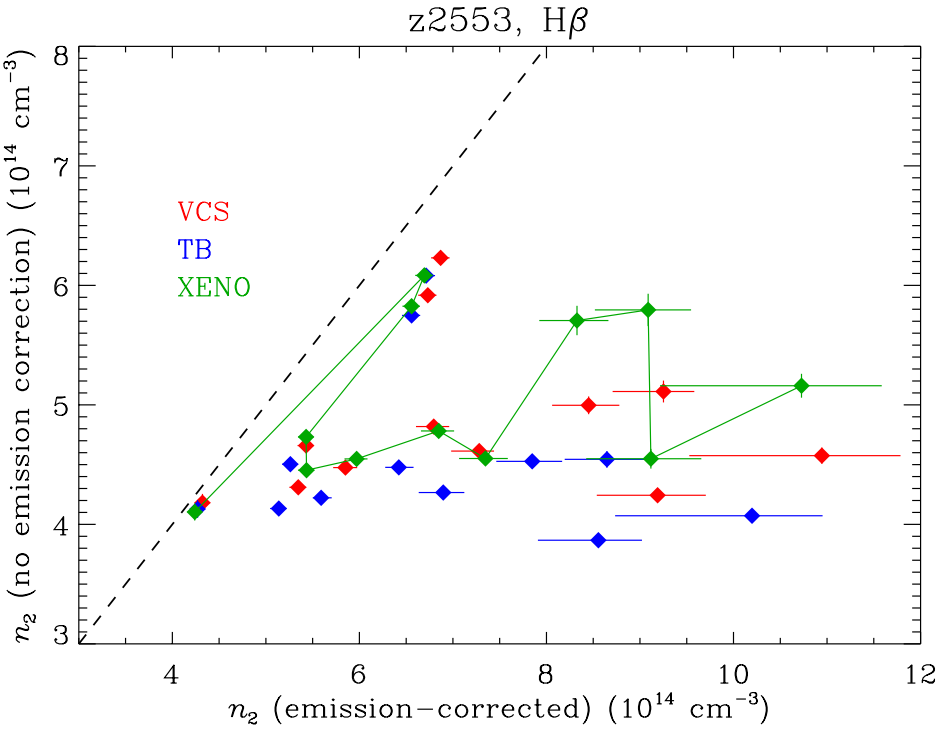

Figure 7.10 Inferred n_2 from fits to transmission extracted from emission-corrected absorption versus that from fits to transmission extracted from absorption with no emission correction. The latter case significantly underestimates n_2, especially for the highest values. We plot the unity line (dashed). Straight line segments connect the points chronologically for one fitting case, Xenomorph (green), where time begins in the bottom left of the plot window.

for $n_{\rm e}$. The spike early in time is apparent for n_2. Also for n_2 we see the increasing uncertainty in time for the emission-corrected case. The case with no emission correction does not show this because it is the uncertainty due to the emission subtraction that dominates the calibration uncertainty $\sigma^{\rm cal}$, which contributes most to the adopted uncertainty later in time.

7.1.3 The Hydrogen Balmer γ Line as a Plasma Diagnostic

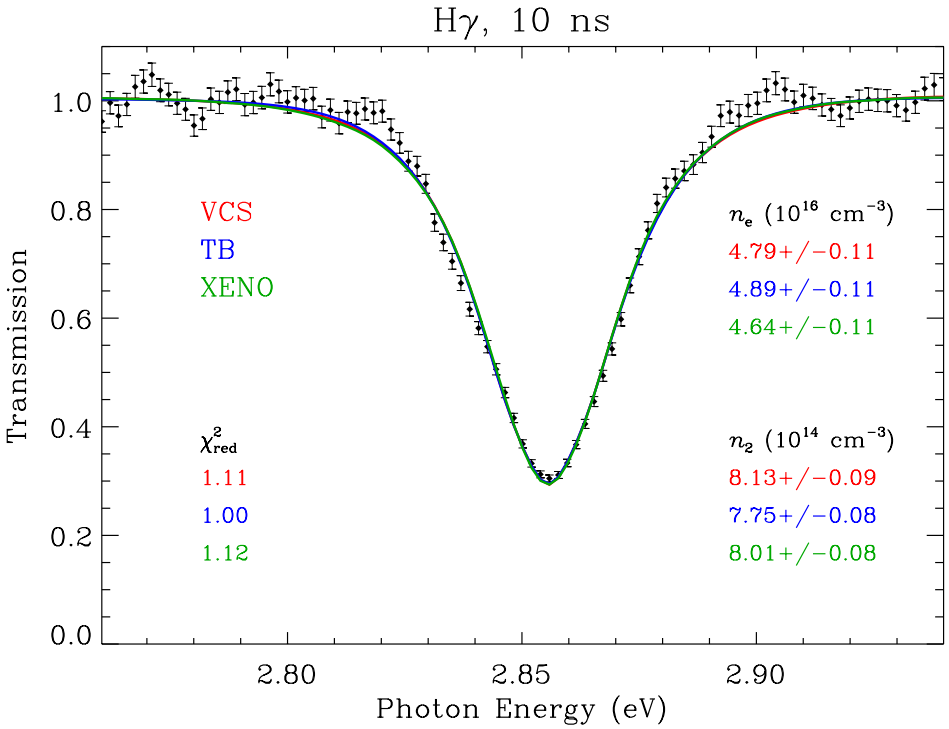

Figure 7.11 Measured Hγ transmission line-out (black diamonds) of our hydrogen plasma from 10–20 ns after the onset of x-rays from experiment z2553. The uncertainties (black, vertical lines) represent the S/N. We show fits using VCS (red), TB (blue), and Xenomorph (green) line profiles and print the corresponding $\chi^2_{\rm red}$, $n_{\rm e}$, and n_2 values.

Let us consider using the Hγ transmission line to diagnose our plasma by performing the same exercise as we do for Hβ. As an example, Figure 7.11 shows fits using VCS (red), TB (blue), and Xenomorph (green) line profiles of our measured Hγ line transmission from a 10-ns line-out beginning at 10 ns after the onset of x-rays from experiment z2553. No line shape stands out as providing the best or worst fit as indicated by the reduced χ^2. In fact, the goodness-of-fit for all line

shapes is quite similar. It starts out $\chi^2_{\rm red} \sim 1$ early in time when the line is deepest and most well-defined and even slightly decreases throughout the plasma evolution as the line shallows and broadens, thus worsening the S/N.

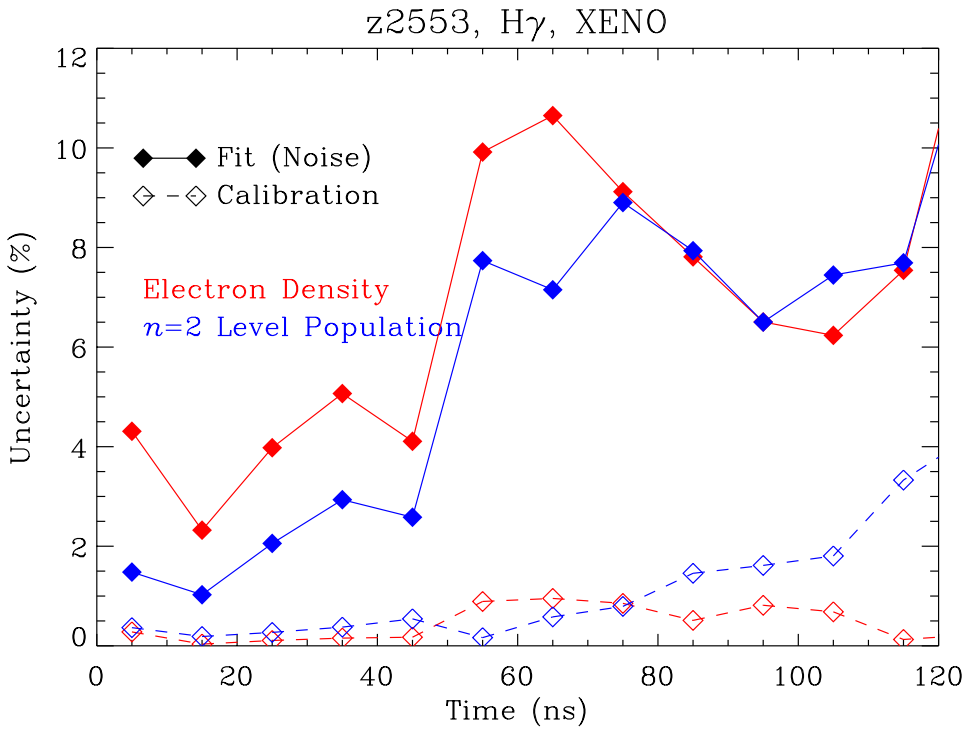

Figure 7.12 Uncertainties in $n_{\rm e}$ (red) and in n_2 (blue) due to the fit or noise (filled diamonds with solid lines) and the calibration (open diamonds with dashed lines) for Hγ transmission line fits throughout time from experiment z2553. Fit uncertainties dominate over calibration uncertainties and increase with time as the line broadens. Since the uncertainties are qualitatively similar between fits using different theoretical line shapes, we plot the results of the fits using only Xenomorph line profiles.

Figure 7.12 shows uncertainties that are qualitatively reversed from those corresponding to Hβ. Instead of the fit uncertainties $\sigma^{\rm fit}$ yielding to the calibration

uncertainties $\sigma^{\rm cal}$, they dominate. Instead of $\sigma^{\rm fit}$ remaining constant throughout time, they increase, and now it is $\sigma^{\rm cal}$ that stays relatively constant. Both of these properties are consistent with two main points: because Hγ is weaker than Hβ, its fits are (1) more sensitive to S/N, and (2) much less sensitive to the emission subtraction, which most significantly contributes to $\sigma^{\rm cal}$. The trends are similar for fits using different theoretical line shapes, so here we plot σ corresponding to only one, Xenomorph.

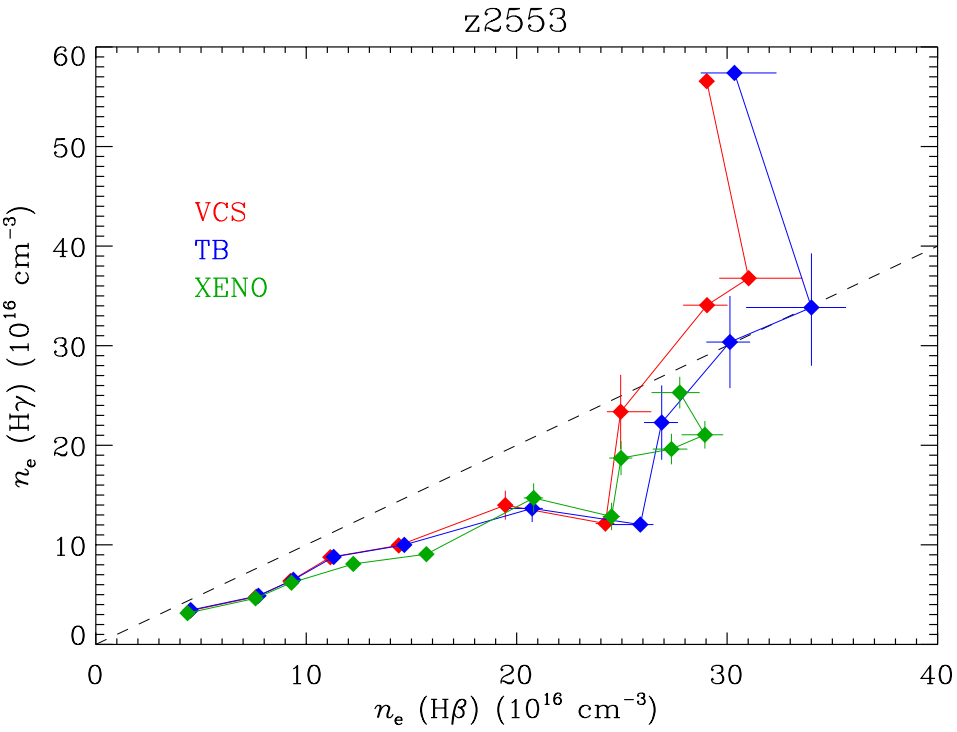

Figure 7.13 Inferred $n_{\rm e}$ from fits to Hβ line transmission versus that from fits to Hγ line transmission. Hγ fits underestimate $n_{\rm e}$ throughout most of the plasma evolution. We plot the unity line (dashed). Straight line segments connect the points chronologically, where time begins at the leftmost point. We include points up to the line-out beginning at 100 ns after the onset of x-rays.

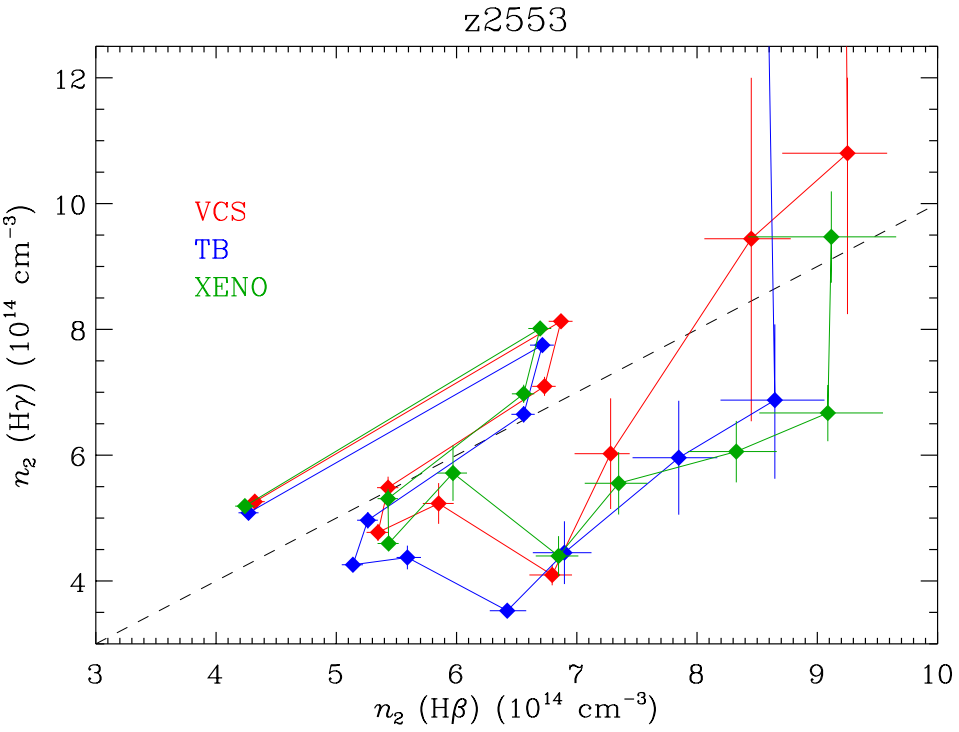

Figure 7.14 Inferred n_2 from fits to Hβ line transmission versus that from fits to Hγ line transmission. In general, Hγ fits underestimate n_2 early in time and overestimate later in time. We plot the unity line (dashed). Straight line segments connect the points chronologically for one fitting case, Xenomorph (green), where time begins at the leftmost point. We include points up to the line-out beginning at 100 ns after the onset of x-rays.

Hγ transmission line fits also infer different plasma conditions than Hβ. They underestimate n_e throughout most of the evolution then either match (using Xenomorph) or exceed (VCS and TB) late in time when the values are highest (Figure 7.13). The fits overestimate n_2 early in time, underestimate at intermediate times, and then overestimate again at the latest times (Figure 7.14). In other words, they exaggerate the temporal evolution inferred from the Hβ fits. Preliminary in-

vestigations into hypotheses for this discrepancy involving systematic uncertainties in the transmission extraction show low likelihood. These do not include the hypothesis that saturation or relatively high optical depths ($\tau > 1$ at line center) may be affecting our Hβ transmission line measurement. We encounter this discrepancy again in Section 7.2.

We chronologically connect the points with line segments. For clarity in Figure 7.14, we do this for only one case, Xenomorph (green). The leftmost point corresponds to the first 10-ns line-out beginning at the onset of x-rays. An important point that Figure 7.14 may not clearly illustrate is that the n_2 values inferred from Hγ follow the same qualitative trend as that from Hβ – the values spike early in time. This is evidence that this spike is real and not a consequence of, say, heavy saturation of the measured Hβ absorption line. Hγ is much weaker than Hβ and likely safely unsaturated with measured optical depths at the line center of $\tau \lesssim 1$.

We also investigate the sensitivity of the inferred parameters from Hγ transmission line fits to the emission subtraction. This subtraction modestly affects the line shape ($\Delta n_{\mathrm{e}} \lesssim$ few percent) because Hγ is not deep. Correspondingly the Hγ emission is not strong. The inferred n_2 remains unscathed *early in time* when the back-lighter emission is bright. Later in time ($\gtrsim 30$ ns), however, fits to Hγ transmission without emission correction significantly underestimate n_2; $\Delta n_2 \sim$ 10–60 %. Therefore, the emission subtraction can, in general, be neglected when inferring n_{e} from Hγ but not n_2.

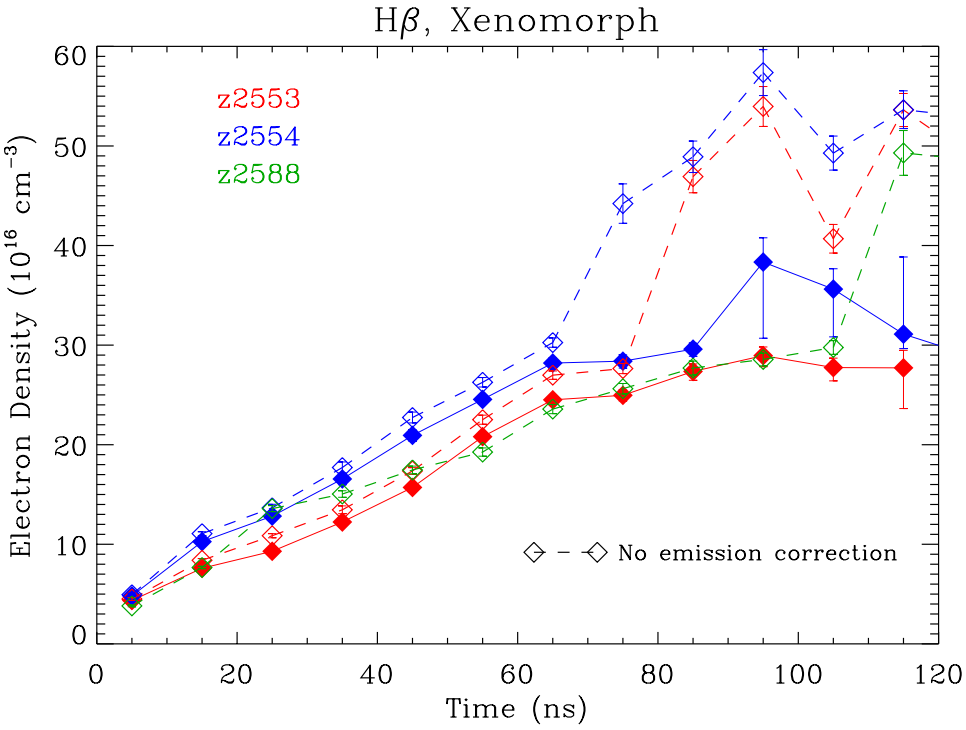

Figure 7.15 Electron density determined from fits to Hβ line transmission show qualitative reproducibility in their absolute values and time evolutions among experiments z2553 (red), z2554 (blue), and z2588 (green). These fits use Xenomorph line profiles. Filled diamonds connected by straight line segments correspond to line transmissions corrected for self-emission. Open diamonds connected by dashed line segments make no emission correction.

7.1.4 Reproducibility of Plasma Conditions

Figure 7.15 confirms the qualitative reproducibility of our hydrogen plasmas. Experiments z2553 (red), z2554 (blue), and z2588 (green) share similar initial conditions. The gas fill pressures are 10.63 ± 0.05, 9.49 ± 0.04, and 10.53 ± 0.05 Torr (Table A.1), respectively, and each observes the plasma at a distance of 10 mm from the gold wall that provides the photoionizing radiation. The peak electrical cur-

rents delivered to the wire arrays are 28.3, 28.6, and 26.9 MA, and the total radial LOS x-ray yields from the z-pinch dynamic hohlraums as measured by bolometers (Spielman et al. 1999) are 1.72, 1.51, and 1.49 MJ, respectively. This all translates to hydrogen plasmas whose electron densities rise from $n_{\rm e} \sim 4 \times 10^{16}\,{\rm cm}^{-3}$ to $n_{\rm e} \sim 30 \times 10^{16}\,{\rm cm}^{-3}$ in ~ 100 ns after the onset of z-pinch x-rays to the gas cell.

This figure includes our inferred $n_{\rm e}$ from fits to Hβ line transmission measured during experiment z2553 using Xenomorph line profiles (Figure 7.5). We assume the plasma emission from z2554 is the same as that from z2553 so that we may use it to perform the emission correction. We cannot easily make this correction for the absorption spectra from experiment z2588 because of a systematic uncertainty in the relative levels of the SVS1 and SVS2 data, so we neglect it in our transmission fits to determine $n_{\rm e}$ (open diamonds connected by dashed line segments). As we show in Figure 7.9 and see again here with the determinations from z2553 and z2554, this causes a slight overestimation of $n_{\rm e}$ until late in time when this overestimation becomes large.

7.2 Line Profile Comparison

Equipped with $n_{\rm e}$ and n_2 determined from our measured Hβ (and Hγ) for each line-out, we calculate the Hγ and Hδ (or just Hδ) transmission lines and plot them against our measurements.

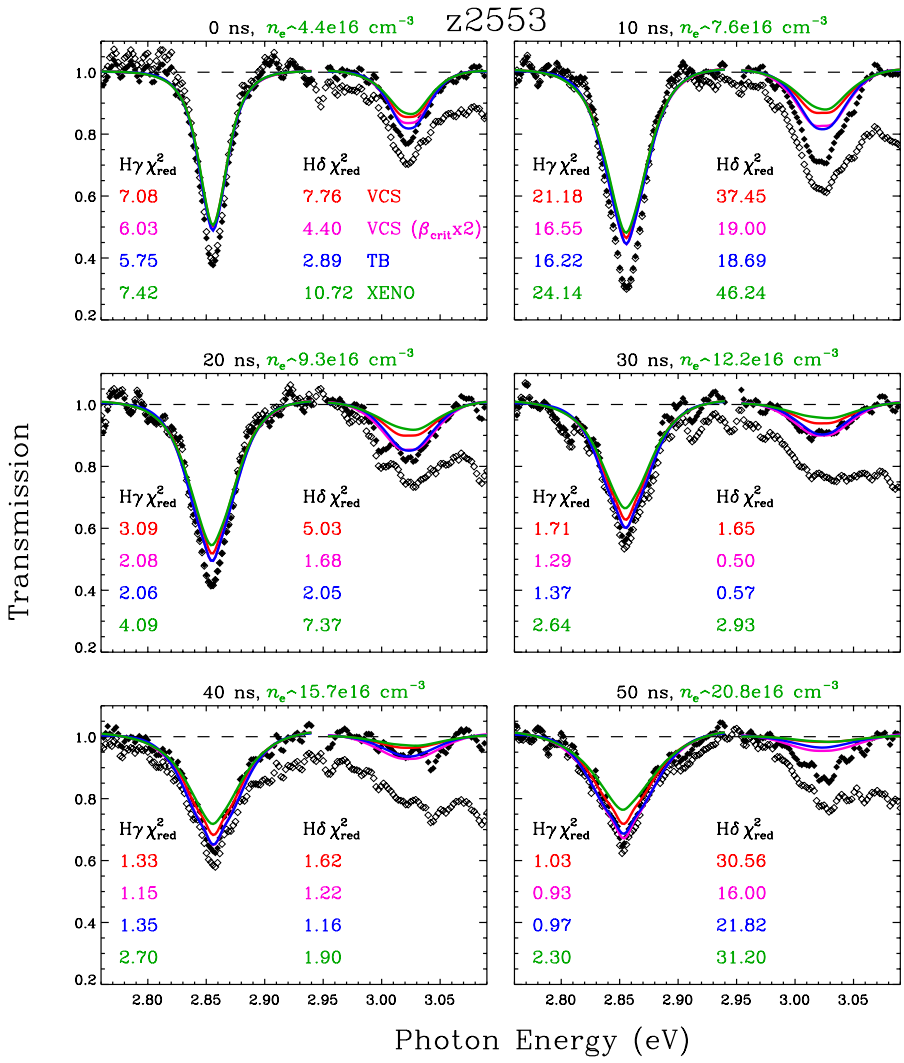

Figure 7.16 Measured Hγ and Hδ line transmission (filled diamonds) and absolute transmission (open diamonds) from the first six 10-ns line-outs from experiment z2553. We plot calculated transmission lines using n_e and n_2 inferred from Hβ transmission line fits using VCS (red), VCS with reduction factor w_u determined using an ad hoc β_{crit} value (pink), TB (blue), and Xenomorph (green) line profiles. We print the corresponding χ^2_{red} values for all line profile fits and n_e from the Xenomorph fit.

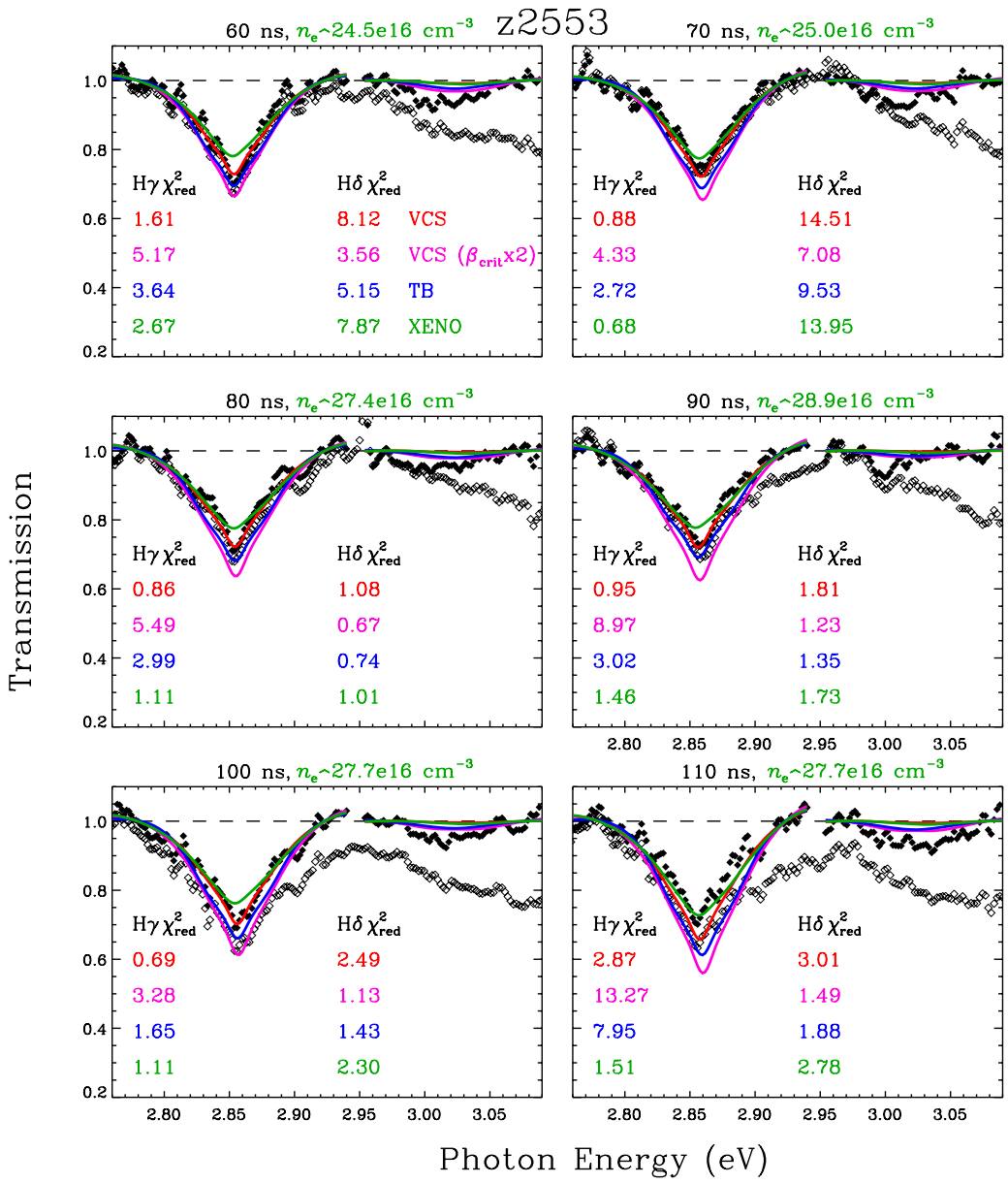

Figure 7.17 Same as Figure 7.16 but for the following six 10-ns line-outs through 110 ns after the onset of x-rays.

7.2.1 Using Conditions Inferred from Hβ

Figures 7.16 and 7.17 plot 10-ns line-outs of our measured line transmission (filled diamonds) and absolute transmission (open diamonds) from experiment z2553. Recall from Section 6.2.1 that we extract line transmission by drawing straight lines in the spectral vicinity of the absorption lines and absolute transmission by using our measured back-lighting continuum shape. At all times we see the combined influence of the Hϵ line (blueward of the plot window) and the bound-free continuum pulling Hδ away from the unattenuated continuum (dashed line at transmission $T = 1$), particular at its blue wing.

Using $n_{\rm e}$ and n_2 determined from fits to the Hβ transmission line (not plotted), we calculate line transmissions for Hγ and Hδ using the theoretical line profiles of VCS (red), TB (blue), and Xenomorph (green).

Our calculations use the reduction factors or occupation probabilities, $w_{\rm u}$, from Seaton (1990), who follow the formalism from Hummer & Mihalas (1988) to define this value as an integration over a probability distribution of electric microfields:

$$w_{\rm u} = \int_0^{\beta_{\rm crit}} P(\beta) d\beta. \tag{7.1}$$

The unitless parameter β describes the characteristic electric microfield that an atom experiences due to a charged particle. Since a plasma consists of many particles, the ensemble distribution is $P(\beta)$, and $\beta_{\rm crit}$ is the critical field beyond which electrons in an upper energy level, $n_{\rm u}$, are ionized. As discussed in Tremblay & Bergeron (2009), different expressions exist for $\beta_{\rm crit}$ (e.g., Hummer & Mihalas 1988;

Seaton 1990; Stehlé & Jacquemot 1993). For the most part, WD atmosphere models have either incorporated $w_{\rm u}$ from Hummer & Mihalas (1988), which uses $P(\beta)$ from Holtsmark (1919), or $w_{\rm u}$ from Seaton (1990), which uses $P(\beta)$ from (Hooper 1968). Before Tremblay & Bergeron (2009), however, $\beta_{\rm crit}$ was multiplied by an ad hoc factor of two because Bergeron (1993) finds that doing so results in an improved consistency between fits to different hydrogen Balmer lines in observed WD spectra as well as laboratory data. For this reason, we also include VCS profiles with the modified $w_{\rm u}$ using $\beta_{\rm crit} \times 2$ (pink) in the calculated line transmission comparisons with our measured transmission.

We first look at Hγ and clearly see, in the line shapes, the manifestation of the discrepancy from Figures 7.13 and 7.14. The calculated widths are larger than the measurement (i.e., $n_{\rm e}$ inferred from Hβ is greater than that from Hγ), and the calculated line depths or strengths are too small early in time and too large late in time.

For Hδ the calculations stratify into two groups. VCS and Xenomorph line shapes are very similar, and VCS with $\beta_{\rm crit} \times 2$ and TB are nearly identical. Consequently,the $\chi^2_{\rm red}$ values within each group are similar. It was the goal of Tremblay & Bergeron (2009) to develop profiles that fit the observations of multiple hydrogen Balmer lines consistently, as the VCS profiles with the ad hoc reduction factors do, but with a physical grounding. It is then expected that these calculations agree with each other.

However, all of the fits for both Hγ and Hδ are, in general, poor. The exceptions, for Hγ, are at 30, 40, and 50 ns when the inferred n_2 from Hβ agrees with

that from Hγ. Hδ shares these first two exceptions, but the 50-ns line-out apparently suffers from a noisy artifact.

For the 60-ns line-out and after, the VCS fits to Hγ have the lowest $\chi^2_{\rm red}$ with the Xenomorph fits close behind, though these fit poorly in the Hγ line center. The worst fits, which are consistently too deep, are the ones using VCS with $\beta_{\rm crit} \times 2$. Late in time after $\sim 80\,$ns, $\chi^2_{\rm red}$ for Hδ is low because this is when Hδ disappears. We discuss this disappearance in Section 7.3.2.

7.2.2 Using Conditions Inferred from Hγ

Let us perform the same exercise but use the plasma conditions, $n_{\rm e}$ and n_2, inferred from Hγ transmission line fits. Figures 7.18 and 7.19 plot 10-ns line-outs of our measured line transmission (filled diamonds) and absolute transmission (open diamonds) from experiment z2553 with these Hγ transmission line fits using VCS (red), VCS with the modified $w_{\rm u}$ using $\beta_{\rm crit} \times 2$ (pink), TB (blue), and Xenomorph (green). We plot the Hδ transmission lines calculated with these fit parameters.

All of the Hγ fits are good with $\chi^2_{\rm red} \sim 1$. The Hδ calculations agree better with the measured line transmissions than those using the plasma conditions inferred from Hβ fits. Unlike the Hβ transmission line fits, no theoretical line profile stands out as performing clearly better fits than the rest.

One shortfall of using plasma conditions inferred from Hγ rather than from Hβ to calculate transmission lines to compare is that these conditions have more scatter between theoretical line profiles. We see this for $n_{\rm e}$ in Figure 7.13. This means that the calculated lines at each time in Figures 7.18 and 7.19 span some

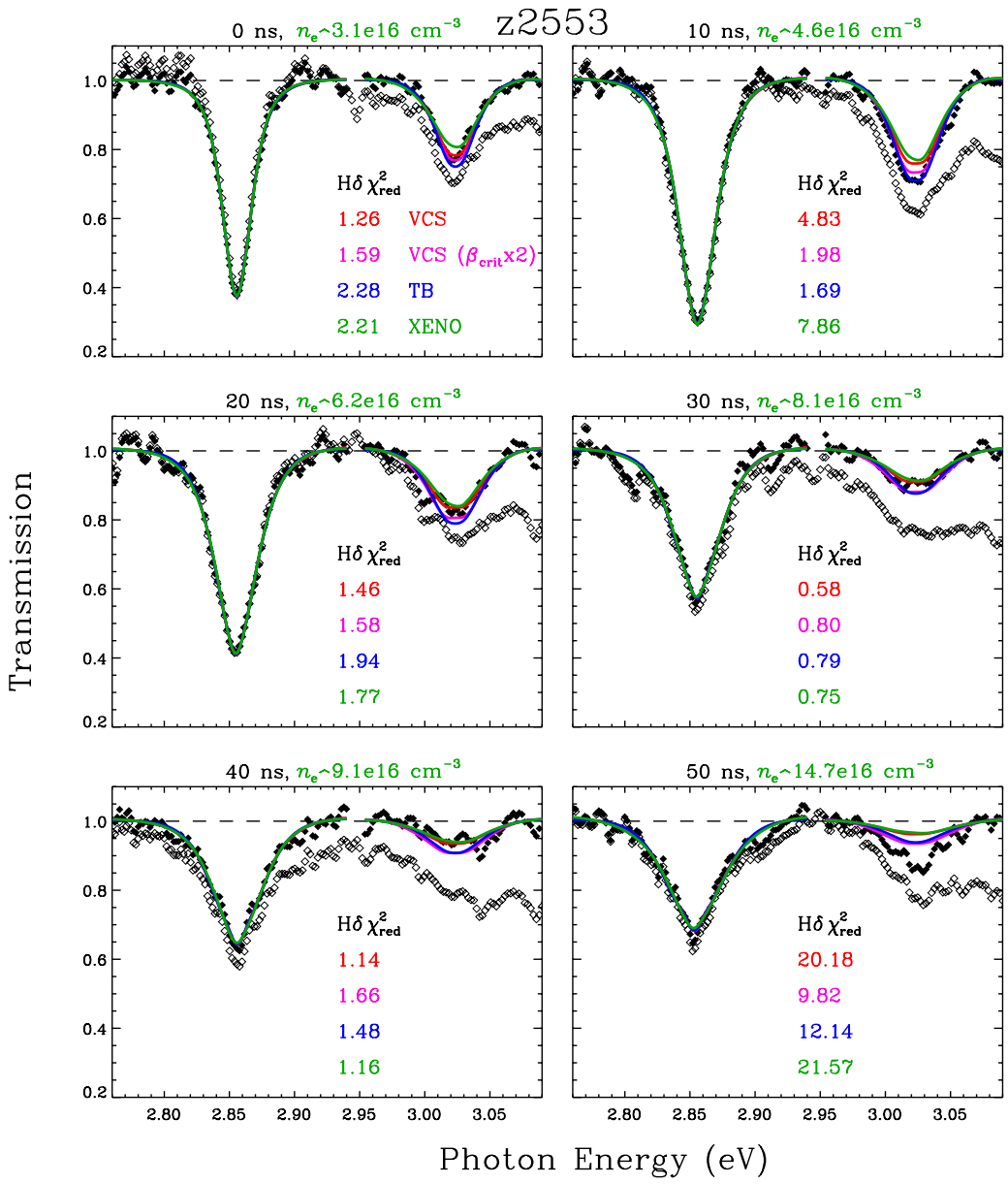

Figure 7.18 Same as Figure 7.16 except we plot the Hγ transmission line fit and Hδ calculated using n_e and n_2 inferred from the Hγ fit.

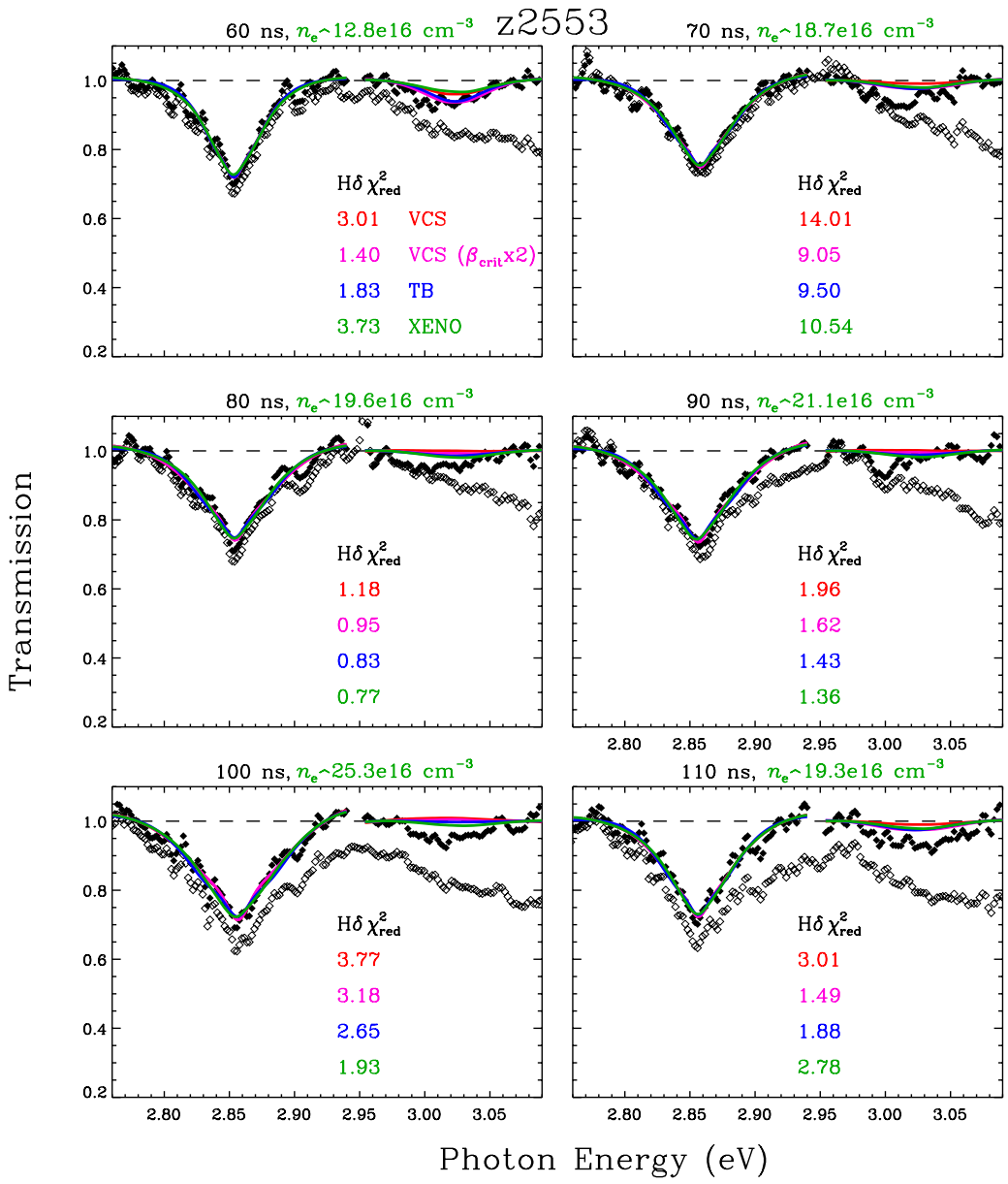

Figure 7.19 Same as Figure 7.18 but for the following six 10-ns line-outs through 110 ns after the onset of x-rays.

range of conditions.

7.3 Measuring the Reduction Factor or Occupation Probability

When submerged within an electric microfield the ionization energy of atoms in a plasma decreases. This effect, known as the *lowering of the ionization potential* or *ionization potential depression* (e.g., Ecker & Kröll 1963; Stewart & Pyatt 1966), can manifest as the probability that an atom exists in some state relative to that when the atom is surrounded by non-interacting particles, i.e., the *occupation probability* (Hummer & Mihalas 1988). Recent laboratory experiments measure the ionization potential depression in hot aluminum plasmas (e.g., Ciricosta et al. 2012; Hoarty et al. 2013; Preston et al. 2013) and may be reaching conflicting conclusions. The interpretation of their results are in question (Iglesias 2014).

Our experiments provide a unique perspective on this problem by measuring multiple absorption lines that share the same lower level population n_1. Figure 7.20 plots our measured reduction factor for Hγ, w_5, (filled diamonds) as a function of electron density, $n_{\rm e}$. We infer w_5 by fitting the Hγ transmission line while fixing $n_{\rm e}$ and n_2 to those inferred from Hβ. Straight line segments chronologically connect the fit results, where time begins with the leftmost point. We also plot the theoretical $w_5(n_{\rm e})$ from Seaton (1990, dotted curve), which is used in WD atmosphere models.

Though we measure a trend with $n_{\rm e}$, notice that at low $n_{\rm e}$ (early in time), the inferred w_5 values are unphysical; a probability cannot exceed one (solid, horizontal line). In Sections 7.1.3 and 7.2 we discuss the discrepancy between our plasma conditions inferred from Hβ versus those from Hγ. Because of this discrep-

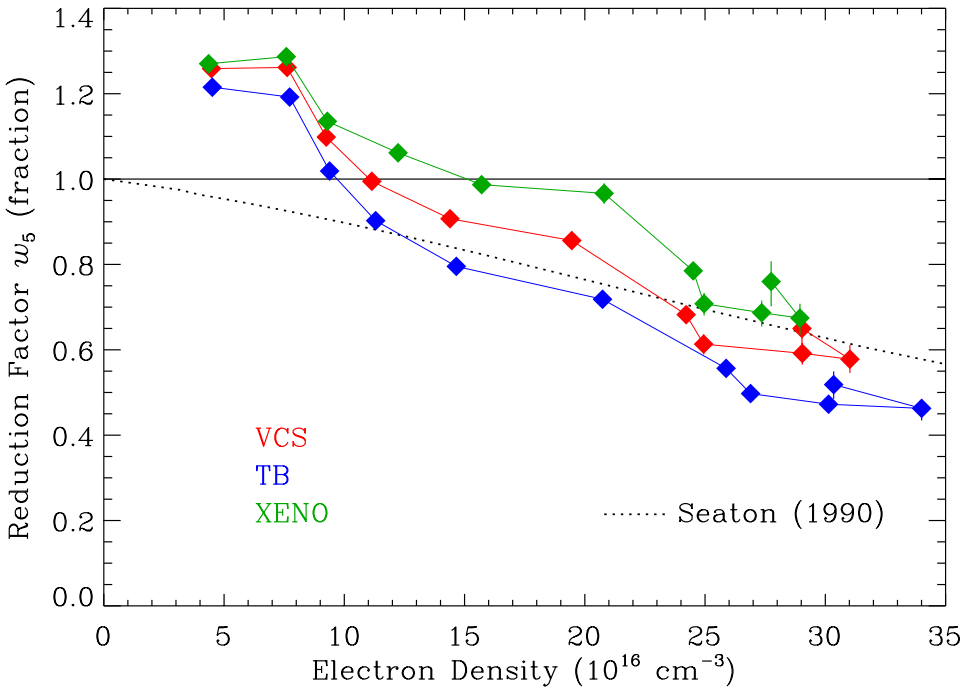

Figure 7.20 Inferred reduction factor w_5 versus electron density from fits to Hγ line transmission. Fits using different theoretical line profiles (colored diamonds) are chronologically connected with line segments; they differ because of the slightly different input n_2 values. We also plot the theoretical $w_5(n_e)$ from Seaton (1990, dotted curve). The inferred parameters early in time are unphysical because they exceed one (solid, horizontal line).

ancy, forcing theoretical line shapes onto Hγ prevents the fits from capturing the measured total integrated transmission because it does not allow the fits to subtly adjust their shape to match the precise measured shapes. These potential adjustments are within the noise of the spectra, so without them the fits are still sufficient ($\chi^2_{\rm red} \lesssim 2$). Also, the differences in input n_2 values, though only $\sim$ few % (Section 7.1, Figure 7.8), are readily apparent in the inferred w_5.

7.3.1 A Revised Approach

These points prompt us to revise our strategy to measure w_5. Let us remove our dependency on the line shape to focus on the total integrated line strengths. Neglecting the instrumental convolution, ψ, we recover the argument of the exponential in Equation 6.4 by taking the natural logarithm of our measured line transmission, i.e., $-\kappa_\lambda^{\rm line} R \approx \ln(T_\lambda^{\rm line})$. It then follows from Equation 6.5 that

$$\frac{\kappa_\lambda^{\rm H\gamma}}{\kappa_\lambda^{\rm H\beta}} = \frac{f_{2\rightarrow5} w_5(n_{\rm e}) \phi_\lambda^{\rm H\gamma}}{f_{2\rightarrow4} w_4(n_{\rm e}) \phi_\lambda^{\rm H\beta}}. \tag{7.2}$$

Since ϕ is area-normalized, $|\phi_\lambda^{\rm H\beta}| = |\phi_\lambda^{\rm H\gamma}|$, and these factors cancel. The reduction factor for Hβ is approximately equal to unity, so

$$w_5(n_{\rm e}) \approx \frac{w_5(n_{\rm e})}{w_4(n_{\rm e})} = \frac{\kappa_\lambda^{\rm H\gamma} f_{2\rightarrow4}}{\kappa_\lambda^{\rm H\beta} f_{2\rightarrow5}}. \tag{7.3}$$

We plot our w_5 values measured following this method in Figure 7.21. The unphysical values early in time retreat to ≤ 1, and the differences between colored curves due to inferred n_2 values vanish. Now the only differences between these curves are the horizontal translations because of slight differences in the inferred $n_{\rm e}$ between fits using VCS (red), TB (blue), and Xenomorph (green) theoretical line profiles.

Our measurements decrease more steeply with $n_{\rm e}$ than predicted by reduction factors from Seaton (1990, dotted curve). Further work is ongoing to scrutinize the validity and robustness of this approach and to quantify uncertainties, particularly those due to emission subtraction.

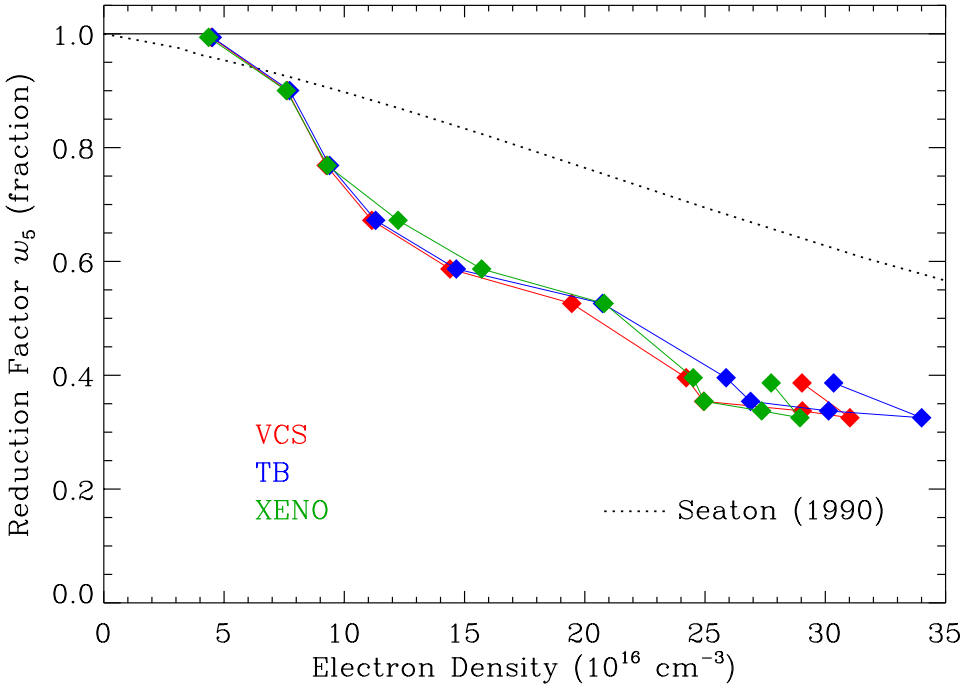

Figure 7.21 Inferred reduction factor w_5 versus electron density following Equation 7.3, which uses measured opacities, κ_λ, of Hβ and Hγ. Shortfalls apparent in Figure 7.20 – the unphysical values early in time and the dependency on ϕ – disappear. We measure a steeper dependence on n_e than predicted by any theory.

7.3.2 Witnessing the Disappearance of Hδ

Because of the weakness of the Hδ transmission line and the encroaching bound-free continuum, it is not as straightforward to measure the corresponding reduction factor w_6. The development of this strategy is still in progress.

However, because our time-resolved absorption/transmission measurements observe a plasma whose n_e increases in time, we see the evolution of Hδ. Early in time Hδ is distinct (Figure 7.16), but late in time it merges into its blueward

Table 7.1. Measured Electron Density of Plasma When Hδ Disappears

Line Profile	n_e (10^{16} cm^{-3})			
	z2553		z2554	
	Hβ	Hγ	Hβ	Hγ
VCS	29	34	30	31
TB	30	30	33	23
XENO	27	20	28	21

neighbor Hϵ and the bound-free continuum (Figure 7.17). For experiment z2553, we observe this event at ~ 80 ns after the onset of x-rays. Using Xenomorph line profiles in the Hβ transmission line fit, our inferred electron density at this time is $n_e \sim 27 \times 10^{16}$ cm^{-3}. Inferred from Hγ, $n_e \sim 20 \times 10^{16}$ cm^{-3}.

We confirm this measurement by locating this event in the following experiment, z2554. The spectra from z2554 are not entirely independent since we use the measured emission from z2553 to correct the absorption. We see Hδ disappear at ~ 70 ns. From transmission line fits using Xenomorph profiles to Hβ and Hγ, at this time we infer $n_e \sim 28 \times 10^{16}$ and $\sim 21 \times 10^{16}$ cm^{-3}, respectively.

Since fits using different theoretical line profiles infer slightly different values, we list n_e from each in Table 7.1. This includes n_e inferred from Hγ, which has increased scatter compared to Hβ (Section 7.2.2), especially late in time.

This determination is unique for multiple reasons. (1) The measurement is in absorption for lines that share the same lower level population n_1. This simplifies

the interpretation of measured relative line strengths. An emission measurement requires knowledge of multiple upper level populations, $n_{\rm u}$, which must be assumed along with local thermodynamic equilibrium (an additional requirement of the experimental plasma) or simulated with hydrodynamic calculations. (2) No other experiment has simultaneously measured multiple spectral lines of a hydrogen plasma at $n_{\rm e} > 10^{17}$ cm^{-3}. This allows us to measure existing lines (Hβ and Hγ) and non-existing lines (Hδ) at the same time. (3) Because our data are time-resolved and we probe a range of $n_{\rm e}$, we observe the continuous change that leads to the disappearance of Hδ. This allows for a precise measurement of the conditions at which this event occurs.

7.4 Summary

The spectra of radiation-driven hydrogen plasmas we measure using our experimental platform provide many insights. Some of these supplement previous work, and some are quite new. Here we summarize our conclusions but first describe the main assumptions we make in the analysis of our measurements. Listing out these assumptions also stimulates ideas for future work.

7.4.1 Assumptions

We assume:

- That our observed plasma is homogeneous in composition (purely H), electron density, $n_{\rm e}$, and lower level population, $n_{\rm l}$, along our LOS. This is specif-

ically relevant to our spectral fitting procedures (Section 6.2.1). Gradients in the plasma conditions exist. Our plasma is finite and has boundaries, so our observing lines of sight traverse a transition from a relatively cool plasma/gas that resides in the buffer cavity to the hydrogen plasma in the central cavity exposed to the gold wall radiation. Our LOS collection beams, which are parallel to the gold wall (and perpendicular to the gold wall radiation), also have a finite diameter (Section 5.3.3.1), and we measure n_{e} decreasing with increasing distance from the gold wall (Section 3.4.1). When we observe our plasma in absorption, the LOS additionally traverses a transition region adjacent to the gold back-lighting surface. Our assumption is that these gradients have minimal effects on our observations and that the goodness of our Hβ transmission line fits, particularly when using Xenomorph line profiles (Section 7.4), indicates that this is so.

- That the electron temperature of our plasma, which we measure indirectly, is consistent with $T_{\mathrm{e}} \sim 1\,\mathrm{eV}$, as predicted by simulations (Sections 3.2.2 and 6.1.2), so that it does not significantly affect the inference of our plasma conditions, n_{e} and n_2, as we investigate in Section 6.3.1.

- That during the formation of our hydrogen plasma and throughout the duration of the experiment, the radiation from the gold wall ($2\,\mathrm{eV} \lesssim T_{\mathrm{rad}} \lesssim 5\,\mathrm{eV}$; Section 6.1.1) is sufficient to completely dissociate the initial gas fill particles of H_2, leaving only neutral hydrogen, protons, and electrons. We assume there are no additional sources of line broadening beyond these particles, such as from molecules, influencing our measured line profiles.

- That we extract transmission spectra that give accurate relative line shapes and strengths within our quoted uncertainties. This includes successful calibrations to correct for the instrumental efficiency (Section 5.3.1), the attenuation of light during the transit from the experiment to the SVS system (Section 5.3.2), and the observed geometry within the gas cell (Section 5.3.3). It then includes the combination of data from multiple SVS systems, particularly correcting the measured absorption by subtracting the measured emission (Section 6.2). We assume scattered light within the gas cell to be negligible.

- That our strategy to extract and analyze line transmission (Section 6.2.1) rather than absolute transmission successfully circumvents the bound-free continuum (e.g., Däppen et al. 1987) and H^- ion (e.g., Griem 1997) opacity sources, allowing us to, like the previous bullet point, accurately measure relative line shapes and strengths.

7.4.2 Conclusions

- Ours is the first experiment to measure the spectra of multiple hydrogen Balmer lines (Hβ, Hγ, and Hδ) *simultaneously* at $n_\mathrm{e} > 10^{17}\,\mathrm{cm}^{-3}$ – greater than that achieved by Wiese et al. (1972, 1975). We measure the spectral lines at a range of electron densities, $4 \times 10^{16} \lesssim n_\mathrm{e} \lesssim 3 \times 10^{17}\,\mathrm{cm}^{-3}$. The only other experiments to spectroscopically measure hydrogen in the range of $10^{17}\,\mathrm{cm}^{-3} < n_\mathrm{e} < 10^{18}\,\mathrm{cm}^{-3}$ are those of Djurović et al. (2005), Katagiri et al. (2007), Parigger et al. (2003, 2008), and Djurović et al. (2009). Only

two of these, however, measure more than one line – this line being Hβ. Katagiri et al. (2007) also measure Hγ but do not achieve sufficient S/N to analyze it, and though Parigger et al. (2008) measure Hα, Hβ, and Hγ, they do not do so simultaneously. Therefore, we provide unique line profile measurements relevant to a regime of hydrogen plasma conditions with limited exploration.

- Within one experiment, our plasma matches the conditions achieved by the benchmark stabilized-arc discharge experiment of Wiese et al. (1972) and then, for the data we show in this work, exceeds it by a factor of three. This is because we measure the evolution of our plasma with time-resolved spectroscopy, and the electron density of our plasma smoothly increases throughout the first ~ 100 ns of our experiment (Figure 7.5), resulting in a continuous measurement throughout the range of $n_{\rm e}$ mentioned in the previous bullet point.

- We obtain data, not analyzed for the scope of this work, for which we infer electron densities approaching $n_{\rm e} \sim 10^{18}$ cm^{-3}.

- We demonstrate the robustness and reproducibility of our experimental platform by inferring similar conditions and temporal evolutions of our plasmas among multiple experiments (Figure 7.1.4).

- We show that both the theoretical line profiles currently used in WD atmosphere models, those of Tremblay & Bergeron (2009) and those previously used from Lemke (1997), which follow the theory of Vidal et al. (1973), do not fit our measured Hβ transmission line as well (larger reduced χ^2) as the

theoretical line profiles of Gomez et al. (2014b) for a range of $n_{\rm e}$ relevant to WD atmospheres. Despite this, all diagnose the line shape ($n_{\rm e}$) and strength (n_2) similarly.

- Xenomorph line profiles (Gomez et al. 2014b) fit our measured Hβ transmission line best with the lowest reduced χ^2 for a range of $n_{\rm e}$ because these calculations better capture the observed asymmetry throughout the entire line profile.

- Among those calculated from Vidal et al. (1973), Tremblay & Bergeron (2009), and Gomez et al. (2014b), no theoretical line profile fits our measurement Hγ transmission lines best. They all fit well with reduced $\chi^2 \sim 1$ throughout our range of $n_{\rm e}$.

- The conditions ($n_{\rm e}$ and n_2) we infer from fits to the measured Hβ line transmission from our experimental plasma do not agree with those inferred from fits to the Hγ line transmission (Section 7.1.3). Hγ fits infer lower $n_{\rm e}$ and exaggerate the temporal evolution of n_2. Our preliminary investigations find no clear hypothesis involving a systematic uncertainty in the transmission extraction to explain this discrepancy. However, saturation may be compromising our Hβ line transmission measurement. If it is not, then it is possible that, for all the theoretical line profiles we investigate here, the relative line shapes between Hβ and Hγ are inaccurate.

- We compare calculated Hγ and Hδ transmission lines, using the plasma conditions inferred from fits to our Hβ transmission lines, to our measured trans-

mission spectra to find, in general, poor agreement for all theoretical line profiles. No theoretical line profile consistently agrees best to the data throughout our entire range of $n_{\rm e}$. At $n_{\rm e} \gtrsim 10^{17}\,{\rm cm}^{-3}$, however, fits to H$\gamma$ using VCS profiles appear to fit best with the lowest $\chi^2_{\rm red}$. Assuming our measured relative line shapes and strengths of Hβ and Hγ are accurate and that our line shape comparison strategy is sound, this is consistent with none of the theoretical line profiles we investigate sufficiently calculating Hγ and Hδ.

- We compare calculated Hδ transmission lines, using the conditions inferred from fitting Hγ, to find relatively good agreement for all theoretical line profiles. This is evidence that the relative calculations of Hγ and Hδ are accurate for all the theoretical line profiles we investigate in this work throughout our range of $n_{\rm e}$. This may also suggest that our Hβ transmission line measurement is systematically erroneous.

- We make the first measurements of $w_5(n_{\rm e})$, the reduction factor or occupation probability associated with Hγ, using spectroscopic absorption data. Since we measure spectral lines from the Balmer series in absorption, each shares the same lower level ($n = 2$) population, which constrains the relative line strengths and allows us to measure the reduction factor, $w_{\rm u}$, of a line as a function of electron density, $n_{\rm e}$.

- We are the first to observe and temporally resolve the disappearance of the Hδ absorption line into Hϵ and the bound-free continuum. Observing this in absorption better constrains the measurement than observing in emission

because a single level population describes the relative line strengths rather than multiple. We find the event to occur in the hydrogen plasmas of two different experiments at $n_{\rm e} \sim 20 \times 10^{16}$ to $30 \times 10^{16}\,{\rm cm}^{-3}$.

7.4.3 Astrophysical Implications

Here we describe a potential implication of our results that reverberates throughout WD astrophysics – a higher mean mass for WDs. This affects numerous studies (Section 1.2), including a significant (up to $\sim 1\,{\rm Gyr}$) decrease in the age of the Galactic disk as determined from WD cosmochronology.

The plasma conditions we infer from fits to our measured Hβ and Hγ transmission lines do not agree. Without an independent plasma diagnostic, we cannot definitively say which set of inferred conditions are truly accurate, if either. Even with another diagnostic, such as optical Thomson scattering (e.g., Gawron et al. 1988; Harvey-Thompson et al. 2012a,b), it is not clear that we can infer conditions to the precision necessary to discriminate between the Hβ and Hγ transmission line fit determinations, since this line-fitting method is so precise ($\sigma_{\rm adopt} \lesssim$ few or several percent; Figures 7.7, 7.8, and 7.12).

Let us suppose that one of these determinations (from Hβ or Hγ) is more accurate than the other. We have motivations to choose either. Theoretically, Hβ is a lower energy transition, so it should be simpler to calculate than Hγ. Experimentally, Hβ has larger optical depth. This results in a higher S/N measurement than Hγ. It also leaves open the possibility of saturation or large optical depth issues systematically affecting our measurement. We continue to scrutinize our experiment

to understand potential measurement uncertainties.

Let us assume that our Hβ measurement is more accurate and therefore so are the inferred plasma conditions. This is interesting in the context of the spectroscopic method used in WD astrophysics because of a long-standing problem in inferring different atmospheric parameters (i.e., $T_{\rm eff}$ and $\log g$) from different hydrogen Balmer lines (e.g., Bergeron et al. 1992). As we discuss in Section 7.2.1, an ad hoc modification ($\beta_{\rm crit} \times 2$) to the reduction factors or occupation probabilities, $w_{\rm u}$, introduced by Bergeron (1993) improves the consistency of conditions inferred from different Balmer lines when using VCS line profiles. Tremblay & Bergeron (2009) further improve the consistency with their approach to calculating H line profiles and without using the ad hoc $w_{\rm u}$ values.

However, all three methods – VCS with $w_{\rm u}$ from Seaton (1990), VCS with $w_{\rm u}$ modified by using $\beta_{\rm crit} \times 2$, and TB with $w_{\rm u}$ from Seaton (1990) – infer systematically lower surface gravities, $\log g$, from lines with increasing principal quantum number, n.

Fitting the Hβ absorption line observed in WD spectra infers the highest $\log g$ and hence highest mass. If the Hβ determination is indeed most accurate, this results in a higher spectroscopic mean mass, which improves the agreement with the mean mass determined using the gravitational redshift method (Chapter 2; Falcon et al. 2010b).

7.5 The Next Generations

We design our experimental platform to measure time-resolved spectra of relatively large photoionized plasmas from multiple lines of sight simultaneously. Future investigations may extend beyond WD astrophysics, beyond plasma physics, and beyond atomic processes. Here we list some future directions.

7.5.1 Testing Complete Redistribution

A widely used assumption or approximation in the theory of radiative transfer is *complete redistribution in frequency* (e.g., Mihalas 1978), whose key consequence, for our interest, is that the emission and absorption profiles of spectral lines are identical. In theory, this assumption is valid at large optical depth (Holstein 1947). Other theoretical cases exist where this assumption fails (e.g., van Trigt 1976). To our knowledge, the validity of *complete redistribution* has never been investigated in the laboratory with line profile measurements. Therefore, the simultaneous measurements of our plasma in emission and absorption provide the first opportunity to do so.

7.5.2 Plasmas Not in Local Thermodynamic Equilibrium

The simultaneous collection of emission and absorption data also allow the measurement of the populations of both the upper and lower energy levels of electronic transitions, respectively. For plasma diagnosis or analysis, this means shedding any dependence on assumptions of relative level populations, such as local thermodynamic equilibrium. It also means not relying on hydrodynamic simula-

tions to determine these populations. Therefore, the simultaneous measurements offer a unique probe of plasmas not in local thermodynamic equilibrium. Since we are the first to spectroscopically measure hydrogen plasmas in absorption at these conditions, simultaneous measurements have never before been exploited in this way.

7.5.3 Other Plasma Compositions

Using a gas cell provides versatility to our experimental platform because it readily accepts fills of many compositions with minimal or zero modifications to our hardware design or fielding procedures. As mentioned in Section 1.1.2, hydrogen dominates the photospheric composition of most WDs, and we classify these as spectral type DA. Beginning our experiments with hydrogen is the logical choice. We are now poised to explore astrophysical problems with WD photospheres composed of other elements.

7.5.3.1 Helium

Helium-dominated (DB) WDs are the next most abundant spectral type (e.g., Koester et al. 1981; Voss et al. 2007; Bergeron et al. 2011). One potential area of exploration is the pressure shifts of helium lines, whose laboratory measurements (e.g., Kobilarov et al. 1989; Heading et al. 1992; Pérez et al. 2003; Omar et al. 2006) need further scrutiny and an extended $n_{\rm e}$ range to validate the precise theoretical calculations (e.g., Dimitrijevic & Sahal-Brechot 1990) critical for observational investigations (e.g., Falcon et al. 2012).

We confirm the feasibility of measuring neutral helium emission lines using our platform in experiments z2153–5.

7.5.3.2 Hydrogen/Helium

The neutral or van der Waals broadening of hydrogen lines by helium is critical to model the atmospheres of cool WDs with mixed compositions (e.g. Bergeron et al. 1991; Koester et al. 2005). Since ours are some of the few experiments to measure any hydrogen line profiles at $n_{\rm e} > 10^{17}\,{\rm cm}^{-3}$ and the only ones to do so for multiple lines simultaneously, we suspect we will be the first to probe hydrogen/helium plasmas at these conditions to measure the aforementioned broadening mechanisms.

7.5.3.3 Carbon/Oxygen

WDs with photospheres dominated by neutral and singly ionized carbon and oxygen (hot DQ) are still a relatively new class (Dufour et al. 2007). Initial spectroscopic fits to their observed spectra were quite poor (Dufour et al. 2008), stimulating new line profile calculations (Dufour et al. 2011) that are ripe for laboratory support.

In experiment z2590 we achieve plasma formation using a carbon dioxide gas fill. Due to a low x-ray yield from that particular pulsed power shot experiment, we require more experiments to assess the feasibility of experimentally measuring relevant carbon/oxygen spectral lines and to confirm the accessible range of plasma conditions.

7.6 Closing Remarks

At the end of this dissertation I remind you that this project is just beginning. Laboratory astrophysics performed this way – by engaging astronomers in experimental physics – is just beginning. It is the assimilation amongst different scientific fields that unites resources (telescopic and laboratory observation), generates perspective (from the astrophysics and high energy density communities), and inspires countless minds (students, researchers, and the public).

We demonstrate a complete cycle. We work with astronomical observations to highlight a clear astrophysical problem concerning white dwarf photospheres. To address that problem, we design an experimental platform that creates and measures macroscopic ($24\,\mathrm{cm}^3$) quantities of white dwarf photospheres. We build this platform up from scratch, developing and maturing it. We perform, analyze, and interpret unique laboratory measurements.

With all that we discover through and because of the process, we never stop asking questions.

"Why couldn't I have learned this even a week ago? It would have saved me so much trouble. And computation time."

Ever-wise Taisuke consoles me. "You'll be saying that for the rest of your life."

Clicks of chopsticks provide accompaniment as the waiter refills my water, refills Thomas' water, bypasses Guillaume's full glass, refills Taisuke's green tea. We each deliver a 'thank you' without disturbing our conversation. Deeply involved as always. And spilling over from the morning's discussions at work. As always.

Random versus systematic uncertainties. Free parameters versus fixed parameters. Unreduced chi squared versus reduced chi squared. The world of spectral fitting routines is just so incredibly sexy, I can't believe it doesn't boast more magazines covers. Rolling Stone, I'm looking at you.

I fumble the unagi with my chopsticks. My hand retreats. And the four of us observe the carefully-crafted nigiri, now overturned like a supine tortoise, undo its strip of seaweed to release its clump of cradled rice. Slowly. Making sure I witness the excruciating consequence of lacking skill with chopsticks.

I'm getting better. Not yet adept. But Taisuke's taught me a lot. About Japanese culture, customs, cuisine. Just as Guillaume's taught us about French culture, customs, cuisine. Just as I've provided explanation for a lot of the weird things we do here in the States.

"It's like I not only have to *do* something myself to understand some technical concept, but I have to *hurt* myself while doing it for it to really sink in."

"Hindsight…" Guillaume doesn't need to finish the saying, as common in France as it is here.

A waitress delivers our miso soup. *With* the meal. As Taisuke explains to us is the custom. We're used to having soup *before* the meal. Here. But in Japan miso

soup is treated differently. It's like French fries (I know Guillaume's right there. Just a coincidence.)

"You don't eat your fries *before* the meal. You eat them *with* the meal."

The waitress smiles, nods. Her accent is deliciously charming. "Yes. Yes. You learn lot from other cultures. We learn lot, too. Good to mix."

Something zaps me. Inside. Mental. Psychological. Whatever. Not corporeal.

Draws my attention to the elegant tableau positioned in my periphery. Our group. Astronomers and experimental physicists. Observers and theorists. Those at this restaurant and those not. A representation having intimated quietly, patiently for some months, years, now deciding to yell out its existence to me. Making sure I see how it all fits together. Where it's going. It. Our expertise. Our backgrounds. Our strengths. Our weaknesses.

Everyone's eyebrows raise. Casting inquisitive stares. Looking at me as if my eyes have gone whichever direction is opposite of cross-eyed.

"Yes…cultures…or scientific disciplines…"

Appendices

Appendix A

Measuring the Gas Fill Pressure

Laboratory experiments investigating plasmas generated inside gas cells often depend upon the precise determination of the particle or atom volume density, which follows from measurement of the gas fill pressure. In particular, those studying photoionized plasmas, such as ours, rely on knowing the particle density in order to understand plasma formation, to design experiments, and to diagnose experiments. However, performing experiments at the *Z* Facility, especially with our experimental configuration, provides unique challenges to measuring this gas fill pressure.

A.1 Challenges

Recall that we field our gas cell inside a large ($> 60\,\mathrm{m}^3$) vacuum chamber. Relatively long ($\lesssim 9\,\mathrm{m}$) feed lines supply the cell with gas fill. Measuring the pressure outside of the vacuum chamber may infer pressures different from inside the cell for multiple reasons, such as the conductivity of the feed lines or obstructions in the system. Also, because of the inherent high-risk of "single shot" experiments, it is a necessary assurance to confirm that gas successfully fills the cell. This motivates the first criterion for our method to measure the gas fill pressure: (1) *in situ*

measurement.

In order to permit sufficient x-ray flux into the cell, we use a thin ($\sim$ 1.5–μm) Mylar window. This window can be susceptible to leaks and, if adjustments are not made, prevent the experiment from reaching the intended initial conditions. More troublesome, leaks can interfere with the conductive properties of the load hardware, possibly faulting the *z* pinch from executing properly. This is especially critical in the ZAPP environment where the consequence could be a failure to obtain data for multiple, independent experiments (Rochau et al. 2014). Our second criterion is: (2) real-time monitoring.

In the center of the *Z* vacuum chamber, the current return canister housing the *z* pinch has nine rectangular apertures (11x13 mm) in its circular wall that provide radial lines of sight to the *z* pinch allowing radiation to escape to irradiate samples and through which for diagnostic instruments to observe. Closer to the pinch, angular space for hardware becomes increasingly limited, and all hardware, samples, and diagnostics coordinate so that all lines of sight are clear. Our third criterion is: (3) the pressure measurement device must be small.

Coupling this device to a gas cell inside the vacuum chamber means destroying the device with each experiment. (4) The pressure measurement device must be relatively inexpensive.

Lastly, there is an additional systematic uncertainty for measuring pressures at *Z*. The radiation and shock environment is unforgiving. This can cause permanently-installed (outside the vacuum chamber) pressure sensors to drift out of

calibration, necessitating frequent re-calibration. Also, the daily operating schedule of a major facility such as *Z* requires highly integrated and coordinated performances by many people in order to execute a pulsed power shot experiment safely, timely, and successfully. (5) The measurement method must accommodate the *Z* environment both physically and logistically.

To satisfy these criteria we arrive upon a "disposable" method that couples a piezoresistive pressure sensor to our gas cell. Piezoresistive pressure sensors work by measuring the change in resistivity of a deformed diaphragm due to applied pressure. This diaphragm is a thin silicon membrane with a wheatstone bridge arrangement of gold wires etched onto the surface. Its deformation leads to a change in length or cross-section of the wires which changes the resistivity and hence output voltage (e.g., Smith 1954; Barlian et al. 2009). The sensor we procure (Omega Engineering Inc. PX72 series) is small, relatively inexpensive, sensitive to our pressure range of interest (< 100 Torr), and independent of gas composition. We perform calibration measurements prior to the *Z* experiment in a separate laboratory so as not to interfere with daily *Z* operations. This appendix describes these calibration measurements and our procedure to extract *in situ* gas fill pressures for our experiment – as well as another ZAPP experiment (Mancini et al. 2009; Hall et al. 2009, 2010, 2011, 2014) – fielded at the *Z* Facility.

A.1.1 The Pressure Sensor

Our pressure sensor (model PX72-1.5GV) couples to the gas cell with a stainless steel nut for $\frac{1}{8}$-inch tube fitting (Swagelok SS-200-NFSET). A bundle of

conformable coaxial cables (Belden Inc. RG-405/U Type 1671A) – each with one end severed, stripped, and soldered to a lead on the pressure sensor – deliver the excitation voltage to the sensor and the differential voltage sensitive to differential pressure to a multimeter or other absolutely-calibrated voltage measurement device.

For the experiment we make two voltage measurements that are in the tens of mV range, the zero voltage, V_0, corresponding to zero gas fill pressure and the fill voltage, V_{fill}, when the gas cell is filled. We divide the difference of these voltages by the linear proportionality factor, $\frac{\Delta V}{\Delta P}$, we measure prior to the experiment during calibrations to arrive at our gas fill pressure, P:

$$P = \frac{V_{\text{fill}} - V_0}{\frac{\Delta V}{\Delta P}}. \tag{A.1}$$

A.2 Calibrations

The primary calibration measurement records how the voltage produced by the sensor changes with pressure, $\frac{\Delta V}{\Delta P}$. By using this, rather than a direct absolute conversion, we shed the concern of any zero voltage (V_0) the sensor my possess. For the PX72-1.5GV model, V_0 can be positive or negative with a magnitude typically $\lesssim$ a few mV.

For the calibration measurements we place a blanked-off gas cell into a test chamber to recreate the vacuum environment at *Z*. After evacuating the test cell and chamber to a vacuum pressure of $< 5 \times 10^{-5}$ Torr, we valve off the cell from the chamber and fill it with neon gas (which is inert and minimally hazardous) in steps, recording the voltage from the pressure sensor (using an absolutely-calibrated

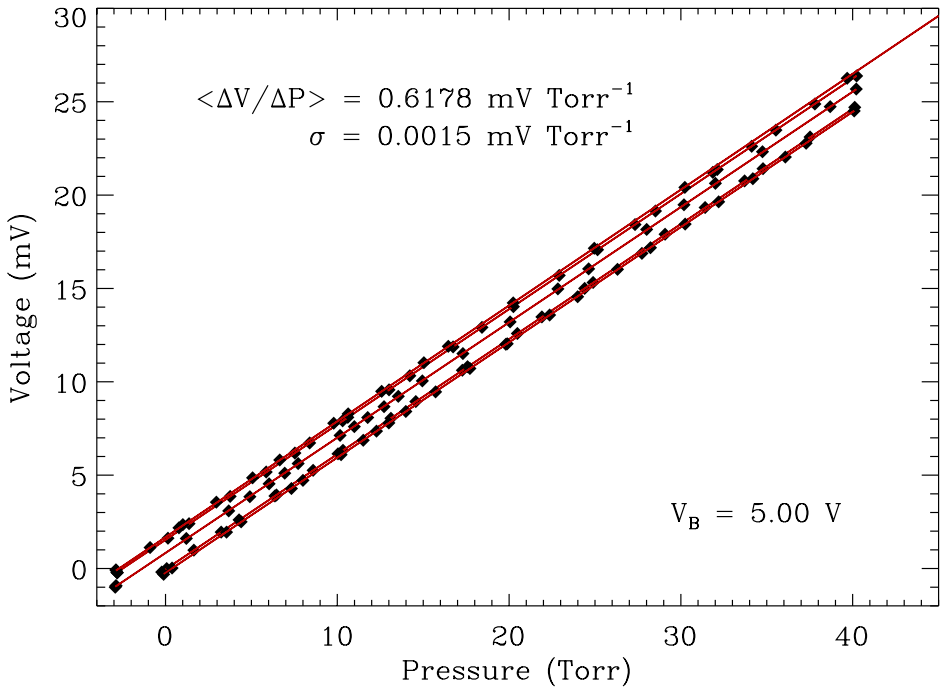

Figure A.1 Calibration measurements of pressure versus voltage for a particular sensor of the PX72-1.5GV model. For each set of measurements, we fit a line (red) to determine $\frac{\Delta V}{\Delta P}$. We repeat these measurements for the same sensor. Though the offset (V_0) may vary, the slope ($\frac{\Delta V}{\Delta P}$) is reproducible within $\sim 0.2\,\%$

Fluke 189 True-rms Digital Multimeter) and the pressure from another transducer (Omegadyne, Inc. model PX01C1-020A5T). Determining a valid $\frac{\Delta V}{\Delta P}$ requires that the differential pressure measured by the Omegadyne transducer is accurate. The absolute level of the pressure measurements is not important. We confirm that ΔP is accurate to within $0.01\,\%$ when compared against an absolutely-calibrated capacitance manometer (Jacobs 1999) (MKS 626B Baritron®). The responses of both our pressure sensor and the Omegadyne transducer are independent of gas

composition. Figure A.1 plots example measurements of pressure versus voltage for a PX72-1.5GV model sensor. We fit lines using a Levenberg-Marquardt least-squares minimization (Markwardt 2009) to recover the linear proportionality factors or slopes, $\frac{\Delta V}{\Delta P}$. Again, any offsets in either axis are unimportant when determing these.

A.2.1 Reproducibility

Since we measure $\frac{\Delta V}{\Delta P}$ away from *Z*, we must confirm that, when we place the sensor in the *Z* vacuum chamber with the gas cell, our $\frac{\Delta V}{\Delta P}$ value remains valid and is reproduced as measured. The ambient temperature away from *Z* and at *Z* are both nominally at room temperature, so we assume $\frac{\Delta V}{\Delta P}$ is free of temperature effects. The actual sensitivity of our pressure sensors to temperature, however, deserves further investigation.

Figure A.1 plots repeated calibration measurements (five) for a particular pressure sensor. We see that V_0 may vary between sets of measurements, but the mean of the slopes $\langle \frac{\Delta V}{\Delta P} \rangle = 0.6178\,\text{mV Torr}^{-1}$ with a standard deviation $\sigma = 0.0015\,\text{mV Torr}^{-1}$, showing that $\frac{\Delta V}{\Delta P}$ is highly reproducible. We adopt σ as the reproducibility in $\frac{\Delta V}{\Delta P}$ for a particular sensor. For this test sensor $\sigma = 0.2\,\%$ of the measured $\frac{\Delta V}{\Delta P}$. Performing the same exercise of making (five) repeated measurements for another pressure sensor (of the same model), we find a reproducibility of $\sigma = 0.1\,\%$, giving evidence that the linear proportionality factors, $\frac{\Delta V}{\Delta P}$, for all sensors are similarly reproducible.

To determine a characteristic value for a typical sensor, we measure $\frac{\Delta V}{\Delta P}$ for

multiple (four) sensors and find a mean value of $0.6039\,\mathrm{mV\ Torr^{-1}}$ with a standard deviation of $0.0118\,\mathrm{mV\ Torr^{-1}}$, or $2.0\,\%$. Later in Section A.3 when we convert voltage to pressure, this characteristic value, $\frac{\Delta V}{\Delta P}^{\mathrm{char}}$, may be substituted for $\frac{\Delta V}{\Delta P}$ for a particular sensor, if needed, while using the standard deviation as the characteristic reproducibility, σ^{char}. To optimize precision and to bypass any systematic uncertainty of an arbitrary sensor possessing a $\frac{\Delta V}{\Delta P}$ value that departs from the norm, we use the measured $\frac{\Delta V}{\Delta P}$ for individual pressure sensors.

A.2.2 Excitation Voltage

Figure A.2 shows how $\frac{\Delta V}{\Delta P}$ changes with excitation voltage, V_{E}, for a particular sensor. This demonstrates the need to supply a precise and constant excitation voltage to the pressure sensor during calibration and during the experiment at *Z*. Not doing so necessitates correcting for mismatched excitation voltage.

The blue diamond in Figure A.2 is the "typical" $\frac{\Delta V}{\Delta P}$ (at $V_{\mathrm{E}} = 5\,\mathrm{V}$) as quoted by the manufacturer. The extrema (connected by the blue, vertical line; also at $V_{\mathrm{E}} = 5\,\mathrm{V}$) span our entire range of measured $\frac{\Delta V}{\Delta P}$ at all V_{E}. As the manufacturer concurs, to ultimately extract precise pressures requires calibration measurements beyond theses nominal values.

Measuring this response to excitation voltage for multiple (six) sensors, we find that $\langle \frac{\Delta V}{\Delta P}/V_{\mathrm{E}} \rangle = 0.120\,\mathrm{mV\ Torr^{-1}V^{-1}}$ with $\sigma = 0.002\,\mathrm{mV\ Torr^{-1}V^{-1}}$ for this collection of sensors. This is the characteristic value of $\frac{\Delta V}{\Delta P}/V_{\mathrm{E}}$ for the PX72-1.5GV sensor. Its characteristic reproducibility of $1.7\,\%$ describes how this value may vary between different pressure sensors of the same model.

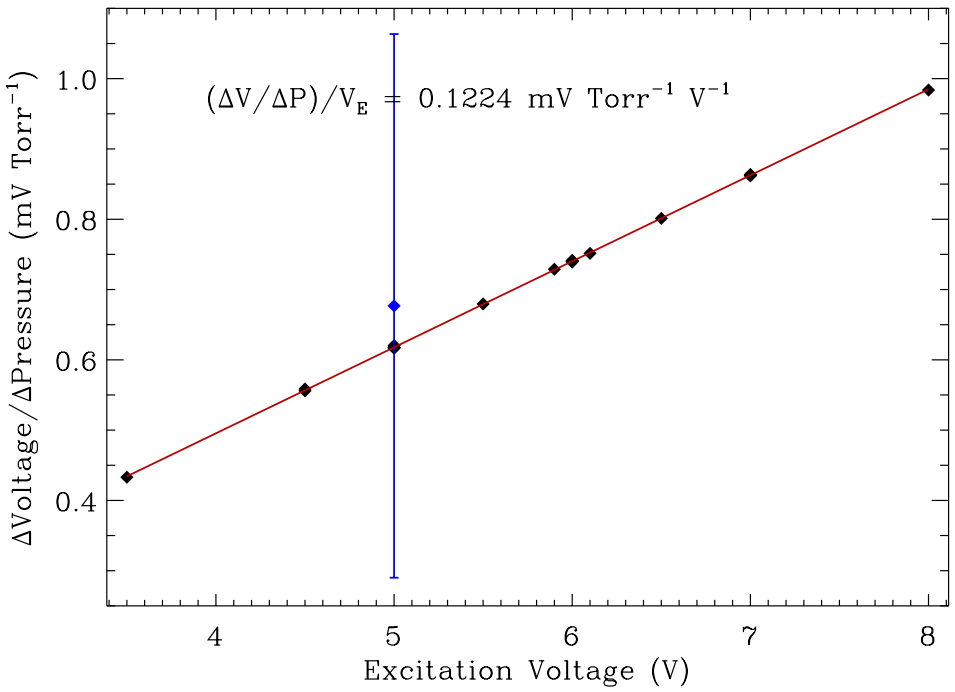

Figure A.2 $\frac{\Delta V}{\Delta P}$ as a function of excitation voltage, V_{E}, for a particular sensor (black diamonds). $\frac{\Delta V}{\Delta P}$ is linearly (red line) sensitive to V_{E}, demonstrating the need for a precise, constant power supply. Our measured values fall within the range quoted by the manufacturer (blue), whose nominal values are not sufficient to extract a precise pressure.

Looking further into dependencies on excitation voltage, we revisit the discussion on reproducibility. In Section A.2.1 we find that $\sigma \leq 0.2\,\%$ for two different test sensors and assume all sensors are similar. This is for $V_{\mathrm{E}} = 5.00\,\mathrm{V}$. Repeating the exercise for two test sensors using $V_{\mathrm{E}} = 6.00\,\mathrm{V}$, we again find small values of $0.1\,\%$. For two sensors using $V_{\mathrm{E}} = 7.00\,\mathrm{V}$, we find 0.1 and $0.4\,\%$. All measured values of reproducibility are minuscule. We take the conservative approach and use the greatest of these values, $\sim 0.4\,\%$, for σ of $\frac{\Delta V}{\Delta P}$ for all V_{E}.

Also in Section A.2.1, we find the standard deviation of $\frac{\Delta V}{\Delta P}$ among sensors, or characteristic reproducibility to be $\sigma^{\mathrm{char}} = 2.0\,\%$ of $\frac{\Delta V}{\Delta P}^{\mathrm{char}}$ when using $V_{\mathrm{E}} = 5.00\,\mathrm{V}$. For three sensors measured using $V_{\mathrm{E}} = 6.00\,\mathrm{V}$, we find $\sigma^{\mathrm{char}} = 2.2\,\%$, and for seven sensors measured using $V_{\mathrm{E}} = 7.00\,\mathrm{V}$, $\sigma^{\mathrm{char}} = 2.5\,\%$.

A.3 Extracting Pressures

We are now ready to attach our sensors to gas cells and place the assemblies into the vacuum chamber at *Z*.

Figure A.3 plots data (black) supplied by a pressure sensor measuring the fill pressure for a hydrogen gas cell used in experiment z2553. Time starts at 0 s when an automated LabVIEW program begins recording a voltage measurement (from a National Instruments PXI-6259 Multifunction Data Acquisition device) each second, providing us with a large number of measurements. We note that this samples the voltage differently than the power meter used for the calibration measurements. The power meter displays values that are averages over many measurements, which smooths away the noise observed in Figure A.3. A National Instruments PXI-4110 Programmable DC Power Supply delivers the excitation voltage to the pressure sensor. The figure shows a fill and purge of our gas cell (a practice to rid the cell of contaminant gases) as well as the end of data recording when the *z*-pinch blast destroys the sensor. For clarity, we remove the idle time between 1500–7850 s. This reveals a slight pressure leak (and confirmed by additional transducers monitoring the gas fill) in our gas cell manifested by the subtle drop in the voltage level bridging these times. We notice a leak this small only because of the real-time monitoring

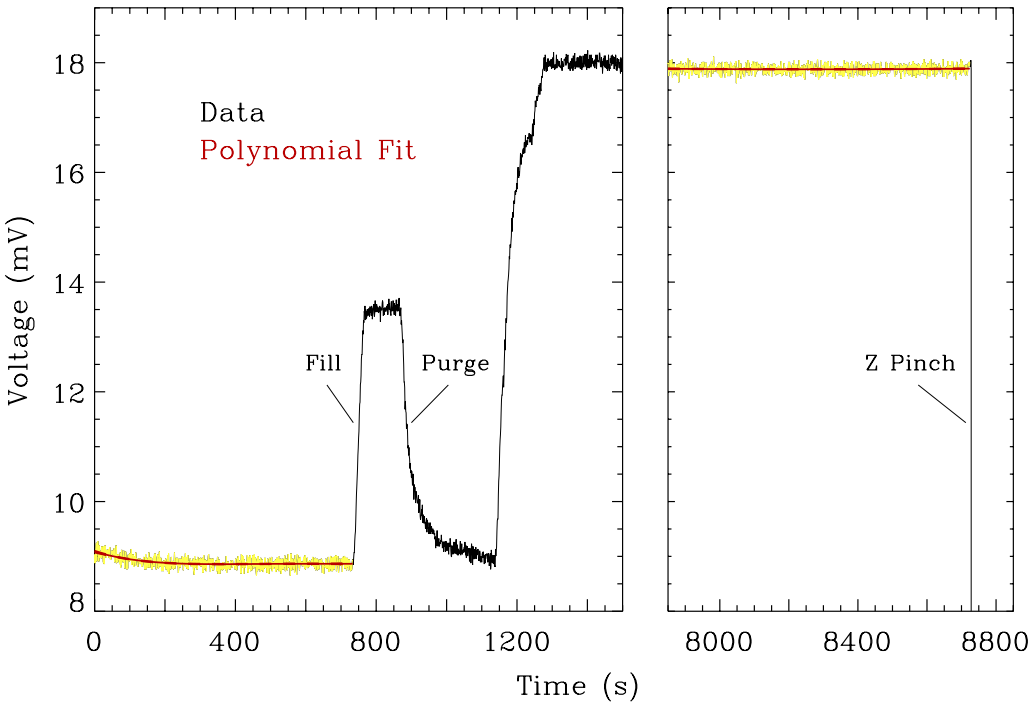

Figure A.3 Example pressure sensor data measuring the fill pressure for a gas cell used in experiment z2553. We leverage the time aspect of our data record by fitting polynomials (red curves) to selected regions (yellow) to precisely measure the zero voltage, V_0, and fill voltage, V_{fill}.

aspect inherent in our method.

We leverage the large number of voltage measurements across time to determine V_0 and V_{fill} to high precision by fitting polynomials (red curves) to selected regions of the data (yellow). For the zero voltage we fit the data recorded before the first fill; the last fit value is V_0. For the fill voltage we fit the data recorded before the z pinch; the last fit value is V_{fill}. Here we use 4^{th}-order and 2^{nd}-order polynomials, respectively. This implicitly assumes that any physical change in pressure in

Table A.1. Measured H_2 Gas Fill Pressures

Experiment	Sensor (PS###)	$\frac{\Delta V}{\Delta P}$ (mV Torr^{-1})	P (Torr)	σ_P (Torr)
z2482	035	0.8264	22.96	0.07
z2483	036	0.8269	19.93	0.06
z2484	037	0.8509	17.85	0.06
z2552	039	0.8031	17.96	0.07
z2553	040	0.8487	10.63	0.05
z2554	041	0.8580	9.49	0.04
z2588	044	0.8583	10.53	0.05
z2589	045	0.8388	9.71	0.04
z2590[a]	046	0.8400	10.71	0.04

[a]This experiment features a CO_2 gas fill instead of the usual H_2.

the gas cell, such as from a leak, is smooth and relatively slow in time and that the observed high-frequency fluctuations in the data are truly noise.

For this example, using the formal uncertainties returned by the fitting routine, we find $V_{\text{fill}} - V_0 = 9.03 \pm 0.02\,\text{mV}$, which is $\sim 0.2\,\%$ uncertainty. Using our measured $\frac{\Delta V}{\Delta P}$ for this particular sensor with the adopted reproducibility $\sigma = 0.4\,\%$ and propagating the uncertainties accordingly, we extract $P = 10.63 \pm 0.05\,\text{Torr}$. Performing the method on other *Z* experiments with other pressure sensors (of the same model) each with their own calibration measurements, we find $\sim 0.4\,\%$ uncertainty in measured gas fill pressure to be typical. Table A.1 gives our measured gas fill pressures, P, (column 3) and uncertainties, σ_P, (column 4) for selected ex-

periments. This table also lists the unique pressure sensor used for each experiment (column 2) following our naming convention (PS###) as well as its measured linear proportionality factor, $\frac{\Delta V}{\Delta P}$.

A.3.1 Systematic Uncertainties

The most significant systematic uncertainty that could lead to an inaccurate measured pressure is in the determination of V_0. It is essential when selecting the data region to fit for V_0 (e.g., yellow region before the first fill in Figure A.3), that the sensor has sufficient time to equilibrate its zero voltage. Sometimes this relaxation is immediate. Sometimes the relaxation takes tens of minutes. This varies between sensors, which hints that it is quite plausibly a result of our fabrication process (i.e., soldering the stripped coaxial cables to the pressure sensor leads). The time scale, though, points toward a temperature effect.

Another possible source of systematic uncertainty is the choice of polynomial used to determine V_0 and V_{fill}. In our example we choose 4^{th}-order and 2^{nd}-order polynomials, respectively, but often polynomials of various degrees are suitable. If we instead use 3^{rd}-order and 2^{nd}-order polynomials, our determined P increases $0.2\,\%$. This is within our uncertainty. However, if we use 4^{th}-order and 3^{rd}-order polynomials or 3^{rd}-order and 3^{rd}-order polynomials, P increases by 0.8 and $0.9\,\%$, beyond our uncertainties but on the same order.

Appendix B

Additional Photographs

In December 2013, two hydrogen plasmas and one carbon/oxygen plasma akin to those that make up DA and hot DQ white dwarf atmospheres, respectively, filled the gas cells shown in Figure B.1. These cells, resting side by side, correspond to experiments z2588, z2589, and z2590, though I cannot say which one is which.

As with the cell in Figure 3.7, debris from the *z*-pinch blast litters the faces of these cells. For the cell on the left and the cell in the center, we see holes in the axial spacers (Section 3.2.3) resulting from shrapnel. Figure B.2 views one of the punctured axial spacers from the side revealing both the entrance and exit wounds.

In Figure B.3 I don Tyvek® coveralls and nitrile gloves, the personal protective equipment required when working with our beryllium-contaminated gas cell hardware once it has survived a pulsed power shot experiment at the *Z* Facility. I title this frontal portrait *Laboratory Gothic*. The *Z* Machine is my house. The gas cell is my pitchfork.

The photograph in Figure B.4, taken at a local Chinese restaurant during lunch, depicts the collaborative nature of our laboratory work. On this day, G. Loisel, T. Nagayama, and I (none pictured) discussed the "Dual Length" gas cell design (Section 4.1.2) using a visual aide created with objects available at our table.

Figure B.1 Gas cells fielded for experiments z2588, z2589, and z2590 in December 2013.

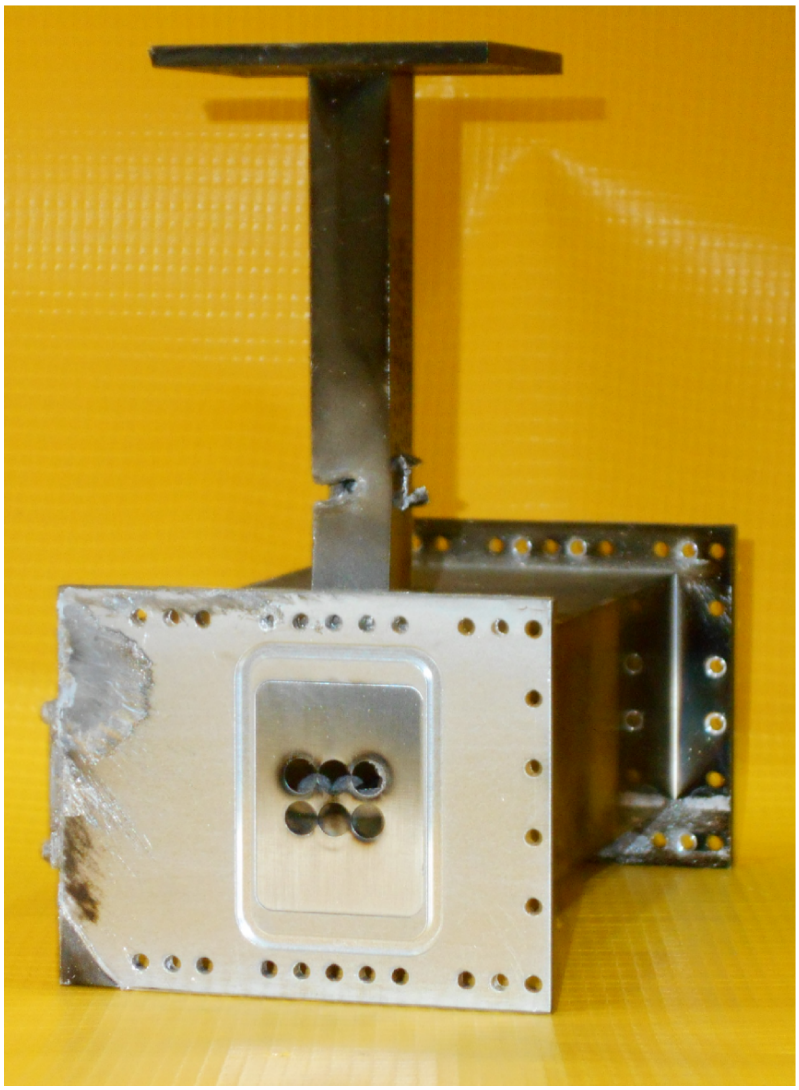

Figure B.2 An axial spacer punctured from shrapnel from the *z*-pinch blast.

This schematic is a top view of the gas cell. *Z*-pinch x-rays (forks) are incident on the central gas cell cavity (horizontal white napkin), flanked by two buffer cavities (vertical white napkins). The sugar (and sugar substitute) packets illustrate different regions of the hydrogen plasma. Both lines of sight, which observe the plasma

Figure B.3 *Laboratory Gothic*: A reverent experimenter spends a quiet moment with his gas cell.

perpendicularly to the x-rays, first traverse a boundary plasma (pink packet) at the interface of the buffer and central cavities. Then each line of sight goes through an intermediate region of the hydrogen plasma that is at the same plasma conditions but a different length (white packets) before seeing the region immediately adjacent to the back-lighting surface (yellow packet). Assuming geometric symmetry, the two

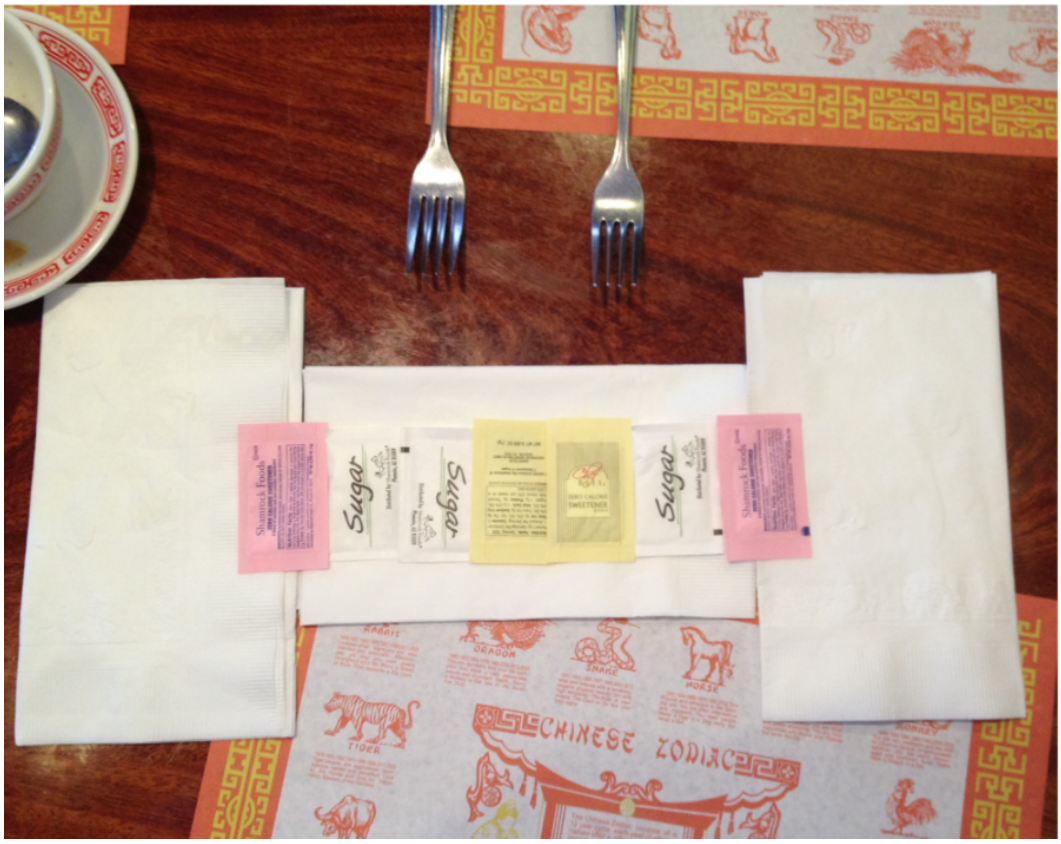

Figure B.4 Schematic of the "Dual Length" gas cell used during discussions at a local Chinese restaurant. X-rays from the *z*-pinch (forks) are incident on the central gas cell cavity (horizontal white napkin) surrounded by its two buffer cavities (vertical white napkins). We illustrate different hydrogen plasma regions with colored sugar (and sugar substitute) packets. This is not made to scale.

lines of sight are identical except for a different length of the intermediate plasma region (white packets). The schematic is not constructed to scale.

Bibliography

Althaus, L. G., & Benvenuto, O. G. 1998, MNRAS, 296, 206

Althaus, L. G., Serenelli, A. M., Córsico, A. H., & Benvenuto, O. G. 2002, MNRAS, 330, 685

Ampleford, D. J., Jennings, C. A., Lebedev, S. V., Bland, S. N., Cuneo, M. E., Sinars, D. B., Bott, S. C., Hall, G. N., Suzuki-Vidal, F., Palmer, J. B. A., & Chittenden, J. P. 2012, Physics of Plasmas, 19, 122711

Baessler, P., & Kock, M. 1980, Journal of Physics B Atomic Molecular Physics, 13, 1351

Bailey, J., Carlson, A. L., Morrison, R. L., & Maron, Y. 1990, Review of Scientific Instruments, 61, 3075

Bailey, J. E., Adams, R., Carlson, A. L., Ching, C. H., Filuk, A. B., & Lake, P. 1997, Review of Scientific Instruments, 68, 1009

Bailey, J. E., Asay, J., Bernard, M., Carlson, A. L., Chandler, G. A., Hall, C. A., Hanson, D., Johnston, R., Lake, P., & Lawrence, J. 2000, J. Quant. Spec. Radiat. Transf., 65, 31

Bailey, J. E., Chandler, G. A., Mancini, R. C., Slutz, S. A., Rochau, G. A., Bump, M., Buris-Mog, T. J., Cooper, G., Dunham, G., Golovkin, I., Kilkenny, J. D.,

Lake, P. W., Leeper, R. J., Lemke, R., Macfarlane, J. J., Mehlhorn, T. A., Moore, T. C., Nash, T. J., Nikroo, A., Nielsen, D. S., Peterson, K. L., Ruiz, C. L., Schroen, D. G., Steinman, D., & Varnum, W. 2006, Physics of Plasmas, 13, 056301

Bailey, J. E., Knudson, M. D., Carlson, A. L., Dunham, G. S., Desjarlais, M. P., Hanson, D. L., & Asay, J. R. 2008, Phys. Rev. B, 78, 144107

Bailey, J. E., Rochau, G. A., Iglesias, C. A., Abdallah, Jr., J., Macfarlane, J. J., Golovkin, I., Wang, P., Mancini, R. C., Lake, P. W., Moore, T. C., Bump, M., Garcia, O., & Mazevet, S. 2007, Physical Review Letters, 99, 265002

Bailey, J. E., Rochau, G. A., Mancini, R. C., Iglesias, C. A., Macfarlane, J. J., Golovkin, I. E., Blancard, C., Cosse, P., & Faussurier, G. 2009, Physics of Plasmas, 16, 058101

Baker, J. 2008, Transition probabilities for one electron atoms, Technical Note 1612, Natl. Inst. Stand. Technol., Washington, DC

Baranger, M. 1958a, Physical Review, 112, 855

—. 1958b, Physical Review, 111, 494

—. 1958c, Physical Review, 111, 481

Barlian, A. A., Park, W., Mallon, J. R., Rastegar, A. J., & Pruitt, B. L. 2009, Proceedings of the IEEE, 97, 513

Bengtson, R. D., & Chester, G. R. 1976, Phys. Rev. A, 13, 1762

Bengtson, R. D., Miller, M. H., Davis, W. D., & Greig, J. R. 1969, ApJ, 157, 957

Bengtson, R. D., Tannich, J. D., & Kepple, P. 1970, Phys. Rev. A, 1, 532

Berg, H. F., Ali, A. W., Lincke, R., & Griem, H. R. 1962, Physical Review, 125, 199

Bergeron, P. 1993, in NATO ASIC Proc. 403: White Dwarfs: Advances in Observation and Theory, ed. M. A. Barstow, 267

Bergeron, P., Gianninas, A., & Boudreault, S. 2007, in Astronomical Society of the Pacific Conference Series, Vol. 372, 15th European Workshop on White Dwarfs, ed. R. Napiwotzki & M. R. Burleigh, 29–+

Bergeron, P., Liebert, J., & Fulbright, M. S. 1995a, ApJ, 444, 810

Bergeron, P., Saffer, R. A., & Liebert, J. 1992, ApJ, 394, 228

Bergeron, P., Wesemael, F., Dufour, P., Beauchamp, A., Hunter, C., Saffer, R. A., Gianninas, A., Ruiz, M. T., Limoges, M.-M., Dufour, P., Fontaine, G., & Liebert, J. 2011, ApJ, 737, 28

Bergeron, P., Wesemael, F., & Fontaine, G. 1991, ApJ, 367, 253

Bergeron, P., Wesemael, F., Fontaine, G., & Liebert, J. 1990, ApJ, 351, L21

Bergeron, P., Wesemael, F., Lamontagne, R., Fontaine, G., Saffer, R. A., & Allard, N. F. 1995b, ApJ, 449, 258

Binney, J., & Merrifield, M. 1998, Galactic Astronomy

Bischoff-Kim, A., Montgomery, M. H., & Winget, D. E. 2008a, ApJ, 675, 1505

—. 2008b, ApJ, 675, 1512

Bland-Hawthorn, J., Shopbell, P. L., & Malin, D. F. 1993, AJ, 106, 2154

Blöcker, T. 1995, A&A, 299, 755

Bockasten, K. 1961, Journal of the Optical Society of America (1917-1983), 51, 943

Bragaglia, A., Renzini, A., & Bergeron, P. 1995, ApJ, 443, 735

Brissaud, A., & Frisch, U. 1971, J. Quant. Spec. Radiat. Transf., 11, 1767

Burgess, D. D., & Mahon, R. 1972, Journal of Physics B Atomic Molecular Physics, 5, 1756

Butterworth, S. 1930, Experimental Wireless and the Wireless Engineer, 7, 536

Cardeñoso, V., & Gigosos, M. A. 1989, Phys. Rev. A, 39, 5258

Carlhoff, C., Krametz, E., Schäfer, J. H., & Uhlenbusch, J. 1986, Journal of Physics B Atomic Molecular Physics, 19, 2629

Castanheira, B. G., & Kepler, S. O. 2009, MNRAS, 396, 1709

Castanheira, B. G., Winget, D. E., Williams, K., Montgomery, M. H., Falcon, R. E., & Hermes, J. J. 2010, in American Institute of Physics Conference Series, Vol. 1273, American Institute of Physics Conference Series, ed. K. Werner & T. Rauch, 160–163

Chandler, G. A., Deeney, C., Cuneo, M., Fehl, D. L., McGurn, J. S., Spielman, R. B., Torres, J. A., McKenney, J. L., Mills, J., & Struve, K. W. 1999, Review of Scientific Instruments, 70, 561

Chandrasekhar, S. 1931, ApJ, 74, 81

—. 1939, An Introduction to the Study of Stellar Structure, ed. S. Chandrasekhar (The University of Chicago Press)

Chen, E. Y., & Hansen, B. M. S. 2011, MNRAS, 413, 2827

Christlieb, N., Wisotzki, L., Reimers, D., Homeier, D., Koester, D., & Heber, U. 2001, A&A, 366, 898

Ciricosta, O., Vinko, S. M., Chung, H.-K., Cho, B.-I., Brown, C. R. D., Burian, T., Chalupský, J., Engelhorn, K., Falcone, R. W., Graves, C., Hájková, V., Higginbotham, A., Juha, L., Krzywinski, J., Lee, H. J., Messerschmidt, M., Murphy, C. D., Ping, Y., Rackstraw, D. S., Scherz, A., Schlotter, W., Toleikis, S., Turner, J. J., Vysin, L., Wang, T., Wu, B., Zastrau, U., Zhu, D., Lee, R. W., Heimann, P., Nagler, B., & Wark, J. S. 2012, Physical Review Letters, 109, 065002

Cochrane, K., Bailey, J. E., Lake, P., & Carlson, A. 2001, Appl. Opt., 40, 150

Colgate, S. A. 1979, ApJ, 232, 404

Córsico, A. H., Althaus, L. G., Miller Bertolami, M. M., Romero, A. D., García-Berro, E., Isern, J., & Kepler, S. O. 2012, MNRAS, 424, 2792

Csikszentmihalyi, M. 1991, Flow: The Psychology of Optimal Experience (New York, NY: Harper Perennial)

Cuneo, M. E., Waisman, E. M., Lebedev, S. V., Chittenden, J. P., Stygar, W. A., Chandler, G. A., Vesey, R. A., Yu, E. P., Nash, T. J., Bliss, D. E., Sarkisov, G. S., Wagoner, T. C., Bennett, G. R., Sinars, D. B., Porter, J. L., Simpson, W. W., Ruggles, L. E., Wenger, D. F., Garasi, C. J., Oliver, B. V., Aragon, R. A., Fowler, W. E., Hettrick, M. C., Idzorek, G. C., Johnson, D., Keller, K., Lazier, S. E., McGurn, J. S., Mehlhorn, T. A., Moore, T., Nielsen, D. S., Pyle, J., Speas, S., Struve, K. W., & Torres, J. A. 2005, Phys. Rev. E, 71, 046406

D'Antona, F. 1987, Mem. Soc. Astron. Italiana, 58, 123

Däppen, W., Anderson, L., & Mihalas, D. 1987, ApJ, 319, 195

Dawson, D. J., Harper, J. M., & Akinradewo, A. C. 1984, Medical Physics, 11, 491

Deeney, C., Douglas, M. R., Spielman, R. B., Nash, T. J., Peterson, D. L., L'Eplattenier, P., Chandler, G. A., Seamen, J. F., & Struve, K. W. 1998, Physical Review Letters, 81, 4883

DeGennaro, S., von Hippel, T., Winget, D. E., Kepler, S. O., Nitta, A., Koester, D., & Althaus, L. 2008, AJ, 135, 1

Dekker, H., D'Odorico, S., Kaufer, A., Delabre, B., & Kotzlowski, H. 2000, in Society of Photo-Optical Instrumentation Engineers (SPIE) Conference Series, Vol. 4008, Society of Photo-Optical Instrumentation Engineers (SPIE) Conference Series, ed. M. Iye & A. F. Moorwood, 534

Dimitrijević, M. S., Kovačević, A., Simić, Z., & Sahal-Bréchot, S. 2011, Baltic Astronomy, 20, 495

Dimitrijevic, M. S., & Sahal-Brechot, S. 1990, A&AS, 82, 519

Djurović, S., Ćirišan, M., Demura, A. V., Demchenko, G. V., Nikolić, D., Gigosos, M. A., & González, M. Á. 2009, Phys. Rev. E, 79, 046402

Djurović, S., Mijatović, Z., & Kobilarov, R. 1988, Contributions to Plasma Physics, 28, 229

Djurović, S., Nikolić, D., Savić, I., Sörge, S., & Demura, A. V. 2005, Phys. Rev. E, 71, 036407

Doherty, L. R., & Turner, E. B. 1955, AJ, 60, 158

Dufour, P., Ben Nessib, N., Sahal-Bréchot, S., & Dimitrijević, M. S. 2011, Baltic Astronomy, 20, 511

Dufour, P., Fontaine, G., Liebert, J., Schmidt, G. D., & Behara, N. 2008, ApJ, 683, 978

Dufour, P., Liebert, J., Fontaine, G., & Behara, N. 2007, Nature, 450, 522

Dunham, G., Bailey, J. E., Carlson, A., Lake, P., & Knudson, M. D. 2004, Review of Scientific Instruments, 75, 928

Ecker, G., & Kröll, W. 1963, Physics of Fluids, 6, 62

Eisenstein, D. J., Liebert, J., Harris, H. C., Kleinman, S. J., Nitta, A., Silvestri, N., Anderson, S. A., Barentine, J. C., Brewington, H. J., Brinkmann, J., Harvanek, M., Krzesiński, J., Neilsen, Jr., E. H., Long, D., Schneider, D. P., & Snedden, S. A. 2006, ApJS, 167, 40

Engelbrecht, A., & Koester, D. 2007, in Astronomical Society of the Pacific Conference Series, Vol. 372, 15th European Workshop on White Dwarfs, ed. R. Napiwotzki & M. R. Burleigh, 289–+

Ershov-Pavlov, E. A., Krat'ko, L. E., Chubruk, N. I., & Shimanovich, V. D. 1987, Journal of Applied Spectroscopy, 46, 317

Falcon, R. E., Rochau, G. A., Bailey, J. E., Ellis, J. L., Carlson, A. L., Gomez, T. A., Montgomery, M. H., Winget, D. E., Chen, E. Y., Gomez, M. R., & Nash, T. J. 2013a, High Energy Density Physics, 9, 82

Falcon, R. E., Rochau, G. A., Bailey, J. E., Ellis, J. L., Carlson, A. L., Gomez, T. A., Montgomery, M. H., Winget, D. E., Chen, E. Y., Gomez, M. R., Nash, T. J., & Pille, T. M. 2013b, in Astronomical Society of the Pacific Conference Series, Vol. 469, Astronomical Society of the Pacific Conference Series, ed. J. Krzesiński, G. Stachowski, P. Moskalik, & K. Bajan, 405–410

Falcon, R. E., Rochau, G. A., Bailey, J. E., Ellis, J. L., Montgomery, M. H., Winget, D. E., Gomez, M. R., & Leeper, R. J. 2010a, in American Institute of Physics Conference Series, Vol. 1273, American Institute of Physics Conference Series, ed. K. Werner & T. Rauch, 436–439

Falcon, R. E., Winget, D. E., Montgomery, M. H., & Williams, K. A. 2010b, ApJ, 712, 585

—. 2012, ApJ, 757, 116

Fich, M., Blitz, L., & Stark, A. A. 1989, ApJ, 342, 272

Finley, D. S., & Koester, D. 1997, ApJ, 489, L79+

Finley, D. S., Koester, D., & Basri, G. 1997, ApJ, 488, 375

Foley, G. M. 1970, Review of Scientific Instruments, 41, 827

Fontaine, G., Bergeron, P., Lacombe, P., Lamontagne, R., & Talon, A. 1985, AJ, 90, 1094

Fontaine, G., Brassard, P., & Bergeron, P. 2001, PASP, 113, 409

Fontaine, G., & Wesemael, F. 1987, 319–326

Fontaine, G., & Wesemael, F. 1997, in Astrophysics and Space Science Library, Vol. 214, White dwarfs, ed. J. Isern, M. Hernanz, & E. Garcia-Berro, 173–+

Foord, M. E., Heeter, R. F., van Hoof, P. A., Thoe, R. S., Bailey, J. E., Cuneo, M. E., Chung, H.-K., Liedahl, D. A., Fournier, K. B., Chandler, G. A., Jonauskas, V., Kisielius, R., Mix, L. P., Ramsbottom, C., Springer, P. T., Keenan, F. P., Rose, S. J., & Goldstein, W. H. 2004, Physical Review Letters, 93, 055002

Gatewood, G. D., & Gatewood, C. V. 1978, ApJ, 225, 191

Gawron, A., Maurmann, S., Böttcher, F., Meckler, A., & Kunze, H.-J. 1988, Phys. Rev. A, 38, 4737

Gianninas, A., Bergeron, P., & Ruiz, M. T. 2011, ApJ, 743, 138

Gigosos, M. A., & Cardeñoso, V. 1996, Journal of Physics B Atomic Molecular Physics, 29, 4795

Gigosos, M. A., González, M. Á., & Cardeñoso, V. 2003, Spectrochimica Acta, 58, 1489

Gilmore, G., Wyse, R. F. G., & Kuijken, K. 1989, ARA&A, 27, 555

Girardi, L., Bressan, A., Bertelli, G., & Chiosi, C. 2000, A&AS, 141, 371

Gomez, M. R., Hansen, S. B., Peterson, K. J., Bliss, D. E., Carlson, A. L., Lamppa, D. C., Schroen, D. G., & Rochau, G. A. 2014a, Review of Scientific Instruments, 85

Gomez, M. R., Rochau, G. A., Bailey, J. E., Dunham, G. S., Kernaghan, M. D., Gard, P., Robertson, G. K., Owen, A. C., Argo, J. W., Nielsen, D. S., & Lake, P. W. 2012, Review of Scientific Instruments, 83, 100000

Gomez, T. A., Mancini, R. C., Montgomery, M. H., & Winget, D. E. 2014b, in preparation

Grabowski, B., Halenka, J., & Madej, J. 1987, ApJ, 313, 750

Greenstein, J. L. 1986, ApJ, 304, 334

Greenstein, J. L., & Trimble, V. L. 1967, ApJ, 149, 283

Griem, H. R. 1997, Proceedings of the Physical Society

Griem, H. R., Kolb, A. C., & Shen, K. Y. 1959, Physical Review, 116, 4

—. 1962, ApJ, 135, 272

Grützmacher, K., & Wende, B. 1977, Phys. Rev. A, 16, 243

—. 1978, Phys. Rev. A, 18, 2140

Hagen, H.-J., Groote, D., Engels, D., & Reimers, D. 1995, A&AS, 111, 195

Halenka, J. 1988, J. Quant. Spec. Radiat. Transf., 39, 347

Halenka, J., & Musielok, J. 1986, J. Quant. Spec. Radiat. Transf., 36, 233

Hall, I. M., Durmaz, T., Mancini, R. C., Bailey, J. E., & Rochau, G. A. 2010, Review of Scientific Instruments, 81, 100000

—. 2011, Ap&SS, 336, 189

Hall, I. M., Durmaz, T., Mancini, R. C., Bailey, J. E., Rochau, G. A., Golovkin, I. E., & MacFarlane, J. J. 2014, Physics of Plasmas, 21, 031203

Hall, I. M., Durmaz, T., Mancini, R. C., Bailey, J. E., Rochau, G. A., Rosenberg, M. J., Cohen, D. H., Golovkin, I. E., Macfarlane, J. J., Sherril, M. E., Abdallah, J., Heeter, R. F., Foord, M. E., Glenzer, S. H., & Scott, H. A. 2009, Ap&SS, 322, 117

Hallensleben, S., Harmer, S. W., & Townsend, P. D. 2000, Optics Communications, 180, 89

Hamuy, M., Phillips, M. M., Maza, J., Suntzeff, N. B., Schommer, R. A., & Aviles, R. 1995, AJ, 109, 1

Hansen, B. M. S., Anderson, J., Brewer, J., Dotter, A., Fahlman, G. G., Hurley, J., Kalirai, J., King, I., Reitzel, D., Richer, H. B., Rich, R. M., Shara, M. M., & Stetson, P. B. 2007, ApJ, 671, 380

Hansen, C. J., Kawaler, S. D., & Trimble, V. 2004, Stellar interiors : physical principles, structure, and evolution, ed. Hansen, C. J., Kawaler, S. D., & Trimble, V.

Hansen, S. B., Fournier, K. B., Bauche-Arnoult, C., Bauche, J., & Peyrusse, O. 2006, J. Quant. Spec. Radiat. Transf., 99, 272

Harris, H. C., Liebert, J., Kleinman, S. J., Nitta, A., Anderson, S. F., Knapp, G. R., Krzesiński, J., Schmidt, G., Strauss, M. A., Vanden Berk, D., Eisenstein, D., Hawley, S., Margon, B., Munn, J. A., Silvestri, N. M., Smith, J. A., Szkody, P., Collinge, M. J., Dahn, C. C., Fan, X., Hall, P. B., Schneider, D. P., Brinkmann, J., Burles, S., Gunn, J. E., Hennessy, G. S., Hindsley, R., Ivezić, Z., Kent, S., Lamb, D. Q., Lupton, R. H., Nichol, R. C., Pier, J. R., Schlegel, D. J., SubbaRao, M., Uomoto, A., Yanny, B., & York, D. G. 2003, AJ, 126, 1023

Harvey-Thompson, A. J., Lebedev, S. V., Patankar, S., Bland, S. N., Burdiak, G., Chittenden, J. P., Colaitis, A., De Grouchy, P., Doyle, H. W., Hall, G. N., Khoory,

E., Hohenberger, M., Pickworth, L., Suzuki-Vidal, F., Smith, R. A., Skidmore, J., Suttle, L., & Swadling, G. F. 2012a, Physical Review Letters, 108, 145002

Harvey-Thompson, A. J., Lebedev, S. V., Patankar, S., Bland, S. N., Burdiak, G., Chittenden, J. P., Colaitis, A., De Grouchy, P., Hall, G. N., Khoory, E., Hohenberger, M., Pickworth, L., Suzuki-Vidal, F., Smith, R. A., Skidmore, J., Suttle, L., & Swadling, G. F. 2012b, Physics of Plasmas, 19, 056303

Heading, D. J., Marangos, J. P., & Burgess, D. D. 1992, Journal of Physics B Atomic Molecular Physics, 25, 4745

Helbig, V., & Nick, K. 1981, Journal of Physics B Atomic Molecular Physics, 14, 3573

Henke, B. L., Gullikson, E. M., & Davis, J. C. 1993, Atomic Data and Nuclear Data Tables, 54, 181

Hermes, J. J., Montgomery, M. H., Gianninas, A., Winget, D. E., Brown, W. R., Harrold, S. T., Bell, K. J., Kenyon, S. J., Kilic, M., & Castanheira, B. G. 2013a, MNRAS, 436, 3573

Hermes, J. J., Montgomery, M. H., Winget, D. E., Brown, W. R., Gianninas, A., Kilic, M., Kenyon, S. J., Bell, K. J., & Harrold, S. T. 2013b, ApJ, 765, 102

Hermes, J. J., Montgomery, M. H., Winget, D. E., Brown, W. R., Kilic, M., & Kenyon, S. J. 2012, ApJ, 750, L28

Hey, J. D., & Griem, H. R. 1975, Phys. Rev. A, 12, 169

Hill, R. A., & Gerardo, J. B. 1967, Physical Review, 162, 45

Hoarty, D. J., Allan, P., James, S. F., Brown, C. R. D., Hobbs, L. M. R., Hill, M. P., Harris, J. W. O., Morton, J., Brookes, M. G., Shepherd, R., Dunn, J., Chen, H., Von Marley, E., Beiersdorfer, P., Chung, H. K., Lee, R. W., Brown, G., & Emig, J. 2013, Physical Review Letters, 110, 265003

Holstein, T. 1947, Physical Review, 72, 1212

Holtsmark, J. 1919, Annalen der Physik, 363, 577

Homeier, D., Koester, D., Hagen, H.-J., Jordan, S., Heber, U., Engels, D., Reimers, D., & Dreizler, S. 1998, A&A, 338, 563

Hooper, C. F. 1968, Physical Review, 169, 193

Hummer, D. G., & Mihalas, D. 1988, ApJ, 331, 794

Iben, Jr., I. 1991, ApJS, 76, 55

Iglesias, C. A. 2006, J. Quant. Spec. Radiat. Transf., 99, 295

—. 2014, High Energy Density Physics, 12, 5

Ispolatov, Y., & Oks, E. 1994, J. Quant. Spec. Radiat. Transf., 51, 129

Ives, H. C., Stygar, W. A., Fehl, D. L., Ramirez, L. E., Dropinski, S. C., Wall, D. L., Anctil, J. S., McGurn, J. S., Pyle, J. H., Hanson, D. L., Allison, B. N., Berninger, M. J., Bryce, E. A., Chandler, G. A., Cuneo, M. E., Fox, A. J., Gilliland, T. L., Haslett, C. L., Leeper, R. J., Lewis, D. F., Lucero, M. A., Mazarakis, M. G.,

McDaniel, D. H., McKenney, J. L., Mills, J. A., Mix, L. P., Porter, J. L., Ritchey, M. B., Ruggles, L. E., Seamen, J. F., Simpson, W. W., Spielman, R. B., Torres, J. A., Vargas, M. F., Wagoner, T. C., Warne, L. K., & York, M. W. 2006, Physical Review Special Topics Accelerators and Beams, 9, 110401

Jacobs, D. 1999, Vacuum & Thinfilm

Johnson, H. L., & Morgan, W. W. 1953, ApJ, 117, 313

Johnston, M. D., Oliver, B. V., Droemer, D. W., Frogget, B., Crain, M. D., & Maron, Y. 2010, Absolute Calibration Method for Nanosecond-Resolved, Time-Streaked, Fiber Optic Light Collection, Spectroscopy Systems, Sandia report, Sandia National Laboratories, Albuquerque, NM

—. 2012, Review of Scientific Instruments, 83, 083108

Jones, B., Deeney, C., Coverdale, C. A., Meyer, C. J., & Lepell, P. D. 2006a, IEEE Transactions on Plasma Science, 34, 213

—. 2006b, Review of Scientific Instruments, 77, 100000

Jordan, S., Koester, D., Vauclair, G., Dolez, N., Heber, U., Hagen, H.-J., Reimers, D., Chevreton, M., & Dreizler, S. 1998, A&A, 330, 277

Katagiri, K., Hasegawa, J., Nishinomiya, S., Ikagawa, H., & Oguri, Y. 2007, Journal of Applied Physics, 102, 113304

Kepler, S. O., Kleinman, S. J., Nitta, A., Koester, D., Castanheira, B. G., Giovannini, O., Costa, A. F. M., & Althaus, L. 2007, MNRAS, 375, 1315

Kepler, S. O., Winget, D. E., Nather, R. E., Bradley, P. A., Grauer, A. D., Fontaine, G., Bergeron, P., Vauclair, G., Claver, C. F., Marar, T. M. K., Seetha, S., Ashoka, B. N., Mazeh, T., Leibowitz, E., Dolez, N., Chevreton, M., Barstow, M. A., Clemens, J. C., Kleinman, S. J., Sansom, A. E., Tweedy, R. W., Kanaan, A., Hine, B. P., Provencal, J. L., Wesemael, F., Wood, M. A., Brassard, P., Solheim, J.-E., & Emanuelsen, P.-I. 1991, ApJ, 378, L45

Kepple, P., & Griem, H. R. 1968, Physical Review, 173, 317

Kerr, F. J., & Lynden-Bell, D. 1986, MNRAS, 221, 1023

Kilic, M., Thorstensen, J. R., & Koester, D. 2008, ApJ, 689, L45

Kilkenny, D., O'Donoghue, D., Koen, C., Stobie, R. S., & Chen, A. 1997, MNRAS, 287, 867

Kleinman, S. J., Harris, H. C., Eisenstein, D. J., Liebert, J., Nitta, A., Krzesiński, J., Munn, J. A., Dahn, C. C., Hawley, S. L., Pier, J. R., Schmidt, G., Silvestri, N. M., Smith, J. A., Szkody, P., Strauss, M. A., Knapp, G. R., Collinge, M. J., Mukadam, A. S., Koester, D., Uomoto, A., Schlegel, D. J., Anderson, S. F., Brinkmann, J., Lamb, D. Q., Schneider, D. P., & York, D. G. 2004, ApJ, 607, 426

Kleinman, S. J., Kepler, S. O., Koester, D., Pelisoli, I., Peçanha, V., Nitta, A., Costa, J. E. S., Krzesinski, J., Dufour, P., Lachapelle, F.-R., Bergeron, P., Yip, C.-W., Harris, H. C., Eisenstein, D. J., Althaus, L., & Córsico, A. 2013, ApJS, 204, 5

Knapp, P. F., Hansen, S. B., Pikuz, S. A., Shelkovenko, T. A., & Hammer, D. A. 2012, Review of Scientific Instruments, 83, 073502

Kobilarov, R., Konjević, N., & Popović, M. V. 1989, Phys. Rev. A, 40, 3871

Koester, D. 1987, ApJ, 322, 852

Koester, D., Kepler, S. O., Kleinman, S. J., & Nitta, A. 2009a, Journal of Physics Conference Series, 172, 012006

Koester, D., Napiwotzki, R., Christlieb, N., Drechsel, H., Hagen, H.-J., Heber, U., Homeier, D., Karl, C., Leibundgut, B., Moehler, S., Nelemans, G., Pauli, E.-M., Reimers, D., Renzini, A., & Yungelson, L. 2001, A&A, 378, 556

Koester, D., Napiwotzki, R., Voss, B., Homeier, D., & Reimers, D. 2005, A&A, 439, 317

Koester, D., Schulz, H., & Wegner, G. 1981, A&A, 102, 331

Koester, D., Schulz, H., & Weidemann, V. 1979, A&A, 76, 262

Koester, D., Voss, B., Napiwotzki, R., Christlieb, N., Homeier, D., Lisker, T., Reimers, D., & Heber, U. 2009b, A&A, 505, 441

Kolb, A. C., & Griem, H. 1958, Physical Review, 111, 514

Konjević, N. 1999, Phys. Rep., 316, 339

Konjević, N., Lesage, A., Fuhr, J. R., & Wiese, W. L. 2002, Journal of Physical and Chemical Reference Data, 31, 819

Konjević, N., & Roberts, J. R. 1976, Journal of Physical and Chemical Reference Data, 5, 209

Konjević, N., & Wiese, W. L. 1976, Journal of Physical and Chemical Reference Data, 5, 259

Kowalski, P. M., & Saumon, D. 2006, ApJ, 651, L137

Kudrin, L. P., & Sholin, G. V. 1963, Soviet Physics Doklady, 7, 1015

Kuijken, K., & Gilmore, G. 1989, MNRAS, 239, 605

Ladislas Wiza, J. 1979, Nuclear Instruments and Methods, 162, 587

Lake, P. W., Bailey, J. E., Rochau, G. A., Moore, T. C., Petmecky, D., & Gard, P. 2004, Review of Scientific Instruments, 75, 3690

Lamontagne, R., Demers, S., Wesemael, F., Fontaine, G., & Irwin, M. J. 2000, AJ, 119, 241

Lawlor, T. M., & MacDonald, J. 2006, MNRAS, 371, 263

Lechien, K. R., Savage, M. E., Anaya, V., Bliss, D. E., Clark, W. T., Corley, J. P., Feltz, G., Garrity, J. E., Guthrie, D. W., Hodge, K. C., Maenchen, J. E., Maier, R., Prestwich, K. R., Struve, K. W., Stygar, W. A., Thompson, T., van den Avyle, J., Wakeland, P. E., Wallace, Z. R., & Woodworth, J. R. 2008, Physical Review Special Topics Accelerators and Beams, 11, 060402

Lechien, K. R., Stygar, W. A., Savage, M. E., Wakeland, P. E., Anaya, V., Artery, D. S., Baremore, M. J., Bliss, D. E., Chavez, R., Coombs, G. D., Corley, J. P., Jones, P. A., Kipp, A. K., Lewis, B. A., Lott, J. A., Lynch, J. J., McKee, G. R., Ploor, S. D., Prestwich, K. R., Roznowski, S. A., Spencer, D. C., White, S. D., &

Woodworth, J. R. 2010, Physical Review Special Topics Accelerators and Beams, 13, 030401

Lemke, M. 1997, A&AS, 122, 285

Levenberg, K. 1944, Quarterly of Applied Mathematics, 2, 164

Liebert, J., Bergeron, P., & Holberg, J. B. 2005, ApJS, 156, 47

Liebert, J., & Sion, E. M. 1994, in Astronomical Society of the Pacific Conference Series, Vol. 60, The MK Process at 50 Years: A Powerful Tool for Astrophysical Insight, ed. C. J. Corbally, R. O. Gray, & R. F. Garrison, 64

Limoges, M., & Bergeron, P. 2010, ApJ, 714, 1037

Loisel, G. P., Rochau, G. A., Bailey, J. E., Nagayama, T., Falcon, R. E., Jones, M. C., MacFarlane, J. J., & Golovkin, I. 2014, in preparation

Lyzenga, G. A., & Ahrens, T. J. 1979, Review of Scientific Instruments, 50, 1421

MacFarlane, J. J. 2003, J. Quant. Spec. Radiat. Transf., 81, 287

Macfarlane, J. J., Bailey, J. E., Chandler, G. A., Deeney, C., Douglas, M. R., Jobe, D., Lake, P., Nash, T. J., Nielsen, D. S., Spielman, R. B., Wang, P., & Woodruff, P. 2002, Phys. Rev. E, 66, 046416

Macfarlane, J. J., Golovkin, I. E., & Woodruff, P. R. 2006, J. Quant. Spec. Radiat. Transf., 99, 381

Madej, J., Należyty, M., & Althaus, L. G. 2004, A&A, 419, L5

Mancini, R. C., Bailey, J. E., Hawley, J. F., Kallman, T., Witthoeft, M., Rose, S. J., & Takabe, H. 2009, Physics of Plasmas, 16, 041001

Markwardt, C. B. 2009, in Astronomical Society of the Pacific Conference Series, Vol. 411, Astronomical Society of the Pacific Conference Series, ed. D. A. Bohlender, D. Durand, & P. Dowler, 251–+

Marquardt, D. W. 1963, J. Soc. Indust. Appl. Math., 11, 431

Matzen, M. K. 1997, Physics of Plasmas, 4, 1519

Matzen, M. K., Sweeney, M. A., Adams, R. G., Asay, J. R., Bailey, J. E., Bennett, G. R., Bliss, D. E., Bloomquist, D. D., Brunner, T. A., Campbell, R. B., Chandler, G. A., Coverdale, C. A., Cuneo, M. E., Davis, J.-P., Deeney, C., Desjarlais, M. P., Donovan, G. L., Garasi, C. J., Haill, T. A., Hall, C. A., Hanson, D. L., Hurst, M. J., Jones, B., Knudson, M. D., Leeper, R. J., Lemke, R. W., Mazarakis, M. G., McDaniel, D. H., Mehlhorn, T. A., Nash, T. J., Olson, C. L., Porter, J. L., Rambo, P. K., Rosenthal, S. E., Rochau, G. A., Ruggles, L. E., Ruiz, C. L., Sanford, T. W. L., Seamen, J. F., Sinars, D. B., Slutz, S. A., Smith, I. C., Struve, K. W., Stygar, W. A., Vesey, R. A., Weinbrecht, E. A., Wenger, D. F., & Yu, E. P. 2005, Physics of Plasmas, 12, 055503

Maxted, P. F. L., & Marsh, T. R. 1999, MNRAS, 307, 122

Maxted, P. F. L., Marsh, T. R., & Moran, C. K. J. 2000, MNRAS, 319, 305

McCook, G. P., & Sion, E. M. 1999, ApJS, 121, 1

McLean, E. A., & Ramsden, S. A. 1965, Physical Review, 140, 1122

McMahan, R. K. 1989, ApJ, 336, 409

Mestel, L. 1952, MNRAS, 112, 583

Mihalas, D. 1978, Stellar atmospheres /2nd edition/

Miller, G. E., & Scalo, J. M. 1979, ApJS, 41, 513

Miller, J. E., Boehly, T. R., Melchior, A., Meyerhofer, D. D., Celliers, P. M., Eggert, J. H., Hicks, D. G., Sorce, C. M., Oertel, J. A., & Emmel, P. M. 2007, Review of Scientific Instruments, 78, 034903

Montgomery, M. H., Klumpe, E. W., Winget, D. E., & Wood, M. A. 1999, ApJ, 525, 482

Montgomery, M. H., & Winget, D. E. 1999, ApJ, 526, 976

Morris, J. C., & Krey, R. U. 1968, Physical Review Letters, 21, 1043

Mukadam, A. S., Bischoff-Kim, A., Fraser, O., Córsico, A. H., Montgomery, M. H., Kepler, S. O., Romero, A. D., Winget, D. E., Hermes, J. J., Riecken, T. S., Kronberg, M. E., Winget, K. I., Falcon, R. E., Chandler, D. W., Kuehne, J. W., Sullivan, D. J., Reaves, D., von Hippel, T., Mullally, F., Shipman, H., Thompson, S. E., Silvestri, N. M., & Hynes, R. I. 2013, ApJ, 771, 17

Nagayama, T., Bailey, J. E., Loisel, G., Hansen, S. B., Rochau, G. A., Mancini, R. C., MacFarlane, J. J., & Golovkin, I. 2014a, Physics of Plasmas, 21, 056502

Nagayama, T., Bailey, J. E., Loisel, G., Rochau, G. A., & Falcon, R. E. 2014b, Review of Scientific Instruments, 85

Nagayama, T., Bailey, J. E., Rochau, G. A., Hansen, S. B., Mancini, R. C., MacFarlane, J. J., & Golovkin, I. 2012a, Review of Scientific Instruments, 83, 100000

Nagayama, T., Mancini, R. C., Florido, R., Mayes, D., Tommasini, R., Koch, J. A., Delettrez, J. A., Regan, S. P., & Smalyuk, V. A. 2012b, Physics of Plasmas, 19, 082705

Nagayama, T., Mancini, R. C., Florido, R., Tommasini, R., Koch, J. A., Delettrez, J. A., Regan, S. P., Smalyuk, V. A., Welser-Sherrill, L. A., & Golovkin, I. E. 2008, Review of Scientific Instruments, 79, 100000

Napiwotzki, R. 2009, Journal of Physics Conference Series, 172, 012004

Napiwotzki, R., Christlieb, N., Drechsel, H., Hagen, H., Heber, U., Homeier, D., Karl, C., Koester, D., Leibundgut, B., Marsh, T. R., Moehler, S., Nelemans, G., Pauli, E., Reimers, D., Renzini, A., & Yungelson, L. 2003, The Messenger, 112, 25

Napiwotzki, R., Christlieb, N., Drechsel, H., Hagen, H.-J., Heber, U., Homeier, D., Karl, C., Koester, D., Leibundgut, B., Marsh, T. R., Moehler, S., Nelemans, G., Pauli, E.-M., Reimers, D., Renzini, A., & Yungelson, L. 2001, Astronomische Nachrichten, 322, 411

Napiwotzki, R., & Rauch, T. 1994, A&A, 285, 603

Nash, T. J., Derzon, M. S., Chandler, G. A., Fehl, D. L., Leeper, R. J., Porter, J. L., Spielman, R. B., Ruiz, C., Cooper, G., McGurn, J., Hurst, M., Jobe, D., Torres, J., Seaman, J., Struve, K., Lazier, S., Gilliland, T., Ruggles, L. A., Simpson, W. A., Adams, R., Seaman, J. A., Wenger, D., Nielsen, D., Riley, P., French, R., Stygar, B., Wagoner, T., Sanford, T. W. L., Mock, R., Asay, J., Hall, C., Knudson, M., Armijo, J., McKenney, J., Hawn, R., Schroen-Carey, D., Hebron, D., Cutler, T., Dropinski, S., Deeney, C., Lepell, P. D., Coverdale, C. A., Douglas, M., Cuneo, M., Hanson, D., Bailey, J. E., Lake, P., Carlson, A., Wakefield, C., Mills, J., Slopek, J., Dinwoodie, T., & Idzorek, G. 2001, Review of Scientific Instruments, 72, 1167

Nash, T. J., Derzon, M. S., Chandler, G. A., Leeper, R., Fehl, D., Lash, J., Ruiz, C., Cooper, G., Seaman, J. F., McGurn, J., Lazier, S., Torres, J., Jobe, D., Gilliland, T., Hurst, M., Mock, R., Ryan, P., Nielsen, D., Armijo, J., McKenney, J., Hawn, R., Hebron, D., Macfarlane, J. J., Petersen, D., Bowers, R., Matuska, W., & Ryutov, D. D. 1999, Physics of Plasmas, 6, 2023

Okasaka, R., Nagashima, M., & Fukuda, K. 1977, Journal of the Physical Society of Japan, 42, 1339

Oks, E., Derevianko, A., & Ispolatov, Y. 1995, J. Quant. Spec. Radiat. Transf., 54, 307

Olchawa, W. 2002, J. Quant. Spec. Radiat. Transf., 74, 417

Olivero, J. 1977, J. Quant. Spec. Radiat. Transf., 17, 233

Olsen, R. W. 1989, in Society of Photo-Optical Instrumentation Engineers (SPIE) Conference Series, Vol. 981, High Speed Photography, Videography, and Photonics VI, ed. G. L. Stradling, 71

Omar, B., Günter, S., Wierling, A., & Röpke, G. 2006, Phys. Rev. E, 73, 056405

Osterbrock, D. E., & Ferland, G. J. 2006, Astrophysics of gaseous nebulae and active galactic nuclei (Astrophysics of gaseous nebulae and active galactic nuclei, 2nd. ed. by D.E. Osterbrock and G.J. Ferland. Sausalito, CA: University Science Books, 2006)

Parigger, C., Plemmons, D. H., & Lewis, J. W. L. 1995, Appl. Opt., 34, 3325

Parigger, C. G., Dackman, M., & Hornkohl, J. O. 2008, Appl. Opt., 47, G1

Parigger, C. G., Plemmons, D. H., & Oks, E. 2003, Appl. Opt., 42, 5992

Partouche-Sebban, D., Holtkamp, D. B., Pélissier, J. L., Taboury, J., & Rouyer, A. 2002, Shock Waves, 11, 385

Pauli, E.-M., Napiwotzki, R., Altmann, M., Heber, U., Odenkirchen, M., & Kerber, F. 2003, A&A, 400, 877

Pauli, E.-M., Napiwotzki, R., Heber, U., Altmann, M., & Odenkirchen, M. 2006, A&A, 447, 173

Peebles, P. J. E. 1993, Principles of Physical Cosmology

Pérez, C., Santamarta, R., Rosa, M. I. D. L., & Mar, S. 2003, European Physical Journal D, 27, 73

Perry, T. S., Springer, P. T., Fields, D. F., Bach, D. R., Serduke, F. J., Iglesias, C. A., Rogers, F. J., Nash, J. K., Chen, M. H., Wilson, B. G., Goldstein, W. H., Rozsynai, B., Ward, R. A., Kilkenny, J. D., Doyas, R., da Silva, L. B., Back, C. A., Cauble, R., Davidson, S. J., Foster, J. M., Smith, C. C., Bar-Shalom, A., & Lee, R. W. 1996, Phys. Rev. E, 54, 5617

Preston, T. R., Vinko, S. M., Ciricosta, O., Chung, H.-K., Lee, R. W., & Wark, J. S. 2013, High Energy Density Physics, 9, 258

Rambo, P. K., Smith, I. C., Porter, Jr., J. L., Hurst, M. J., Speas, C. S., Adams, R. G., Garcia, A. J., Dawson, E., Thurston, B. D., Wakefield, C., Kellogg, J. W., Slattery, M. J., Ives, III, H. C., Broyles, R. S., Caird, J. A., Erlandson, A. C., Murray, J. E., Behrendt, W. C., Neilsen, N. D., & Narduzzi, J. M. 2005, Appl. Opt., 44, 2421

Redfield, S., & Falcon, R. E. 2008, ApJ, 683, 207

Reid, I. N. 1996, AJ, 111, 2000

Renedo, I., Althaus, L. G., Miller Bertolami, M. M., Romero, A. D., Córsico, A. H., Rohrmann, R. D., & García-Berro, E. 2010, ApJ, 717, 183

Richter, R., Heber, U., & Napiwotzki, R. 2007, in Astronomical Society of the Pacific Conference Series, Vol. 372, 15th European Workshop on White Dwarfs, ed. R. Napiwotzki & M. R. Burleigh, 107–+

Riess, A. G., Filippenko, A. V., Challis, P., Clocchiatti, A., Diercks, A., Garnavich, P. M., Gilliland, R. L., Hogan, C. J., Jha, S., Kirshner, R. P., Leibundgut, B.,

Phillips, M. M., Reiss, D., Schmidt, B. P., Schommer, R. A., Smith, R. C., Spyromilio, J., Stubbs, C., Suntzeff, N. B., & Tonry, J. 1998, AJ, 116, 1009

Rochau, G. A., Bailey, J. E., Chandler, G. A., Cooper, G., Dunham, G. S., Lake, P. W., Leeper, R. J., Lemke, R. W., Mehlhorn, T. A., Nikroo, A., Peterson, K. J., Ruiz, C. L., Schroen, D. G., Slutz, S. A., Steinman, D., Stygar, W. A., & Varnum, W. 2007, Plasma Physics and Controlled Fusion, 49, 591

Rochau, G. A., Bailey, J. E., Falcon, R. E., Loisel, G. P., Nagayama, T., Mancini, R. C., Hall, I., Winget, D. E., Montgomery, M. H., & Liedahl, D. A. 2014, Physics of Plasmas, 21, 056308

Rochau, G. A., Bailey, J. E., & Macfarlane, J. J. 2005, Phys. Rev. E, 72, 066405

Rochau, G. A., Bailey, J. E., Maron, Y., Chandler, G. A., Dunham, G. S., Fisher, D. V., Fisher, V. I., Lemke, R. W., Macfarlane, J. J., Peterson, K. J., Schroen, D. G., Slutz, S. A., & Stambulchik, E. 2008, Physical Review Letters, 100, 125004

Rybicki, G. B., & Lightman, A. P. 1979, Radiative processes in astrophysics

Salaris, M., Cassisi, S., Pietrinferni, A., Kowalski, P. M., & Isern, J. 2010, ApJ, 716, 1241

Salpeter, E. E. 1955, ApJ, 121, 161

Sanford, T. W. L., Lemke, R. W., Mock, R. C., Chandler, G. A., Leeper, R. J., Ruiz, C. L., Peterson, D. L., Chrien, R. E., Idzorek, G. C., Watt, R. G., & Chittenden, J. P. 2002, Physics of Plasmas, 9, 3573

Sanford, T. W. L., Nash, T. J., Mock, R. C., Spielman, R. B., Seamen, J. F., McGurn, J. S., Jobe, D., Gilliland, T. L., Vargas, M., Whitney, K. G., Thornhill, J. W., Pulsifer, P. E., & Apruzese, J. P. 1997, Review of Scientific Instruments, 68, 852

Santos, M. G., & Kepler, S. O. 2012, MNRAS, 423, 68

Saumon, D., Holberg, J. B., & Kowalski, P. M. 2014, ArXiv e-prints

Schlüter, H., & Avila, C. 1966, ApJ, 144, 785

Schoenberner, D. 1983, ApJ, 272, 708

Schoning, T. 1994, A&A, 282, 994

Seaton, M. J. 1990, Journal of Physics B Atomic Molecular Physics, 23, 3255

Seidel, J. 1977, Zeitschrift Naturforschung Teil A, 32, 1195

Shipman, H. L. 1979, ApJ, 228, 240

Shipman, H. L., & Mehan, R. G. 1976, ApJ, 209, 205

Shipman, H. L., & Sass, C. A. 1980, ApJ, 235, 177

Shu, F. H. 1991, Physics of Astrophysics, Vol. I (University Science Books)

Shumaker, J. B., & Popenoe, C. H. 1968, Physical Review Letters, 21, 1046

Silvestri, N. M., Oswalt, T. D., Wood, M. A., Smith, J. A., Reid, I. N., & Sion, E. M. 2001, AJ, 121, 503

Sinars, D. B., Wenger, D. F., Pikuz, S. A., Jones, B., Geissel, M., Hansen, S. B., Coverdale, C. A., Ampleford, D. J., Cuneo, M. E., McPherson, L. A., & Rochau, G. A. 2011, Review of Scientific Instruments, 82, 063113

Sion, E. M., Greenstein, J. L., Landstreet, J. D., Liebert, J., Shipman, H. L., & Wegner, G. A. 1983, ApJ, 269, 253

Sion, E. M., Holberg, J. B., Oswalt, T. D., McCook, G. P., & Wasatonic, R. 2009, AJ, 138, 1681

Slutz, S. A., Bailey, J. E., Chandler, G. A., Bennett, G. R., Cooper, G., Lash, J. S., Lazier, S., Lake, P., Lemke, R. W., Mehlhorn, T. A., Nash, T. J., Nielson, D. S., McGurn, J., Moore, T. C., Ruiz, C. L., Schroen, D. G., Torres, J., Varnum, W., & Vesey, R. A. 2003, Physics of Plasmas, 10, 1875

Smartt, S. J. 2009, ARA&A, 47, 63

Smith, C. S. 1954, Physical Review, 94, 42

Smith, E. W., Cooper, J., & Vidal, C. R. 1969, Physical Review, 185, 140

Spencer, G. H., & Murty, M. V. R. K. 1962, Journal of the Optical Society of America (1917-1983), 52, 672

Spielman, R. B., Deeney, C., Chandler, G. A., Douglas, M. R., Fehl, D. L., Matzen, M. K., McDaniel, D. H., Nash, T. J., Porter, J. L., Sanford, T. W. L., Seamen, J. F., Stygar, W. A., Struve, K. W., Breeze, S. P., McGurn, J. S., Torres, J. A., Zagar,

D. M., Gilliland, T. L., Jobe, D. O., McKenney, J. L., Mock, R. C., Vargas, M., Wagoner, T., & Peterson, D. L. 1998, Physics of Plasmas, 5, 2105

Spielman, R. B., Deeney, C., Fehl, D. L., Hanson, D. L., Keltner, N. R., McGurn, J. S., & McKenney, J. L. 1999, Review of Scientific Instruments, 70, 651

Spielman, R. B., Ruggles, L. E., Pepping, R. E., Breeze, S. P., McGurn, J. S., & Struve, K. W. 1997, Review of Scientific Instruments, 68, 782

Spitzer, L., & Härm, R. 1953, Physical Review, 89, 977

Stambulchik, E., Fisher, D. V., Maron, Y., Griem, H. R., & Alexiou, S. 2007, High Energy Density Physics, 3, 272

Stambulchik, E., & Maron, Y. 2006, J. Quant. Spec. Radiat. Transf., 99, 730

Stamm, R., Smith, E. W., & Talin, B. 1984, Phys. Rev. A, 30, 2039

Stehlé, C. 1994, A&AS, 104, 509

Stehlé, C., & Hutcheon, R. 1999, A&AS, 140, 93

Stehlé, C., & Jacquemot, S. 1993, A&A, 271, 348

Stewart, J. C., & Pyatt, Jr., K. D. 1966, ApJ, 144, 1203

Strömgren, B. 1939, ApJ, 89, 526

Stygar, W. A., Cuneo, M. E., Headley, D. I., Ives, H. C., Leeper, R. J., Mazarakis, M. G., Olson, C. L., Porter, J. L., Wagoner, T. C., & Woodworth, J. R. 2007, Physical Review Special Topics Accelerators and Beams, 10, 030401

Stygar, W. A., Olson, R. E., Spielman, R. B., & Leeper, R. J. 2001, Phys. Rev. E, 64, 026410

Tomita, A. 1982, Appl. Opt., 21, 2655

Torres, F., Gigosos, M. A., & Mar, S. 1984, J. Quant. Spec. Radiat. Transf., 31, 265

Touma, J. E., Oks, E., Alexiou, S., & Derevianko, A. 2000, J. Quant. Spec. Radiat. Transf., 65, 543

Tremblay, P.-E., & Bergeron, P. 2008, ApJ, 672, 1144

—. 2009, ApJ, 696, 1755

Tremblay, P.-E., Bergeron, P., & Gianninas, A. 2011a, ApJ, 730, 128

Tremblay, P.-E., Bergeron, P., Kalirai, J. S., & Gianninas, A. 2010, ApJ, 712, 1345

Tremblay, P.-E., Ludwig, H.-G., Steffen, M., Bergeron, P., & Freytag, B. 2011b, A&A, 531, L19

Tremblay, P.-E., Ludwig, H.-G., Steffen, M., & Freytag, B. 2013a, A&A, 552, A13

—. 2013b, A&A, 559, A104

Uhlenbusch, J., & Viöl, W. 1990, J. Quant. Spec. Radiat. Transf., 44, 47

Unsöld, A. 1948, ZAp, 24, 355

van Etten, W., Lambo, W., & Simons, P. 1985, Appl. Opt., 24, 970

van Trigt, C. 1976, Phys. Rev. A, 13, 734

Varma, B. P., & Ghosh, C. 1973, Journal of Physics D Applied Physics, 6, 628

Vennes, S., Thejll, P. A., Galvan, R. G., & Dupuis, J. 1997, ApJ, 480, 714

Vidal, C. R., Cooper, J., & Smith, E. W. 1973, ApJS, 25, 37

Voss, B., Koester, D., Napiwotzki, R., Christlieb, N., & Reimers, D. 2007, A&A, 470, 1079

Vujnović, V., Harrison, J. A., & Craggs, J. D. 1962, Proceedings of the Physical Society, 80, 516

Wagner, R. E., & Sandahl, C. R. 1982, Appl. Opt., 21, 1381

Wang, L., Yorke, E., Desobry, G., & Chui, C. 2002, Journal of Applied Clinical Medical Physics, 3, 51

Wegner, G. 1979, AJ, 84, 1384

Wegner, G., & Reid, I. N. 1991, ApJ, 375, 674

Weidemann, V., & Koester, D. 1984, A&A, 132, 195

Weiss, J. D. 1992, Journal of Lightwave Technology, 10, 531

Werner, K., Heber, U., & Hunger, K. 1991, A&A, 244, 437

Wheeler, J. C. 2012, ApJ, 758, 123

Wheeler, J. C., & Hansen, C. J. 1971, Ap&SS, 11, 373

Whelan, J., & Iben, Jr., I. 1973, ApJ, 186, 1007

Wiese, W. L., Kelleher, D. E., & Helbig, V. 1975, Phys. Rev. A, 11, 1854

Wiese, W. L., Kelleher, D. E., & Paquette, D. R. 1972, Phys. Rev. A, 6, 1132

Wiese, W. L., Paquette, D. R., & Solarski, J. E. 1963, Physical Review, 129, 1225

Williams, K. A., Bolte, M., & Koester, D. 2009, ApJ, 693, 355

Winget, D. E., Hansen, C. J., Liebert, J., van Horn, H. M., Fontaine, G., Nather, R. E., Kepler, S. O., & Lamb, D. Q. 1987, ApJ, 315, L77

Winget, D. E., & Kepler, S. O. 2008, ARA&A, 46, 157

Winget, D. E., Kepler, S. O., Campos, F., Montgomery, M. H., Girardi, L., Bergeron, P., & Williams, K. 2009, ApJ, 693, L6

Winget, D. E., Nather, R. E., Clemens, J. C., Provencal, J., Kleinman, S. J., Bradley, P. A., Wood, M. A., Claver, C. F., Frueh, M. L., Grauer, A. D., Hine, B. P., Hansen, C. J., Fontaine, G., Achilleos, N., Wickramasinghe, D. T., Marar, T. M. K., Seetha, S., Ashoka, B. N., O'Donoghue, D., Warner, B., Kurtz, D. W., Buckley, D. A., Brickhill, J., Vauclair, G., Dolez, N., Chevreton, M., Barstow, M. A., Solheim, J. E., Kanaan, A., Kepler, S. O., Henry, G. W., & Kawaler, S. D. 1991, ApJ, 378, 326

Wisotzki, L., Christlieb, N., Bade, N., Beckmann, V., Köhler, T., Vanelle, C., & Reimers, D. 2000, A&A, 358, 77

Wood, M. A. 1995, in White Dwarfs, Proceedings of the 9th European Workshop on White Dwarfs Held at Kiel, Germany, 29 August - 1 September 1994. Lecture

Notes in Physics, Vol. 443, edited by Detlev Koester and Klaus Werner. Springer-Verlag, Berlin Heidelberg New York, 1995., p.41, ed. D. Koester & K. Werner, 41–+

Woosley, S. E., & Weaver, T. A. 1986, ARA&A, 24, 205

York, D. G., Adelman, J., Anderson, Jr., J. E., Anderson, S. F., Annis, J., Bahcall, N. A., Bakken, J. A., Barkhouser, R., Bastian, S., Berman, E., Boroski, W. N., Bracker, S., Briegel, C., Briggs, J. W., Brinkmann, J., Brunner, R., Burles, S., Carey, L., Carr, M. A., Castander, F. J., Chen, B., Colestock, P. L., Connolly, A. J., Crocker, J. H., Csabai, I., Czarapata, P. C., Davis, J. E., Doi, M., Dombeck, T., Eisenstein, D., Ellman, N., Elms, B. R., Evans, M. L., Fan, X., Federwitz, G. R., Fiscelli, L., Friedman, S., Frieman, J. A., Fukugita, M., Gillespie, B., Gunn, J. E., Gurbani, V. K., de Haas, E., Haldeman, M., Harris, F. H., Hayes, J., Heckman, T. M., Hennessy, G. S., Hindsley, R. B., Holm, S., Holmgren, D. J., Huang, C.-h., Hull, C., Husby, D., Ichikawa, S.-I., Ichikawa, T., Ivezić, Ž., Kent, S., Kim, R. S. J., Kinney, E., Klaene, M., Kleinman, A. N., Kleinman, S., Knapp, G. R., Korienek, J., Kron, R. G., Kunszt, P. Z., Lamb, D. Q., Lee, B., Leger, R. F., Limmongkol, S., Lindenmeyer, C., Long, D. C., Loomis, C., Loveday, J., Lucinio, R., Lupton, R. H., MacKinnon, B., Mannery, E. J., Mantsch, P. M., Margon, B., McGehee, P., McKay, T. A., Meiksin, A., Merelli, A., Monet, D. G., Munn, J. A., Narayanan, V. K., Nash, T., Neilsen, E., Neswold, R., Newberg, H. J., Nichol, R. C., Nicinski, T., Nonino, M., Okada, N., Okamura, S., Ostriker, J. P., Owen, R., Pauls, A. G., Peoples, J., Peterson, R. L., Petravick, D., Pier, J. R.,

Pope, A., Pordes, R., Prosapio, A., Rechenmacher, R., Quinn, T. R., Richards, G. T., Richmond, M. W., Rivetta, C. H., Rockosi, C. M., Ruthmansdorfer, K., Sandford, D., Schlegel, D. J., Schneider, D. P., Sekiguchi, M., Sergey, G., Shimasaku, K., Siegmund, W. A., Smee, S., Smith, J. A., Snedden, S., Stone, R., Stoughton, C., Strauss, M. A., Stubbs, C., SubbaRao, M., Szalay, A. S., Szapudi, I., Szokoly, G. P., Thakar, A. R., Tremonti, C., Tucker, D. L., Uomoto, A., Vanden Berk, D., Vogeley, M. S., Waddell, P., Wang, S.-i., Watanabe, M., Weinberg, D. H., Yanny, B., & Yasuda, N. 2000, AJ, 120, 1579

Zhu, H., Hill, G., Besen, M., Smith, D., & Blackborow, P. 2012, Ultrahigh Brightness and Broadband Laser-Driven Light Source, Technical note, Energetiq Technology, Inc., Woburn, MA

Zimmerman, G., Kershaw, D., Bailey, D., & Harte, J. 1978, Journal of the Optical Society of America (1917-1983), 68, 549